博士論文

A thesis submitted for the degree of Doctor of Philosophy

農業・食品廃棄物由来セルロースナノファイバーによるPickeringエマルションの不安定化機構の解明

Elucidation of instability mechanisms for Pickering emulsions using cellulose nanofibers derived from agricultural/food waste

横浜国立大学大学院　理工学府

Yokohama National University

Graduate School of Engineering Science

金井　典子

Noriko KANAI

2023年　9月

September 2023

Table of Contents

Abstract

This thesis studied Pickering emulsions (PEs) stabilized by cellulose nanofibers (CNFs) isolated from agricultural/food waste. The first half of the thesis focused on the development CNFs as stabilizers, while the second half elucidated the instability mechanisms of PEs. PE, a system stabilized by diverse micro- or nanoparticles alternative to conventional surfactants concerning for their environmental pollution, has a great deal of interest as an environmentally friendly technology in food, cosmetics, and pharmaceutical industries.

CNFs obtained from cellulose fibrils in plant cell walls through fibrillation have shown promise as stabilizer/emulsifier for oil-in-water PEs. While wood has been the primary source of CNFs worldwide on both laboratory and industrial scales, agricultural/food waste is an attractive lignocellulose source which is inexpensive, abundant, and renewable. It is expected that the source of cellulose does not significantly impact the emulsification capacity for PE due to the common crystal structure, cellulose I. Thus, two agricultural/food wastes, spent coffee grounds and hop stems, were explored as new agricultural/food waste CNF sources.

Among several CNF isolation methods have been developed, 2,2,6,6-tetramethylpiperidinyl-1-oxyl (TEMPO)-mediated oxidation is widely recognized as an energy efficiency technique to obtain surface-carboxylated CNFs having uniform widths of cellulose microfibrils (3–4 nm) and high aspect ratio (> 150). These TEMPO-oxidized CNFs (TCNFs) were reported to inhibit droplet coalescence with lower concentrations than mechanically fibrillated CNFs.

Due to the high adsorption energy, CNFs strongly and irreversibly adsorb at the oil/water interface, forming a thick coat around oil droplets. Excess CNFs also form an entangled network and act as thickening agents in the continuous phase. These stabilization mechanisms provide higher stability than conventional emulsions and prevent various instability mechanisms such as flocculation, coalescence, and Ostwald ripening. However, the long-term instability behaviors of PEs, which are determined by the balance of multiple factors including CNF morphology, concentrations, surface characters as well as oil properties, have not been fully elucidated. This thesis aimed to

elucidate instability mechanisms for PEs using TCNFs derived from agricultural/food waste to achieve highly stable PEs with low TCNF concentrations.

The first phase involved isolation of TCNFs from spent coffee grounds and hop stems as new sources of agricultural/food waste. The pretreatment scheme prior to TEMPO-mediated oxidation was optimized based on the contents of cellulose, hemicellulose, and lignin. The morphology and widths of the obtained TCNFs were measured using field emission scanning electron microscopy and atomic force microscopy. The crystal structure and microfibril widths were determined from X-ray diffraction patterns while the purity and crystallinity of TCNFs were examined using solid-state nuclear magnetic resonance (NMR). The thermal decomposition temperatures were measured using thermogravimetric analysis. TCNFs derived from spent coffee grounds exhibited the same crystal structure and comparable thermal stability as wood-derived TCNFs. However, TEMPO-mediated oxidation consumed 3–18 times more sodium hypochlorite than wood-derived TCNFs, and the low yield posed a significant challenge for their use as stabilizers. On the contrary, TCNFs derived from hop stem yielded around 25% and possessed comparable fiber morphology, purity, thermal stability, and viscosity to wood-derived TCNFs, which was applicable to PE stabilizers.

The second phase aimed to prepare stable oil-in-water PEs for one month after emulsification. The preparation conditions of hop stem-derived TCNFs concentrations, water/oil ratios, and oil types (dodecane and olive oil) were investigated. The long-term instability of dodecane and olive oil PE was systematically compared over the period of one month using droplet size distribution analysis, microscopy observations, and viscosity measurements. Stable PEs were successfully obtained with 1% TCNF and less than 20% oil ratios. The droplet size obtained at the identical TCNF concentration depended on the oil types. Olive oil, which includes multicomponents such as triglycerides and other polar components, tended to form less stable PE than dodecane as a single oil. The dodecane and olive oil PEs underwent multiple instability mechanisms with different contributions for one month.

In the third phase, high resolution magnetic resonance imaging (MRI) employed ‘entire’ PE to visualize the long-term instability behavior and investigate relaxation times (T_1 and T_2) and diffusion properties. The MR images provided deep insights into the microstructure of dodecane and olive oil PEs with a resolution of 100–200 micrometers, successfully visualizing aggregated/coalesced oil droplets near the PE surface. The entire PEs were mapped by voxelwise T_1, T_2, and apparent diffusion coefficient from T_1-weighted, T_2-weighted, and diffusion-weighted images, respectively to investigate the effects of TCNF concentration and oil type. Also, the relaxation and diffusion properties of bulk oils obtained by MRI and NMR were compared, and the advantages and limitations of MRI techniques were discussed. While T_2 distributions were significantly influenced by the MRI sequence, T_1 maps reflected the microstructural changes due to the droplet coalescence and aggregation evolution, suggesting that T_1 maps can non-invasively evaluate the relaxation time and microstructure of PE.

The research significances of this study are (i) the isolation of TCNFs from new promising waste sources comparable to wood, (ii) the systematic elucidation of the stabilization factors for PEs, and (iii) the demonstration of high-resolution MRI as a powerful evaluation technique for understanding instability mechanisms of PEs.

These results will contribute to the development of a circular economy and sustainable waste revalorization in the fields of agricultural chemistry, food science, and materials science.

List of Publication

This thesis is a summary of the following publications referred to by their Roman numbers from I to IV throughout the thesis.

I. **N. Kanai**, T. Honda, N. Yoshihara, T. Oyama, A. Naito, K. Ueda, I. Kawamura "Cellulose nanofibers isolated from spent coffee grounds and their composite films with poly(vinyl alcohol): a new non-wood source" (2020) ***Cellulose*** 27, 5017–5028.

II. **N. Kanai**, K. Nishimura, S. Umetani, Y. Saito, H. Saito, T. Oyama, I. Kawamura "Upcycling of waste hop stems into cellulose nanofibers: isolation and structural characterization" (2021) ***ACS Agric. Sci. Technol.*** 1, 347–354.

III. **N. Kanai**, T. Sakai, K. Yamada, S. Kumagai, I. Kawamura "Using cellulose nanofibers isolated from waste hop stems to stabilize dodecane or olive oil-in-water Pickering emulsions" (2022) ***Colloids Surf. A*** 653, 129956.

IV. **N. Kanai**, S. A. Willis, A. Gupta, I. Kawamura, W. S. Price "Evaluating the stability of cellulose nanofiber Pickering emulsions using MRI and relaxometry" (2023) ***Langmuir*** 39, 3905–3913.

Reference journal articles are listed below.

V. **N. Kanai**, N. Yoshihara, I. Kawamura "Solid-state NMR characterization of triacylglycerol and polysaccharides in coffee beans" (2019) ***Biosci. Biotechnol. Biochem.*** 83, 803–809.

VI. K. R. Harris, **N. Kanai**, W. S. Price, A. M. Torres, S. A. Willis, T. Rodopoulos, J. Veder, T. Rüther "A volumetric and intra-diffusion study of solutions of $AlCl_3$ in two ionic liquids - [C_2TMEDA][Tf_2N] and [C_4mpyr][Tf_2N]" (2022) ***Phys. Chem. Chem. Phys.*** 24, 24924–24938.

VII. **N. Kanai**, W. S. Price, O. Söderman "Self-diffusion coefficients of heavy water in low *n*-alkanes" (2023) ***J. Mol. Liq.*** 388, 122713.

VIII. K. Yamada, **N. Kanai**, I. Kawamura “Evaluation of the water repellency and structure of cellulose nanofibers derived from waste hop stems using a fluoroalkyl silane coupling treatment” (2023) ***Waste Biomass Valori.*** In press.

The other related book chapters written in Japanese are listed below.

i. 金井 典子, 川村 出 “コーヒー粕を原料としたセルロースナノファイバーとコンポジットフィルム” ***コンバーテック***, Vol. 569, No. 48, pp. 116–119 (2020)

ii. 金井 典子, 川村 出 第 1 編 第 2 章 5 節 “農業廃棄物からの CNF 製造” ***NTS 出版***『セルロースナノファイバー研究と実用化の最前線』pp. 155–161 (2021)

iii. 金井 典子, 川村 出 “ホップ蔓由来セルロースナノファイバーの製造” ***月刊 JETI*** Vol. 70, No. 4, pp. 43–45 (2022)

iv. 金井 典子, 山田 浩平, 川村 出 第 IV 編 第 11 章 “農業／食品廃棄物からのセルロースナノファイバー製造と乳化安定剤への使用” ***CMC 出版***『食品ロス削減と食品廃棄物資源化の技術』pp. 228–237 (2023)

v. 金井 典子, 川村 出 “ピッカリングエマルションの粒子安定剤としての農業/食品廃棄物由来セルロースナノファイバーの利用” ***繊維学会誌***, Vol. 79, No. 5, pp. 145–149 (2023)

Conference Presentations

International Conferences

[Oral presentations]

1. **N. Kanai**, S. A. Willis, A. Gupta, I. Kawamura, W. S. Price, Elucidation of instability mechanisms for cellulose nanofiber Pickering emulsions using MRI. *ICC2022+1*, Hiroshima, Japan, 26th-28th September, **2023**.
2. **N. Kanai**, S. A. Willis, A. Gupta, I. Kawamura, W. S. Price, MRI relaxation and diffusion studies evaluating cellulose nanofiber Pickering emulsions stabilization. *APNMR 2023*, Taipei, Taiwan, 6th-9th September, **2023**.
3. **N. Kanai**, S. A. Willis, A. Gupta, I. Kawamura, W. S. Price, MRI and relaxation studies of evaluating Pickering emulsions stabilization. *ANZMAG 2022*, Peppers Marysville, Victoria, Australia, 4th-8th December, **2022**.
4. **N. Kanai**, K. Ueda, A. Naito, I. Kawamura, Solid-state NMR characterization of cellulose nanofibers isolated from spent coffee grounds. *Pacifichem 2021,* Virtual, 16th-21st December, **2021**.
5. **N. Kanai**, A. Naito, I. Kawamura, Spent coffee grounds as a new source of cellulose nanofibers. *9th (biennial) Western Sydney University & Inaugural Asian Symposium on NMR, MRI & Diffusion 2020*, zoom Webinar, 2nd-3rd December, **2020**.

[Poster presentations]

1. **N. Kanai**, S. A. Willis, A. Gupta, I. Kawamura, W. S. Price, MRI relaxation and diffusion studies evaluating cellulose nanofiber Pickering emulsions stabilization. *APNMR 2023*, Taipei, Taiwan, 6th-9th September, **2023**.
2. **N. Kanai**, K. Nishimura, I. Kawamura, Solid-state NMR Characterization of Cellulose Nanofibers Isolated from Waste Hop Stem. *ISMAR-APNMR-NMRSJ-SEST 2021*, Online Webinar, 22nd-27th August, **2021**.

Domestic Conferences (in Japan)

[Oral presentations]

1. **金井 典子**, 梅谷 世龍, 西村 恒亮, 大山 俊幸, 川村 出, 農業廃棄物ホップつるからのCNF生成と構造解析 *セルロース学会第28回年次大会*, オンライン開催, 2021年9月

30日~10月1日

2. **金井 典子**, 川村 出, William S. Price, パルス磁場勾配NMRによるコーヒー粕由来脂質成分の自己拡散係数測定 *第59回NMR討論会*, 群馬, 2020年11月17日~11月19日

[Poster presentations]

1. **金井 典子**, 川村 出, William S. Price, パルス磁場勾配NMRによるコーヒー粕由来脂質成分の自己拡散係数測定 *第59回NMR討論会*, 群馬, 2020年11月17日~11月19日

Abbreviations

Abbreviation	**Name**
AFM	Atomic force microscopy
AFW	Agricultural/food waste
BCN	Bacterial cellulose nanocrystal
BW	Bandwidth
CLSM	Confocal laser scanning microscopy
CNC	Cellulose nanocrystal
CNF	Cellulose nanofiber
COM	Calcium oxalate monohydrate
CP	Cross polarization
CP-MAS	Cross polarization combined with magic angle spinning (solid-state NMR sequence)
CPMG	Carr-Purcell-Meiboom-Gill (transverse relaxation measurement sequence)
CSA	Chemical shift anisotropy
DSD	Droplet size distribution
DWI	Diffusion weighting imaging
FAW	Fat and water
FE-SEM	Field emission scanning electron microscopy
FID	Free induction decay
FLASH	Fast low-angle shot (MRI sequence)
FOV	Field of view
FWHM	Full width at the half maximum
GCB	Green coffee bean
HS	Hop stem
MAS	Magic angle spinning
MCC	Microcrystalline cellulose
MFC	Microfibrillated cellulose
MRI	Magnetic resonance imaging

MSME	Multi-slice-multi-echo (MRI sequence)
NC	Nanocellulose
NMR	Nuclear magnetic Resonance
o/w, w/o	Oil-in-water, Water-in-oil
PE	Pickering emulsion
PGSE	Pulsed gradient spin-echo
PGSTE	Pulsed gradient stimulated-echo
PVA	Poly(vinyl alcohol)
RARE	Rapid acquisition with relaxation enhancement (MRI sequence)
RAREVTR	RARE with variable recycle delay (MRI sequence)
RCB	Roasted coffee bean
rf	Radio frequency
ROI	Selected region of interest
SCG	Spent coffee ground
TAG	Triacylglycerol
TCNF	TEMPO-oxidized cellulose nanofiber
TEMPO	2,2,6,6-tetramethylpiperidine-1-oxyl
TGA	Thermogravimetric analysis
XRD	X-ray diffraction analysis

Symbol	**Definition**
ADC	Apparent diffusion coefficient (m^2 s^{-1})
b	Diffusion weighting factor
$\mathbf{B}_0$	Static magnetic field (T)
$\mathbf{B}_1$	Radio-frequency field (T)
$\mathbf{B}_{\mathbf{eff}}$	Effective magnetic field (T)
CI_{NMR}	Crystallinity index determined from NMR (%)
CI_{XRD}	Crystallinity index determined from XRD (%)
D	Self-diffusion coefficient (m^2 s^{-1})
d_v	Mean diameter of the droplet

$\mathbf{g}$	Applied magnetic field gradient
$\mathbf{G}$	Applied magnetic field gradient for MRI
g	Strength of applied magnetic field gradient (T m^{-1})
h	Planck’s constant
I	Spin angular momentum
$\mathbf{M}_0$	Net magnetization
$\mathbf{r}$	Position of a particle or voxel
T_E	Echo time in an MRI pulse sequence
T_R	Repetition time in an MRI sequence
Δ	Diffusion time (s)
T_1	Longitudinal relaxation time (s)
T_2	Transverse relaxation time (s)
δ	Chemical shift (ppm)
δ	Duration of the gradient pulse (s)
δ_iso	Isotropic average of the chemical shift (ppm)
γ	Gyromagnetic ratio
$\boldsymbol{\mu}$	Magnetic moment
ρ	Nuclear spin density
σ	Interfacial tension
τ	Interval between pulses (s)
ω, ν	Frequency (rad s^{-1}) or (Hz)
ω_0	Larmor frequency (rad s^{-1})

Chapter 1 – Cellulose Nanofibers

1.1. Cellulose in Plants

Cellulose is a polysaccharide polymer of β-(1→4) D-glucopyranosyl units, and the repeat unit is D-glucose (not cellobiose) including hydroxy groups at C2, C3, and C6 (**Fig. 1**).[1] The intrachain hydrogen bonding between those hydroxyl groups and oxygen molecules of the adjoining ring take responsible for the stable conformation of cellulose in the linear chain.[2] Cellulose, biosynthesized by photosynthesis in plants, is the main component of plant cell walls along with hemicellulose and lignin, and provide the physical strength to plans. Van der Waals and intermolecular hydrogen bonds facilitate the parallel stacking of multiple cellulose chains forming elementary fibrils that further aggregate into cellulose microfibrils. Cellulose microfibrils in wood are polymerized by terminal enzyme complexes in cell walls and are generally 3–4 nm wide (consist of 30–40 chains of cellulose, depending on species) and contain both crystalline and amorphous regions.[3] The underlying structure of cellulose microfibril provides long-term strong resistance against various external stress (e.g., gravity, rain, and biological attack) (**Fig. 2**).

The crystal allomorphs of cellulose microfibrils were unraveled by ^{13}C solid-state nuclear magnetic resonance (NMR) in the 1980s. Native cellulose, produced by diverse organisms (e.g., plants, trees, algae, and bacteria) in nature, has a common crystal structure of cellulose I, and cellulose I is a mixture of two different crystal phases, Iα and Iβ, which coexist in various proportions among species.[4] There are several different

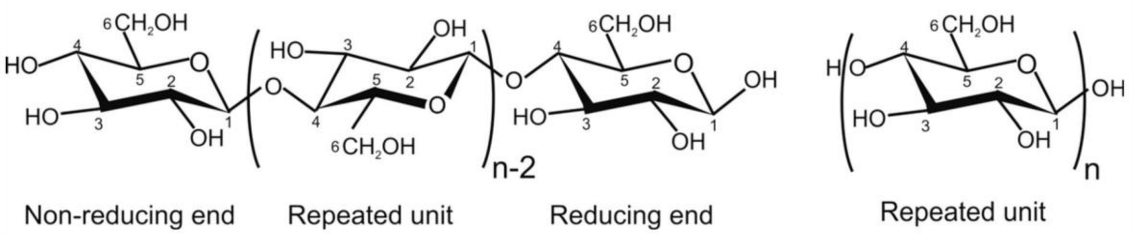

Fig. 1. Depictions of the chemical structure of cellulose that conform to established convention (adapted from French[1]).

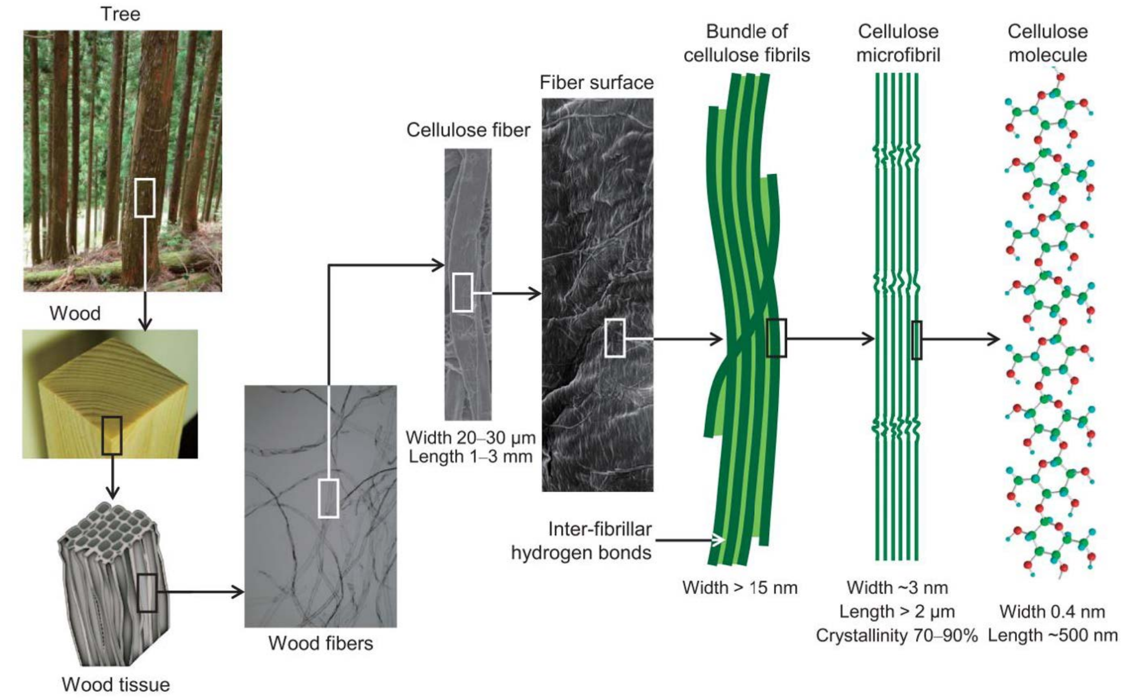

Fig. 2. Hierarchical structure, showing the arrangement of cellulose fiber, microfibrils, and molecules in plant cell walls (adapted from Isogai et al.[3]).

polymorphs of cellulose that have been reported, e.g., cellulose II, III_I, III_{II} IV_I, IV_{II}, but native cellulose I will be focused in the thesis.

The cellulose Iα structure has a triclinic structure and is dominant for algae and bacteria,[5] whereas the cellulose Iβ has a monoclinic structure and is dominant for higher plants where the major component is the secondary wall (**Fig. 3**).[4] Nishiyama et al. determined the detail crystallographic structures (better than 1Å resolution) and hydrogen-bonding arrangement in Iα and Iβ using X-ray and electron diffraction techniques in 2002 and 2003.[6,7] The distinct difference between Iα and Iβ is characterized by the relative displacement of cellulose sheets in the chain direction – each sheet is similarly shifted in the *c*- axis direction by +c/4 for Iα while the displacement alternates between +c/4 and −c/4 for Iβ.[2,8]

1.2. Characteristics of Cellulose Nanofibers

Since the 2000s, a nanometer wide cellulose (i.e., nanocelluloses; NCs) was isolated from plants by cutting numerous hydrogen bonds present between cellulose microfibrils and

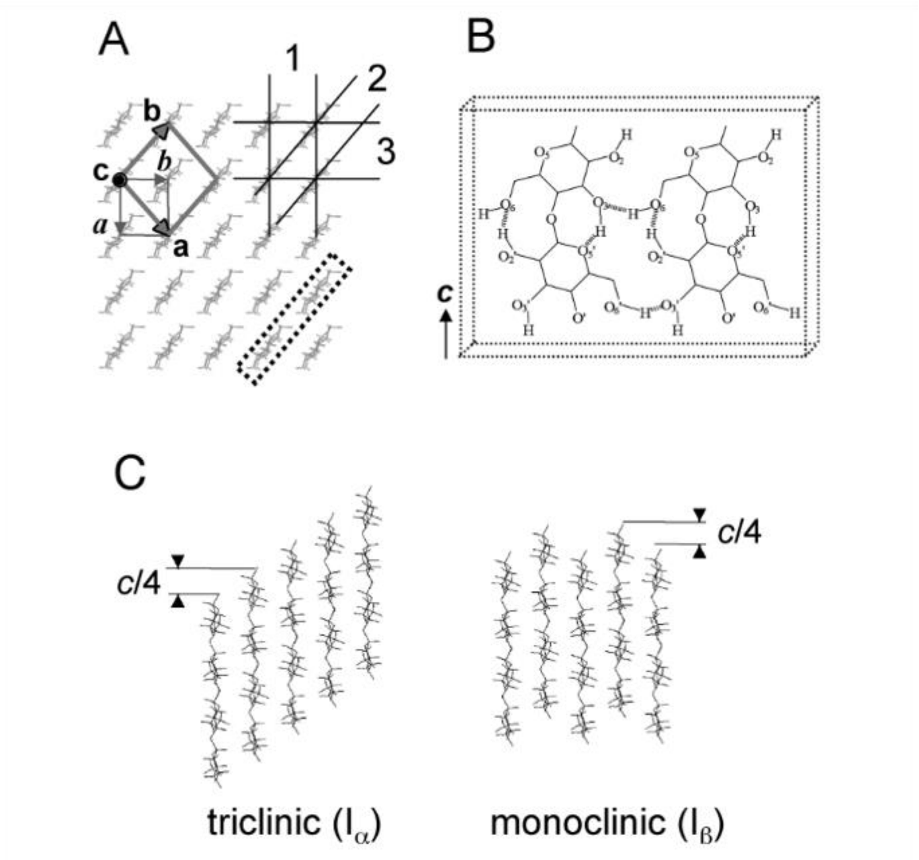

Fig. 3. Current structural model of crystalline native cellulose. (A) Cross-sectional view of a cellulose I crystal. The unit cells of I_α and I_β crystals are shown by thin and bold lines, respectively. As outlined in the dotted box, sheets are formed by molecular chains stabilized by the network of H-bondings described in (B). (C) the displacement of the hydrogen bonding sheets for I_α of +c/4, and I_β alternating +c/4 and –c/4. The figure and caption were adapted from Imai et al.[8] and Moon et al.[2]

was named cellulose nanofibers (CNFs). CNFs are defined as those of < 100 nm wide and originate from cellulose microfibrils or their bundles.[9] CNFs have unique and fascinating properties in materials science such as excellent resistance, chemical inertness, renewability, transparent appearance, stiffness, biocompatibility, high specific area, biodegradability, low thermal expansion coefficient, stable structure, low density, high surface area-to-volume ratio.[10] Taking advantage of these properties, cellulose nanomaterials have been extensively investigated as mechanical reinforcement, packaging/coatings, biomedical or drug delivery matrix, electrical/optical materials, and thickening agent/emulsion stabilizer in food and cosmetic products (**Fig. 4**).

Fig. 4 Main applications of nanocellulose adapted from Mateo et al.[10].

Various applications of CNFs have been gradually commercialized. According to Yano Research Institute Ltd., global CNF production in 2022 is expected to reach 80 tons (140.4% of the previous year's production) and will hit to 3,000 tons by 2030. CNF is attracted worldwide attention as a biobased nanomaterial driven by the demand for the establishing sustainable society, forming of a non-petroleum-based industrial infrastructure, and the reduction of carbon dioxide emissions.[11]

1.3. Source of Cellulose Nanofibers

1.3.1. Wood

Wood has been the primary source for CNFs (**Table 1**). Therefore, the supply of CNF raw materials is closely linked to the forestry and paper industries. Softwoods used for wood pulp production in the Japanese paper industry are, for example, pines, Japanese cedar,

Table 1. List of 100 CNF sources with publication counts adapted from Pennells et al.[12]

#	CNF Source	Count	#	CNF Source	Count	#	CNF Source	Count
1	Wood	1724	35	Triticale	4	69	Persimmon	1
2	Bacteria	404	36	Water hyacinth	3	70	*Pandanus*	1
3	Cotton	136	37	Rapeseed	3	71	*Panax ginseng*	1
4	Bamboo	92	38	Cassava	3	72	Olive	1
5	Palm fruit bunch	56	39	Barley	3	73	Napier grass	1
6	Sugarcane	53	40	Tobacco	2	74	Municipal waste	1
7	Rice	49	41	Sunflower	2	75	Mulberry	1
8	Algae	44	42	Roselle	2	76	Marram grass	1
9	Wheat	42	43	Quince	2	77	Lime	1
10	CELISH	38	44	Mangosteen	2	78	Licorice	1
11	Banana	38	45	Lupin hull	2	79	*Leucaena*	1
12	Kenaf	31	46	Kapok	2	80	Lemongrass	1
13	Jute	31	47	Ginger	2	81	Khaya seeds	1
14	Sisal	27	48	Garlic	2	82	Japanese hop	1
15	Maize	27	49	Fique	2	83	Grass	1
16	Hemp	22	50	Dandelion	2	84	Ginkgo	1
17	Flax	19	51	Almond	2	85	Durian	1
18	Paper sludge	18	52	Abaca	2	86	Cellulosic residue	1
19	Pineapple	14	53	Teabags	1	87	Colocynth	1
20	Spinifex	13	54	Taro	1	88	Cogon	1
21	Oat	13	55	Tagasaste	1	89	Coffee filters	1
22	Soybean	10	56	Sweet potato	1	90	Citronella	1
23	Orange	9	57	Sudachi	1	91	Cattail	1
24	Tunicate	8	58	Satingrass	1	92	*Calotropis procera*	1
25	Sugar beet	8	59	Ryegrass	1	93	Cabbage	1
26	Canola	8	60	Rutabaga	1	94	Beavertail cactus	1
27	Curaua	7	61	Reed	1	95	*Bassia eriophora*	1
28	Coconut	7	62	Red pepper	1	96	Argan	1
29	Agave	7	63	Ramie	1	97	Apple	1
30	Mango	6	64	Potato	1	98	*Amorpha*	1
31	Beer residue	6	65	*Posidonia oceanica*	1	99	*Aloe*	1
32	Alfa	6	66	Pomelo	1	100	Acai palm	1
33	Isora	5	67	Pomace	1		Unknown	285
34	Carrot	5	68	Pistachio	1		N/A	1665

and spruce, while hardwoods are Japanese beech, maple, and poplar. The α-cellulose content is approximately 50% for softwoods and 48% for hardwoods.[13] After the wood is cut into wood chips, lignin is removed by a kraft process using sodium hydroxide and sodium sulfide. The kraft pulp is then bleached with oxygen and chlorine dioxide to obtain bleached kraft pulp having high cellulose contents. Bleached softwood/hardwood kraft pulps contain more than 85% cellulose and is used as the starting material for CNF in the laboratory level.

Imported wood accounts for about 70% of the CNF source produced in Japan.[14] In May 2021, due to the rapid demand for building materials during the COVID-19 pandemic, the future price of lumber was recorded as nearly four times higher than before the pandemic. Using domestic softwoods such as Japanese cedar as raw material for CNF has been considered, but their competition with building materials has been concerned.

1.3.2. Agricultural/food Waste

Agricultural/food waste (AFW) offers an attractive alternative to CNF sources. AFW refers to by-products of crops harvested primarily for food/beverage or generated from industrially-processed biomass. AFW is characterized as lignocellulosic biomass which is inexpensive, renewable, and fast generation. The chemical composition difference between wood and AFW, such as cellulose, hemicellulose, and lignin contents are a critical factor in the production of CNF. Vassilev et al.[15] summarized cellulose, hemicellulose, and lignin contents of 53 herbaceous/agricultural biomass. The difference in cellulose content was not significant between wood and herbaceous/agricultural biomass sources, typically 35–50 %. The hemicellulose content tends to be slightly higher in herbaceous/agricultural biomass typically 25–35 %, and the lignin content tends to be lower, around 20%.

Various AFW has been investigated for sources of CNFs as shown in **Table 1**, such as empty fruit bunches of palm trees, squeezed lees of sugar cane, banana peels, pineapple leaves, and mandarin orange peels. Detailed isolation, characterization, and potential applications from these AFW for CNFs are presented elsewhere.[10,12,16] Importantly, AFW-derived CNF generally offers similar properties and performance to wood-derived CNF while also fulfilling upcycling or waste revalorization of raw materials.[12] We explored two AFW as new CNF sources, spent coffee grounds and hop stems. These two AFW will be described in the following two subsections.

1.3.3. Spent Coffee Grounds

Coffee beans were seeds of trees belonging to the botanical family Rubiaceae genus *Coffea*. The most commercialized species in the coffee market are *Coffea arabica* (Arabica coffee) and *Coffea canephora* (Robusta coffee).[17] After harvest and several processes of extractions, washing, and drying, the beans are called green coffee beans (GCBs). GCBs are typically roasted up to 210 – 240 °C to gain the characteristic aroma and flavour of coffee. Then the roasted coffee beans (RCBs) are ground to brew coffee beverage. After brewing, spent coffee grounds (SCGs) are discharged as solid residues.

Around 10 million tons of RCBs were consumed in 2020, and 6 million tons of SCGs are estimated to be generated annually on the industrial scale.[18,19] Traditionally, SCGs were reused as solid fuel or fertilizer otherwise just landfilled as most. However, there have been some concerns that the landfilled SCGs might cause environmental pollution since some components, such as caffeine, tannins, and polyphenols were harmful to soil organisms.[20]

Coffee beans contain a complex mixture of hundreds of different compounds. **Table 2** shows the major components of GCBs and SCGs. With growing interest in environmental issues, waste revalorization of SCGs in an environmentally friendly way or upcycling SCGs into value-added biomaterials has rapidly increased since the 2010s. First, SCGs having microporous structures derived from cell walls with a surface area of 300–1000 m^2/g can adsorb metal ions.[21] The use of SCGs as a water purification agent by removing heavy metals and as an electrode material for electric double-layer capacitors has been reported.[22,23] Second, extracting useful bioactive substances with antioxidant and anti-inflammatory effects, such as caffeine,[24] chlorogenic acid,[25] and cafestol,[26] are expected to use as additives in food or pharmaceutical industries. Third, biorefinery research on converting the lipid components, triacylglycerol (TAG) in SCGs into raw materials for biodiesel fuels. TAGs represents about 10–20 wt% of SCGs, consists of oleic and linoleic fatty acids, and exists in cell wall pores in a liquid state (reference journal V).[27] Using hexane for solvent combined with Soxhlet extraction has been reported as the most efficient method to extract TAGs from SCGs.[28] The esterification reaction of the obtained TAG with methanol yields fatty acid methyl esters that can be used as biodiesel fuel.[29]

Polysaccharides composed of cellulose and hemicelluloses such as galactomannan and arabinogalactan are primary components of RCBs and SCGs, which make up about 50% (by weight) of the insoluble thick cell walls.[17,30,31] Ballesteros et al.[31] evaluated the constituent sugars in SCGs and reported that they were mainly mannose, galactose, and arabinose from hemicellulose and glucose from cellulose. Cellulose constitutes approximately 10% of SCGs.[31–33] Extracting cellulose from SCGs requires severe hydrolysis conditions such as lower pH, higher temperature, and longer reaction time because cell walls form a strong honeycomb structure, which makes hydrolysis and cellulose extraction inefficient.[30] There had been no investigation of extracting CNF from SCGs before 2020 (Chapter 4).

Table 2. Chemical composition of green coffee beans and spent coffee grounds.

Component	GCB Composition[17] (g / 100 g)	SCG Content[34] (wt %)
Carbohydrates/fiber		
Polysaccharides	34–44	
Cellulose		8.6–13.3
Hemicellulose		30–40
Lignin	3.0	25–33
Pectin	2.0	
Nitrogenous compounds		
Protein/peptides	10.0–11.0	6.7–13.6
Free amino acids	0.5	
Caffeine	0.9–1.3	0.02
Trigonelline	0.6–2.0	
Lipids		
Coffee oil (e.g., triacylglycerol)	15–17.0	10–20
Diterpenes (free and esterified)	0.5–1.2	
Polyphenols (e.g., chlorogenic acids)	4.1–7.9	2.5
Minerals	3.0–4.2	

1.3.4. Waste Hop Stem

Hop (*Humulus lupulus*) is a perennial, herbaceous climbing plant that belongs to the Cannabaceae family.[35] The several hop components in the female inflorescence (cones) give a refreshing bitter taste and aroma to beer brewing.[36] As an essential ingredient of beer, hop was produced around 130,000 metric tons worldwide in 2020.[37] Hop plants, characterized by long stems, grows up to 10 meters high in the harvest season in summer. The hop cones, stems, and leaves are collected altogether during the harvest, and only cones are selected in the factory. The rest of the hop stems and leaves, accounting for 75% of the hop cultivation, are typically landfilled.[38] Tono city in Iwate, one of the largest production areas for hop cultivation in Japan, produces approximately 50 tons of hop cones and disposed of 150 – 180 tons of hop stems (HS) as AFW every year. The disposal cost of HS imposes a heavy burden on farmers (> one million yen) and leads to the reduction of the number of hop growers in Japan. In addition, the recycling-based society in the local communities has not yet been established, preventing sustainable development.

Traditionally, young HS have been eaten as a vegetable in some regions in Europe, but it seems not so common these days.[39] Only a few investigations regarding the use of HS were reported so far. For instance, for removing lead(II) ions[38] or as reinforcements for polypropylene composites.[40] Reddy et al.[41] isolated the alkaline extraction of natural cellulose fibers (not CNF) from HS that were 16.5 μm wide and 2.0 mm long. They concluded that HS showed similar properties to that of hemp, which was also known as one of the CNF sources. Thus, their paper indicated that HS could be used as an AFW source of CNF. However, no report had investigated the isolation of CNF from HS, and even the components of HS had not been analyzed before our report in 2021 (Chapter 5).

1.4. Isolation of Cellulose Nanofibers

CNFs are mainly classified into "mechanically fibrillated CNF" or "chemically processed CNF."[42] The mechanically fibrillated CNFs are generally obtained by high-pressure homogenization in water and have a relatively high distribution of widths (20–100 nm). Such CNFs exhibit heterogeneous morphology and remain unfibrillated fractions that are larger than the wavelength of light. Therefore, water dispersions of mechanically fibrillated CNFs are translucent or opaque. The chemically processed CNFs are prepared by position-selectively introducing a high density of negatively charged groups on the surface of the crystalline cellulose microfibrils followed by a gentle fibrillation process. The obtained CNF exhibits homogeneous morphology of typically 3 nm, the same size as cellulose microfibrils, and average lengths of > 500 nm. The CNF water dispersions are highly viscous and transparent due to the high aspect ratio (i.e., length/width ratio).

For obtaining CNF having microfibril widths, several chemicals have been discovered.[11] For example, 2,2,6,6-tetramethylpiperidinyl-1-oxyl (TEMPO) for surface-carboxylated CNF, solid sodium hypochlorite ($NaClO\cdot 5H_2O$) for C2/C3-dicarboxylated CNF, and ammonium dihydrogen phosphate [$(NH_4)H_2PO_4$] and urea for phosphorylated CNF. In the following section, the most widely used TEMPO-oxidized CNF will be described.

1.4.1. TEMPO-Mediated Oxidized Cellulose Nanofibers

In 2006, Saito and Isogai from the University of Tokyo and their colleagues developed an innovative CNF production technique using a water-soluble nitro radical catalyst, TEMPO.[43] TEMPO allows cellulosic materials to disintegrate into cellulose microfibrils in water, and completely nano-dispersed TEMPO-oxidized CNF (TCNF) can be obtained at room temperature. Their breakthrough techniques dramatically reduced the energy requirements compared to the conventional mechanical disintegration method using a high-pressure homogenization (e.g., > 200 kWh/kg) at that time and triggered the CNF research development later on.[3,44]

A catalytic amount of TEMPO and sodium bromide (NaBr) are added to the cellulosic materials, such as wood-derived kraft pulp or lignocellulosic biomass. Then, TEMPO-mediated oxidation is launched by adding sodium hypochlorite (NaClO) as a primary oxidant at pH 10–11. The amount of NaClO significantly impacts the amount of carboxyl groups introduced on the surface of cellulose microfibrils, thus optimizing the NaClO amounts is important to proceed with the TEMPO oxidation reaction efficiently. During the reaction, pH in the system should be kept around pH 10 by adding NaOH. Note that the decrease of the degree of polymerization is unavoidable due to the alkaline condition.[3] The end of the oxidation reaction can be detected when pH does not change anymore. Importantly, lignin and hemicellulose in the starting cellulosic materials are removed as water-soluble degraded fractions as NaClO consumption proceed.[3] TCNF can be obtained as a water-insoluble slurry by the filtration then is washed with distilled water a couple of times to remove water-soluble fractions, e.g., hemicellulose. The slurry is treated with grinder treatment at the laboratory level (e.g., homogenizer) to gain TCNF water dispersion with TCNF concentrations of < 2 wt%. The obtained TCNF water dispersion exhibits high viscosity and turns almost transparent. Typical TCNF has a width of 3–4 nm and a high aspect ratio above 150. The amount of carboxyl groups in cellulose increases from 0.01 to 0.8–1.7 mmol g^{-1}, but again, it significantly depends on the amount of NaClO added.

The mechanism of TEMPO/NaBr/NaClO catalytic oxidation systems at pH 10 is shown in **Fig. 5.** The detailed oxidation process was described in the review by Isogai.[45] Theoretically, TEMPO, having hour methyl groups like butterfly wings, position-selectively binds and unbinds primary hydroxy groups (termed C6 position) rather than

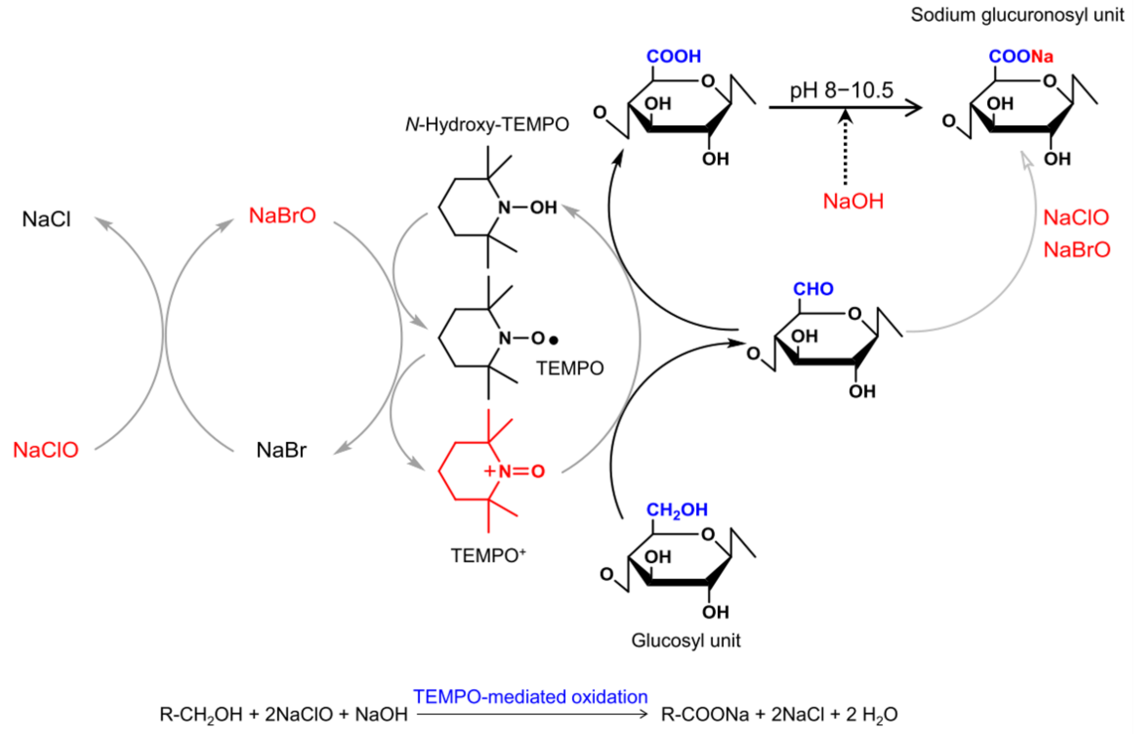

$$\text{R-CH}_2\text{OH} + 2\text{NaClO} + \text{NaOH} \xrightarrow{\text{TEMPO-mediated oxidation}} \text{R-COONa} + 2\text{NaCl} + 2\,\text{H}_2\text{O}$$

Fig. 5 Mechanism of TEMPO-mediated oxidation for the conversion of primary hydroxy groups in cellulose into sodium C6-carboxylate groups using TEMPO/ NaBr/NaClO in water at pH 10 (adapted from Isogai et al.[44]).

secondary hydroxy groups due to the steric hindrance, and thus only the C6 hydroxy groups are oxidized. At around pH 10, a C6 hydroxyl group of cellulose is slightly ionized in water to form R-O^{-} (pKa > 13) and is bound with the oxidized TEMPO^{+}. When the reduced TEMPO is unbound, the C6 hydroxy group is oxidized to an aldehyde group. In most cases, further oxidation process occurs for the aldehyde group to the carboxy group. While small amounts of the C6-aldehydes (~ 0.1 mmol g^{-1}) remains as intermediate structures, the C6-aldehydes cause the significant depolymerization by β-elimination as well as the brown discoloration by heating.[3,46] The cellulose microfibrils surface exhibits the dense negative charge derived from the carboxy groups (normally bound with Na^{+} as counterions). The strong electrostatic repulsion between fibrils and/or the osmotic effects in water isolates the individualized TCNF.

The high transparency, viscosity, and uniformity of TCNF as well as the dense negative charge, are highly desirable properties for 'Pickering emulsion' stabilizers. We developed the isolation method for TCNFs isolated from waste HSs, and the obtained TCNF exhibited similar fiber morphology to wood-derived TCNFs and high purity (Chapter 5). Therefore, PEs stabilized by HS-derived TCNF was studied for potential food or cosmetics applications (Chapter 6). The stabilization mechanisms of PEs, the choice of stabilizers, the latest NC-stabilized PEs, and AFW-derived NC-stabilized PEs will be described in the next chapter.

Chapter 2 – Pickering Emulsion

2.1. Pickering Emulsion and Wettability

Emulsions are consisting typically two immiscible liquids (e.g., oil and water) and inherently thermodynamically unstable systems.[47] One of the liquids is dispersed as spherical droplets in the other liquid. The simplest types of emulsions are classified as water-*in*-oil (w/o) or oil-*in*-water (o/w) emulsions. In order to delay the separation into the two phases, emulsifiers (also working as stabilizers) are commonly added. The emulsifiers require amphiphilic properties for absorbing onto the surface of droplets to prevent the aggregation of the emulsion droplets. In 1903, Ramsden[48] and a few years after, Pickering[49] found that solid colloidal particles absorbed at fluid interfaces, and this new type of emulsion was named 'Pickering emulsion.' Pickering emulsions (PE), however, did not attract much attention before the micro- or nanoparticles were developed and a lot of advantages of using them were found by colloidal researchers in the 2000 s.[50]

The PE types are determined by the amphiphilic properties of particles (usually nano- or microscale), so called 'wettability'. The particle wettability is described by the contact angle (θ) at the oil-particle-water interfaces (**Fig. 6**). The well-known Young's equation describes the contact angle with the static relationship of three interfacial tensions,

$$\sigma_{po} - \sigma_{pw} = \sigma_{ow} \cos\theta \tag{1}$$

where σ_{po}, σ_{pw}, σ_{ow} are the particle-oil, particle-water, and oil-water interfacial tensions, respectively. The energy of adsorption of a single spherical particle of radius R at an oil-water interface is described using Eq. (1),[51]

$$E = \pi R^2 \sigma_{ow} \left(1 + \cos\theta\right)^2 \tag{2}$$

Eq. (2) implies particles with an angle of 90° are held most strongly at the interface. Also, for hydrophilic particles with $\theta < 90°$, the majority of the particle would immerse in the aqueous phase, and thus inducing the formation of o/w PE, whereas hydrophobic particles

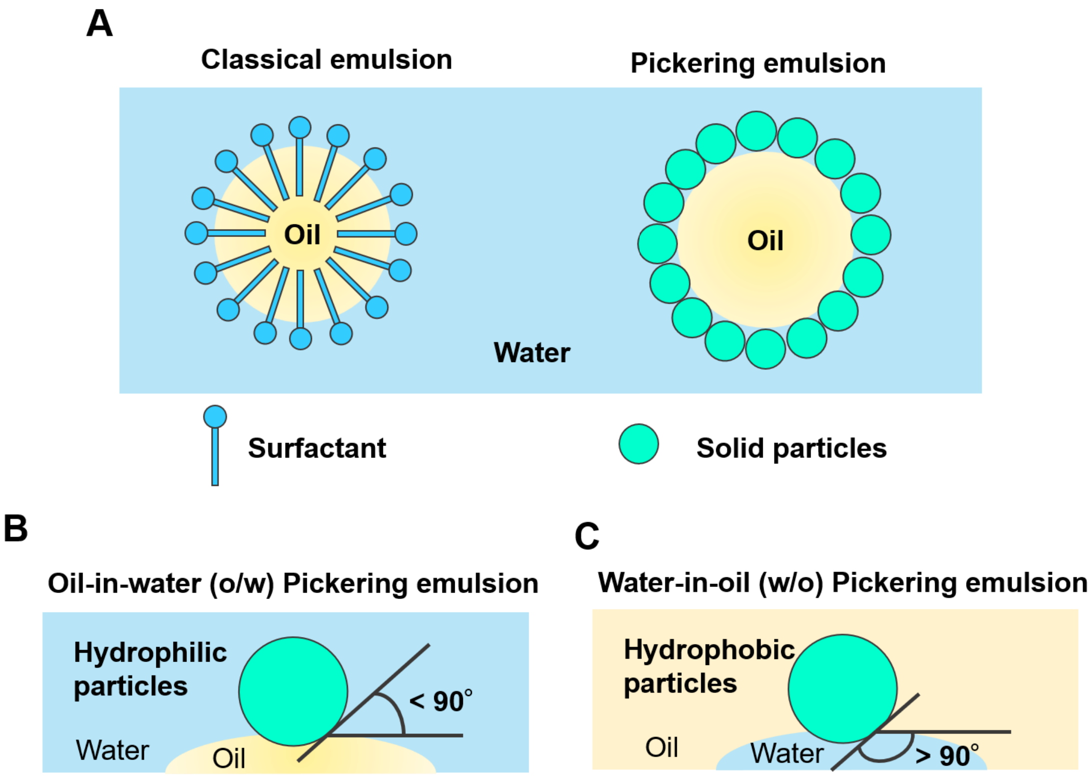

Fig. 6. (A) The stabilized mechanisms of oil-*in*-water classical emulsion and Pickering emulsion. (B) The hydrophilic particles are wetted more by water than by oil and forms o/w Pickering emulsion for a contact angle less than 90° measured through the aqueous phase. (C) The hydrophobic particles are wetted more by oil and forms w/o Pickering emulsion for a contact angle greater than 90°.

with $\theta > 90°$ would form w/o PE.[50] According to Eq. (2), the intermediate particles with $\theta = 90°$ should be most strongly held in the interface, resulting in obtaining the stable PE.

The different adsorption mechanisms between PE and molecular-based classical emulsions are highlighted in their behavior during formation and stabilization. At first, molecular surfactants tend to rapidly adsorb onto interfaces during emulsification and then exist in equilibrium with the non-adsorbed form, whereas particle emulsifiers adsorb irreversibly.[52] For molecular-based emulsions, the system hydrophile-lipophile balance (HLB) determines the form of aggregated surfactants (e.g., micelles or microemulsion droplets) in water, oil, or third phase, corresponding to the contact angle for PE.[53] Also, the particles form a coating around droplets that prevents them from coalescing mainly through steric repulsion. The particle emulsifiers partially wetted by both oil and water phases are strongly adsorbed at interfaces so that they cannot be desorbed. These stability mechanisms make it possible to achieve higher stability against deformation than conventional emulsions. Therefore, they are one of the most advantages of PE and are excellent for enhancing quality attributes and shelf-lives of emulsion-based food.

2.2. Stabilizer

The earlier studies of stabilizers for PE started from investigating inorganic particles whose size was already known and whose distribution was monodisperse, such as carbon black,[54] latex,[55] and silica nanoparticles.[51,56] Then, various types of particles were suggested such as paramagnetic particle,[57] titanium dioxide,[58] and carbon nanotube.[59] Apart from spherical shape, other types of 'odd' shape (e.g., ellipsoid, sheet, cylinder, rod, fiber) stabilizers which have anisotropic morphology emerged later on.[50]

Inorganic particles, however, has limited use in food, cosmetic, and pharmaceutical industries due to the concern of health issues.[52,60] As an alternative, natural biopolymers have attracted attention among non-spherical colloidal particles with the development of sustainable nanoparticles since in the late 2010s.[61] This movement has also driven by the United Nation's agenda for sustainable development, the growing demand for sustainable products. For this reason, replacing synthetic emulsifiers with renewable ones is of global interest today.[60]

2.3. Nanocellulose-Stabilized Pickering Emulsion

Biopolymers explored to date as stabilizers for PE include proteins,[62,63] polysaccharides,[64] and NCs.[65–71] NCs are promising emulsifiers for o/w PE.[72] In 2011, Kalashnikova and colleagues pioneered the use of NCs as stabilizers for PE.[73] Their research team used bacterial cellulose nanocrystals (BCNs) as the stabilizer and hexadecane for the oil, and prepared the monodispersed stable o/w PE (**Fig. 7 a-c**). They reported that the irreversible adsorption of the BCNs to the droplet surface and steric hindrance of the network derived by the excess BCNs at the interfaces are critical for achieving high stability. In the following year, they found that amphiphilic characters of NCs led to the stabilization of PE, essentially a $(200)\beta/(220)\alpha$ hydrophobic edge plane took responsibility for the wettability of the NC at the oil/water interface (**Fig. 7 d,e**).[74]

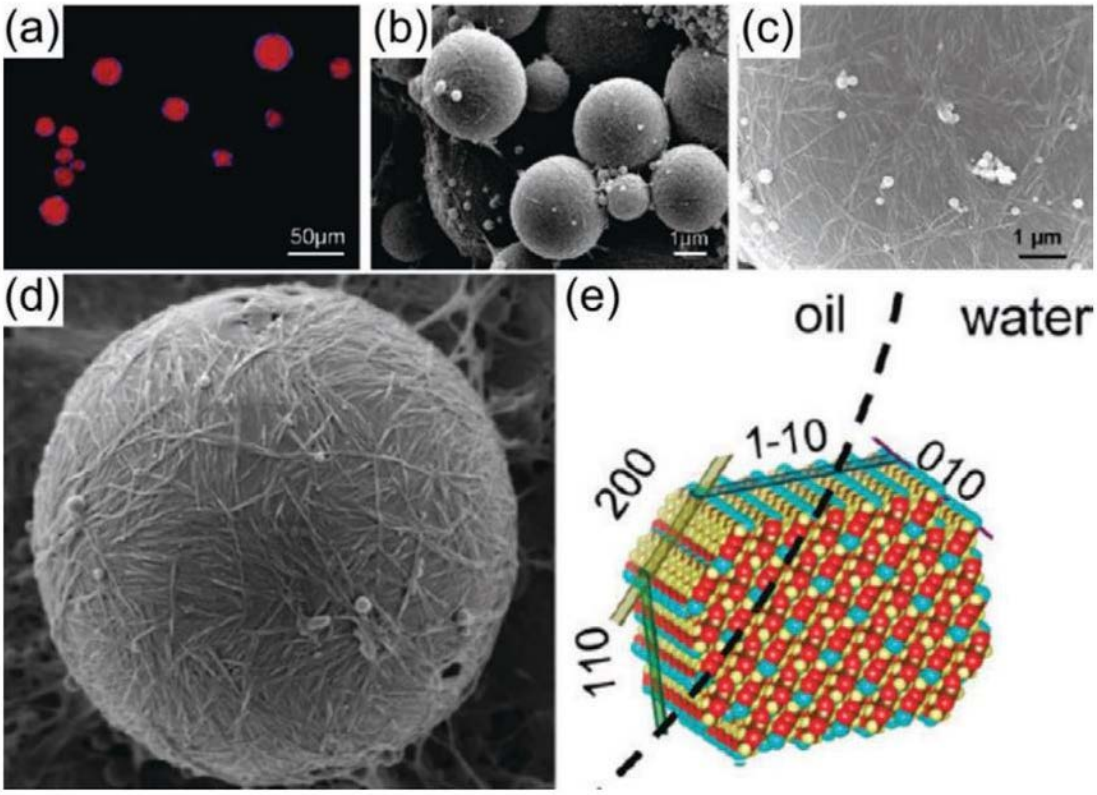

Fig. 7. (a) Confocal laser scanning microscopy image of hexadecane droplets stabilized by BCNs where the oil phase appears red and BCN appears blue. (b–d) Scanning electron microscopy images of the BCN-stabilized styrene PE to visualize the location of BCN at the interface. (e) Orientation of the Iβ cotton cellulose nanocrystals at the oil–water interface showing the hydrophobic (200) plane with no hydroxyl groups (adapted from Kedzior et al.[70])

Subsequent researches revealed that the overall balance of diverse factors shown below as examples decide NC-emulsified PE stability. First, NC loadings significantly impact the final droplet sizes. Aveyard and Binks et al.[75] proposed that the droplet size typically decreases with the particle concentration until a limiting size is reached and excess particles appear in the continuous phase. Following this theory, Kalashnikova et al.[73] reported that BCN-stabilized hexadecane o/w PE reached to the critical droplet size of around 4 μm. They concluded that when emulsification process (e.g., sonication) stopped, rapid coalesce occurred between partially covered droplets by NCs, and this coalescence lasted until the interfaces were sufficiently protected. Gestranius et al.[66]

prepared dodecane o/w PE stabilized by three different NCs, cellulose nanocrystal (CNC), CNF, and TCNF. They reported that the droplet size distribution decreased when either stabilizer or oil concentration increased. In most cases, the relationship between droplet size and concentrations of NC is in inverse proportion, but depending on the conditions of homogenization energy or NC viscosity.

Next, the morphology of NC brings an interesting difference in stability mechanisms. Kalashnikova and coworkers studied the relationship between aspect ratios of NCs and emulsion morphology in 2013.[76] Three different aspect ratios (from 13 to 160) of nanocrystals (originated from cotton, bacteria cellulose, and green algae) significantly influenced the surface coverage ratio of droplets. The short nanocrystals (i.e., low aspect ratio) aligned side by side on the surface via attractive forces achieving a high coverage (> 80%) and thus obtaining isolated droplets. On the contrary, the longer nanocrystals (i.e., high aspect ratio) restricted the coverage (~ 40%) due to their steric hindrance. Instead, the interconnected network of droplets was induced by longer nanocrystals resulting in stable system. Lu et al.[68] explained these stabilization mechanism differences from the fiber flexibility. The multiple use of NCs having different aspect ratios is another strategy for enhancing the stability. Bai et al.[77] prepared sunflower oil o/w PE stabilized by the mixture of short CNC and long CNF. CNCs were distributed at the interfaces, mainly stabilizing the droplets whereas CNFs get network restricted the movement of droplets, avoiding the separation.

Then, the surface properties of NC including hydrophobic/hydrophilic balance and surface charge also regulate the PE stability. NCs is high hydrophilic polymer by nature and this might lead to poor wettability by a hydrophobic phase and obtain less stable PE without modification.[78] Various hydrophobic modifications of NCs have been performed with various molecules. Octenyl succinic anhydride (OSA) has been used for decades in the food industry for the modification of starch and therefore, the straightforward example.[78] In 2018, Chen et al.[79] successfully enhanced the emulsification performance using CNCs grafted OSA with above 0.3 wt% in Pickering high-internal-phase-emulsions (HIPEs) system. Seo et al. grafted alkylamines with different number of alkyl chains onto the TEMPO-oxidized bacterial cellulose for stabilizing decane, olive oil, fomblin oil, and silicone oil o/w PE. The authors estimated that the C18 alkyl chain was essential to generate the strong hydrophobic interactions between alkyl chains.[80] It is worth mentioning that the applications of PE stabilized with hydrophobically-modified NC are possibly restricted due to the safety concerns for human body.[52]

Surface charges, the cause of electrostatic interaction, can be also altered by the surface modification on NC. Sulfuric acid hydrolysis for CNC or TEMPO-mediated oxidation for CNF are commonly used for producing negatively charged NC.[81] Saelices and Capron[82] prepared hexadecane o/w PE stabilized by four different NCs including unmodified CNF and TCNF. They reported that electrostatic repulsion induced by the carboxyl groups in the TCNF-stabilized system were entangled and strongly connected, forming the nano-emulsions (350 nm) and exhibiting excellent mechanical resistance against deformation (**Fig. 8**). Silva et al.[83] synthesized cationic CNF using glycidyltrimethylammonium chloride and compared the stability with anionic TCNF. They concluded the cationic CNF were more stable in almond oil o/w PE due to the attractive interactions with negatively charged deprotonated oleic acid in the oil.

Besides emulsifiers, other components of PE systems also affect stability. Given pH and ionic strength or salt concentration, e.g. NaCl, influenced the surface charge of the stabilizers, defining the activity and the stability.[84] Oil properties such as viscosity and polarity impact the stability of PE.[85] The types of oils used in publications varies, alkanes

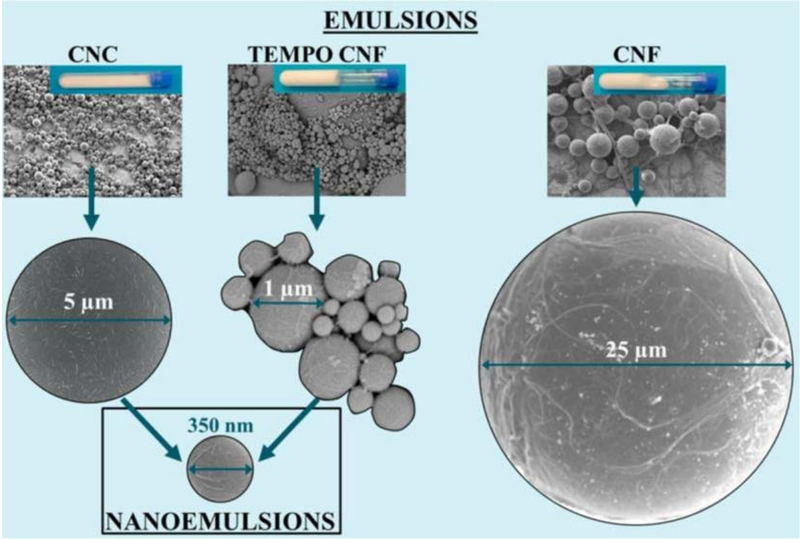

Fig. 8 Comparison of droplet size of CNC, TCNF, and unmodified CNF-stabilized o/w adapted from Saelices and Capron.[82]

have often been used as well-defined models among them, e.g., decane, dodecane, hexadecane. This comes to the fact that NCs are efficiently working when the oil polarity is low, or oil/water interfacial tension (i.e., σ_{ow}) is high in o/w PE.[86] According to Albert et al.,[87] biocompatible oils rather than petroleum-derived oils are preferable for use PE in food or pharmaceutical applications. Therefore, plant-derived natural oils are a suitable choice for designing sustainable PE. However, PE formed by those natural oils, including multiple components, may lead to less stability.

2.4. Pickering Emulsion Stabilized by Agricultural/food Waste-Derived Nanocellulose

Using AFW-derived NC as stabilizers for PE facilitate the development of the circular economy and waste revalorization. Importantly, the source of cellulose does not significantly impact the stability of NC-emulsified PE.[72] This assumption underlies the common crystal structure, cellulose I, of native cellulose. Winuprasith and Suphantharika[88] firstly explored the AFW-derived NC using mangosteen (Thailand tropical fruits) rind for PE stabilizers in 2013. They obtained microfibrillated cellulose (MFC) using alkaline extraction followed by the different number of homogenization passes (**Fig. 9**). The soybean o/w PE stabilized with 0.7% MFC through the high number of homogenization passes exhibited smaller droplet sizes and higher stability. In 2015, the same research group reported that the droplet size increased with increasing AFW-derived MFC loading, which was the opposite behavior of most literatures mentioned in the previous subsection.[89] They assumed that the higher viscosity of the continuous phase with the higher MFC loadings might have avoided the MFC movement to the droplet surface during emulsification, resulting in larger droplets.

Various kinds of AFW-derived NC have been investigated for PE stabilizers to date and was summarized in the recent review by Perrin et al.[90] These researches mainly targeted o/w PEs stabilized with CNC or CNF with typical concentrations of 0.1 to 1 wt% driven by an effort to use as much as a lower amount of NC. For the oil phase, natural plants-based oils, e.g., corn oil, soybean oil, and sunflower oil, were more frequently used than petroleum-derived oils for potential use in food or cosmetic applications. The CNC-

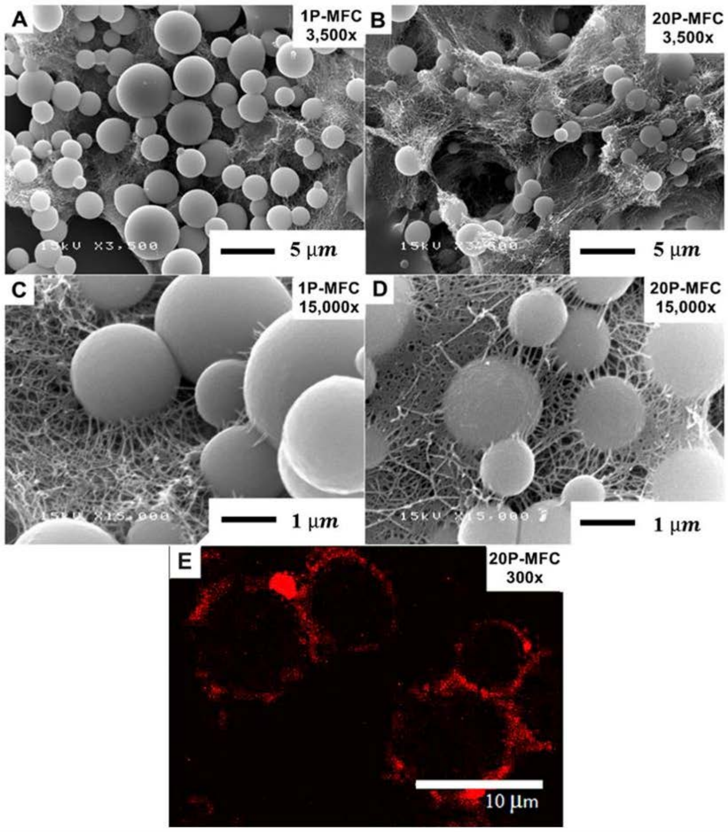

Fig. 9 Scanning electron microscopy images of MFC-stabilized soybean o/w emulsions (30% oil, 0.7% MFC in aqueous phase) obtained with 1 pass (A, C) and 20 passes (B, D) through the homogenizer. (E) Confocal laser scanning microscopy image of emulsion droplets stabilized by MFC obtained with 20 homogenization passes (adapted from Winuprasith and Suphantharika.[88])

stabilized o/w PEs, for instance, were from corncob (in 2014),[91] rice bran (in 2017),[92] pistachio shells (in 2018),[93] and ginkgo seed shells (in 2020).[94] These CNCs were isolated by acid hydrolysis process and were unmodified. The CNF-stabilized o/w PEs were reported from banana peels (in 2018),[95] *Miscanthus floridulus* straw (in 2019),[96] palm peach (in 2020),[97] oil palm empty fruit bunch (in 2020),[67] lemon seeds (in 2021),[65] and pomelo spongy tissue (in 2023).[98] These CNFs were extracted mainly from the combination of pretreatment (e.g., alkaline treatment) to remove lignin or hemicellulose and mechanical defibrillation (e.g., high pressure of homogenization), and the use of surface modified-CNF is yet to be minor.

As mentioned earlier, surface-carboxylated TCNFs are expected to exhibit a higher emulsifying capability for o/w PEs than unmodified (i.e., mechanically fibrillated) CNFs. TCNF-stabilized systems are entangled and strongly connected due to the electrostatic repulsion caused by carboxyl groups, exhibiting excellent mechanical resistance against deformation.[82] The viscosity of TCNF dispersions is very high compared to mechanically fibrillated CNFs due to the high aspect ratio of TCNF and therefore, TCNFs are expected to inhibit the droplet coalescence with lower concentrations than mechanically fibrillated CNFs.[66] Also, the cellulose origin should not significantly impact the formation of PEs.[72] Therefore, AFW-derived TCNFs are expected to have the same emulsifying capability comparable to wood-derived TCNFs and superior to mechanically fibrillated CNFs.

Li et al.[67] was the only investigation using AFW-derived TCNF from oil palm empty fruit bunch for stabilizing dodecane o/w PE. They concluded that 2.0% TCNF loading was required to prevent separation for one month. Assume that any AFW-derived TCNF exhibits a similar emulsifying capacity to Li et al.'s systems, this work will provide further knowledge for the use of AFW-derived TCNFs as stabilizers for PEs and facilitate their versatility in the fields of agricultural chemistry, food science, and materials science.

2.5. Aims and Objectives

This thesis aims to elucidate instability mechanisms for PEs using TCNFs derived from AFW to obtain highly stable PEs with low TCNF concentrations. The following primary two objectives were set into two phases. The first phase is the development of CNFs as emulsifiers from unexplored AFW sources (Chapters 4 and 5), and the second phase is the development of o/w PEs using AFW-derived TCNFs and evaluation of their instability mechanisms (Chapters 6 and 7).

In Chapter 4, SCGs were used for isolating TCNF. SCGs only contain around 10 % cellulose and thus severe experimental conditions had reported required for extracting cellulose. Therefore, TEMPO-mediated oxidation was applied to isolate surface-carboxylated TCNFs. The obtained SCGs-derived TCNFs were characterized using the following methods: TCNF widths were determined using field emission scanning electron microscopy (FE-SEM), the crystal structure and microfibril widths were determined from X-ray diffraction analysis (XRD), the purity and crystallinity were investigated using solid-state nuclear magnetic resonance (NMR), and the thermal decomposition temperatures were assessed using thermogravimetric analysis (TGA). Also, the compatibility to forming the composite film of SCGs-derived TCNF was investigated with poly(vinyl alcohol) (PVA) as a versatile matrix. Finally, SCGs-derived TCNF were compared to wood-derived TCNF, and the discussed the characteristics, difficulty, and possibility as an AFW source for TCNF.

In Chapter 5, HSs were used for isolating TCNFs. Due to the limited literature regarding HS, the chemical composition analysis was conducted to investigate the contents of cellulose, hemicellulose, and lignin. Based on information of the composition, the pretreatment scheme prior to TEMPO-mediated oxidation was optimized. TCNFs were obtained from pretreated and non-pretreated HSs. The morphology of the obtained TCNFs was investigated using FE-SEM and atomic force microscopy (AFM). Solid-state NMR and XRD characterizations were performed to discuss the purity and crystallinity.

In Chapter 6, the isolating scheme for HSs-derived TCNF was further improved to remove residual calcium oxalate revealed in Chapter 6 and established how to obtain highly pure and uniform TCNFs for o/w PE stabilizers. Aiming at preparing PEs stabilized by HSs-derived TCNF without separation for one month after emulsification at ambient temperature, the first objective for this chapter was to clarify the emulsification conditions such as oil types (dodecane or olive oil), oil/water ratio, and critical TCNF concentrations. The second objective is to elucidate the stability mechanism of the system using confocal laser scanning microscopy (CLSM) and FE-SEM. The final objective was to systematically compare dodecane PE and olive oil PE about the relationship between the instability mechanism (e.g., flocculation and coalescence), oil droplet size, and distribution structure controlled by oil types and TCNF loadings.

In Chapter 7, the applicability of magnetic resonance imaging (MRI) was investigated to evaluate the deformation mechanisms and relaxation/diffusion properties of PEs. The entire dodecane PE and olive oil PE samples were captured by high-resolution MRI aiming at visualizing the time evolution of the microstructures and creaming behavior for one month after the emulsification. MRI relaxation and diffusion measurements and mapping were explored to investigate the effects of the TCNFs and oil type on longitudinal relaxation, transverse relaxation, and apparent diffusion coefficients.

Also, the voxel-wise MRI and spectroscopic NMR relaxation and diffusion properties were compared and the MRI's advantages and limitations were discussed. The influence of experimental factors and observed artifacts on the MRI measurements was considered in detail.

A little digression 1: in the third year of my undergraduate, I started researching the structural analysis of the triacylglycerols and polysaccharides in "RCBs," (Reference journal V). One day, I found that RCBs and SCGs showed similar spectra in solid-state NMR spectra, i.e., the similar composition of RCBs and SCGs. This finding made me focus on the cellulose that remained in SCGs and upcycling AFW by isolating value-added TCNF. However, using SCGs as an AFW source of TCNFs revealed the difficulty due to the low cellulose contents (~10%), which led to the low yield of TCNF. Exploring an undiscovered AFW for obtaining higher quantities and qualities of CNFs brought me to waste HS. After developing the isolation and characterization techniques of HS-derived TCNF, I discovered the throughout PhD research subject on TCNF for the use of PE emulsifiers.

A little digression 2: for seven months during my Master's, I stayed at Western Sydney University to learn the diffusion NMR techniques through collaborative research measuring diffusion coefficients of ionic liquids (Reference journal VI). Based on this experience, I designed a joint PhD research project using PEs at Yokohama National University in Japan and Western Sydney University in Australia.

Chapter 3 – Nuclear Magnetic Resonance Theory and Techniques

3.1. Nuclear Spin and Net Magnetization

Nuclei have a spin, and NMR observable (active) nuclei takes the spin angular momentum of $I \neq 0$. For example, ^{1}H and ^{13}C are $I = 1/2$, the most frequently encountered two nuclei for NMR measurements. While ^{1}H has 99.98% natural abundance, only 1.1% ^{13}C is available for NMR experiments in nature.[99] As a result of this spin, the nucleus displays a magnetic moment (**μ**), given by:

$$\boldsymbol{\mu} = \frac{\gamma \boldsymbol{I} h}{2\pi} \tag{3}$$

where the proportionality constant γ is the gyromagnetic ratio (rad s^{-1} T^{-1}) and h is Planck's constant.

NMR involves the application of a strong static magnetic field, $\mathbf{B_0}$ along the z-axis. In the presence of $\mathbf{B_0}$, a nuclear spin starts precessing about the direction of $\mathbf{B_0}$. This motion could be described by the analogy of a spinning bicycle wheel hung by one end of its axle.[100] The angular frequency of precession, ω_0 (rad s^{-1}) is denoted as Larmor frequency (or the resonance frequency) and its magnitude is dependent on the applied magnetic field strength as

$$\omega_0 = \gamma B_0 \tag{4}$$

The nuclear spins arrange themselves in "allowed" two orientations, parallel and antiparallel to a magnetic field due to the quantization of the energy. It is the perturbation of these nuclear spin orientations that is detected in the NMR experiment. The transition energy between these two states is given by:

$$\Delta E = \frac{\gamma h B_0}{2\pi} \tag{5}$$

Eq. (5) refers to resonance condition of nuclear magnetic resonance results when a nucleus of gyromagnetic ratio γ is placed in a magnetic field $\mathbf{B_0}$ and a radiation of frequency $\nu = \gamma B_0/2\pi$ (Hz) is applied.[101]

If the system is in thermal equilibrium, the splitting of two energy states of α and β (Zeeman splitting) follow a Boltzmann distribution of orientation populations:

$$N_\alpha / N_\beta = \exp(h\nu / kT) \tag{6}$$

where N_α and N_β are the number of spins in the lower (+1/2) and the higher (–1/2) orientations, respectively.[101]

The spins are most randomly oriented with only a small preference towards the direction of the applied magnetic field. However, since an extraordinary number of nuclei includes in the probed sample, this statistically tiny alignment can induce a net magnetization, $\mathbf{M_0}$ (**Fig. 10**). The description 'net' note that the magnetization is a property of the whole sample.[100] For NMR, the radiation frequency is in the radio frequency region (3 kHz – 300 GHz), and thus the excess spin population $\mathbf{M_0}$ is of the order 1 in 10^5 nuclear spins.

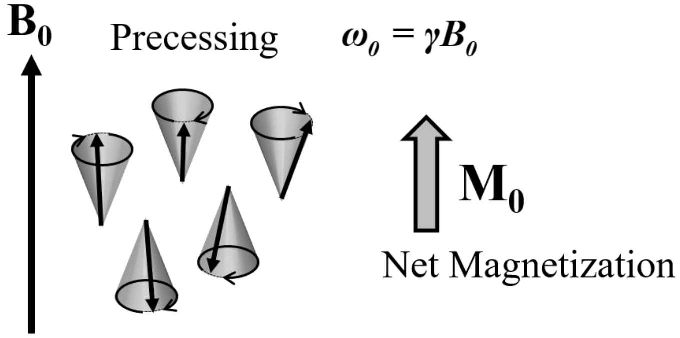

Fig. 10. The nuclear spins begin precessing depending on the strength of the static magnetic field, $\mathbf{B_0}$ resulting in inducing the net magnetization $\mathbf{M_0}$ parallel to $\mathbf{B_0}$.

3.2. Chemical Shift

Eq. (4) represents resonance frequency should be equal among identical nuclei. However, the magnetic field experienced at the observed nucleus is affected by surrounding electrons. The electron shells 'shield' the nucleus from the applied magnetic field $\mathbf{B_0}$, and thus the magnetic field experienced at the observed nucleus is decreased to $\mathbf{B_{eff}}$ given by

$$\mathbf{B}_{\mathbf{eff}} = \mathbf{B}_{\mathbf{0}}(1-\sigma) \tag{7}$$

where σ is nuclear shielding.[101] The difference between resonance frequency to Larmor frequency brings the concept of chemical shift (δ). As experimental, the chemical shift is defined as a shift from a 'reference' compound such as trimethylsilane.[99] Also, the chemical shift is divided with the Larmor frequency to be independent of the magnetic field strength and multiplied by 10^6 to express in units of parts per million (ppm) given by:

$$\delta = \frac{(\omega - \omega_0)}{\omega_0} \times 10^6 \tag{8}$$

3.3. Detection

How can we rotate the net magnetization away from the thermal equilibrium position? A powerful superconducting magnet supplies the static magnetic field $\mathbf{B_0}$ and it is impossible to switch it off quicky.[102] Therefore, the idea is to apply a radio frequency (rf) field, $\mathbf{B_1}$, oscillating at or near the Larmor frequency for a short time. This pulse that generates transverse magnetization denotes as a rf pulse, and this is a starting point of NMR experiment. The rf pulse used in NMR is termed by its rotation angle, e.g., 180° pulse or π pulse.[100]

After the rf pulse is turned off, the net magnetization, now in the transverse plane (*xy*-plane) starts to precess about $\mathbf{B_0}$. The precession of the net magnetization changes the magnetic field inducing an electric current via Faraday induction in a receiver coil aligned in the *xy*-plane. The induced current is amplified and record as a time dependent signal referred to the free induction decay (FID). The FID will be a complicated sum of waveforms and thus is difficult to obtain the information of the probed sample. Therefore, the Fourier transform is applied to the FID converting the information contained in the 'time-domain' FID into a 'frequency-domain' spectrum.[103]

3.4. Relaxation

After the rf pulse is switched off, the net magnetization returns to the equilibrium position by a process called relaxation. Remind that there is only longitudinal magnetization along the applied magnetic field (z-axis) in the equilibrium state (i.e., $\mathbf{M_0}$ = [0, 0, M_z]), the net magnetization has potentially both longitudinal and transverse components after the application of the rf pulse (i.e., $\mathbf{M_0}$ = [M_x, M_y, M_z]). Therefore, relaxation includes two separate processes: (i) the loss of the transverse magnetization (M_x and M_y) to zero (i.e., transverse relaxation) and (ii) the returning of the longitudinal magnetization back to its equilibrium value M_0 (i.e., longitudinal relaxation).[104] Both longitudinal and transverse relaxations generally appear as exponential functions of time with time constants T_1 and T_2, respectively.

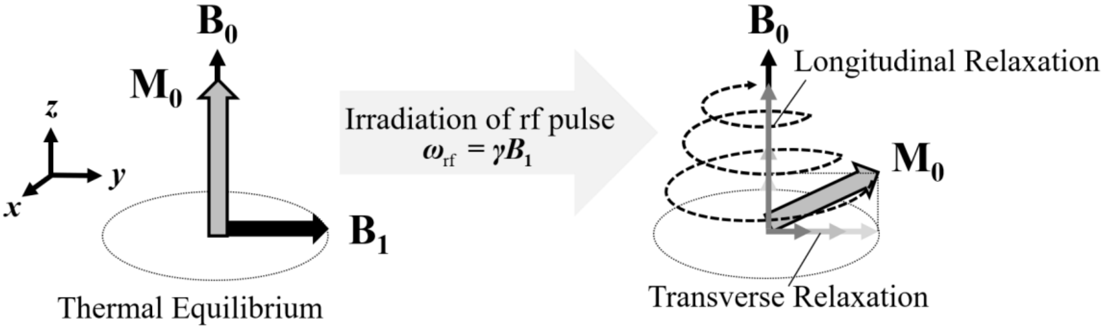

Fig. 11. The application of the rf pulse on the net magnetization, $\mathbf{M_0}$, induces the relaxation. The relaxation includes the reduction of the transverse magnetization to zero (transverse relaxation) and the recovery of the longitudinal magnetization at thermal equilibrium (longitudinal relaxation).

3.4.1. Longitudinal Relaxation Time Constant, T_1

Longitudinal relaxation refers to the transfer of energy between nuclear spins and their ‘surroundings’ to reach back to the thermal equilibrium. Classically, these surroundings were studied as the crystal ‘lattices’ and thus “spin–lattice relaxation” is also used for longitudinal relaxation.[104] This relaxation is an enthalpic process where the return of the z-component of the net magnetization (M_z), to its equilibrium value (M_0) is given by:

$$\frac{dM_Z}{dt} = -\frac{(M_Z - M_0)}{T_1} \tag{9}$$

Eq. (9) refers to M_z returns to 63% of its equilibrium value after one T_1, and to almost 100% of its equilibrium value after five T_1 times.

T_1 can be measured by the inversion recovery method (**Fig. 12**).[105] The inversion recovery pulse sequence contains a π (180°) pulse first, an interval τ, a 2/π (90°) pulse, and a recycle delay of $\geq 5T_1$. The sequence is repeated with different values of τ to obtain a profile of the recovery of the longitudinal magnetization. The intensity of the observed longitudinal magnetization is transformed from Eq. (9):

$$M(\tau) = M_0(1 - 2e^{-\tau/T_1}) \tag{10}$$

T_1 is then estimated from regression onto the magnetization recovery profile (~ 10 points).

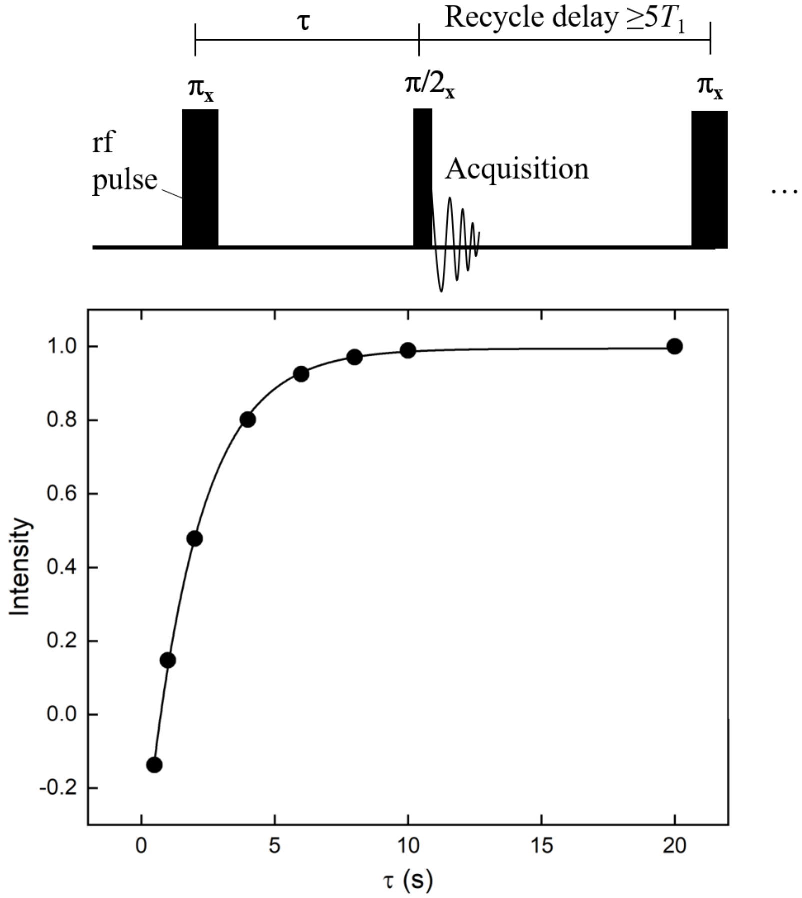

Fig. 12. The inversion recovery sequence (top) and an example of T_1 profiles of methyl peak in dodecane obtained from various τ (bottom).

3.4.2. Transverse Relaxation Time Constant, T_2

Transverse relaxation, also known as spin-spin relaxation, refers to the transfer of energy between nuclear spins and their 'surroundings' to destroy the transverse magnetization to zero. This relaxation is an entropic process where the loss of the x and y component of magnetization (M_x and M_y) given by:

$$\frac{dM_{x\,or\,y}}{dt} = -\frac{M_{x\,or\,y}}{T_2} \tag{11}$$

T_2 can be roughly estimated by the line-width at half height of the signal, but the obtained T_2 may include the influence on imperfect shimming or magnetic susceptibility inhomogeneities from the sample. Therefore, Carr-Purcell-Meiboom-Gill (CPMG) sequence based on Hahn spin-echo sequence is used to determine T_2 accurately (**Fig. 13**).[106] In the modified Hahn spin-echo sequence, the net magnetization is firstly excited by a 90° pulse to precess in the x-y plane. Due to the inhomogeneities of the magnetic field and different chemical shifts, the magnetization components start precessing at

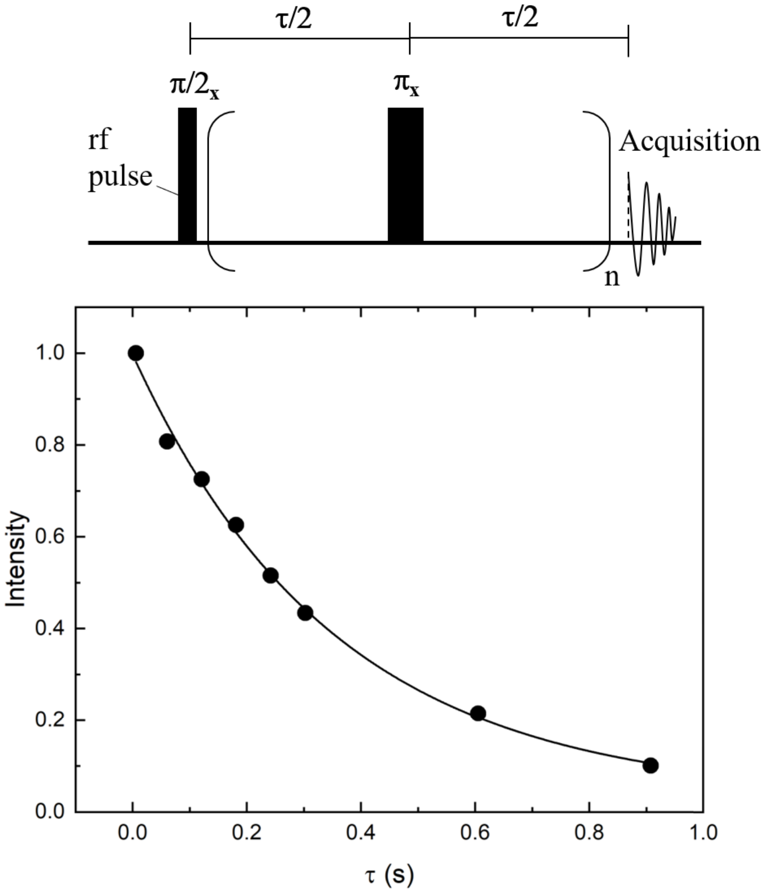

Fig. 13. The Hahn spin-echo based CPMG sequence (top) and an example of T_2 profiles of methyl peak in dodecane obtained from the train of π pulses (bottom).

slightly different rates. The following π pulse applied after time τ/2 invert the magnetization and thus refocus the components after another time τ/2. In CPMG sequence, the single π pulse is replaced by a train of n × π pulses to minimize the inhomogeneous effects. The intensities of the echo signals of the observed transverse magnetization are transformed from Eq. (11) given by:

$$M = M_0 e^{(-\tau/T_2)} \tag{12}$$

T_2 is then determined from regression onto the magnetization decay curve (~ 10 points).

3.5. Solid-State NMR

3.5.1. Chemical Shift Anisotropy

Solid-state NMR is a powerful method for structural characterization for insoluble biomacromolecules, such as polysaccharides in plant cell walls, membrane proteins, and amyloid peptides. In a solution sample, the rapid tumbling motions of the nuclei (molecules) averages the various interactions involving nuclear spins on the NMR timescale, and thus the shape of the signal is significantly simplified. The nucleus in the identical chemical environment of a molecule gives an isotropic chemical shift followed by Eq. (8).

In a solid or gel/liquid crystal sample, on the other hand, the slow tumbling motions of molecules are not fast enough to average a series of interactions among nuclear spins and thus cause the signal line-broadening. For example, spin-spin dipolar couplings are typically in the 0–20 kHz range, and quadrupolar couplings range from 100 kHz to tens of MHz for nuclear spins greater than 1/2. These interactions depend on the sample orientation relative to the magnetic field direction, thus giving the chemical shift anisotropy (CSA).[99]

Recall that the origin of the chemical shift is brought by the effect of the magnetic field, $\mathbf{B_0}$ on the electrons around a nucleus (see subsection 3.2). Hence, in a solid sample, the degree to which the electron density affects the resonance frequency of a nucleus depends on the orientation of the molecule (electron cloud) about $\mathbf{B_0}$.[107] To simplify this, assume that C=O moieties are randomly oriented to $\mathbf{B_0}$ (say along z-axis) (**Fig. 14**). When the narrowest part of the electron cloud is oriented along $\mathbf{B_0}$, the largest ^{13}C chemical shift is given due to the deshielding effect, while the smallest shift is given when the widest part of the electron cloud is oriented along $\mathbf{B_0}$. When the molecular orientation is perpendicular to *z*-axis, the chemical shift is given in-between. These three chemical shifts, referred to δ_{11}, δ_{33}, and δ_{22}, respectively, constitute three principal components of CSA. The isotropic average of the chemical shift tensor is given by:

$$\delta_{\text{iso}} = \frac{1}{3}\left(\delta_{11} + \delta_{22} + \delta_{33}\right) \tag{13}$$

In powder samples, the numerous spins are randomly oriented, and all the possible molecular orientations provide a broad powder pattern. The left and right edges of the C=O signal correspond to the chemical shifts δ_{11} and δ_{33}, respectively, and the position of the maximum intensity of the pattern corresponds to δ_{22}. Therefore, information on the geometries and mobility of the solid sample can be obtained from the powder pattern.

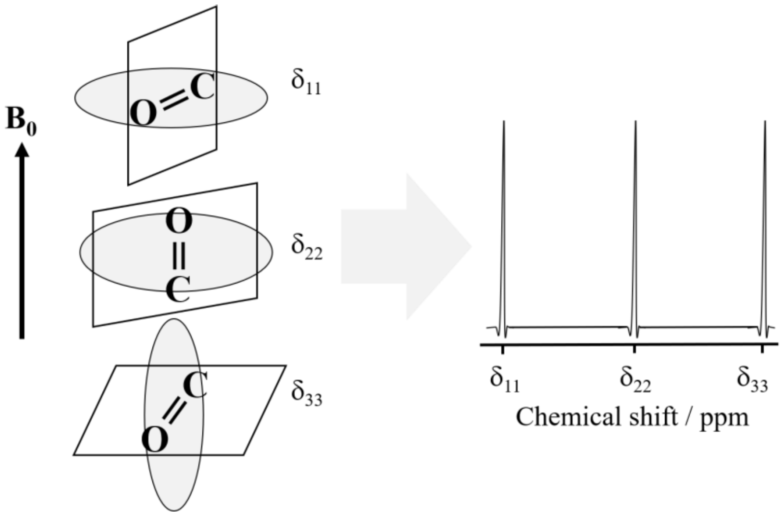

Fig. 14. Example of CSA with three different carbonyl group orientations; the ellipse behind C=O represents the electron cloud (adapted from Laws et al.[107]).

3.5.2. Magic Angle Spinning and Decoupling

However, in most cases, the CSA needs to be eliminated to obtain high-resolution spectra.[99] This is achieved by magic angle spinning (MAS), where samples are spun around an axis that is tilted by 54.7° from the static magnetic field (**Fig. 15**).[108,109] This angle derived from the anisotropy of NMR interactions is given by a second-rank tensor,

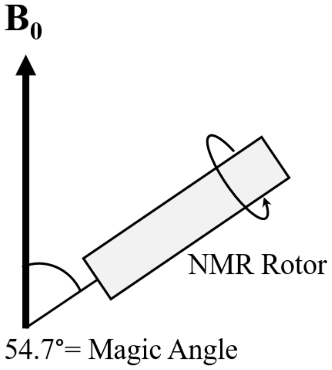

Fig. 15. Magic angle spinning for solid state NMR experiments.

whose time average vanishes at 54.7° (i.e., satisfied with $3\cos^2\theta - 1 = 0$). Today, solid-state NMR experiments are widely carried out under MAS rates of 5–100 kHz using cylindrical rotors with diameters between 0.7 and 7 mm.[99]

Strong heteronuclear dipolar interactions between the nuclear magnetic moments of two different nuclear spins, for example, ^{1}H–^{13}C and ^{1}H–^{15}N are not completely averaged out under MAS. Since each spin represents a nuclear magnetic moment that produces a small magnetic field, the *S* spin (refer to “rare” spin, e.g., ^{13}C or ^{15}N) will "feel" the magnetic field produced by the *I* spin (refer to “abundant” spin, mainly ^{1}H) and vice versa when the two spins are within reasonable proximity of each other (< 10 Å).[107] The magnetic field produced by the *I* spin will alter the external field felt by the *S* spin (depending on the internuclear vector of the *I* spin perpendicular to the magnetic field) and induce the effective local magnetic field at the site of *S* spin. Thus, the local field induced from dipolar interaction changes the resonance frequency and gives broadening to the chemical shift. For example, a typical coupling constant for a bonded ^{1}H–^{13}C pair at about 1Å distance is around 30 kHz.[107]

The dipolar interaction can be eliminated by applying a continuous or pulsed rf irradiation on a nuclear spin channel, called decoupling.[110] The rf irradiation induce the fast transition between parallel and anti-parallel spins and average the orientation of the *I* spin magnetic moments to zero, thereby dipolar decoupling is averaged away.[107] Therefore, the combination of MAS and decoupling provide the isotropic chemical shift and are critical techniques for enhancing the resolution and sensitivity of the observed nuclei.

3.5.3. Cross-Polarization Magic Angle Spinning

Longitudinal relaxation is on the order of milliseconds for abundant *I* spins such as ^{1}H, whereas it is on the order of minutes for rare *S* spins such as ^{13}C and ^{15}N nuclei with low natural abundance.[111] Therefore, a long repetition time is required between each scan to wait for the magnetization recovery ($5\times T_1$ or more), resulting in a low accumulation efficiency for solid-state NMR. This issue is solved by cross-polarization (CP), which enhances the signal sensitivity by transferring the magnetization from the abundant and high γ nuclei (usually ^{1}H) to the rare and low γ nuclei. The combination of CP, high-power proton decoupling, and MAS is referred to as CP-MAS and is widely used as a standard high resolution solid-state NMR technique (**Fig. 16**).[109,110]

In the CP-MAS method, a $\pi/2$ pulse is firstly irradiated to flip the proton magnetization onto the *xy* plane. By applying a $\mathbf{B}_{1H}$ rf field with a different phase of 90°, the magnetization of ^{1}H is held in the direction of the oscillating magnetic field $\mathbf{B}_{1H}$ (*y*-axis) for a certain period (spin locking). Simultaneously, the oscillating magnetic field $\mathbf{B}_{1S}$ is irradiated to *S* spins in the rotating system to fulfill the Hartmann–Hahn conditions:

$$\gamma_{1H}\mathbf{B}_{1H} = \gamma_{S}\mathbf{B}_{1S} \tag{14}$$

When Eq. (14) is satisfied for a period of τ_{CP} (contact time), the energy differences between the transition of the ^{1}H and ^{13}C can be equal in the rotating system. The energy transfer occurs from ^{1}H to ^{13}C through dipolar interaction, i.e., the polarization is transferred to eliminate the difference in the relative number of occupied spins between

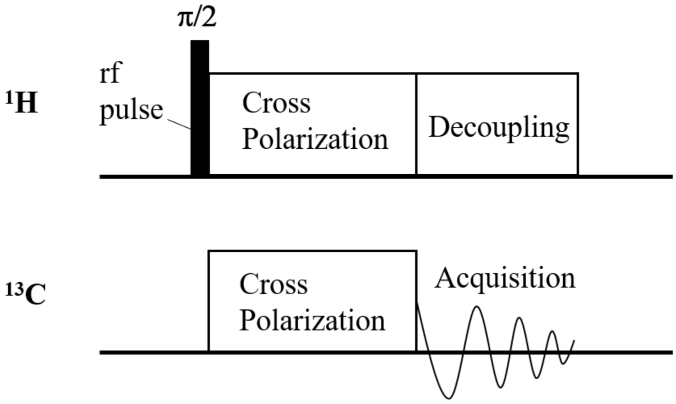

Fig. 16. CP-MAS sequence. ^{13}C is used as an example of *S* spin.

the two orientations (parallel and antiparallel). As a result, CP enhances the sensitivity of the measurement is improved by a factor of $\gamma_{\mathrm{1H}}/\gamma_{\mathrm{S}}$ compared to without CP. For example, the Hartmann–Hahn conditions for ^{13}C CP-MAS is,

$$\boldsymbol{B}_{\mathbf{1H}} = 4\boldsymbol{B}_{\mathbf{1C}} \tag{15}$$

The ^{13}C spins are enhanced by the ^{1}H spins by a factor of 4. Another advantage of the CP is that the repetition time can be set to T_1 of ^{1}H, significantly reducing the measurement time. The CP-MAS method is valid for solid samples but not for solution samples whose dipolar interactions are averaged out. The dipolar interactions are modulated by the molecular motion or the functional group's local motion; thus, the surrounding environment significantly affects the CP efficiency. Also, it should be noted that signal intensities/integrals are not quantitative after applying CP.

3.6. Pulsed Gradient Spin-Echo NMR

3.6.1. Magnetic Gradients and Self-Diffusion Coefficient

NMR is also useful for elucidating molecular dynamics in chemical and biological systems such as translational diffusion.[112] The random Brownian motion of molecules or ions in a pure liquid at thermal equilibrium is termed "self-diffusion" and is characterized by a self-diffusion coefficient, D (m^2 s^{-1}) measured over the millisecond to second time scale. Measuring D requires applying spatially homogeneous magnetic gradient pulses, **g** (T m^{-1}) throughout the sample.

In the following, it is assumed that $\mathbf{B_0}$ is oriented in the z-direction and nuclear spins have the Larmor frequency according to Eq. (4). If in addition to $\mathbf{B_0}$, there is a magnetic gradient **g** (T m^{-1}) defined by the **grad** of the magnetic field components parallel to $\mathbf{B_0}$ (components perpendicular to $\mathbf{B_0}$ can be neglected):[113]

$$\mathbf{g} = \nabla B_z = \frac{\partial B_z}{\partial x}\mathbf{i} + \frac{\partial B_z}{\partial y}\mathbf{j} + \frac{\partial B_z}{\partial z}\mathbf{k} \tag{16}$$

where **i**, **j**, and **k** are unit vectors of the laboratory frame of reference. Therefore, the magnitude of the magnetic field at position **r** is

$$B(\mathbf{r}) = \boldsymbol{B}_0 + \mathbf{g}\cdot\mathbf{r} \tag{17}$$

Eq (17) refers a homogeneous gradient brings a linear spatial change in the magnetic field in the direction of the gradient applied. Therefore, Larmor frequency in Eq. (4) becomes,

$$\omega(\mathbf{r}) = \gamma\left(\boldsymbol{B}_0 + \mathbf{g}\cdot\mathbf{r}\right) \tag{18}$$

Importantly, Eq (18) refers the nuclear spins in the different locations are spatially 'labelled' by **g** within the sample and becomes a function of the position **r**. The use of gradient pulses allows diffusion to be added the standard NMR observables of chemical shifts and relaxation time constants (e.g., T_1 or T_2) as well as spatial resolution in NMR imaging (see Section 3.7).

3.6.2. Pulsed Gradient Spin-Echo Sequence

The simplest and the most common pulse sequence for determining D is pulsed gradient spin-echo (PGSE) sequence, also called Stejskal and Tanner sequence. The PGSE sequence is a modified Hahn spin-echo sequence[114] and contains five important elements: (i) an initial π/2 rf pulse, (ii) a pulsed field gradient of duration δ and magnitude g inserted into τ delay, (iii) a waiting period Δ–δ, including a π rf pulse in the middle, (iv) another gradient with the identical duration and magnitude as (ii), and (v) acquisition that begins at the maximum echo (**Fig. 17**).[115]

The net magnetization $\mathbf{M_0}$ is oriented along the z-axis at thermal equilibrium and flipped onto the xy-plane by a π/2 pulse and thus the nuclear spins start precessing about the z-axis. The first gradient pulse is applied when the spins are precessing, resulting in each spin being spatially encoded in the direction of the applied gradient (assume that it is along the z-axis). The molecules or ions self-diffuse during the period Δ–δ with carrying the spatially encoded spins. At the end of the first τ period, a π pulse is applied, reversing the sign of the precession of the transverse magnetization. Then, the second magnetic gradient pulse decodes the special information of the spins by the first gradient pulse.

Importantly, if the spins have not undergone any translational motion with respect to the z-axis, the effects of the two applied gradient pulses cancel and thus transverse magnetization is completely refocused at time 2τ, and thus the maximum echo signal is obtained. However, if the spins change their positions due to the self-diffusion, refocusing of the transverse magnetization is incomplete and thus the echo signal is attenuated.[103] Hence, greater diffusion and/or larger gradient pulses gives a larger attenuation of the echo signal. The amplitude of the Hahn spin-echo signal with rectangular-shaped pulses is given by:[114]

$$S(2\tau) = M_0 \exp\left(-\frac{2\tau}{T_2}\right)\exp\left(-\gamma^2 g^2 D\delta^2\left(\Delta-\delta/3\right)\right) \tag{19}$$

The echo intensity is normalized with respect to the signal for $g = 0$, more practically, 1% of $g_{\max}$ is to obtain the signal attenuation equation:[103,113]

$$\begin{aligned} E(g,\Delta) &= \frac{S(g,\Delta)}{S(0,\Delta)} \\ &= \exp\left(-\gamma^2 g^2 D\delta^2\left(\Delta-\delta/3\right)\right) \\ &= \exp(-bD) \end{aligned} \tag{20}$$

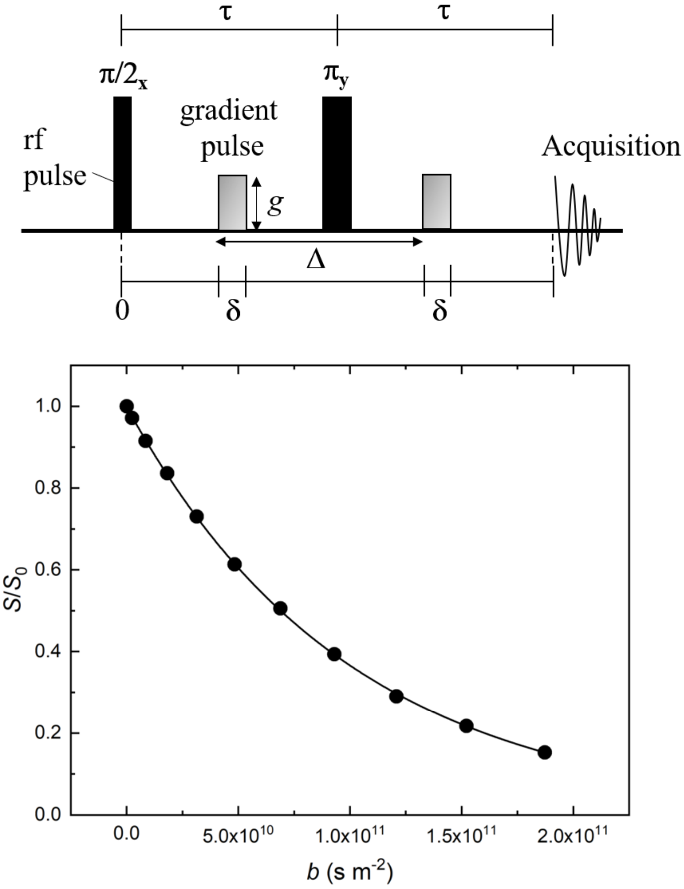

Fig. 17. PGSE sequence for measuring the self-diffusion coefficient, *D* (top) and an example of the dodecane signal attenuation due to the self-diffusion (bottom).

where Δ is the diffusion time between gradient pulses and these have duration δ. A series of PGSE experiments is performed with at least ten different g, δ, or Δ and constant τ. The NMR peak is integrated to correct the attenuation data E. Then, plot ln(E) versus b, and D can be obtained from the regression slope. However, perfect rectangular pulses are technically unable to achieve, and the rapid rise of the gradient pulses can generate eddy currents in the surrounding conducting surfaces.[113] Instead, non-rectangular pulses (e.g., sine or trapezoidal shaped) are often used, as a consequence, altering the diffusion weighting factor, b in Eq. (20). The PGSE attenuation equation with a half-sine shaped gradient is given by Eq. (20) with D and[116,117]

$$b = \gamma^2 g^2 \delta^2 \frac{(4\Delta - \delta)}{\pi^2} \tag{21}$$

3.6.3. Pulsed Gradient Stimulated-Echo Sequence

In the PGSE sequence, the second π pulse must be applied before the signal decays on the xy-plane, i.e., during the transverse relaxation process. Therefore, for short T_2 samples, e.g., ionic liquid (see Reference journal VI), the pulsed gradient stimulated-echo (PGSTE) is used instead of the PGSE (**Fig. 18**).[118] Importantly, the π pulse in the PGSE is replaced by $\pi/2 - \tau_2 - \pi/2$ in the PGSTE. The magnetization is stored along the z-axis during τ_2 (i.e., most of Δ) and thus only longitudinal relaxation is involved in meanwhile. It is possible to set up the PGSTE experiment for $T_1 >> T_2$ samples with shorter τ_1 and longer Δ to minimize the transverse relaxation loss and eddy current. The normalized PGSTE attenuation equation is the same as Eq. (20).

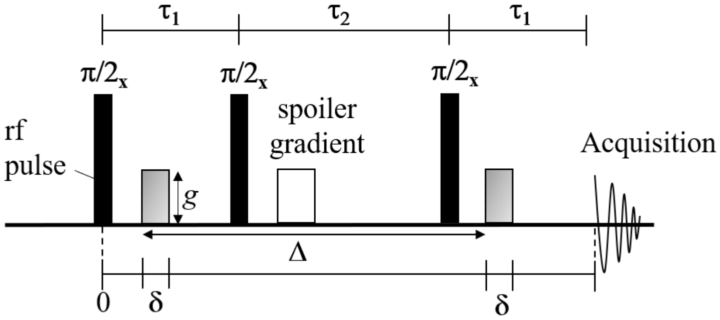

Fig. 18. PGSTE sequence for measuring *D* in short T_2 samples.

3.7. NMR Imaging

NMR imaging, commonly referred to as magnetic resonance imaging (MRI), provides deep insight into internal microstructure and dynamics in spatially inhomogeneous samples.[119] In MRI, the sample is notionally broken into volume elements (voxels), and the contrast in the image reflects the spatial variation in NMR observables. MRI has been recognized as one of the most powerful and non-invasive imaging techniques for clinical diagnosis (e.g., cancer) using highly abundant ^{1}H nuclei.[120,121] For such medical purposes, most clinical MRI have magnetic strengths of 1.5 or 3 T, generally providing the resolution in millimeters. On the contrary, for research purposes (non-clinical), high-field MRI such as 14.1 T can offer voxel sizes less than (100 μm)^3 and provide critical information on the spatial distribution of chemical species, relaxation times and self-diffusion coefficients in diverse areas of science (e.g., food industry, plant physiology, porous materials, molecular dynamics).

Unlike spectroscopic information can be obtained from the entire sample for NMR, MRI can be considered a map of the spatial nuclear spin density ρ.[121] As seen in Eq. (18), each spin at different position **r** can be spatially labelled by a unique resonance frequency ω when a magnetic gradient for MRI, **G** (T m^{-1}) is applied,

$$\omega(\mathbf{r}) = \gamma\left(\mathbf{B_0} + \mathbf{G}\cdot\mathbf{r}\right) \tag{22}$$

The first term in Eq. (22) is the spatially homogeneous contribution while the second term is the spatially inhomogeneous contribution.[120] If magnetic strength is constant in a plane, the resonance frequency also becomes constant in that plane. Importantly, the distribution of Larmor frequencies in the presence of the magnetic gradient forms the basis for MRI.[122] From Eq. (22), it can be defined using a reciprocal space vector, **k** (m^{-1})

$$\mathbf{k} = \frac{\gamma \mathbf{G} t}{2\pi} \tag{23}$$

Such k-space can be transverse by either changing the magnitude of G or duration, t. The observed signal S(**k**) is

$$S(\mathbf{k}) = \int \rho(\mathbf{r})\ \exp^{i2\pi\mathbf{k}\cdot\mathbf{r}}\ \mathrm{d}\mathbf{r} \tag{24}$$

S(**k**) can be also expressed using the nuclear spin density ρ by applying Fourier transformation,

$$\rho(\mathbf{r}) = \int S(\mathbf{k})\ \exp^{-i2\pi\mathbf{k}\cdot\mathbf{r}}\, d\mathbf{k} \tag{25}$$

Note that ρ is a three-dimensional (3D) quantity, and the acquisition of a two-dimensional (2D) or 3D image is theoretically achieved by using three orthogonal magnetic gradients. A combination of the gradients (one for each spatial dimension) and rf pulses are applied to obtain an image of $\rho(\mathbf{r})$ into k-space in the form of the signal $S(\mathbf{k})$. These three gradients are used for spatial imparting (encoding) processes: (1) slice selection, (2) phase encoding, and (3) frequency encoding.

3.7.1. Spatial Encoding Magnetic Gradient

The first gradient is termed 'the slice gradient.' The slice gradient is used to select a slice (2D plane) of a sample. The slice selection is performed by a well-defined gradient usually along the z-axis throughout the sample with a frequency-selective rf pulse. The slice gradient G_z gives an individual Larmor frequency of the spins linearly along with the z-axis, and frequency selective rf pulse only excites a selected frequency band of spins.[100] Thus NMR signals are corrected only from the magnetization of the selected slice. The magnetization components within the slice are dephased quickly after the $\pi/2$ rf pulse causing interference but a negative gradient after that is applied to refocus the magnetization, otherwise using a self-refocusing π rf pulse.[120]

After the slice selection, the other two gradients perpendicular to G_z spatially encode each voxel within the selected slice by 'phase' and 'frequency' to get a different signal.[100,121] The second gradient is termed the 'phase gradient.' The phase gradient, G_y, along with the y-axis, varies the phases of the spins resulting in precessing at slightly different frequencies as a function of position y. At every repetition, the amplitude of the phase gradient is changed from $-G_y$ to $+G_y$ to get full set of echoes. The last gradient is termed the 'frequency gradient' or 'readout gradient.'[120] The frequency gradient, G_x, is applied during the signal acquisition along with the x-axis. Therefore, all the spins in the selected slice are now spatially encoded along with x and y positions by their frequencies and phases and thus have a unique signal. The corrected signal echoes with different phase gradients are then digitized and stored in a raw data matrix called 'k-space.' Data in k-space are finally converted into an 2D or 3D image by 2D Fourier transform.[123]

The basic scheme of spin-echo based MRI sequence is shown **Fig. 19**. The spin echo sequence is characterized by the rf pulses, three gradients (i.e., slice, phase, and frequency gradients), and two distinct time duration, the echo time and repetition time. The echo time, T_E, is the time between the rf pulse to the maximum echo acquisition while the repetition time, T_R, is the time from the beginning of the sequence to the start of the next.

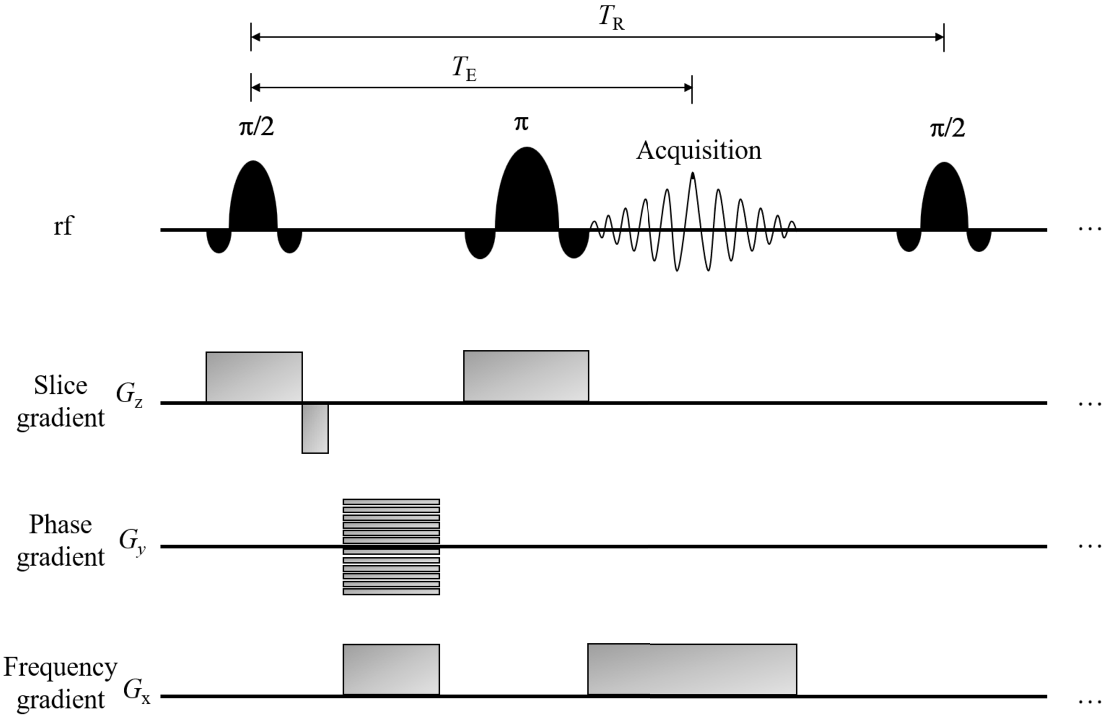

Fig. 19. The basic spin-echo MRI sequence. The shape of rf pulse is approximate sinc function. The slice, phase, and frequency gradients can be applied along the *z*-, *y*-, and *x*-axes, respectively. The phase gradient is shown as the horizontal line group to stand for the amplitude change at every repetition.

3.7.2. T_1, T_2, and Diffusion-Weighted Image

The different components in the sample (e.g., fat and water) will give the different intensities for images. The image contrast (intensity) is determined by various contributions such as spin density, relaxation times (e.g., T_1 and T_2), and diffusion.[100] It is possible to emphasize (so called 'weight') and determine those factors (e.g., relaxation times) by adjusting the lengths of T_E or T_R and using a particular MRI sequence. For example, a T_1-weighted image can be obtained by the rapid acquisition with relaxation enhancement with variable recycle delay (RAREVTR), which is the spin echo-based imaging sequence.[124] As for a T_2-weighted image, multi-slice-multi-echo (MSME) sequence is an available choice.[125] A volume average (voxel-wise) T_1 or T_2 values can be obtained from the signal intensities of multiple T_1-weighted images acquired with different T_R fitting by Eq. (10) while T_2-weighted images are acquired with different T_E and Eq. (12). Other than the relaxation, the diffusion gradient pulses can be incorporated into the MRI pulse sequences (e.g., spin-echo sequence).[126] The diffusion weighting imaging (DWI) is one of the most common methods for obtaining the voxel-wise diffusion coefficient, apparent diffusion coefficient [ADC ($m^2\ s^{-1}$)]. Therefore, in diffusion MRI, D in Eq. (20) is replaced with ADC. MRI has the advantage compared to spectroscopic NMR that the obtained voxel-wise T_1, T_2, and ADC can be presented as 'maps' to visualize the difference as the image contrast.

Chapter 4 – Structural Characterization of Cellulose Nanofibers Isolated from Spent Coffee Grounds

Structural characterization of cellulose nanofibers isolated from spent coffee grounds and their composite films with poly(vinyl alcohol): A new non-wood source

---

N. Kanai, T. Honda, N. Yoshihara, T. Oyama, A. Naito, K. Ueda, I. Kawamura *Cellulose* **27**, 5017-5028 (2020)

4.1. Abstract

The waste valorization of spent coffee grounds (SCGs), which are obtainable in large amounts worldwide for new non-wood source has been considered. Cellulose nanofibers derived from SCGs have been successfully produced by 2,2,6,6-tetramethylpiperidine-1-oxyl radical (TEMPO)-mediated oxidation of SCGs containing 10% cellulose (dry weight). The TEMPO-oxidized cellulose nanofibers (TCNFs) are 20-35 nm wide observed by scanning electron microscopy. X-ray diffraction showed that TCNFs are present in a cellulose crystal form I. The average crystal size corresponding to a fiber width was 4.2 nm, as determined from the diffraction pattern. Solid-state NMR shows that hemicellulose and lignin were mostly removed from SCGs via TEMPO-mediated oxidation, but small amounts of triacylglycerols remained in the TCNFs. Thermogravimetric analysis of TCNFs showed two major steps of thermal decomposition at 251 °C and 267 °C, which were higher than the coffee roasting temperature range. Furthermore, in order to investigate an interaction of these TCNFs with a polymer, a SCG-derived TCNF composite film with poly(vinyl alcohol) (PVA) as a water-soluble polymer was prepared. We found the TCNFs were successfully integrated into the polymer. The outcome of this study indicated that SCGs could be used as well as wood as an alternative source for producing TCNFs, thus contributing to the development of sustainable green chemistry.

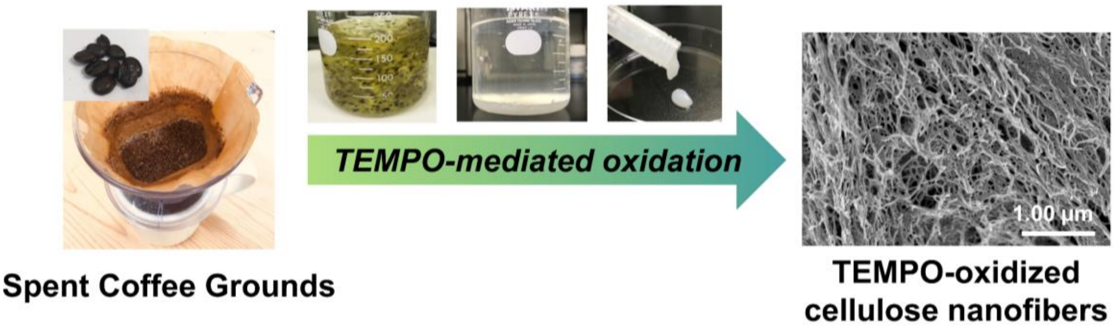

Fig. 20. The graphical abstract of Chapter 4.

4.2. Introduction

More than nine million tons of coffee products were consumed worldwide in 2018.[127] At present, approximately six million tons of spent coffee grounds (SCGs) are generated annually worldwide.[19] Approximately half of the overall SCGs are generated by the instant (i.e., soluble) coffee industry and major part of those SCGs are simply discarded or burned as fuel in the coffee industry.[128,129] That results in the release of considerable amount of carbon dioxide and biologically toxic components, which pose environmental hazards.[20,29,33]

Over the last decade, research on SCGs aimed at waste revalorization has significantly increased, including novel approaches to reuse SCGs effectively in an eco-friendly manner.[21,34,130] The valorization of SCGs have been proposed without any fractionation as substrates for the cultivation of microorganisms,[131] lead removals from contaminated water,[22] and electrode materials.[23] As low-cost raw material, bioactive components were extracted from SCGs, such as caffeine,[24] chlorogenic acid,[25] kahweol and cafestol[26] for variety use in the food and pharmaceutical industries.[19] In particular, extracting lipids containing 10-20% SCGs and its transformation into biodiesel oil has been demonstrated as a potential fuel feedstock.[29,132–135] However, recycling SCG for the purposes mentioned above is still challenging due to its heterogeneity and economic inefficiency.

Almost half of the dry weight of SCGs consists of cellulose and hemicellulose, which can be exploited as sources of value-added materials.[33,130,136] Cellulose constitutes approximately 10% of SCGs.[31–34] Extracting cellulose from SCGs requires extreme hydrolysis conditions such as lower pH, higher temperature, and reaction times.[33] This is caused by the fact that the coffee bean cell walls are formed with a strong honeycomb structure,[27,30] making hydrolysis at mild conditions and the consequent cellulose extraction inefficient.

Native cellulose can be selectively isolated from plant cell walls by catalytic oxidation, using the 2,2,6,6-tetramethylpiperidine-1-oxyl radical (TEMPO).[137] When cellulose is oxidized with TEMPO, only hydroxyl groups on microfibril surface are converted to sodium carboxylate groups. These TEMPO-oxidized cellulose nanofibers

(TCNFs) can be transformed into discrete cellulose nanofibers with an average width of 3-5 nm by gently mechanical disintegration in water.[3,44] The CNFs have been extracted not only from wood, but also from various non-wood materials including industrial residues, e.g., bamboo,[138] cassava bagasse,[139] pineapple leaf,[140] banana peel,[141] oil palm.[142] The number of non-wood CNF research publications constitutes more than 50% of the wood CNF publications in 2018;[12] however, the preparation of CNFs from SCGs has not been reported yet.

In this study, we report SCGs as a completely new non-wood source of CNFs. SCG-derived TCNFs have been produced and characterized using field emission scanning electron microscopy (FE-SEM), solid-state nuclear magnetic resonance spectroscopy (NMR), X-ray diffraction (XRD), and thermogravimetric analysis (TGA). We also present some preliminary results (SEM, solid-state NMR, TGA) for nano-composite films of the SCG-derived TCNFs with poly(vinyl alcohol) (PVA) as the matrix. In this paper, we presented SCGs have potential to be alternative source of wood-derived CNF as a view of structure of the TCNF.

4.3. Materials and Methods

Preparation of Spent Coffee Grounds

Commercially available robusta roasted coffee beans (RCBs) from Indonesia and arabica RCBs from Tanzania were ground using an electric coffee grinder (Kalita, EG-45, Japan) for 70 s. Hot water was added to the ground RCBs. Wet-ground RCBs were spread thinly on filter paper and dried at room temperature for at least 1 day. Completely dried ground RCBs were termed SCGs. Triacylglycerol (TAG), the main lipid present in SCGs, was removed by stirring in *n*-hexane for 2 days.[27] After delipidization, SCGs were termed solid residues. As a comparative sample, microcrystalline cellulose (MCC, 20 μm wide) was purchased from Sigma-Aldrich.

TEMPO-Mediated Oxidation

Solid residues (1 g) were suspended in distilled water (130 mL) containing TEMPO (20 mg, 98%, Sigma-Aldrich) and NaBr (0.1 g, ≧ 99.0%, Sigma-Aldrich). TEMPO-mediated oxidation was initiated with the addition of NaClO (60 mL, 3-5%, Sigma-Aldrich) at pH 10-10.5 and room temperature. The TEMPO-mediated oxidation was performed for 3 h upon continuous stirring, and the pH was kept at 10-10.5 by adding 0.5 M NaOH or 1 M HCl during oxidation. The end of the oxidation reaction was detected when pH did not change for 10 min.[9] Ethanol (10 mL) was added to quench TEMPO-mediated oxidation. The oxidized cellulose was filtered out under vacuum (filter paper with 3.0 μm pores) and then washed 3 times with distilled water. An aliquot of the collected cellulose slurry was lyophilized with a freeze-dryer (EYELA, FDU-2100) for 2 days to determine its dry mass. The cellulose slurry was dispersed to 1.5 wt% in distilled water and sonicated for 2-3 min with a homogenizer (BRANSON, Sonifier Analog Series 250) using the setting of output:3 and duty cycle:41% to obtain a gel-like TCNF dispersion.

Preparation of Composite Films

PVA (polymerization degree approximately 1500, saponification degree 86.0-90.0 mol%, Wako Pure Chemicals Co., Japan) powder was solution (1.0 M) was added into distilled water for 10 min, and subsequently stirred at 90 °C for 1 h. After cooling to room temperature, 1.0 M PVA solution was added to a TCNF dispersion (1.5 wt%) at 50 wt% loading and stirred for 3 days. PVA/TCNF dispersion was then carefully and uniformly cast into a Teflon square dish and dried with a constant temperature dryer (DRV320DE, Advantec Tokyo Co., Ltd., Japan) at 40 °C overnight *in vacuo*.

Scanning Electron Microscope

The gel-like TCNF dispersion (0.5 g) was washed with *tert*-butanol (10 mL, ≧ 99.0%, Sigma-Aldrich). The dispersion was centrifuged at 15000 *g* for 5 min (MX-305, Suprema 21, TOMY), and the supernatant was removed. This process was repeated 10 times, replacing solvent; after that, the TCNFs were lyophilized for 6 days. The completely dried TCNF powder was observed on a field emission scanning electron microscopy (FE-SEM) (HITACHI, SU8010) coated with osmium at 1.0 kV (**Fig. 21a**) and with Pt-Pd at 0.5 kV (**Fig. 21b**). PVA/TCNF composite films covered with Pt-Pd coating were also observed, with an accelerating voltage of 1.0 kV.

Solid-State NMR

The solid materials such as TCNF powder, PVA film, and PVA/TCNF composite films were directly packed into a 4.0 mm outer diameter zirconia rotor. ^{13}C cross-polarization magic angle spinning (CP-MAS) solid-state NMR spectra were recorded on a 600 MHz NMR spectrometer (Bruker Avance III) equipped with a 4.0 mm ^{1}H-^{13}C-^{15}N triple resonance E-free MAS probe at room temperature with a contact time of 1.0 ms and a recycle delay time of 3 s. MAS frequencies were 13, 10 and 12.5 kHz for TCNF powder, MCC samples, and composite films, respectively. ^{13}C chemical shifts were externally referenced to tetramethylsilane (0.0 ppm). The NMR measurements were operated in TOPSPIN software as well as the data processing and peak deconvolution.

X-ray Diffraction

XRD experiments were performed using an X-ray diffractometer operating at 40 kV and 45 mA at room temperature. The hydrated sample was placed on a non-reflective sample plate and was dried for three hours using by vacuum dryer. The powder-XRD patterns were recorded with Cu Kα radiation ($\lambda = 0.15418$ nm) at a step size of 0.05° over the 5-50° 2θ range with a scanning speed of 0.3°/min. The patterns were corrected using a blank and then analyzed using the pseudo-Voigt function for peak deconvolution.[143]

Thermogravimetric Analysis

TGA was performed to compare the stability of TCNFs and MCC. Approximately 1 mg of each sample was placed in an aluminum pan, using an empty pan as a reference. TGA was performed using an STA 2500 Regulus (NETZSCH Co., Ltd, Germany) at a temperature range of 30-450 °C with an increasing temperature rate of 10.0 ℃ /min under a helium stream with a flow rate of 50.0 mL/min. The neat PVA and the composite PVA/TCNF films were also measured by a TGA-50 (Shimadzu Co., Ltd, Japan) using a platinum cell from 25 to 800 °C with an increase of 10.0 °C /min, under a nitrogen gas stream at a flow rate of 50.0 mL/min. The derivative thermogravimetric data of the films were smoothed with a 50-point adjacent averaging smooth function.

4.4. Results

4.4.1. Characterization of SCG-Derived TCNFs

SEM images of TCNFs prepared from SCGs are shown in **Fig. 21**. As shown in **Fig. 21a**, TCNFs are susceptible to partial aggregation during the drying process, which makes it difficult to distinguish the borders of TCNF; however, most TCNFs are well separated from each other (**Fig. 21b**). The termination of TCNFs tends to be bent as shown in **Fig. 21b**. The diameters of SCG-derived TCNFs were found to be in a range of 20-35 nm with an average diameter of 25 nm (n = 30, n: the number of TCNFs to calculate the average diameter).

To characterize the final material, we performed ^{13}C solid-state NMR experiments. The signals at 60-110 ppm correspond to glucose units in cellulose (**Fig. 22**). Namely, the C6 (62.8 and 65.3 ppm), C2, C3, C5 (72.4 and 75.0 ppm), C4 (83.9 and 89.1 ppm), and C1 (105.3 ppm) groups were assigned. Hemicelluloses, which mainly contain mannose, galactose, and arabinose, and lignin signals did not appear in the ^{13}C NMR spectrum;[33,144,145] however, traces of TAG appeared at 20-35 ppm.[27] The lower field isolated peak at 174.2 ppm was assigned to a carboxylic acid (COO^-), indicating the successful TEMPO-mediated oxidation of SCGs.[137] Furthermore, the ^{13}C chemical shifts of C4 and C6 carbon are highly sensitive to the cellulose crystal structure and hence, the

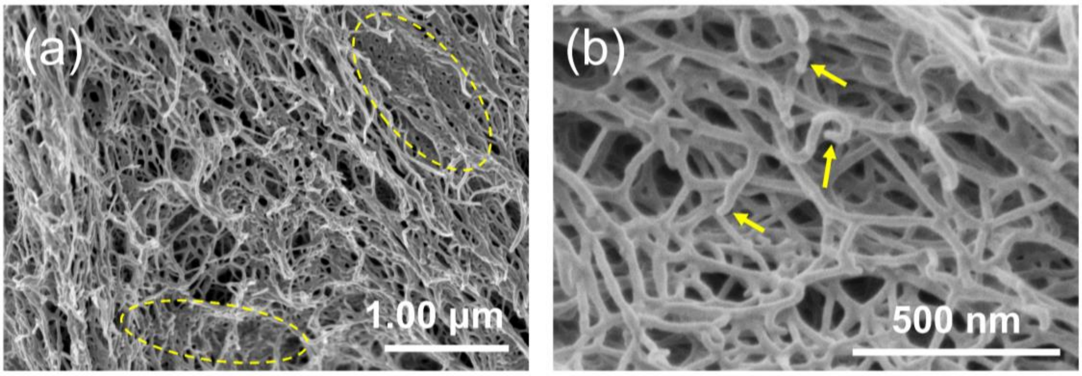

Fig. 21. SEM images of SCG-derived TCNFs differing in scale bars: (a) 1.00 µm and (b) 500 nm.

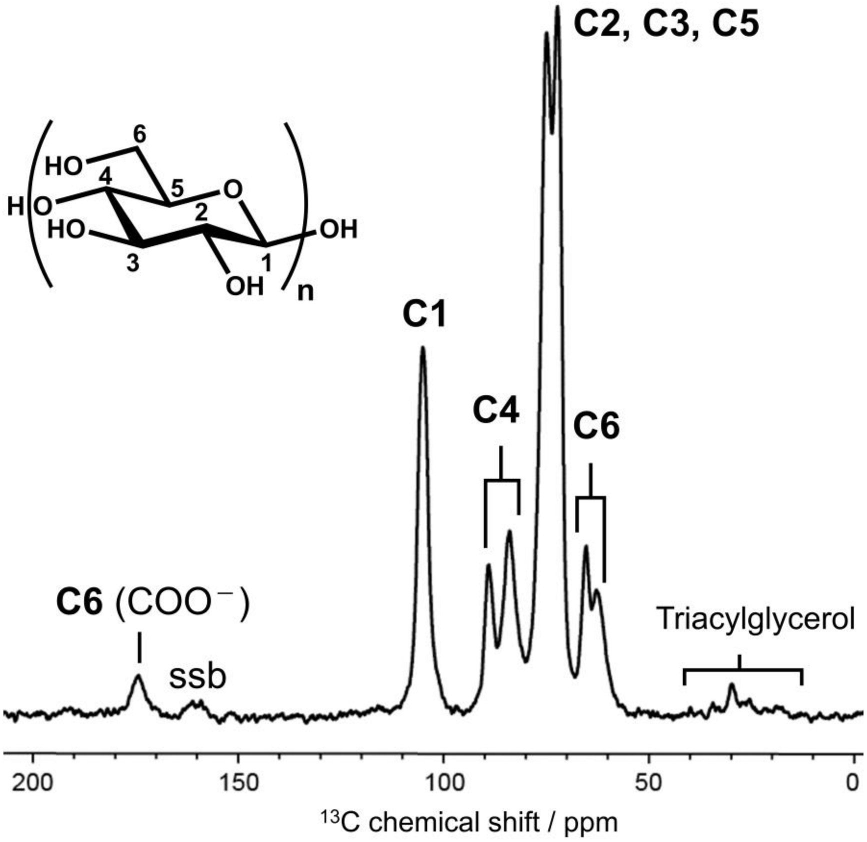

Fig. 22. ^{13}C CP-MAS NMR spectrum of SCG-derived TCNFs with signal assignment. ''ssb'' represents spinning sidebands. The chemical structure of cellulose is shown on the upper left.

crystallinity of the TCNFs could be determined by comparing the separated areas.[146] The C4 of the TCNFs resonated at 89.1 ppm for the crystalline state, and 83.9 ppm for the non-crystalline (or amorphous) state.[147] The crystallinity of TCNFs was estimated to be 32% by deconvolution analysis of the C4 NMR signal, which is 16% lower than that of MCC (supporting **Fig. S2**).

The powder-XRD pattern was recorded in order to determine the crystal structure and degree of crystallinity of the SCG-derived TCNFs (**Fig. 23**). The XRD patterns showed typical cellulose I as expected, with two distinct crystal phases Iα and Iβ in various proportions.[7,148] The three main peaks at 14.9°, 16.7°, and 22.6° for cellulose Iβ were assigned to Miller indices of (1–10), (110), and (200), respectively, which are the counterparts to the (100), (010), and (110) peaks of the cellulose Iα pattern.[149] The average crystal size corresponding to fiber width of the TCNF was 4.2 nm, as calculated from the (22.6°) diffraction peak using the Scherrer equation.[150] The shape factor, i.e., *K*

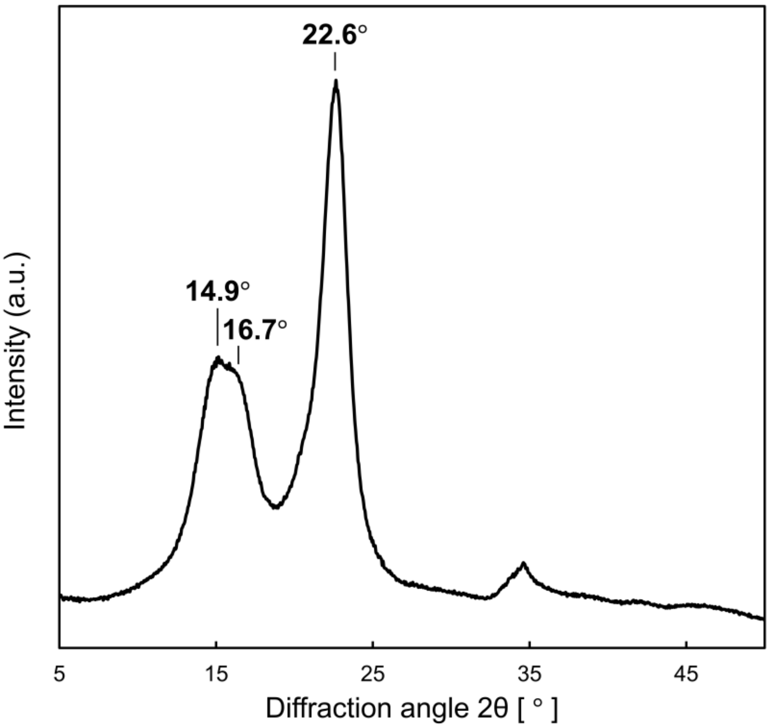

Fig. 23. Powder-XRD pattern of SCG-derived TCNFs (a.u., arbitrary unit) measured at room temperature.

was taken as 0.9. Furthermore, it was possible to evaluate the sample crystallinity by deconvolution of the XRD pattern.[143,147] The crystallinity of the TCNF (72%) was slightly lower than MCC (79%) (**Fig. S3** and **Fig. S4**), which was consistent with the trend calculated from NMR deconvolution analysis of the C4 signal.

As shown by the solid black line in **Fig. 24**, the TCNF started to degrade earlier than MCC. The TCNF showed gradual weight loss due to the strongly bounded water beginning at around 100 °C. Then, overlapping degradation occurred within 150 °C and 250 °C due to decarboxylation of the sodium carboxylate groups and dehydration of the cellulose chains.[151] The major degradation process of the TCNF occurred in two steps at 251 °C and 267 °C. In the first step, sodium hydro-glucuronate units were decomposed and in the second step, unaltered cellulose units were decompose.[152] The second degradation temperature is 77 °C lower than maximum weight loss of MCC. This indicates that crystalline cellulose chains decrease in peak points due to thermally unstable anhydroglucuronate units in the TCNF.[153] Compared to MCC, the TCNF showed

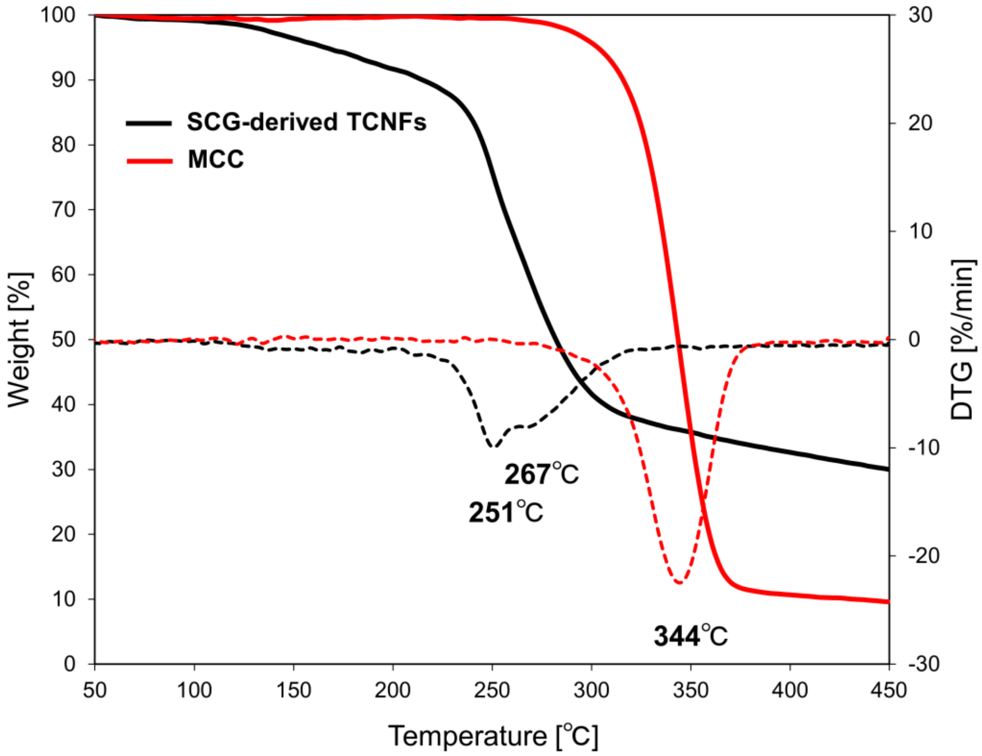

Fig. 24. Thermogravimetric curves of SCG-derived TCNFs (solid black line) and MCC (solid red line), and derivative thermogravimetric curves (SCG-derived TCNFs: dashed black line, MCC: dashed red line). Thermal degradation temperature of each sample is shown in derivative TG curves.

much higher char residues (30 wt%) at 450 °C. According to Lichtenstein and Lavoine,[151] sodium cation as a counterion influenced the char production.

4.4.2. Structural Characterization of PVA/TCNF Composite Film

In order to investigate an interaction of the TCNF with PVA polymer, structure of composite film was characterized by solid-state NMR and TG/derivative TG (DTG). A transparent composite film of 1:1 PVA/TCNF was prepared, and it became slightly yellowish during a drying procedure (**Fig. S5**). Morphology of the PVA/TCNF composite film was observed by SEM as shown in **Fig. 25**. The surface of the film confirmed a high degree of uniformity, although air bubbles were observed when water was evaporated (**Fig. 25a**). TCNFs aggregated in the film during the drying process and appeared as sharp tips in the cross-sections (**Fig. 25b**).

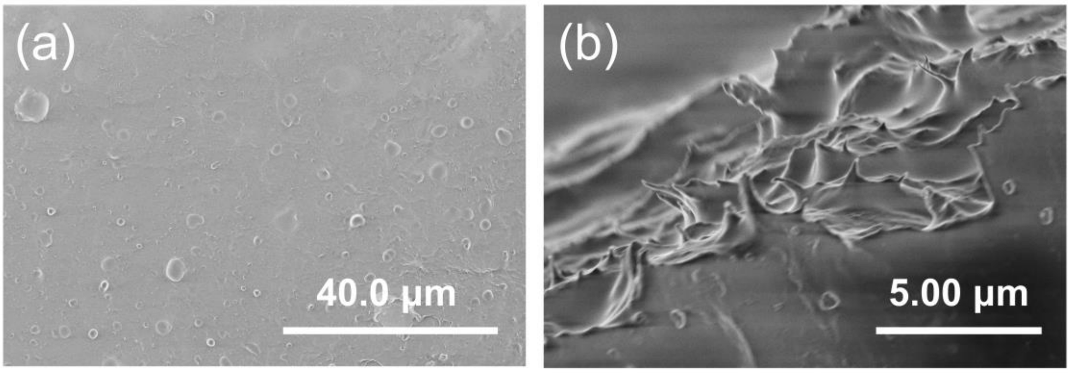

Fig. 25. SEM images of a PVA/TCNF (1:1) transparent composite film: (a) on surface and (b) in cross-sections

In the ^{13}C solid-state NMR spectrum of PVA/TCNF (1:1), the TCNF and PVA signals were unambiguously observed (**Fig. 26**). The identifiable C1, C4 and carbonyl signals corresponding to TCNF in the composite film were slightly shifted compared to that of the TCNFs itself (the TCNF in the composite film / the SCG-TCNF; C1 104.8 / 105.3 ppm, C4 88.9/89.1 and 83.9/83.9 ppm, carbonyl 173.3 / 174.2 ppm). Especially, the carbonyl carbon of the TCNF, which appeared originally at 174.2 ppm, slightly higher-field shift to 173.3 ppm on blending with the PVA polymer. The systematic NMR peak shifts of carbonyl carbon signals in cellulose acetate / VP-MMA polymer indicated that the blending with the VP-MMA copolymer disrupted intra- and inter-hydrogen bonding in the original cellulose acetate itself.[154] Therefore, the obtained NMR result of the composite film is suggested that the blending with PVA polymer altered the hydrogen bonding behavior of the TCNF, resulting the presence of interaction of the TCNF with the water-soluble polymer. The signals at 60-80 ppm and 36-51 ppm have been assigned to the methine and methylene groups in PVA, respectively. Hydrogen bonding in the PVA film broadened the CH signal significantly.[155,156] The low-intensity peak at 30 ppm corresponds to the remaining TAG. The saponification degree of PVA was 86.0-90.0 mol%, and therefore signals derived from polyvinyl acetate (PVAc, **Fig. S1**) appeared at 21.4 ppm and 171.2 ppm in both spectra.[157]

The TGA and corresponding DTG curves of TCNF, PVA/TCNF, and PVA films

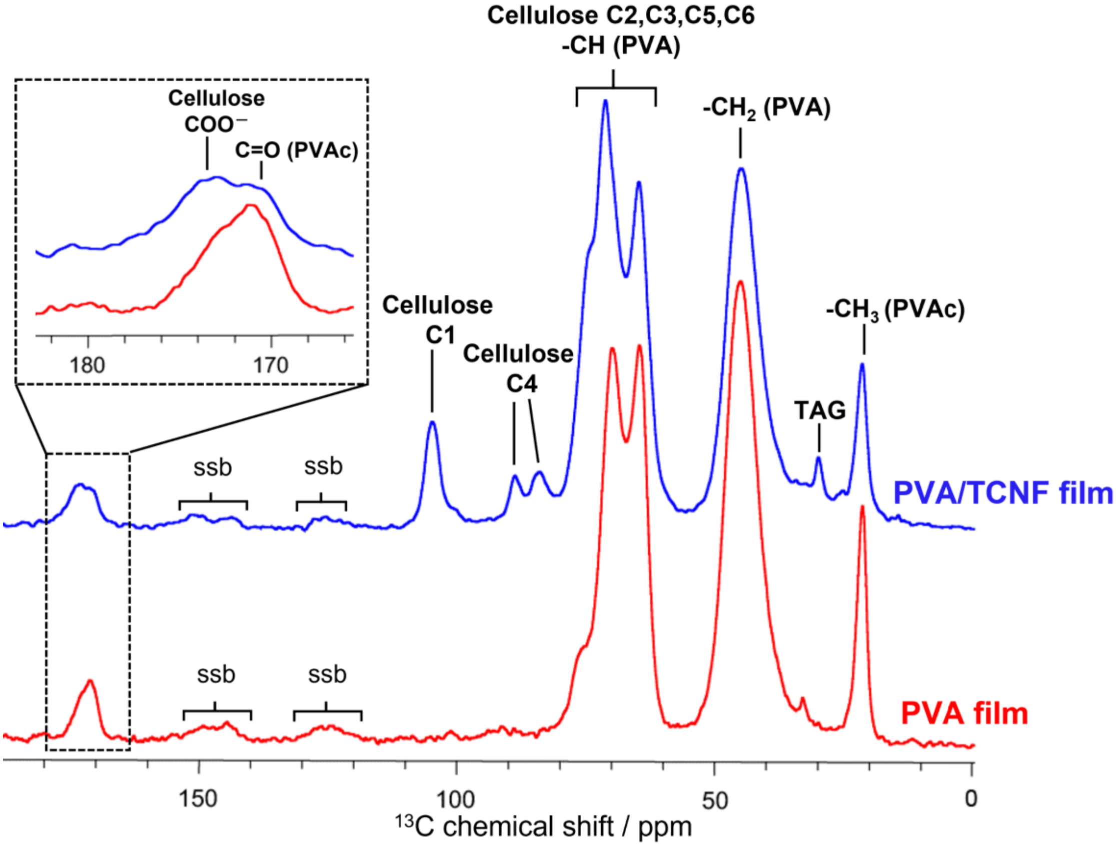

Fig. 26. ^{13}C solid-state NMR spectra of PVA/TCNF (blue) and PVA (red) films. ssb: spinning sidebands.

are shown in **Fig. 27**, respectively. There is an initial weight loss of up to 8 % for all the three samples at around 100 °C corresponding to absorbed moisture in the films.[158,159] Neat TCNF and PVA films were found to show maximum weight loss at 255 °C (**Fig. 27b** t_1) and 313 °C (**Fig. 27b** p_1), respectively, as extracted from the corresponding DTG curves. In the case of PVA/TCNF composite film, the decomposition temperature was recorded at about 289 °C which lies between those of the respective single films (**Fig. 27b** pt_1). This result confirms that TCNFs were successfully integrated into the PVA, most probably via hydrogen bonding between hydroxyl groups in TCNFs and PVA. On the other hand, the weight loss occurred at around 380 °C in the neat TCNF (**Fig. 27b** t_2) and 435 °C in the neat PVA (**Fig. 27b** p_2) films showed a similar temperature to those two corresponding degradations in the PVA/TCNF composite film (**Fig. 27b** pt_2 and pt_3). Those two steps were probably due to each respective decomposition of PVA and cellulose structure in the films or carbonaceous matter.[164]

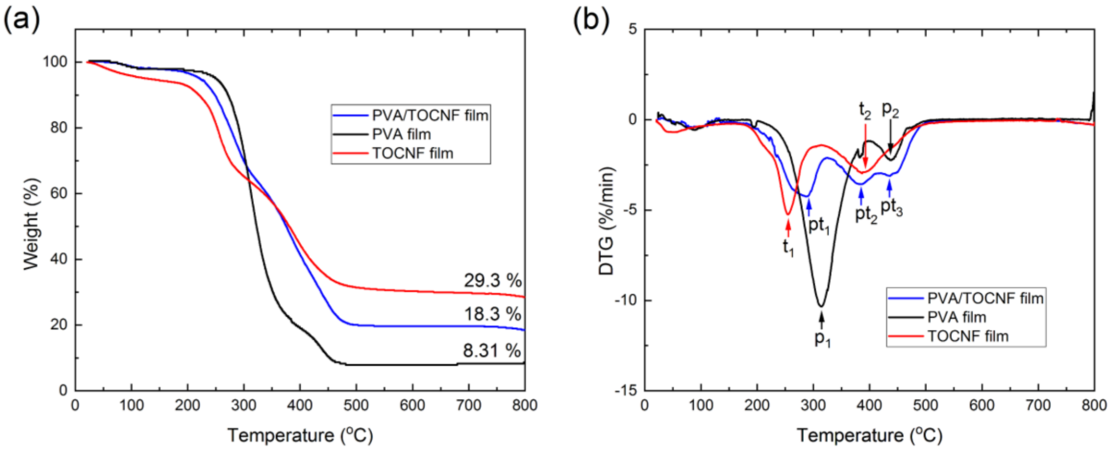

Fig. 27. (a) Thermogravimetric (TG) and (b) derivative thermogravimetric (DTG) curves of PVA/TCNF (blue), PVA (black) and TCNF (red) films.

4.5. Discussion

Cellulose microfibrils vary widely in size, from 2 to 30 nm, depending on the cellulose source.[160] As an example, the completely individualized microfibril obtained from wood is 3-4 nm wide, which is the smallest elements next to cellulose molecules consisting of 30-40 cellulose chains.[3] The average diameter of SCG-derived TCNFs was 25 nm, as shown in **Fig. 21**, suggesting that a few microfibril units are still fibrillated in the average crystal size revealed from the powder-XRD pattern. The most likely reason for insufficient fibrillation is quite high ratio of hemicelluloses (30-40 wt%), lignin (19.8-29.8 wt%) and TAG in SCGs.[21] Remaining TAG revealed in the ^{13}C CP-MAS NMR spectrum (**Fig. 22**) may prevent complete disconnection. Also, there is a possibility that unobservable small amounts of hemicelluloses and lignin in NMR spectrum remain in TCNFs. According to Isogai et al.,[3] hemicelluloses and lignin can be removed as water-soluble degraded fractions in TEMPO/NaBr/NaClO oxidation system. In this study, the required amount of NaClO in the TEMPO system was 3-18 times higher than holocelluloses reported by Kuramae et al.[161] This suggests that plenty of NaClO was consumed in solubilization of hemicelluloses and lignin. The most beneficial feature of using TEMPO is to be able to get 3-4 nm narrow fibers. In order to achieve nanofibrillation into the completely individualized microfibril, some pre-treatment with mild alkali and sodium chlorite for removing hemicelluloses and lignin to some extent is considered to be needed.[162]

Another crucial structural feature estimated from chemical shifts in the ^{13}C NMR spectrum (**Fig. 22**) is the conformation of CH_2OH (C6-OH) in cellulose. There are three possible conformations that can be distinguished. The C6 signal is sensitive to this conformational change and can be considered as a diagnostic region; *gauche−gauche* (*gg*, 60−62.6 ppm), *gauche−trans* (*gt*, 62.5−64.5 ppm), and *trans−gauche* (*tg*, 65.5-66.5 ppm).[163] In our case, the signal at 65.3 ppm corresponding to C6 can indicate the presence of the *tg* conformer. Native cellulose predominantly displays the *tg* conformation inside microfibrils, allowing the formation of intramolecular hydrogen bonds between O3 and O5, and O6 and O2.[7,164] On the other hand, the amorphous C6 peak at 62.8 ppm reflects the structure of the surface cellulose chains and may have both *gt* and *gg* conformations.[165,166]

The different crystallinity of the TCNFs were estimated by XRD and NMR analysis (72% and 32%). There are several reasons for significant differences in crystallinity index can be observed depending on whether XRD peak or ^{13}C4 NMR peak deconvolutions is used.[167] Firstly, the results from the former method usually generate higher values than the latter, because of differences in measurement principles and analysis techniques.[147,168] Secondary, the XRD crystallinity index of textured sample has a tendency to be higher than that of non-textured sample.[167,169] Thus, the density and thickness of our XRD sample might influence the index. Thirdly, adding of signals of paracrystalline layers of crystalline and amorphous domains in C4 NMR peak deconvolution leads to decrease of a crystalline index value.[167] It is previously suggested that there is a paracrystalline region in cellulose, which is less ordered with a somewhat larger mobility than the crystalline cellulose structure.[170] The surface induced by fibril aggregation is often presented as a disordered form with a very broad component around 84 ppm. However, the observed C4 signal at 83.9 ppm of SCGs-derived TCNFs was not so much broad than that of crystalline component at 89.1 ppm (**Fig. 22**). By dynamic nuclear polarization (DNP) NMR experiments, well-resolved narrow C4 NMR signals of ball-milled cotton cellulose around 84 ppm suggested partial order component has been identified in the disordered domains.[143,171] Therefore, above reasons can be assumed that the difference of the crystallinity index of the TCNFs. Importantly, the ^{13}C NMR method is reasonable to use with lignin-removed cellulose samples.[172] As compared with ^{13}C CP-MAS NMR spectra of RCBs and hexane-treated coffee residues,[27] our SCG-derived TCNFs did not contain mostly lignin and hemicellulose as mentioned above.

The average crystal size of the TCNFs (4.2 nm) from XRD is ~1 nm larger than that of other non-wood resources but relatively close to that of TEMPO-oxidized cellulose from softwood (3.8 nm) and hardwood (3.8 nm).[161,173,174] This demonstrates that SCG-derived TCNFs show similar characteristics as wood-based TCNFs. In addition, further investigation to generate completely individualized TCNF is warranted.

Inserting sodium carboxylate groups via TEMPO-mediated oxidation resulted in a significant decrease in temperature of thermal degradation; however, our results are within the temperature range of wood-based material,[158] indicating that the thermal stability of SCG-derived TCNFs may be comparable to that of wood-derived TCNFs. The roasting temperature of coffee beans is generally in the range of 170-230 °C for 10-15 min;[175] therefore, the celluloses contained in coffee beans and the resulting SCGs are not degraded during the roasting process.

PVA was chosen as a versatile matrix because of its film-forming ability as well as biocompatibility for TCNFs.[176,177] Further investigation of composite materials based on SCG-derived TCNFs will need to be performed but these preliminary results indicate compatibility.

4.6. Conclusions

This is a detailed structural study report of cellulose nanofibers derived from SCGs as a promising new non-wood source of CNFs. We have shown that TEMPO-mediated oxidation can be used to produce CNFs from SCGs without pre-processing steps of crushing. Purified SCG-derived TCNFs were defined fibers in the width of 25 nm. In ^{13}C CP-MAS NMR spectrum of SCGs-derived TCNFs, the isolated carbonyl peak appeared, indicating the successful TEMPO-mediated oxidation to the cellulose in SCGs. The XRD analysis revealed the crystal structure of the TCNFs is present in a typical polymorphic cellulose I form. The TCNFs showed a characteristic thermal decomposition behavior by the TEMPO-mediated oxidation. Namely, structure and thermal property of the SCG-derived TCNFs was similar to wood-derived TCNFs.

Further, using the SCGs-derived TCNFs, the composite film with PVA polymer was prepared. Solid-state NMR and TG/DTG experiments of the film revealed that the TCNFs were sufficiently integrated with the PVA polymer. Thus, the SCGs-derived TCNFs provides a possibility of compatibility to forming the composite film.

Chapter 5 – Structural Characterization of Cellulose Nanofibers Isolated from Waste Hop Stem

Upcycling of waste hop stems into cellulose nanofibers: isolation and structural characterization

---

N. Kanai, K. Nishimura, S. Umetani, Y. Saito, H. Saito, T. Oyama, I. Kawamura *ACS Agric. Sci. Technol.* **1**, 347–354 (2021)

ACS
AGRICULTURAL
SCIENCE & TECHNOLOGY

July/August 2021 Volume 1 Number 4

pubs.acs.org/acsagscitech

Upcycle

ACS Publications
Most Trusted. Most Cited. Most Read.

www.acs.org

Fig. 28. The journal front cover image of Chapter 5. CNFs isolated from waste hop stem are painted on the canvas in front of the hop farm in Tono city.

5.1. Abstract

Hop (*Humulus lupulus*) is cultivated to harvest female flowers that lend a deep flavor, aroma, and bitter taste to beer. However, the rest of the plant is burned or land filled as agro-industrial waste. This work upcycles hop stems (HS), which contain 44% cellulose, and demonstrates their suitability as raw materials to isolate cellulose nanofibers (CNFs). The Wise method followed by alkaline pretreatment removed lignin and hemicellulose. 2,2,6,6-tetramethylpiperidine-1-oxyl radical-mediated oxidation fibrillated CNFs from pretreated and non-pretreated HS. A uniform height distribution was inferred from atomic force microscopy, with a median of ~2 nm for pretreated and non-pretreated HS-derived CNFs. Solid-state nuclear magnetic resonance and X-ray diffraction characterizations indicated that the pretreatment enhanced the purity and crystallinity of the CNFs, though traces of triacylglycerols and calcium oxalate monohydrate remained. The two CNF samples exhibited similar two-step thermal degradation at 255–260 °C and 300 °C, though lower char residues were produced by the pretreated CNFs.

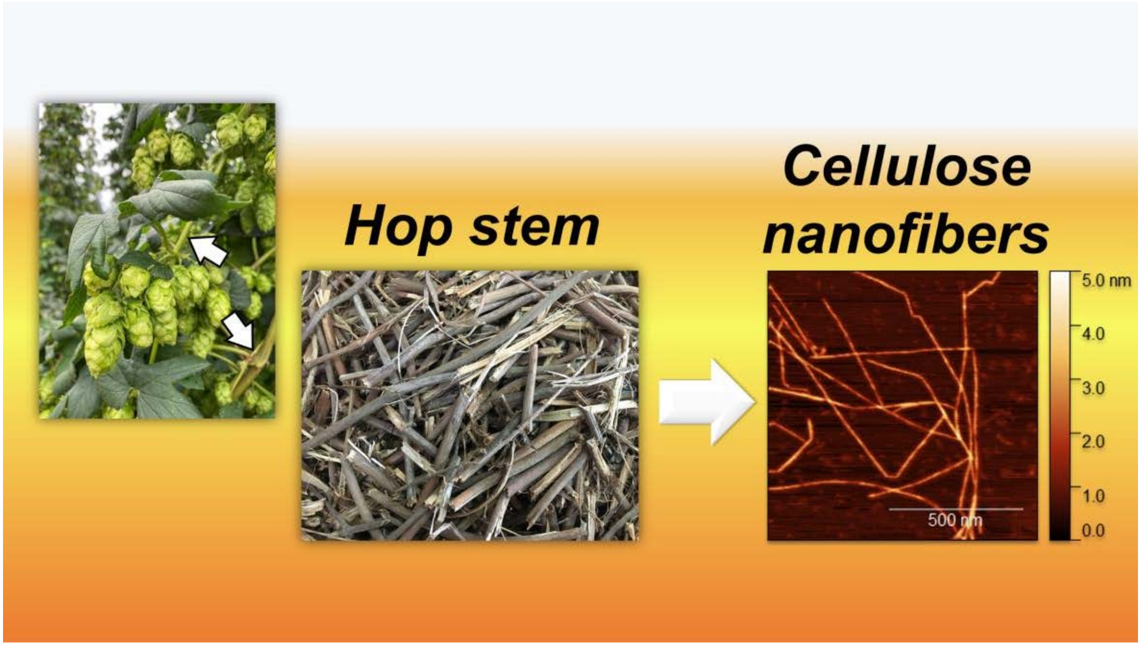

Fig. 29. The graphical abstract of Chapter 5.

5.2. Introduction

Hop [*Humulus lupulus*, **Fig. 30a)**] is a perennial, herbaceous climbing plant belonging to the family of Cannabaceae, whose cones (i.e., female flowers, **Fig. 30b**) have been used for centuries as an essential ingredient of beer.[35,36] The global hop production reached a record-high of approximately 130 thousand metric tons in 2019.[178] Stems and leaves, accounting for approximately 75% of the biomass produced by hop cultivation, are typically burned or land filled after harvesting the cones.[38] The average mass of dried stems per plant is approximately 600–900 grams (**Fig. 30b**).[179] The city of Tono in Japan started to cultivate hop since 1963, and currently produces approximately 50 tons of hop cones annually. Approximately 150–180 tons of hop stems are discharged as an agro-industrial waste every year in Tono (**Fig. 30c**). Hence, hop stems contribute globally to a significant amount of waste every year.[38,41]

The problem of disposing and managing hop stems is a major concern in its producing regions. Young hop shoots have traditionally been consumed in spring in Europe.[39] A few studies have also been conducted on the potential use of hop stems, for example, for the removal of lead(II) ions,[38] or as reinforcements for polypropylene composites.[40]

Recently, the use of agro-industrial waste derived from plants has attracted great interest for waste revalorization and upcycling.[180,181] Producing value-added biomaterials from agro-industrial waste would reduce the amount of disposal and develop a new business opportunity by building a circular recycling system at the local level. Agro-industrial waste is generally lignocellulosic biomass, which is inexpensive, renewable, and abundant.[182] The cell walls in plants consist of cellulose microfibrils in an amorphous matrix of lignin and hemicellulose. The chemical compositions of cellulose, hemicellulose, and lignin vary widely depending on the source of the fibers.[183] Since the 2000s, there has been a growing trend toward the nanofibrillations of various lignocellulosic resources for extracting cellulose nanofibers (CNFs) due to their outstanding properties including light weight, high tensile strength, large specific surface area, and low coefficients of thermal expansion.[3,12,174,184]

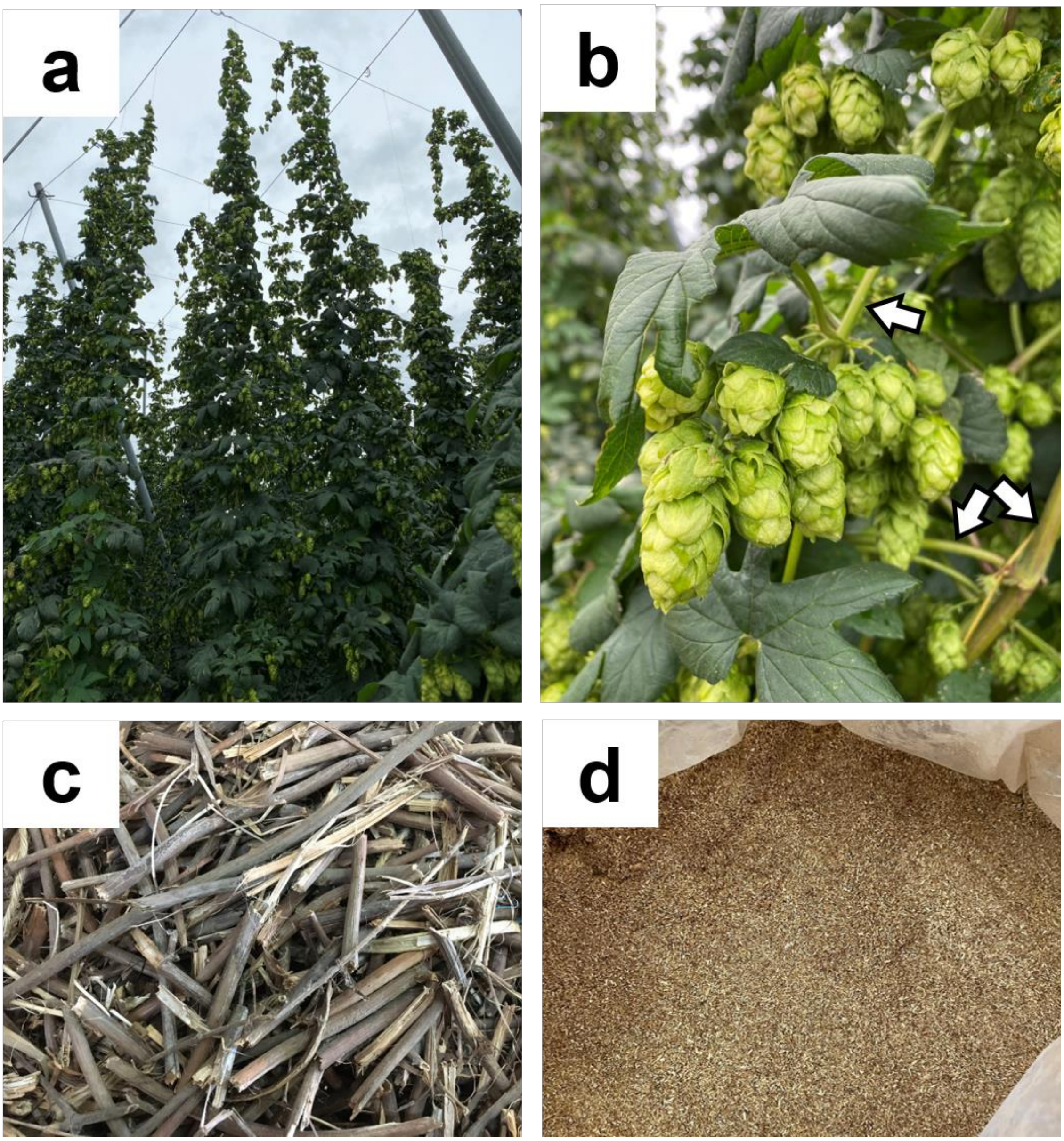

Fig. 30. (a) Hop plants during the harvest season in Tono city, Iwate, Japan, and (b) their cones for beer production, and stems (shown by white arrows) that become agricultural waste. Collected hop stems were air-dried (c) and subsequently mechanically milled into fine particles (d).

Generally, CNFs are extracted via pretreatment steps (e.g., purification) followed by refinement steps (e.g., chemical or enzymatic treatments).[185–187] When specific fibrillation pretreatment using TEMPO (2,2,6,6-tetramethylpiperidine-1-oxyl radical) are applied to wood cellulose followed by gentle mechanical disintegration in water, CNFs with a width of 3–4 nm can be obtained.[3,137] TEMPO-oxidized CNFs have been successfully extracted from wood as well as from a variety of non-wood resources including agro-industrial wastes such as pineapple leaves,[188] banana pseudo-stems,[189] grapefruit peels,[190] and spent coffee grounds.[191] To our knowledge, no attempt has been made to isolate CNFs from hop stems. N. Reddy et al.[41] reported the extraction of natural cellulose fibers having 16.5 μm width and 2.0 mm length from hop stems, indicating that hop stems could be used as a source of CNFs.

Herein, we pioneer the isolation of CNFs from hop stems (HSs) using TEMPO-mediated oxidation. Reducing the amount of lignin and hemicellulose in lignocellulose fibers prior to TEMPO-mediated oxidation (i.e., pretreatment) is an effective method for improving the degree of nanofibrillation.[161] Pretreated and non-pretreated HS were used in this study to investigate the influence of pretreatment on the nanostructure and properties of the CNFs produced. The morphology of the CNFs was assessed by field emission scanning electron microscopy (FE-SEM) and atomic force microscopy (AFM), and structural characterization was carried out using solid-state nuclear magnetic resonance (NMR), X-ray diffraction (XRD), and thermogravimetric analysis (TGA).

5.3. Materials and Methods

Preparation of Raw Materials

HSs were air-dried for over a year prior to use and mechanically milled into fine dried particles using a dry-defibrating machine (West Japan Engineering, Inc.), as shown in **Fig. 30d**. The HS used were a mixture of bines and shoots. 3.0 g of the HS were de-waxed by stirring in either *n*-hexane or acetone/water mixture (9:1 v/v) at room temperature for 2 d. All chemicals, including acetone, acetic acid, potassium hydroxide, NaClO (+5.0 %), TEMPO (98%), sodium bromide (> 99.0%), HCl, NaOH, and *tert*-butanol were used without further purification (Wako Pure Chemicals Co., Ltd., Japan).

Wise Method & Alkaline Pretreatment

The Wise method[162] followed by alkaline pretreatment was performed to remove lignin and hemicellulose.[192] The de-waxed dried sample (~ 90 wt.% of HS) was heated at 75 °C in 150 mL of sodium chlorite (1.25 g, $NaClO_2$) solution containing 0.2 mL of acetic acid (CH_3COOH) for 1 h, and then a further 1 g of $NaClO_2$ and 0.2 mL of CH_3COOH were added every hour over two more hours, i.e., the delignification process (i.e., the Wise method) was repeated three times. The solid fraction was filtered through a glass filter (17G-3) and was then washed with distilled water until the pH of the filtrate became 7. Approximately 2.0 g (~ 65 wt.% of HS) of the dried fraction was heated at 80–85 °C in 150 mL of 4 wt.% potassium hydroxide (KOH) for 2 h and subsequently washed five times with distilled water. The dry weight of the final fraction following alkaline pretreatment was approximately 1.0 g (~ 30 wt.% of HS).

TEMPO-Mediated Oxidation

TEMPO-mediated oxidation was performed on two de-waxed HS samples, one which underwent pretreatment (stem_{w}) and one which didn't ($\text{stem}_{w/o}$). Either 1.0 g of stem_{w} or 2.7 g of $\text{stem}_{w/o}$ was suspended in distilled water (130 mL) containing 20 mg of TEMPO and 0.1 g of NaBr. TEMPO-mediated oxidation was initiated by adding different amounts of NaClO, 54 mmol/g-stem_{w}, and 60 mmol/g-$\text{stem}_{w/o}$. The oxidation was performed as reported in a previous study.[191] To prepare a CNF dispersion, the cellulose slurry was dispersed in distilled water at 1.0 wt.% concentration and sonicated for 3 min using a homogenizer (BRANSON, Sonifier Analog Series 250) at the output setting of 3 and the duty cycle set at 41%. The CNF dispersion obtained from stem_{w} was termed CNF_{w}, and that from $\text{stem}_{w/o}$ was termed $\text{CNF}_{w/o}$. The yield of each slurry before sonication for CNF_{w} and $\text{CNF}_{w/o}$ were 23.6 wt.% and 47.8 wt.% of HS, respectively. The carboxylate contents determined from the electric conductivity titration method were 0.69 mmol/g for CNF_{w} and 0.67 mmol/g for $\text{CNF}_{w/o}$ (**Fig. S7**).[193] The procedure for obtaining CNF_{w} and $\text{CNF}_{w/o}$ is summarized in **Fig. 31**.

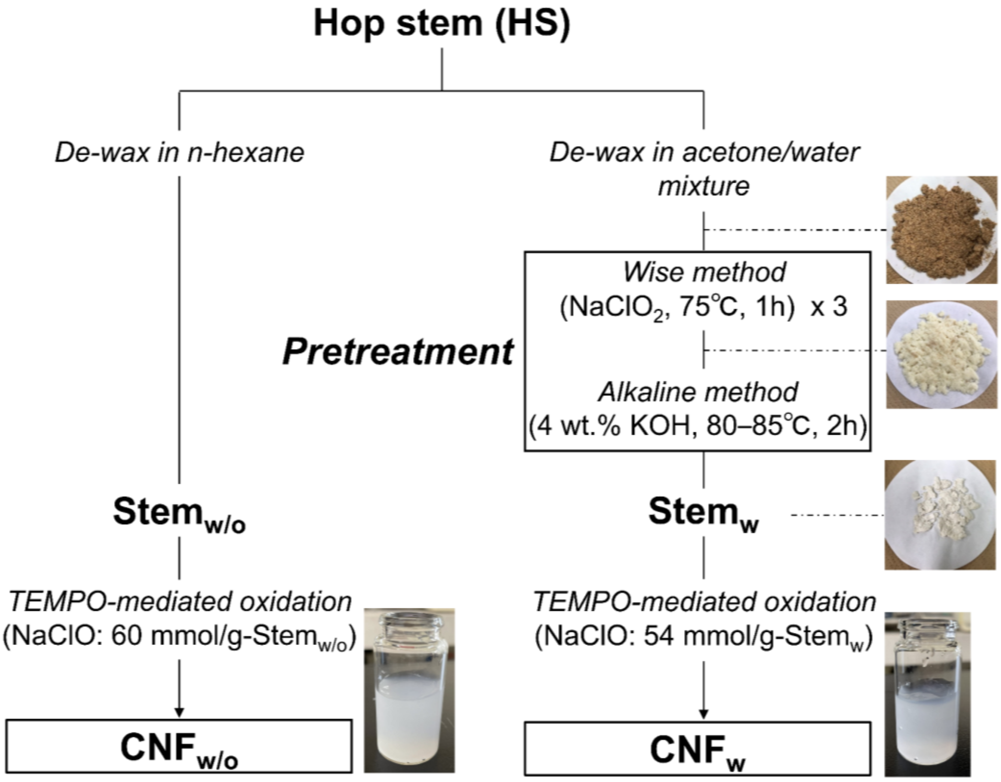

Fig. 31. Experimental procedure for the preparation of $CNF_{w/o}$ from non-pretreated HS and CNF_w from pretreated HS. The photographs of the final $CNF_{w/o}$ and CNF_w 0.8 wt.% dispersions are also shown along with the dried fraction after each step.

Chemical Composition Analysis

The chemical composition of the HS in terms of cellulose, hemicellulose, and lignin was determined from the combination of two standard test methods: the neutral detergent fiber method according to AOAC 2002:04/ISO 16472:2006, and the acid detergent fiber method according to ISO 13906:2008.

Field-Emission Scanning Electron Microscopy

CNF_w and $CNF_{w/o}$ were completely dried by solvent replacement in *tert*-butanol for observation by field emission scanning electron microscopy (FE-SEM) (HITACHI, SU8010). The dried CNF_w and $CNF_{w/o}$ were coated with Pt-Pd in advance and SEM images were obtained at the accelerating voltage of 1.0 kV.

Atomic Force Microscopy

The heights of $\mathrm{CNF_w}$ and $\mathrm{CNF_{w/o}}$ were probed using AFM (SPA-400, Seiko Instruments) by depositing 1 μL of a 0.001 wt.% dilute suspension of $\mathrm{CNF_w}$ or $\mathrm{CNF_{w/o}}$ on a freshly-cleaved mica plate followed by drying for 10 min at room temperature. AFM images were captured in the tapping mode in air using an aluminum-coated silicon cantilever having a spherical tip of 10 nm radius and a spring constant of 13 N $\mathrm{m^{-1}}$ (SI-DF20, HITACHI, Japan). Images were taken of 1.0 μm × 1.0 μm regions, and subsequently processed and analyzed using Gwyddion 2.56. Two hundred CNFs were randomly selected from 16 images to investigate the height distribution for each CNF sample, which was determined by flattening the images and drawing a line across an isolated CNF, followed by measuring the peak height in the profile (see **Fig. S8**).

Solid-State NMR

The HS, the delignified HS obtained from the Wise method, and one dried CNF sample each of $\mathrm{CNF_w}$ and $\mathrm{CNF_{w/o}}$ were directly packed into a zirconia NMR rotor of 4.0 mm outer diameter. ^{13}C cross-polarization magic angle spinning (CP-MAS) solid-state NMR spectra were recorded on a 600 MHz NMR spectrometer (Bruker Avance III) equipped with a 4.0 mm ^{1}H/^{13}C/^{15}N triple resonance E-free MAS probe at room temperature with a contact time of 1–1.5 ms and a delay time of 3 s. The HS sample was measured with a MAS frequency of 12.8 kHz and 20480 scans. The delignified HS, $\mathrm{CNF_w}$ and $\mathrm{CNF_{w/o}}$ were measured with a MAS frequency of 12.5 kHz and 30000, 55000, and 28000 scans, respectively. The ^{13}C chemical shifts were indirectly referenced to methylene carbon resonance in solid adamantane at 38.48 ppm. All NMR measurements including data processing and peak deconvolution were performed using TopSpin software (ver. 3.6.1). The two peaks of cellulose C4 (i.e., amorphous and crystalline) were deconvoluted and fitted to the convolution of Gaussian and Lorentzian curves to determine the NMR crystallinity index (CI_{NMR}) of the CNFs using:

$$\mathrm{CI}_{NMR}\,(\%) = \frac{S_{\mathrm{cry}}}{S_{\mathrm{cry}} + S_{\mathrm{amo}}} \times 100 \tag{26}$$

where S_{cry} is the integral of the C4 crystalline region at 89 ppm, and S_{amo} is the integral of the C4 amorphous region at 84 ppm.[147]

X-ray Diffraction

The crystal structure information of $\mathrm{CNF_w}$, $\mathrm{CNF_{w/o}}$ and the HS was evaluated from XRD patterns acquired using a parallel beam geometry. The sample was placed on a non-reflective sample plate, which was additionally used as a blank, and pre-pressed to fit in the plate. The measurements were conducted on an X-ray diffractometer (Rigaku, SmartLab) operating at 40 kV and 45 mA using Cu Kα radiation ($\lambda = 0.15418$ nm) at a step size of 0.05° in the 2θ range of 5–45° at a scanning speed of 0.3°/min. The crystalline and amorphous peaks were separated in the diffraction patterns according to the XRD peak deconvolution method suggested by Park et al.[147] using OriginPro 2021, and the XRD crystallinity index (CI_{XRD}) of the CNFs was determined using:

$$\mathrm{CI}_{XRD}\ (\%) = \frac{A_{\mathrm{cry}}}{A_{\mathrm{cry}} + A_{\mathrm{amo}}} \times 100 \tag{27}$$

where A_{cry} is the total cellulose crystalline area, and A_{amo} is the broad amorphous area centered at $2\theta = 21°$ in the deconvoluted XRD pattern following subtraction of the background spectra. In addition, the average crystal size of the CNFs was calculated from diffraction peaks in cellulose I using the Scherrer equation, given as follows:[150]

$$\mathrm{L} = \frac{K\lambda}{\beta\cos\theta} \tag{28}$$

where L is the crystal size, K is the shape factor (0.9), λ is the wavelength of Cu Kα radiation (i.e., 0.15418 nm), β is the full width at half-maximum (FWHM) of the diffraction peaks in radians, and θ is the Bragg diffraction angle.

Thermogravimetric Analysis

The degradation temperatures of $\mathrm{CNF_w}$, $\mathrm{CNF_{w/o}}$ and the HS were determined by TGA, performed using a TGA-50 (Shimadzu Co., Ltd, Japan). The sample in a platinum cell was heated from room temperature up to 650 °C at the rate of 10.0 °C/min using helium as the carrier gas (50.0 mL $\mathrm{min^{-1}}$). The derivatives of the thermogravimetric curves for the three samples were smoothed using a 50-point adjacent-averaging smoothing function.

5.4. Results and Discussion

5.4.1. Chemical Composition

The chemical composition of the HS was compared to three major CNF sources: softwood, hardwood, and cotton (**Table 3**). The HS were found to be composed of cellulose, lignin, and hemicellulose (in decreasing order of content), which is the same trend as that seen in softwood stems.[15] The cellulose content of HS was equivalent (44%) to that of wood resources, however, its hemicellulose content (13%) was lower than that in wood or cotton stalks. Comparatively, the HS showed a lower hemicellulose content than most herbaceous and agricultural biomass.[15]

Although the HS had been stored at room temperature for over a year, they contained 8.7% moisture. Miao et al.[194] controlled moisture content by air-drying (7%–10%) or adjusting (15%), and concluded that a high moisture level increased the specific energy consumption for the comminution of particles to size finer than 2 mm. Air-dried HS should possess an advantage as raw materials in terms of energy consumption for mechanical size reduction for producing CNFs.

Table 3. Chemical composition of HS compared to those of three major CNF resources.

	HS[a]	Softwood[b]	Hardwood[b]	Cotton stalks[b]
Cellulose	44	43.3	46.8	66.2
Hemicellulose	13	27.9	30.4	18.4
Lignin	26	29.3	22.8	15.4

[a] Composition (g / 100 g dry) of the 8.7% moisture-containing HS (- wet).

[b] Composition data on dry ash-free basis normalized to 100.0% from an overview summarized by Vassilev et al.[15]

5.4.2. Microscopic Observation and Height Distribution

CNF_w and $CNF_{w/o}$ were observed using two different microscopy techniques (i.e., FE-SEM and AFM), as shown in **Fig. 32a, b, d,** and **e**. FE-SEM is a convenient method for obtaining an overview of a CNF sample, including CNF aggregation, and can thus serve as an essential and rapid initial step for the analysis of CNFs.[187,195] The two CNF samples

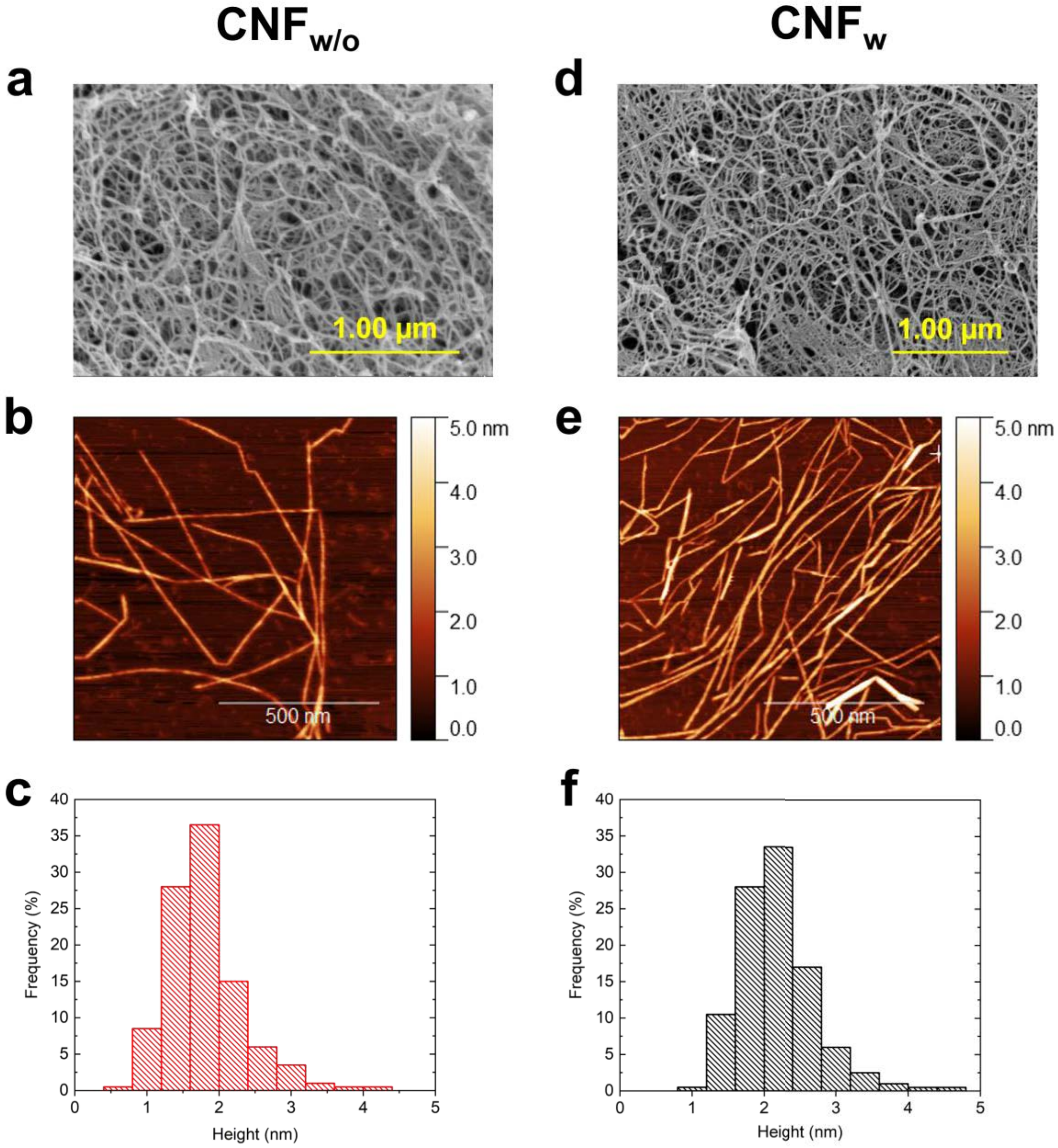

Fig. 32. Overview images of hop-derived TEMPO-oxidized (a and b) $CNF_{w/o}$ and (d and e) CNF_w via FE-SEM (a and d) and AFM (b and e). The height distributions of (c) $CNF_{w/o}$ and (f) CNF_w were determined from the extracted profiles of AFM.

derived from the HS produced similar FE-SEM images, including partial aggregation during the drying process (**Fig. 32a, d** and **Fig. S9**). Nevertheless, the resolution of FE-SEM is insufficient to probe the degree of nanofibrillation; therefore, the morphology of CNFs was assessed using AFM (**Fig. 32b, e**). A single layer of CNF_w or $CNF_{w/o}$ on the substrate possessed sharp bends and fibril splitting.[196] TEMPO-mediated CNFs have been reported to possess a relatively constant cross-section and a wide range of lengths (~ 0.1–1 μm).[196]

Generally, the CNF height and width values obtained by AFM vary mainly due to tip convolution effect.[197,198] CNF_w and $CNF_{w/o}$ were assumed to possess smaller widths than the radius of the tip of the AFM cantilever (i.e., 10 nm). Therefore, to avoid artifacts, only the height distributions are shown in the histograms (**Fig. 32c, f**). The median heights of CNF_w and $CNF_{w/o}$ were 2.2 ± 0.5 and 1.8 ± 0.5 nm, respectively. Importantly, individual CNFs having a height of ~2 nm could be obtained from HS via TEMPO-mediated oxidation regardless of whether they were pretreated. The AFM height distributions of the CNFs captured in air returned a smaller average than those in water as well as the cellulose microfibril size calculated from XRD, because of the large difference in the spring constant of the cantilever in air and water.[161]

5.4.3. Solid-State NMR

High-resolution solid-state NMR combined with CP-MAS is one of the most powerful techniques to investigate the atomic-level structure of solid biomass such as CNFs. In **Fig. 33**, the spectra of CNF_w and $CNF_{w/o}$ were overlaid to emphasize the slight difference in the shape of each peak. The HS and delignified HS produced by the Wise method are shown as well. Peak separation, chemical shifts, and assignments are shown in **Fig. S10** and **Table S1**. The HS showed a typical lignocellulosic spectrum which mainly contained broad peaks assigned to cellulose (60–110 ppm), hemicellulose (21.1, 98.7, and 173.5 ppm), and lignin (56 and 120–160 ppm). The H_1 and H_3 peaks, belonging to hemicellulose, corresponded to acetyl methyl and acetyl carbonyl groups, respectively.[199,200] Lignin peaks were assigned to the aromatic carbons except L_1 at 56 ppm, which was assigned to the methoxy group. Chen et al.[201] identified the monosaccharides mannose, rhamnose, glucose, galactose, xylose, and arabinose from the high-performance liquid

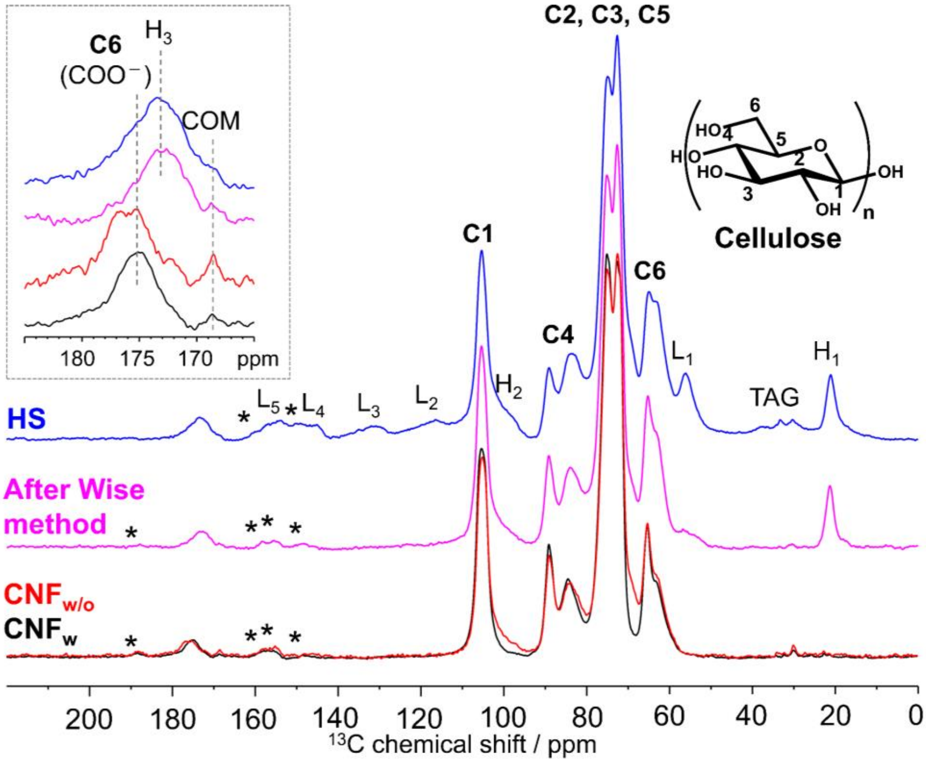

Fig. 33. ^{13}C CP-MAS NMR spectra of HS (blue), delignified stem produced by the Wise method (pink), CNF$_{w/o}$ (red), and CNF$_w$ (black). C1-6 correspond to the cellulose structure on the upper right. The carbonyl region was shown in the inset on the upper left. Asterisks were identified as spinning sidebands. Abbreviations: H, hemicellulose; L, lignin; TAG, triacylglycerol; COM, calcium oxalate monohydrate.

chromatography (HPLC) of hop cones. A similar constituent sugar is expected to be confirmed in the HS as well.

The Wise method mostly removed the lignin peaks, although the hemicellulose peaks remained. The C4 and C6 cellulose peaks were composed of two sets of peaks: sharp peaks (89 ppm/65 ppm) corresponding to the crystalline region in the lower field, and comparatively broad peaks (84 ppm/63 ppm) corresponding to the amorphous (also called as disordered or non-crystalline) region in the higher field.[143,168] The amorphous C4 and C6 peaks decreased in intensity. In contrast, the crystalline peaks increased in intensity and their line width decreased.

In both the CNF spectra, lignin and hemicellulose peaks nearly disappeared. According to Isogai et al., hemicelluloses and lignin in lignocellulose biomass can be mostly removed as water-soluble degraded fractions using the TEMPO/NaBr/NaClO oxidation system as NaClO consumption proceeded.[3] The NaClO in the system for obtaining CNF$_{w/o}$ mostly removed both hemicellulose and lignin. In addition, an isolated peak derived from oxidized C6 carboxylate groups (COO$^-$) appeared at 175 ppm as the intensity of amorphous C6 decreased further from that of the delignified stem. The overall spectra of CNF$_w$ and CNF$_{w/o}$ were similar, although CNF$_{w/o}$ seemed to contain a small amount of remaining hemicellulose (e.g., H$_2$).[202] In addition, the small peaks attributed to triacylglycerol (TAG) and calcium oxalate monohydrate (COM) were identified in the spectra of the two CNF samples (**Fig. S11**).[27,191,203] A detailed discussion of the remaining COM is mentioned in the XRD section.

5.4.4. X-ray Diffraction

The X-ray diffraction patterns of CNF$_w$ and CNF$_{w/o}$, as well as the HS, showed typical cellulose I, which is a mixture of two polymorphs, Iα (triclinic) and Iβ (monoclinic) (**Fig. 34**).[6,7] Three patterns showed similar overviews, consisting of three major peaks (at 2θ =

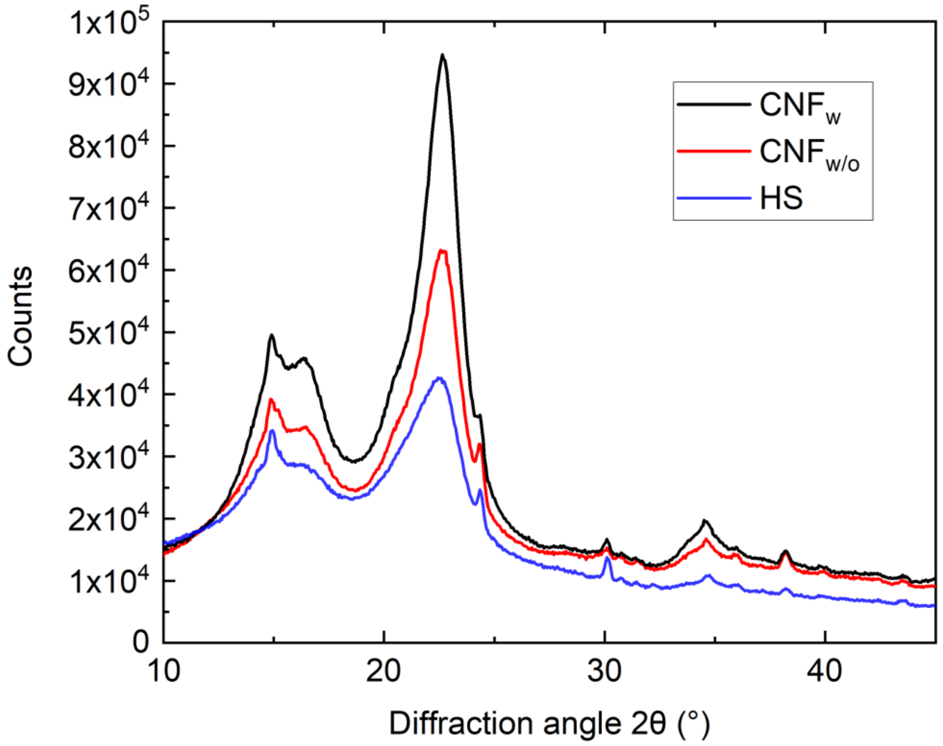

Fig. 34. XRD patterns of CNF$_w$ (black), CNF$_{w/o}$ (red), and HS (blue).

14.9°, 16.6°, and 22.7°) corresponding to the (1-10), (110), and (200) planes, respectively, and a moderate peak (in the vicinity of $2\theta = 34.5°$) corresponding to the (400) plane of cellulose Iβ (**Fig. S12**).[149] These broad peaks gained sharpness in the order: HS < $\mathrm{CNF_{w/o}}$ < $\mathrm{CNF_w}$ because of the increase in the crystallinity index (see the following section).

The small, sharp peaks at $2\theta = 14.9°$, 24.4°, 30.0°, and 38.2° were assigned to $CaC_2O_4 \cdot H_2O$ (COM) in the monoclinic system.[204] The presence of COM is known to accumulate crystals in specific cells in plants, and such crystals, working as internal carbon pools (e.g., CO_2) are often found in large numbers.[205] COM remained in both $\mathrm{CNF_w}$ and $\mathrm{CNF_{w/o}}$. COM crystals in the sizes of 0.1–0.2 μm were observed in AFM images (**Fig. S13**). Faradilla et al.[206] reported that alkaline pretreatments and TEMPO-mediated oxidation were insufficient to remove calcium oxalate; however, acid-treatment using H_2SO_4 dissolved out the residual COM; therefore, acid pretreatment can be employed to enhance the purity of CNFs isolated from HS.

5.4.5. Crystallinity Index and Crystal Size

The crystallinity index (CI) is an important parameter that describes the relative amount of crystalline material in cellulose. Park et al.[147] summarized how to estimate the CI from ^{13}C CP-MAS NMR and XRD using the most-studied methods. In accordance with their study, the CI was determined using the NMR deconvolution method (CI_{NMR}; Eq.(26)) and the XRD deconvolution method (CI_{XRD}; Eq. (27)), and are given in **Table 4**. CI_{NMR} were lower than CI_{XRD} due to differences in the principle of measurement and technique for analysis, as mentioned in the literature.[147] Importantly, the CI exhibited a similar trend ($\mathrm{CNF_w} > \mathrm{CNF_{w/o}}$) for the two methods. Comparing the NMR spectra of $\mathrm{CNF_w}$ and $\mathrm{CNF_{w/o}}$, there is an increase in the intensity of the amorphous C4 NMR signal due to the residual hemicellulose that appears as the shoulder peak in $\mathrm{CNF_{w/o}}$. The CI and crystal size of the original cellulose sources remain unchanged by TEMPO-mediated oxidation[3] therefore, the removal of non-crystalline lignin and hemicellulose via pretreatment increases the CI, as indicated in **Fig. 33**.

The crystal size of the CNFs, corresponding to the cellulose microfibril size, was determined from the highest peak at $2\theta = 22.7°$ using Eq. (28), and is shown in **Table 4**. These crystal sizes are ~2.5 nm smaller than the AFM height median for each CNF sample, as mentioned earlier. Different cellulose resources have widely varying crystal sizes, and HS-derived CNFs have similar sizes to those derived from wood sources (3–5 nm), though smaller than those derived from cotton (7–15 nm).[160]

Table 4. The crystallinity index and crystal sizes of the CNFs calculated from NMR and XRD.

Sample	CI_{NMR} (%)	CI_{XRD} (%)	Crystal size (nm)
CNF_{w}	42	81	4.5
$CNF_{w/o}$	38	73	4.3

5.4.6. Thermogravimetric Analysis

Fig. 35 shows the thermogravimetric (TG) and the derivative TG (DTG) curves for CNF_{w}, $CNF_{w/o}$, and HS. Up to 5% of the initial weight, comprising the moisture content, was lost from all three samples by 100 °C. The HS had a similar moisture content (8.7 %), as shown in **Table 3**. The HS exhibited a gradual weight loss between 200 and 400 °C due to the mixture of cellulose, hemicellulose, and lignin. Lignin degraded at a higher temperature of approximately 350 °C compared to the CNF samples.[207] In contrast, the majority of the degradation of the two CNF samples occurred in two steps as follows: in the first step, sodium hydro-glucuronate units introduced by TEMPO-mediated oxidation were decomposed at 255 °C for CNF_{w} and 260 °C for $CNF_{w/o}$.[152] Secondly, at 300 °C the decomposition of unaltered cellulose units was occurred in both CNF_{w} and $CNF_{w/o}$.[152] The char residues of CNF_{w} at the final temperature (i.e., 650 °C) produced 3.7% lower mass than CNF_{w}, verifying the higher purity.[189]

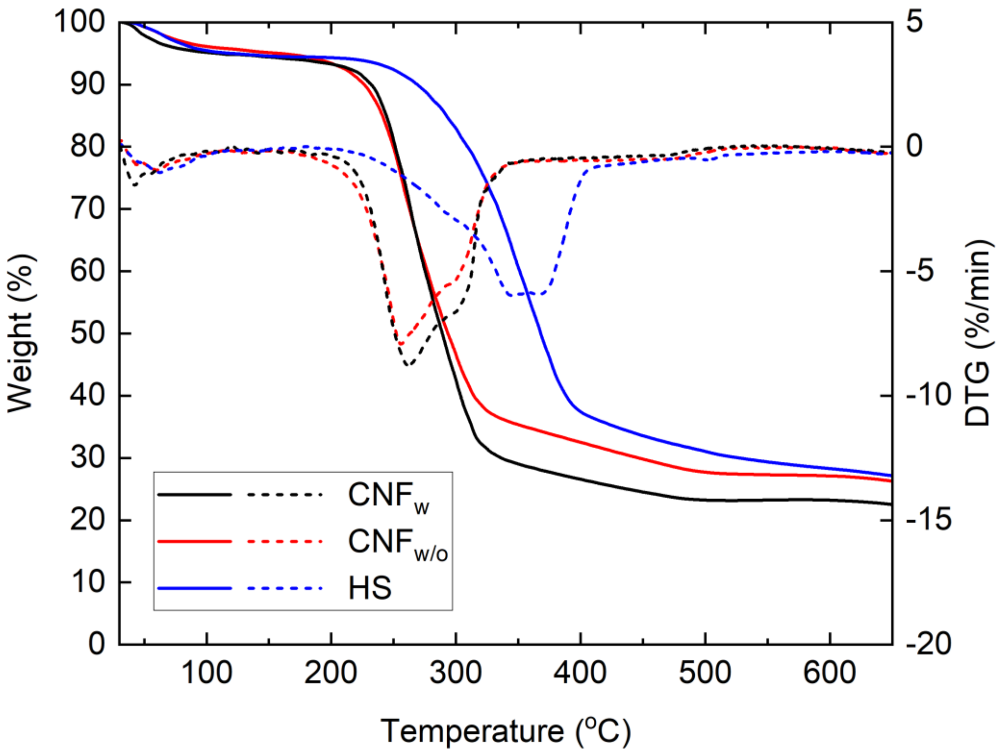

Fig. 35. The TG curves of CNF$_w$ (solid black line), CNF$_{w/o}$ (solid red line), and HS (solid blue line), shown alongside the DTG curves (CNF$_w$, dashed black line; CNF$_{w/o}$, dashed red line; HS, dashed blue line).

5.5. Conclusions

This is the first report of cellulose nanofibers isolated from hop stems (HS) as main agro-industrial waste in hop production. The HS contained 44% cellulose and had a lower hemicellulose content than wood or cotton. TEMPO-oxidized CNFs were isolated from pretreated and non-pretreated HS. AFM observation revealed that the HS-derived CNFs had similar height distributions with a median of ~2 nm, regardless of pretreatment. Solid-state NMR and XRD results indicated that the Wise method, followed by alkaline pretreatment, enhanced both the purity and crystallinity of the CNFs. However, a small amount of triacylglycerol and calcium oxalate monohydrate remained in the CNFs. The two CNF samples showed similar thermal degradation behavior in the two steps at 255–260 °C and 300 °C, and gave slightly lower char residues in the pretreated CNFs.

Chapter 6 – Development of Pickering Emulsions Stabilized by Hop Stem-Derived Cellulose Nanofibers

Using cellulose nanofibers isolated from waste hop stems to stabilize dodecane or olive oil-in-water Pickering emulsions

N. Kanai, T. Sakai, K. Yamada, S. Kumagai, I. Kawamura *Colloids Surf. A* **653**, 129956 (2022)

6.1. Abstract

TEMPO-oxidized cellulose nanofibers (TCNF) were isolated from agricultural waste hop stems and used as stabilizers of oil-in-water Pickering emulsions. The TCNF-stabilized emulsions were prepared using two types of oils (dodecane and olive oil), different TCNF concentrations (0.5, 0.8, and 1.0% in the continuous phase), and multiple oil/water ratios (10–30 % oil by weight). The stability of dodecane/TCNF (d-CNF) and olive oil/TCNF (o-CNF) emulsions were investigated over one month at ambient temperature. While the instability behavior in d-CNF and o-CNF emulsions was different, their stabilities were enhanced with TCNF concentrations and/or the lower oil ratios. The addition of TCNF above 0.8% prevented separation for one month by sufficiently covering the oil/water interface and forming the entangled structure in the continuous phase. The mean diameter of oil droplets (d_v) in d-CNF emulsions was 5–14 µm, depending on the initial TCNF loading. As for o-CNF emulsions, d_v was relatively smaller than that of d-CNF (3–8 µm), and flocculation and Ostwald ripening were considered to dominate the destabilization at o/w 10:90 showing a monomodal droplet size distribution, while coalescence also contributed at o/w 20:80, showing a bimodal distribution.

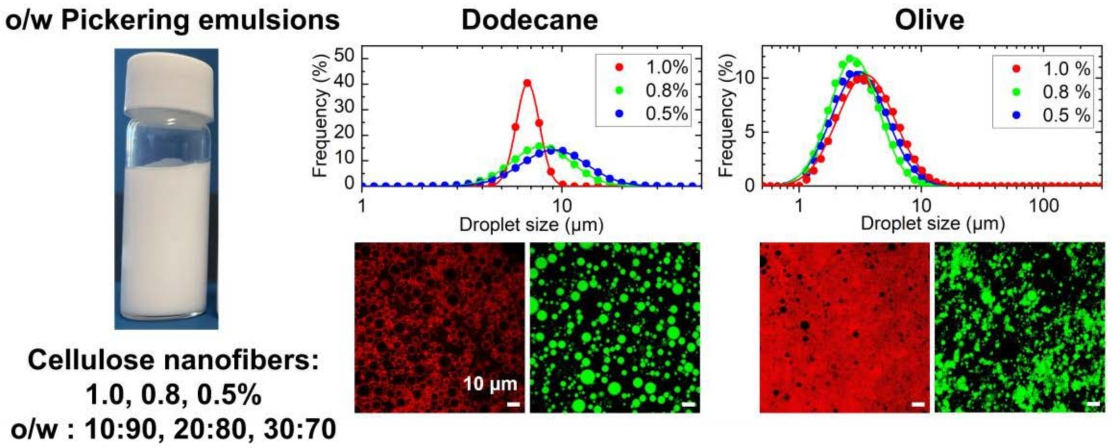

Fig. 36. The graphical abstract of Chapter 6.

6.2. Introduction

Pickering emulsion,[49] a system stabilized by solid particles, has been an important research subject among hydrocolloid materials in recent years.[62,78,208,209] Unlike surfactant-stabilized (i.e., molecular-based) emulsions, the colloidal particles in Pickering emulsions require a balanced interfacial wettability to absorb at the oil/water interfaces irreversibly. The wettability determines the form of a Pickering emulsion, whether oil-*in*-water or water-*in*-oil,[210] resulting in the entire system having superior stability, versatility, and functionality.[50,72,208,211] Traditionally, inorganic particles (e.g., SiO_2) are the most commonly studied stabilizer; however, there is limited use in food, cosmetic, and pharmaceutical industries.[52,60] As an alternative, natural biopolymers have been proposed as stabilizers,[52,212] such as proteins, e.g., gliadin nanoparticles,[62,63] or polysaccharides, e.g., starch modified by OSA,[64] or nanocellulose.[65–69]

Nanocelluloses, having native cellulose I crystal structure, are isolated from diverse plant-based sources via mechanical and/or chemical disintegration/refinement treatments and are mainly classified as cellulose nanofibers (CNF) or cellulose nanocrystals (CNC).[187] Their anisotropic fiber morphology and amphiphilic surface character are expected to stabilize oil/water interfaces at a low loading level.[74] The stability of CNC adsorption to the oil phase is attributed to the $(200)\beta/(220)\alpha$ hydrophobic edge plane;[74] however, their native high hydrophilicity might limit their use as stabilizers without modification.[78]

Researchers have attempted to improve emulsion stability through various surface modifications of nanocellulose. Surface charge, the cause of electrostatic interaction, is considered a critical factor in enhancing Pickering emulsion stability.[72,74] A variety of surface hydroxyl group modifications has been conducted. 2,2,6,6-tetramethylpiperidine-1-oxyl (TEMPO)-mediated oxidation is widely used for extracting surface-carboxylated CNF, generally having 3-4 nm widths and high aspect ratios.[3] Saelices and Capron[82] prepared oil-in-water emulsions stabilized with four different nanocelluloses, including unmodified CNF and TEMPO-oxidized CNF (TCNF). They concluded that the TCNF-stabilized system displayed excellent mechanical resistance toward deformation and coalescence. The droplets in the nanometer scale were strongly connected by forming networks and electrostatic repulsion induced by the carboxylates that lead to entangled systems.[82]

Agricultural and food waste (AFW) has attracted great attention as a CNF source of emulsifier for eco-friendly Pickering emulsions,[90] such as lemon seeds,[65] mangosteen rind,[88] and pineapple peels.[213] AFW is lignocellulosic biomass, and their upcycling into functional and advanced materials has excellent benefits in developing a circular bioeconomy, sustainable utilization, and reducing disposal costs locally.[214]

Hop stems and its leaves are major AFW in cultivating hop flowers (*Humulus lupulus*), the essential ingredient for beer production. In 2020, the global hop production hit 122,000 metric tons.[37] A significant amount of stems and leaves is abandoned, which is estimated to make up 75% of the biomass in hop cultivation.[38] We previously reported upcycling waste hop stem (HS) into TCNF.[215] HS contained 44% cellulose, 13% hemicellulose, and 26% lignin. The cellulose content was comparable to that of hard/softwood, the most widely used CNF sources.[15] Therefore, HS is a new promising AFW for isolating value-added TCNF and worth exploring their application to Pickering emulsion stabilizers.

To the best of our knowledge, only few studies investigated on Pickering emulsions stabilized by TCNF derived from AFW.[67] The source of cellulose has little effect on the ability to form the Pickering emulsion due to the common crystal allomorphs;[72] If the HS-derived TCNF exhibits a similar emulsified capacity to other reported TCNF emulsion systems, this work could facilitate a versatility of AFW with respect to TCNF-stabilized emulsions. Further, oil properties such as viscosity and polarity also impact the stability of Pickering emulsions.[85] Petroleum-derived oils (e.g., alkane) have often been used as well-defined models in the literature, however, biocompatible oils are required for use in food or pharmaceutical applications.[87] Olive oil, a typical natural oil, consists mainly of triglycerides with ~80% monounsaturated fatty acids (e.g., C18:1), ~10% saturated acids (e.g., C16:0), and a variety of polar minor components (e.g., phenolic compounds).[216,217] A comparison of TCNF-stabilized *n*-dodecane (d-CNF) emulsion and olive oil (o-CNF) Pickering emulsions will highlight any stability differences between a single-component oil and a multi-component oil for identical HS-derived TCNF emulsifier.

6.3. Materials and Methods

Raw Material Characterization

Air-dried and mechanically milled hop stems (HS) were used as raw materials for TCNF and the sugar composition analysis. The sugar composition was determined from sulfuric acid hydrolysis treatments followed by GC/MS analysis according to the National Renewable Energy Laboratory, Laboratory Analytical Procedure, Technical Reports (NREL/TP-510-42618, Determination of Structural Carbohydrates and Lignin in Biomass).

All chemicals, including dodecane (99.0+%, 0.746–0.752 g/mL), olive oil (0.909–0.915 g/mL), Congo Red, Nile Red, NaClO (+5.0%), TEMPO (98%), NaBr (>99.0%), HCl, and NaOH were used without further purification (Wako Pure Chemicals Co., Ltd.).

TEMPO-Mediated Oxidation

TEMPO-oxidized cellulose nanofibers (TCNF) were isolated from HS using a modified procedure of our protocols.[215] Twelve g of the HS particles were dewaxed in an acetone/water mixture [9:1 (v/v)] for two days. The dewaxed sample was stirred in 200 mL of a 1 M trisodium citrate solution to remove calcium oxalate monohydrate (COM) at 50 °C for one hour. The solid fraction was filtered, rinsed with distilled water, and dried in a thermostatic chamber at 37 °C. The catalytic quantities of TEMPO (20 mg) and NaBr (0.1 g) were added to the dried sample, and TEMPO-mediated oxidation was initiated by adding 60 mmol/g of NaClO. During the reaction, pH was adjusted to 10 by adding 1 M NaOH using an automatic titration system (AUT-701, DKK-TOA, Japan). The obtained cellulose slurry (0.4 g, dry weight) was dispersed in sterilized water at 1.0% by weight (i.e., w/w) and sonicated for 1.5 min using a homogenizer (BRANSON, Sonifier SFX250) in the pulse mode with a 1/4" microtip at an amplitude setting of 40%. TCNF was diluted with 0.5 or 0.8% w/w from 1.0% w/w dispersion stock using sterilized water. The carboxylate content of TCNF determined from the electric conductivity titration method was 0.84–0.85 mmol/g.[193]

Preparation of Oil-in-Water Emulsion Stabilized by TCNF

Either dodecane or olive oil (3–9 g) was added to 0.5, 0.8, 1.0% w/w TCNF dispersions, and the mixture (30 g each) was maintained at 20 °C and then pre-stirred by Vortex. TCNF-stabilized oil-in-water Pickering emulsions were prepared by sonication for 1 min with oil/water ratios (o/w) of 10:90, 20:80, and 30:70 by weight. Note that the emulsification day is defined as day 0 in this paper. TCNF-stabilized dodecane (d-CNF) emulsions and olive oil (o-CNF) emulsions were stored at ambient temperature.

Visual Observation of Emulsions

The freshly prepared emulsion (3.0 g) was carefully poured into a clear glass vial (14 mm o.d. 45 mm height) with a screw cap and stored at ambient temperature for 30 days after emulsification. Note that there was no change in the weight of the samples during the observation period. Emulsion stabilities were monitored over time and assessed by plotting the relative height of each layer as a function of time; free oil layer on the top (H_{FO}), opaque emulsion layer including cream layer (H_E, it is difficult to distinguish the boundary of these two layers), and transparent serum layer on the bottom (H_S).[47] Each height parameter was calculated as the ratio of the total height of the samples in the vial (H_T).

Atomic Force Microscopy

According to the previous procedure,[215] the heights of TCNF were probed using atomic force microscopy (AFM). Briefly, 10 μL of a dilute suspension of TCNF (0.001% w/w) was placed on a freshly-cleaved mica plate and dried at room temperature. AFM images were captured with SPA-400 (Seiko Instruments) in the tapping mode in the air using an aluminum-coated silicon cantilever having a spherical tip of 10 nm radius and a spring constant of 13 N/m (SI-DF20, HITACHI, Japan). To determine the TCNF height distribution, each profile was processed and analyzed using Gwyddion 2.56.

X-ray Diffraction and Solid-State NMR

The TCNF was completely dried by solvent replacement in *tert*-butanol for structural characterization using X-ray diffraction (XRD) and solid-state nuclear magnetic resonance (NMR). The measurements and analysis were performed based on the previous report.[215] Briefly, the XRD pattern was acquired on an X-ray diffractometer (Rigaku, SmartLab) operating at 40 kV and 45 mA using Cu Kα radiation ($\lambda = 0.15418$ nm) at a step size of 0.05° in the 2θ range of 5−45° at a scanning speed of 0.3°/min. ^{13}C cross-polarization magic angle spinning (CP-MAS) SSNMR spectrum was recorded on a 600 MHz NMR spectrometer (Bruker Avance III) equipped with a 4.0 mm $^{1}H/^{13}C/^{15}N$ triple-resonance E-free MAS probe at ambient temperature with a MAS frequency of 12.5 kHz, a contact time of 1 ms, and a delay time of 3 s.

Field-Emission Scanning Electron Microscopy

The small amount of freshly prepared oil/water 20:80 d-CNF emulsions on day 0 was spread thinly on the bottom of a glass vial and lyophilized for one day. The microstructure of d-CNF emulsions was observed using field emission scanning electron microscopy (FE-SEM). The dried emulsion sample was coated with Pt-Pd in advance, and SEM images were obtained by SU8010 (HITACHI) at the accelerating voltage of 1.0 kV.

Droplet Size Distributions

The droplet size distribution (DSD) of d-CNF and o-CNF emulsions were determined on days 1(or 2), 7, and 30 using a laser scattering particle size distribution analyzer (LA-950V2, HORIBA) in wet mode. A drop of the emulsions was added to the water medium until the light transmittance percentage of the red laser and blue LED reached 90–80% and 90–70%, respectively. The sample was de-bubbled by sonication, followed by stirring and circulating at 2000 rpm. The refractive indices were set at 1.60 for oil and 1.33 for water. DSD was determined on a volume basis over the range of 0.01–2000 μm. The standard percentile DSD parameters of D_{50}, $D_{10,}$ and D_{90} were measured. The DSD width was characterized by the ratio D_{90}/D_{10}.[218] The mean droplet diameter (d_v) was determined by fitting DSD data using a log-normal distribution curve using OriginPro 2022.

Confocal laser Scanning Microscopy

The microstructure of Pickering emulsions was observed with a confocal laser scanning microscopy (CLSM). Five μL of Nile Red (1 mg mL^{-1}) or Congo Red (1 mg mL^{-1}-ethanol) solution was added to the freshly prepared emulsions (0.5 g each) for dying oil or TCNF and mixed with a Vortex at the final concentration of 0.001% w/w. The stained samples were kept at room temperature and observed with CLSM on days 1(or 2), 7, and

30. One μL of the stained emulsion was placed on a microscope glass slide and covered with a coverslip which was then sealed with nail top coat to avoid vaporization.

CLSM images were captured by a Carl Zeiss LSM5 controlled by ZEN2009 software. A plan-apochromat 63×/1.4 oil-immersion DIC objective lens was used for scanning. The fluorescence of the Nile Red-stained sample was excited with Ar 488 nm line, and a 505-530 nm band-pass filter was used for emission, while Congo Red-stained sample was with Ar 488 nm/HeNe 543 nm lines for excitation and a 560 nm long-pass filter for emission. The images were processed in ZEN2009 by adjusting the black/white levels of the histogram to acquire better contrast.

Zeta Potential Measurements

The zeta (ζ) potential measurements were performed with a Zetasizer (Zetasizer Nano ZSP, Malvern Panalytical). The 1.0% TCNF dispersions or Pickering emulsions were diluted in 0.08% w/w. All measurements were repeated three times, and each value was represented as the average and standard deviation of the three repetitions.

Rheological Measurements

The viscosity of the TCNF dispersions, d-CNF, and o-CNF emulsions were investigated by a rotational rheometer, RheolabQC (Anton Paar), with a temperature control unit (C-PTD 180) and concentric cylinder measuring system (CC-27). The viscosity data were collected at 20 °C using a logarithmic ramp between the shear rate range of 0.1–100 s^{-1} with 50 points obtained every 5 s duration except low viscosity 0.5% emulsions for 1– 100 s^{-1} with 20 points. The shear rate was programmed to rise from 0.1 or 1 s^{-1} to 100 s^{-1} (i.e., upward) and then fall back (i.e., downward). All rheological experiments were carried out in duplicate.

6.4. Results and Discussion

6.4.1. Sugar Composition Analysis of HS and Characterization of TCNF

According to the sugar composition analysis, hop stems (HS) contained 40%-dry glucose from cellulose, and xylose (13%-dry) was the most significant sugar in HS hemicellulose, followed by galactose (1.6%-dry), mannose (1.3%-dry) and arabinose (1.2%-dry). The high hemicellulose content of xylose exhibited a similar tendency in hardwood. Having more disordered structures, most hemicelluloses are degraded into water-soluble fractions during TEMPO-oxidation.[3] However, xylan has relatively high resistance to decomposition due to the absence of C6-OH groups.[219] The broad shoulder in the solid-state NMR spectrum appearing at lower ppm (i.e., 100 ppm) of the C1 signals (**Fig. S14**) indicated that a small amount of hemicellulose remained in TCNF. The sets of sharp calcium oxalate monohydrate (COM) peaks (i.e., $2\theta = 14.9°$, $24.4°$, $30.0°$, and $38.2°$) were not detected in powder XRD patterns of TCNF, indicating COM removal by trisodium citrate (**Fig. S15**). According to previous reports, it is most likely that citrate complexed with Ca^{2+} and formed a soluble chelate.[220,221] Consequently, the crystallinity of TCNF calculated from XRD (i.e., 82%) slightly increased compared to TCNF without citrate pretreatments (i.e., 73%) in our previous report.[215]

The median height of TCNF was determined to be 1.7 ± 0.7 nm from AFM images, which demonstrated that the individualized TCNF was obtained (**Fig. S16**). Thus, when HS is used as the starting material, almost all hemicelluloses (xylan) and COM decompose during TEMPO-oxidation combined with citric acid washing as water-soluble fractions and preparations provide the high purity of TCNF. The turbidity and viscosity of the TCNF dispersions increased with concentration (**Table S2**). The viscosity of TCNF dispersions of 0.5 and 0.8% showed typical shear thinning behavior over the whole shear rate range (**Fig. S17**). On the other hand, 1.0% consisted of three regions with different slopes, possibly reflecting the self-assembled, nematic ordered structure in dispersions.[222,223]

6.4.2. TCNF-Stabilized Emulsion Stability

TCNF-stabilized dodecane (d-CNF) emulsions and olive oil (o-CNF) emulsions were formed using 0.5, 0.8, and 1.0% TCNF dispersions with various o/w of 10:90, 20:80, and 30:70 (**Fig. 37** and **Fig. S18**). The emulsions were stored at ambient temperature, and the

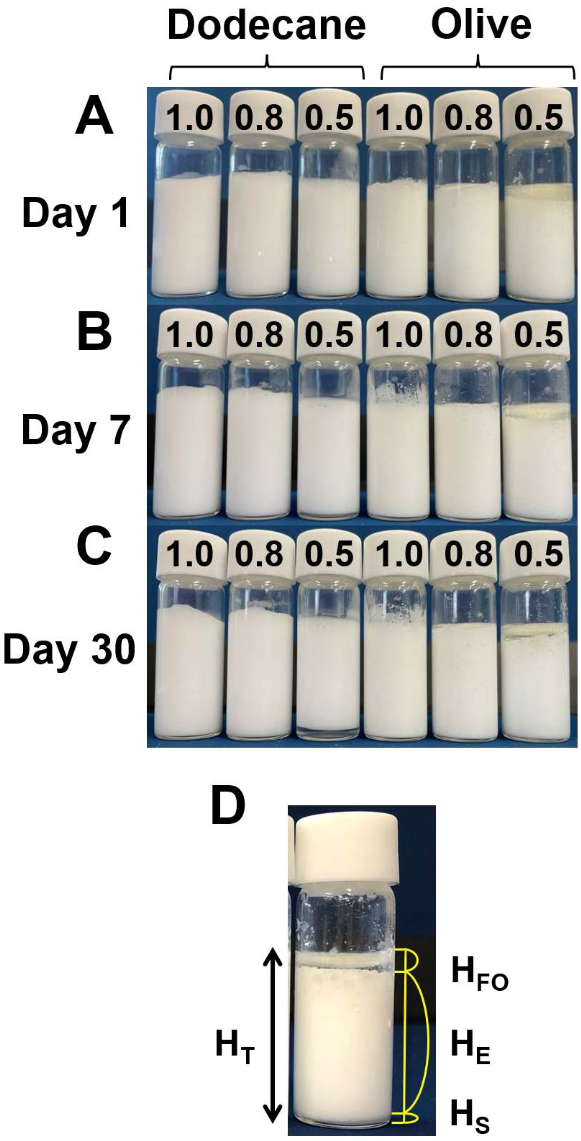

Fig. 37. Photographs of o/w 30:70 dodecane/CNF (d-CNF) and olive/CNF (o-CNF) emulsions with various TCNF concentrations (i.e., 0.5, 0.8, 1.0 wt%) on (A) day 1, (B) day 7, and (C) day 30. (D) The relative thickness of each layer was monitored; free oil layer (H_{FO}), emulsion layer, including cream layer (H_E), and serum layer (H_S).

relative thickness of each layer; free oil layer (H_{FO}), opaque emulsion layer (H_E), and serum layer (H_S), was recorded based on the total height of the samples (H_T) over two months (**Fig. S19**). On day 1 (i.e., the next day of emulsification), 0.8 and 1.0 % d-CNF emulsions didn't have visible separations in any o/w ratios whereas the free oil layer (i.e., oiling-off) appeared in 0.5 % TCNF at o/w 20:80 and 30:70.[47] Regarding o-CNF emulsions, H_{FO}/H_T in 0.5 or 0.8 % did not greatly change once the free oil appeared, but some condensation/liquid droplets appeared on the upper walls of the vials with storage time, which possibly impacted the H_{FO}/H_T slightly. Note that H_{FO}/H_T is relatively small, making it difficult to analyze accurately.[47] A droplet-depleted serum layer appeared on day 30 in 0.5% d-CNF (o/w 20:80, 30:70) and 0.5% o-CNF emulsion (o/w 30:70), and its thickness (i.e., H_S/H_T) increased over time as droplets moved upwards.[47] Basically, the stabilities of d-CNF and o-CNF emulsion became superior with increased TCNF concentrations, and 0.8–1.0% TCNF exhibited a good emulsifying capacity without separation over one month. In contrast, 0.5% TCNF was insufficient to stabilize the system for one month using more than 20% of either dodecane or olive oil.

While there are many emulsion instability mechanisms (e.g., flocculation, coalescence, Ostwald ripening),[47] it is clear that the instability behavior of the d-CNF system is different to that of o-CNF as seen in **Fig. 37**. This difference in stability could be related to the differences in oil properties. While dodecane ($C_{12}H_{26}$) is non-polar and single component oil, olive oil consists of long-chain triglycerides with ~80% monounsaturated fatty acids and ~10% saturated acids, as well as various polar minor components.[216,217] Goi et al.[86] reported that TCNF having hydrophilic surfaces are absorbed more efficiently onto o/w interfacial when Pickering emulsion is formed using oils having lower polarity or high o/w interfacial tensions. For this reason, it is reasonable to assume that d-CNF o/w emulsion system had higher stability with lower TCNF loadings than that of o-CNF emulsion.

6.4.3. Droplet Size Distributions and Droplet Mean Diameter

Fig. 38 shows the DSD of d-CNF (**Fig. 38A**) and o-CNF (**Fig. 38B**) emulsions. DSD was fitted by a log-normal distribution curve to determine the mean diameter of the oil droplet (d_v) **(Fig. 39)**. The standard percentile DSD parameters of D_{10}, D_{50}, and D_{90}, and the DSD width parameter of D_{90}/D_{10}, are summarized in **Table S3-Table S6**. The entire d-CNF emulsions were well described by a log-normal distribution ($R^2 > 0.99$), and exhibited a monomodal having narrow to medium distributions (D_{90}/D_{10} = 1.4–2.8). On the other hand, o-CNF emulsions at o/w 10:90 were monomodal having medium to broad distributions (D_{90}/D_{10} = 2.9–4.1) and turned to bimodal during storage at o/w 20:80, having broad to very broad distributions (D_{90}/D_{10} = 4.0–18.2).[218] This broad DSD can be seen in other Pickering emulsions using triglyceride-based oils.[209,224,225] The 1.0% o/w

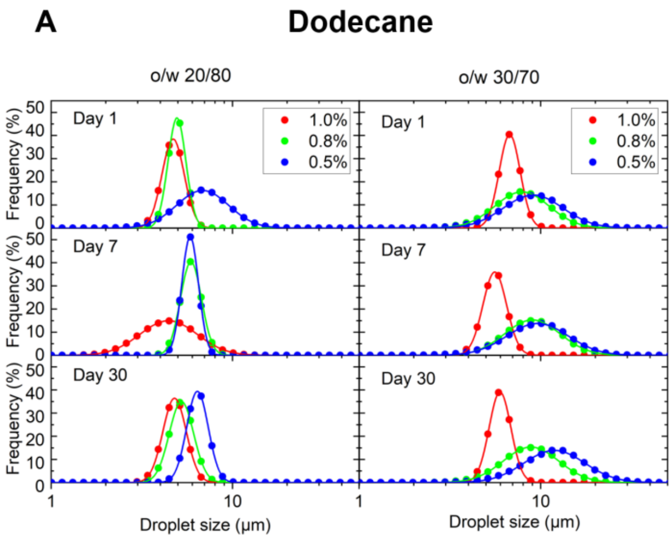

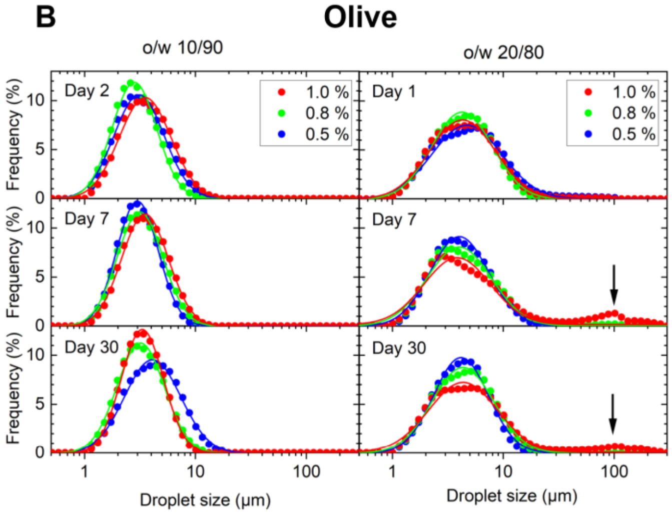

Fig. 38. The droplet size distributions (DSD) of (A) d-CNF and (B) o-CNF emulsions stabilized by 1.0% (red), 0.8% (green), and 0.5% (blue) TCNF dispersions on days 1(or 2), 7, and 30. The o/w ratios are 20:80 and 30:70 for d-CNF, 20:80 and 10:90 for o-CNF. The solid lines represent a fit by a log-normal distribution curve.

20:80 o-CNF emulsions formed a bimodal distributions having two different modes at around 2–6 μm and 100 μm, probably due to the heterogeneous coalescence process.[47]

As seen in **Fig. 39**, the mean diameter of oil droplets (d_v) in d-CNF emulsions was 5–8 μm at o/w 20:80, 6–14 μm at o/w 30:70, while o-CNF showed smaller values of 3–6 μm at o/w 10:90, 6–8 μm at o/w 20:80. Also, the lower oil ratios led to smaller droplet sizes regardless of oil types. These results indicated that more TCNF was available to stabilize smaller droplets at lower oil amounts. At the same TCNF concentration, there was a significant d_v increase in 0.5% d-CNF emulsions during storage, mainly due to coalescence, which agrees with visual observation. However, there was no substantial

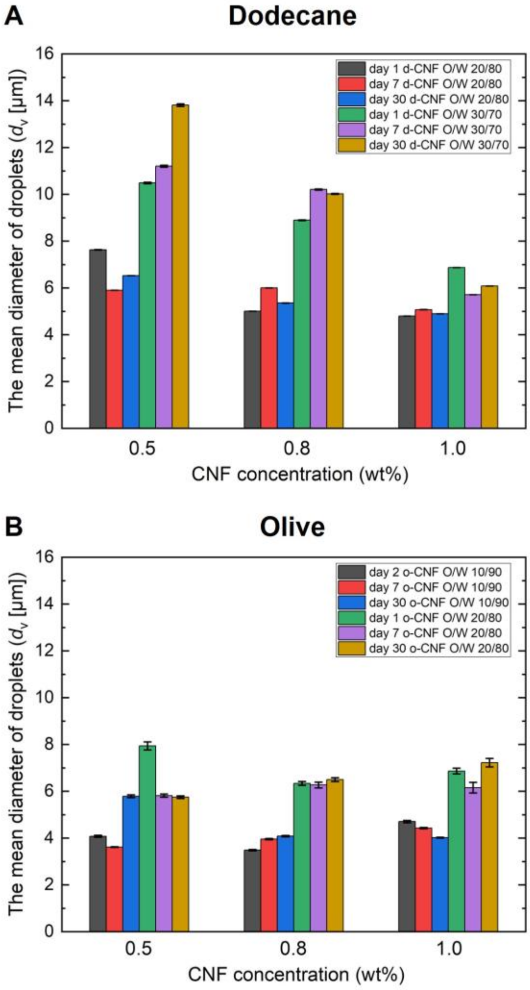

Fig. 39. The mean diameter of oil droplets (dv [μm]) in (A) o/w 20:80 and 30:70 d-CNF emulsions, and (B) o/w 10:90 and 20:80 o-CNF emulsions on days 1(or 2), 7, and 30.

change in any other system for one month. At the same storage time, meanwhile, the higher TCNF concentration led to the smaller d_v in d-CNF emulsions, whereas there was no significant difference in o-CNF emulsions. Previous studies using various o/w Pickering emulsion systems reported that d_v decreased with increasing particle loadings and thereafter reached a constant value. Kalashnikova et al.[73] described this behavior from the size limitation obtained by the sonication process. Aveyard et al.[75] suggested that the droplet size was set by the initial particle loadings until a limiting size was reached and an excess of particles appeared in the continuous phase. Therefore, the initial TCNF loadings might have determined the droplet size in d-CNF emulsions. In contrast, the droplet size possibly reached a critical value in o-CNF emulsions by sonication process even at the lowest TCNF loading. Li et al.[67] reported that 2.0% TCNF extracted from oil palm empty fruit bunch was a critical concentration without separation for one month in dodecane o/w 20:80 emulsions. Whereas 0.8% TCNF adequately stabilized the same system in this study. The slightly higher carboxy content and smaller and uniform droplet diameter might significantly impact the minimum TCNF loading.

6.4.4. Microstructure and Surface Charge of Pickering Emulsions

TCNF and oil droplets in d-CNF Pickering emulsion were visualized in CLSM images (**Fig. 40, Fig. S20, Fig. S21**). Congo Red directly dyes cellulose in water by absorbed on the hydrophobic surface via various interactions (e.g., van der Waals force).[226] As seen in Congo Red-stained images (**Fig. 40A** and **Fig. S20**), TCNF displayed in red was located on the interfaces of spherical dodecane droplets as well as distributed in the continuous phase. The gradient color (i.e., red to black) was seen in the continuous phase, indicating that the TCNF was not homogenously distributed due to aggregation. Note that the brightness of each CLSM image is not comparable to the others due to the optimized process of contrast.

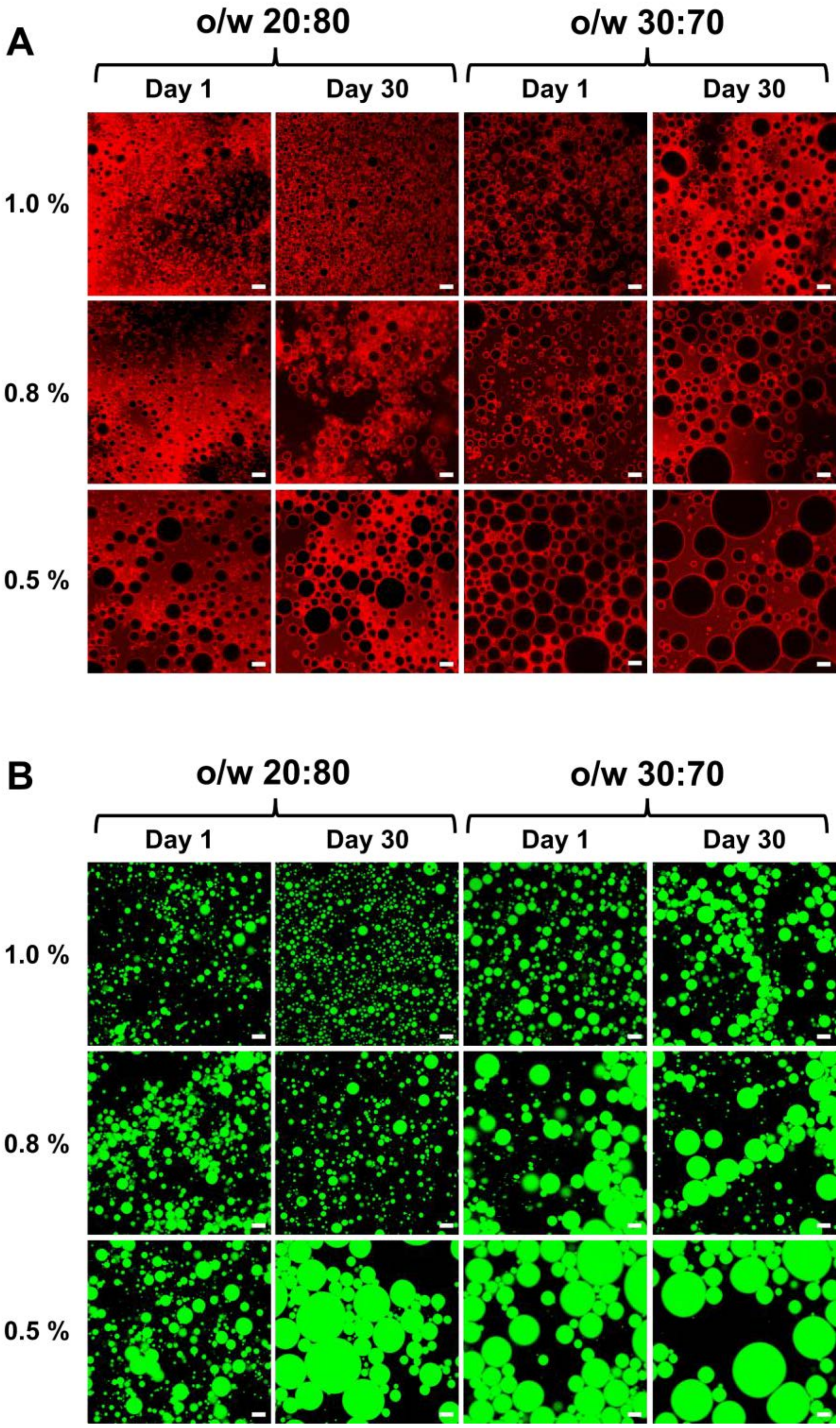

Fig. 40. CLSM images of o/w 20:80 and 30:70 d-CNF stained with (A) Congo Red and (B) Nile Red by different concentrations of 1.0%, 0.8%, and 0.5% TCNF dispersions on days 1 and 30. Scale bars represent 10 μm.

The data in both **Fig. 40A** and **Fig. 40B** indicate that higher TCNF concentrations and/or lower oil ratios led to fine droplets, which agreed with the DSD results. At o/w 20:80 d-CNF emulsions, droplets were well isolated on day 1 at all concentrations and 0.8 or 1.0% TCNF was kept unchanged until day 30. Meanwhile, the distance between droplets at 0.5% TCNF became closer and then stuck together during storage, forming flocs. Besides, the droplets stabilized with 0.5% TCNF were rapidly merged (i.e., coalesced) over one month. There was a pronounced increase in droplet size at o/w 30:70 d-CNF emulsions compared to o/w 20:80 at the same concentrations, forming flocs in 0.5 and 0.8% since day 1 and 1.0% on day 30. Self-association of TCNF at the boundary of droplets and their entangled network in the continuous phase provides excellent long-term stability and thus prevent coalescence.[73,84] The addition of TCNF above 0.8% at o/w 20:80 or 1.0% at o/w 30:70 seemed to be sufficient to inhibit the droplet size growth by covering the oil/water interface and forming network structure.

Freeze-dried d-CNF emulsions at o/w 20:80 were probed by FE-SEM (**Fig. 41**).

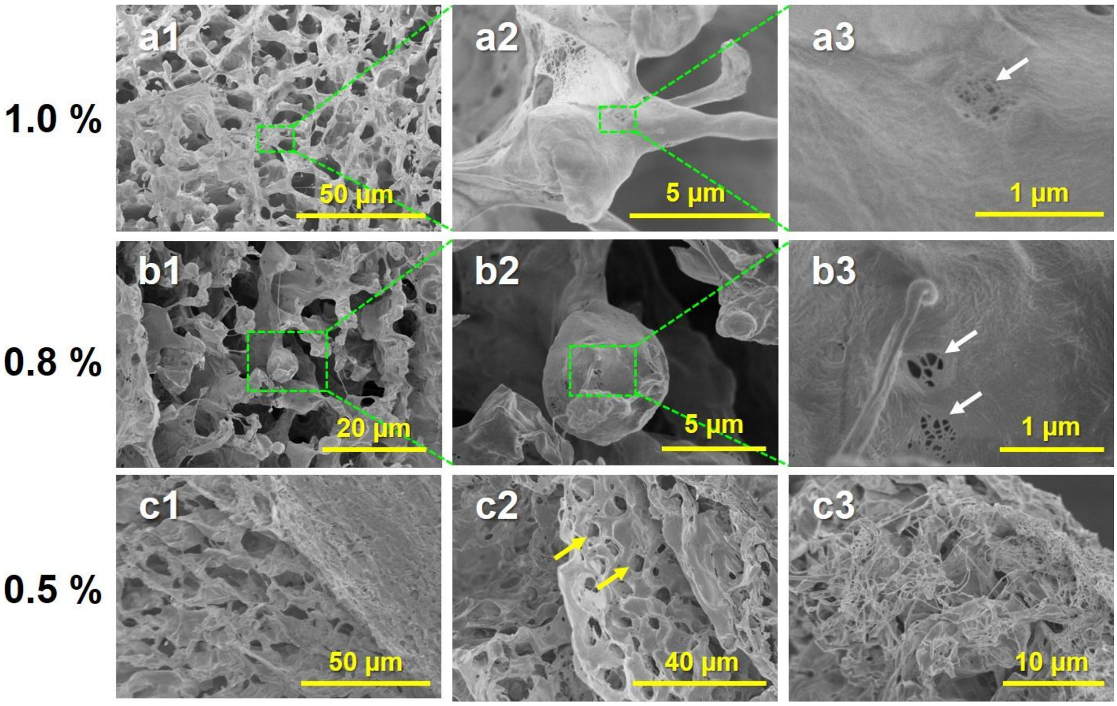

Fig. 41. FE-SEM images of o/w 20:80 d-CNF emulsions stabilized with (a1, a2, a3) 1.0%, (b1, b2, b3) 0.8%, and (c1, c2, c3) 0.5% TCNF. White and yellow arrows show TCNF present on the surface of the oil droplets and pores derived from oil droplets, respectively.

A cluster of round oil droplets appeared between the aggregated TCNF thin layers at 1.0 and 0.8% TCNF concentration (**Fig. 41a1, b1**). TCNF covered the surface of droplets and formed a strong entangled network (see the white arrows in **Fig. 41a3, b3**). Huang et al.[227] reported that oil droplets stabilized by a relatively low chitin nanofibers were removed by sublimation during the drying process, and micropores derived from oil droplets were observed. For this reason, the pores in 0.5% probably indicated the insufficient TCNF coverage or network strength for the pressure change during drying (see the yellow arrows in **Fig. 41c2**).

The microstructure of o-CNF emulsion was significantly different from d-CNF. With oil-stained CLSM images, droplets of various sizes packed closely and formed clusters (**Fig. 42A**). Each cluster was partially connected and aligned to the flow direction. This cluster structure was not clearly detected in TCNF-stained fluorescence images but in the transmission images (**Fig. 42B inset**). Researchers have reported that the concentration gradient of excess CNF surrounding droplets induced an attractive osmotic force.[68,228] As this attractive interaction between droplets was strong enough, it led to the formation of flocculation and eventually caused droplet clusters in olive oil o/w emulsions.[68]

Despite the DSD result, a couple of big droplets of several tens of micrometers were confirmed in 0.5 and 0.8% TCNF loadings at o/w 10:90 (see white arrows in **Fig. 42**). The rapid growth of droplets was most likely due to Ostwald ripening. Ostwald ripening occurs notably in nanoemulsions based on diffusion of oil from small droplets to larger droplets through the continuous phase.[229] The rate of Ostwald ripening increases as oil solubility in the water phase increases.[230] Wooster et al.[229] examined the Ostwald ripening rate of various *n*-alkanes and triglycerides and found the glycerol headgroup in triglycerides gave amphiphilicity and resulted in relatively higher solubility than *n*-alkanes with similar oil molar volume. The fatty acid chain length of triglycerides in olive oil (e.g., C18) is much longer than the hydrocarbon chain length in dodecane (i.e., C12), nevertheless, amphiphilicity of triglycerides could be one reason for the occurrence of Ostwald ripening in o-CNF emulsions.

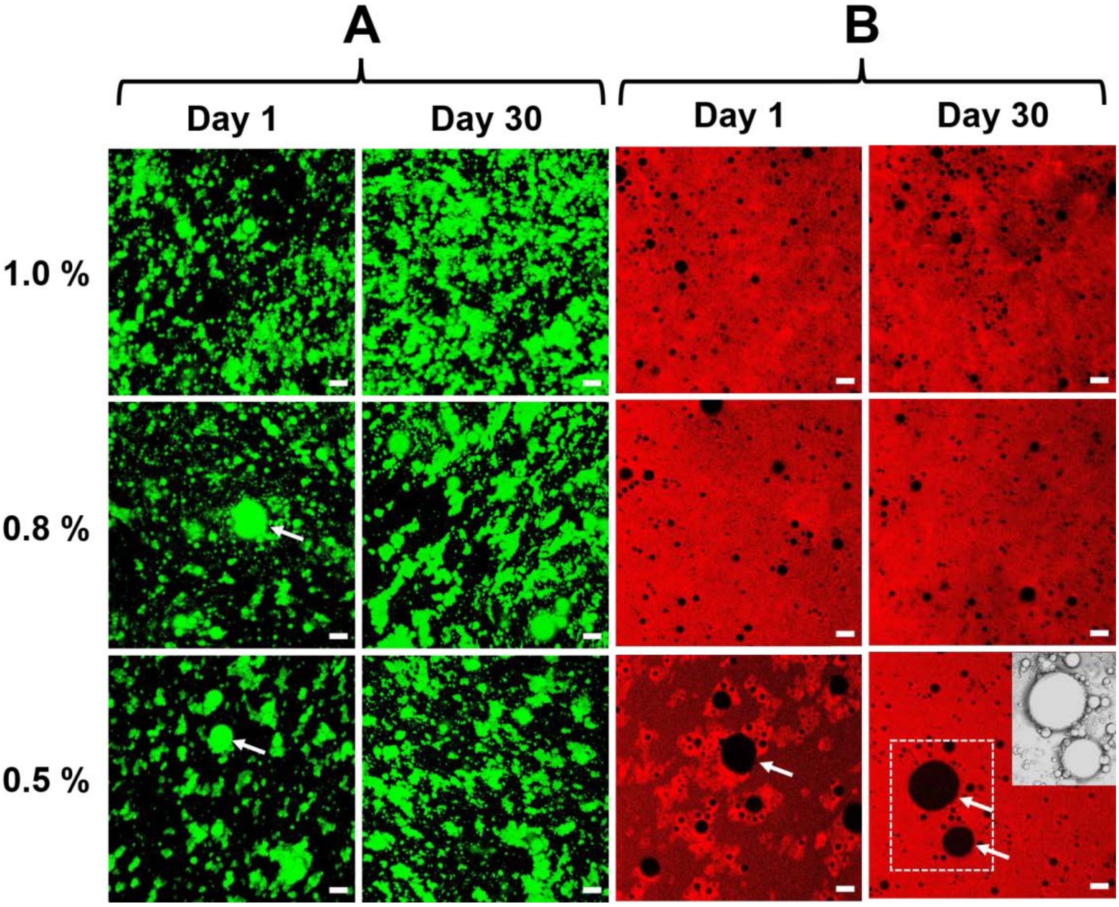

Fig. 42. CLSM images of o/w 10:90 o-CNF stained with (A) Nile Red and (B) Congo Red by different concentrations of 1.0%, 0.8%, and 0.5% TCNF dispersions on days 1 and 30. Scale bars represent 10 µm. White arrows show the large droplets caused by Ostwald ripening. The inset shows droplet clusters in the transmittance image.

According to McClements,[47] it is difficult to distinguish Ostwald ripening from coalescence by microscopy techniques. McClements suggests, as an alternative, the difference can be seen in DSD; Ostwald ripening gives a monomodal distribution, whereas coalescence shows a bimodal distribution. Therefore, flocculation and Ostwald ripening dominated the destabilization at o/w 10:90 showing a monomodal distribution, while coalescence also contributed at o/w 20:80, showing a bimodal distribution.

The emulsions showed significantly larger negative ζ-potential than 1.0% TCNF dispersions (–24.0 mV at pH = 7.4); –32.0 to –45.3 mV for d-CNF, –41.3 to –53.3 mV for o-CNF (**Fig. S22**). Isogai et al.[3] reported that the ζ-potential of TCNF dispersions relates to the surface density of dissociated carboxyl groups, not to the carboxy contents. The large difference between dispersions and emulsions could be associated with the formation of interfacial layer by TCNFs, altering the location of the shear plane where the ζ-potential was measured.[231,232] The ζ-potential of the emulsions was overall similar with different o/w ratios or TCNF concentrations, indicating that oil volume and TCNF concentration had little effects on the ζ-potential.

6.4.5. Rheological Characterization

The apparent viscosity of Pickering emulsions was investigated on days 1, 7, and 30, and the downward curves are shown in **Fig. 43**. All emulsions exhibited shear-thinning behavior derived from TCNF dispersions, and their viscosities considerably increased with TCNF concentration, as expected from the increased dispersion viscosities. Both d-CNF and o-CNF emulsion viscosities slightly increased during storage, suggesting the thickening effect of flocculation.[47] Moreover, d-CNF emulsions had a higher viscosity than o-CNF at the same shear rate, indicating a higher resistance for the deformation by slowing down the movement of droplets. While the viscosity of o-CNF emulsions on day 1 within the experimental shear rate ranges almost matched with TCNF dispersions, that of d-CNF emulsion slightly increased (compare **Fig. 43** for the emulsions to **Fig. S17** for the dispersions). This may be related to the difference in microstructures between d-CNF and o-CNF emulsions as seen in **Fig. 40** and **Fig. 42**.

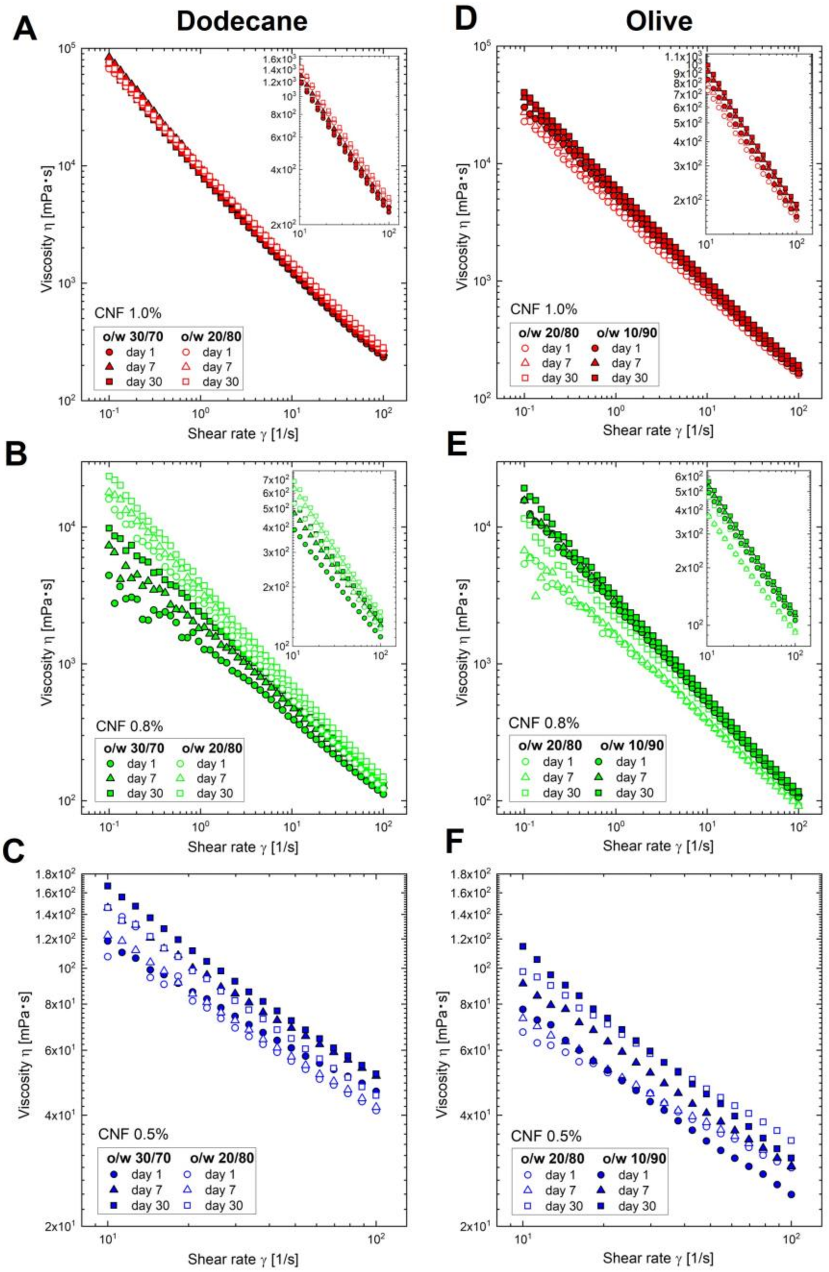

Fig. 43. Viscosity of (A-C) d-CNF and (D-F) o-CNF emulsions stabilized by 1.0% (red), 0.8% (green), and 0.5% (blue) TCNF dispersions on days 1 (circle), 7 (triangle), and 30 (square). The different o/w ratio data was overlaid; 30:70 (filled symbols) and 20:80 (empty symbols) for d-CNF, 20:80 (empty symbols) and 10:90 (filled symbols) for o-CNF. The inset graphs are expanded area of 10-100 s^{-1} shear rate.

6.5. Conclusions

In this study, TCNF was extracted from agricultural waste hop stems and used as a stabilizer of *n*-dodecane or olive oil-in-water Pickering emulsions. A comparison of TCNF-stabilized emulsions using two different types of oils showed a considerable difference in (i) long-term stability, (ii) DSD, and (iii) microstructure (**Fig. 44**).

(i) Long-term stability: An increase in TCNF concentration (in the continuous phase) and/or the lower oil ratios provided superior stability against a series of deformations at each system. 0.8–1.0% exhibited an excellent emulsifying capacity without separation for one month, whereas 0.5% was insufficient when using more than 20% of either dodecane or olive oil.

(ii) DSD: The entire d-CNF emulsions exhibited monomodal DSD, and a significant d_v increase was observed during storage in 0.5% d-CNF emulsions at o/w 30:70 due to coalescence. The d_v decreased with TCNF concentrations, indicating that the initial TCNF loading was vital in determining d_v. During storage, o-CNF exhibited relatively broad DSD and turned monomodal (o/w 10:90) to bimodal (o/w 20:80), which was most likely affected by heterogenous coalescence.

(iii) Microstructure: The sphere droplets in 0.8–1.0% d-CNF emulsions showed high resistance against flocculation and coalescence over one month owing to TCNF coverage of the interface and formation of the entangled network in the continuous phase. The entire o-CNF emulsions formed floc clusters induced by an attractive osmotic force regardless of TCNF concentrations. Also, the presence of very large droplets in several tens of micrometers indicated Ostwald ripening.

Since the TCNF used in this study produced less stable Pickering emulsions with olive oil containing long-chain triglycerides, the enhancement of hydrophobicity via surface modification of the TCNF can be suggested as one way to improve the o-CNF emulsion stability, and that work is the subject of our future work. Our findings propose upcycling of AFW-derived TCNF as stabilizers of Pickering emulsions for potential application in food and cosmetic fields.

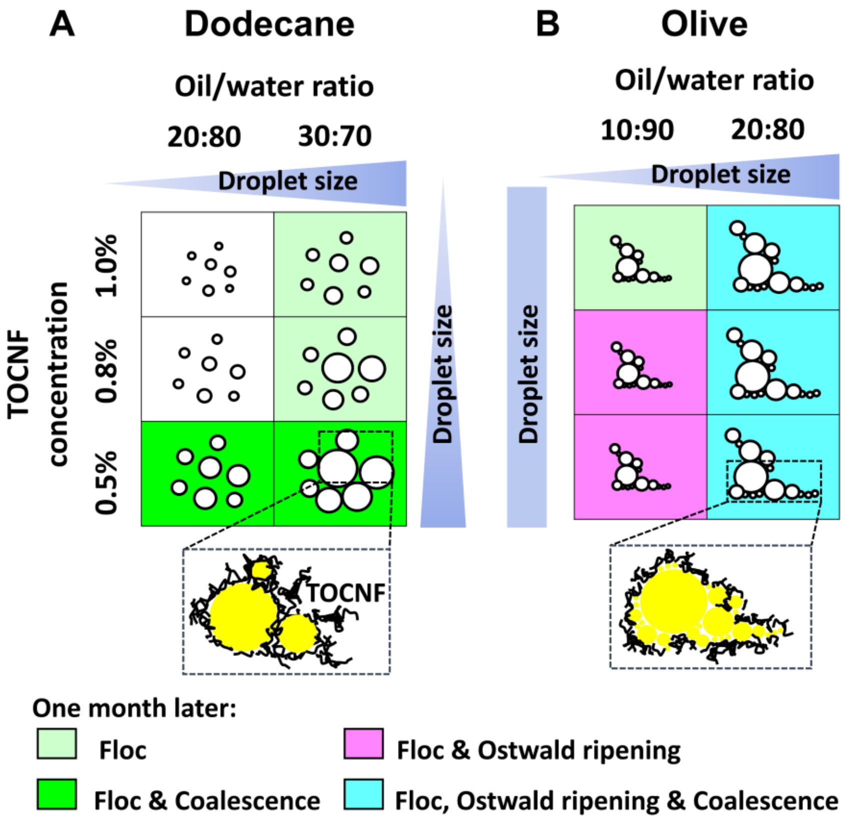

Fig. 44. Schematic diagram of o/w Pickering (A) dodecane-CNF and (B) olive oil-CNF emulsions on day 1 showing the droplet size relationship between TCNF concentrations and oil/water ratios. The color of the squares indicates the suspected instability mechanism for the samples one month later.

Chapter 7 – MRI Relaxation and Diffusion Studies of Pickering Emulsions

Evaluating the stability of cellulose nanofiber Pickering emulsions using MRI and relaxometry

---

N. Kanai, S. A. Willis, A. Gupta, I. Kawamura, W. S. Price *Langmuir* **39**, 3905–3913 (2023)

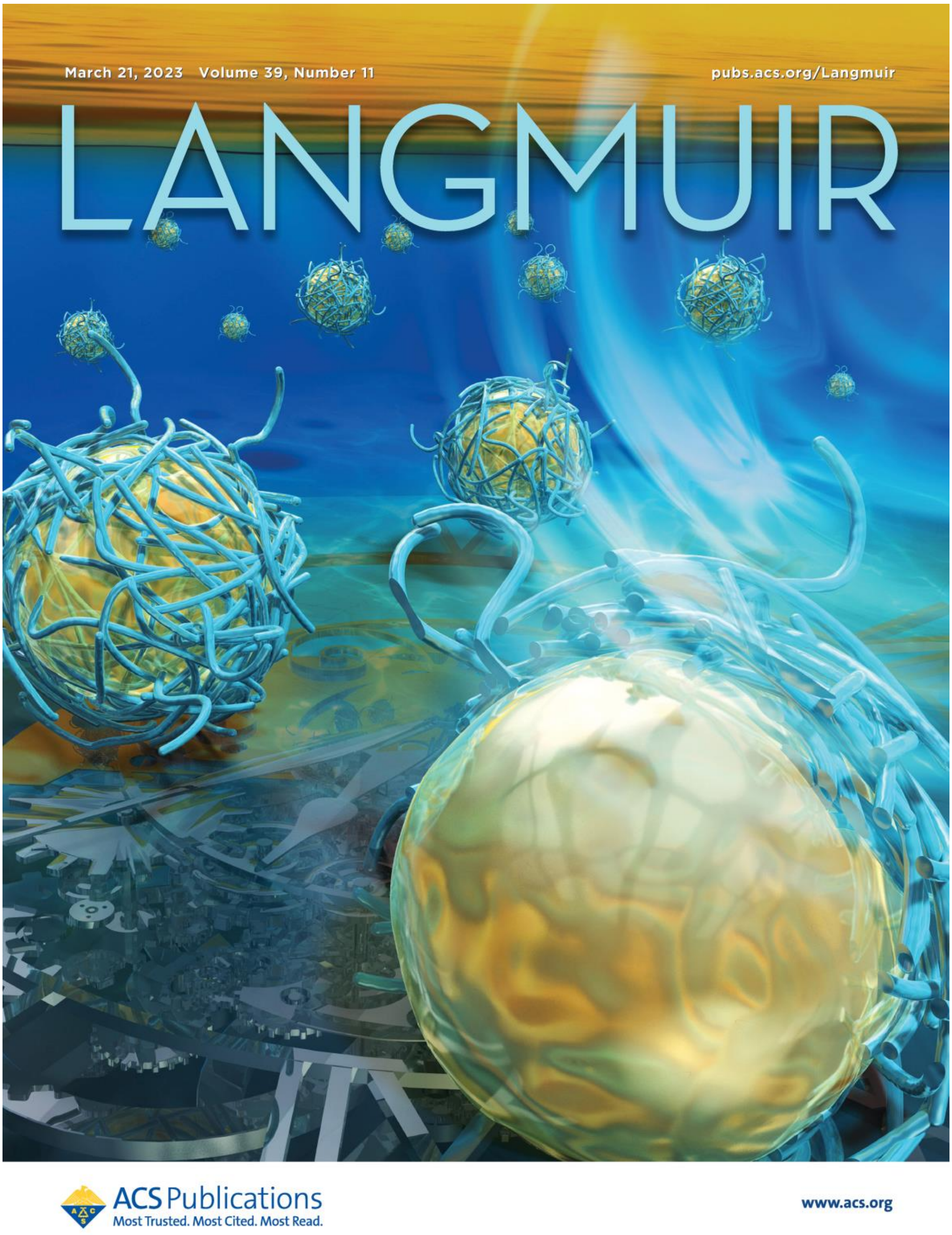

Fig. 45. The journal supplementary cover image of Chapter 7. Magnetic resonance imaging relaxometry and diffusion methods were used to investigate the instability mechanisms of oil-in-water Pickering emulsions stabilized by cellulose nanofibers isolated from waste hop stems over a period of one month after emulsification.

7.1. Abstract

Magnetic resonance imaging (MRI) relaxometry and diffusion methods were used to highlight the instability mechanisms of oil-in-water Pickering emulsions stabilized by TEMPO-oxidized cellulose nanofibers (TCNFs). Four different Pickering emulsions using different oils (n-dodecane and olive oil) and concentrations of TCNFs (0.5 and 1.0 wt %) were systematically investigated over a period of one month after emulsification. The separation into a free oil, emulsion layer and serum layer, and the distribution of flocculated/coalesced oil droplets in several hundred micrometers were captured in MR images using fast low-angle shot (FLASH) and rapid acquisition with relaxation enhancement (RARE) sequences. The components of the Pickering emulsions (e.g., free oil, emulsion layer, oil droplet, and serum leyer) were observable by different voxelwise relaxation times and apparent diffusion coefficients (ADC) and reconstructing in the apparent T_1, T_2, and ADC maps. The mean T_1, T_2, and ADC of the free oil and serum layer corresponded well with MRI results for pure oils and water, respectively. Comparing the relaxation properties and translational diffusion coefficients of pure dodecane and olive oil obtained from NMR and MRI resulted in similar T_1 and ADC but significantly different T_2 depending on the sequence used. The diffusion coefficients of olive oil measured by NMR were much slower than dodecane. The ADC of the emulsion layer for dodecane emulsions did not correlate with the viscosity of the emulsions as the TCNF concentration increased, suggesting the effects of restricted diffusion of oil/water molecules due to droplet packing.

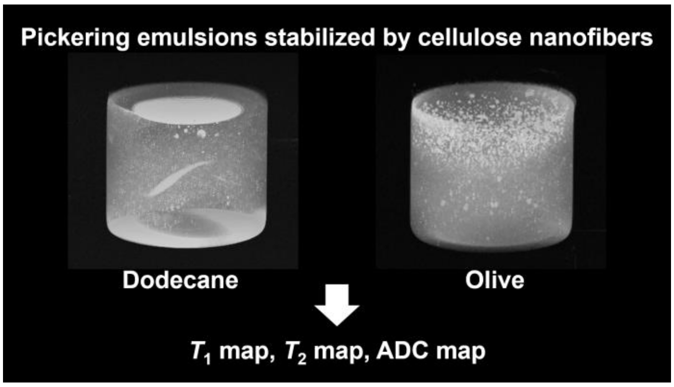

Fig. 46. The graphical abstract of Chapter 7.

7.2. Introduction

Pickering Emulsions

Emulsions, consisting of typically two immiscible liquids (e.g., oil and water), are thermodynamically unstable, and therefore, emulsifiers (stabilizers) are commonly added to prevent the instability mechanisms (e.g., flocculation, coalescence, and Ostwald ripening).[47] A Pickering emulsion is a system stabilized by solid particles instead of traditional molecular-based surfactants.[49] The solid particles require a balanced wettability (i.e., hydrophilicity/hydrophobicity) to adsorb irreversibly at the oil/water interfaces, resulting in Pickering emulsions exhibiting superior stability against coalescence.[50,210] Over the past few decades, there has been interest in developing polysaccharide-based particles and exploring the effects of their size, shape, surface charge, and hydrophobicity on enhancing emulsion stability for potential use in food, cosmetic, drug delivery, and biomedical applications.[52,72]

Cellulose nanofibers (CNFs) are promising emulsifiers for Pickering emulsions offering amphiphilic character, biocompatibility, and sustainability.[67,69,71,72,96,233] Several works demonstrated that surface-carboxylated CNFs by 2,2,6,6-tetramethylpiperidine-1-oxyl (TCNF) exhibited higher stability than unmodified CNFs owing to the negative surface charge.[66,82,86] Fujisawa et al.[72] reported that the cellulose origin should not significantly impact the formation of Pickering emulsions. Inspired by their research, we previously studied TCNFs isolated from agricultural waste hop stems (HS) as an emulsifier for oil-in-water Pickering emulsions using dodecane or olive oil as the oil.[234] A notable difference in physicochemical properties (e.g., droplet size distribution) was found when using the two different types of oils (i.e., single- or multicomponent). However, the opacity of the emulsions limited the use of microscopy to evaluate the instability mechanisms.

Magnetic Resonance Imaging of Emulsions

Magnetic resonance imaging (MRI) can provide deep insight into the internal microstructure and dynamics in spatially inhomogeneous samples.[119] In MRI, the sample is notionally broken into volume elements (voxels) instead of a single volume element, and the contrast in the image reflects the spatial variation in nuclear magnetic resonance (NMR) observables. Such NMR observables include, depending on the particular MRI pulse sequence used, the concentration, nuclear magnetic relaxation times (i.e., longitudinal and transverse relaxation), and the translational diffusion coefficients of species containing the observed nuclei (typically protons).[113] Longitudinal relaxation refers to the buildup of the longitudinal magnetization to its equilibrium value as a result of the nonsecular interactions between the spins and the surroundings. Transverse relaxation refers to the destruction of the transverse magnetization to zero as a result of both secular and nonsecular interactions between the nuclear spins and their surroundings and is related to the reorientational correlation times (of the order of nanoseconds) of the spins.[104] Both longitudinal and transverse relaxations generally appear as exponential functions of time with time constants T_1 and T_2, respectively.

Translational diffusion reflects the random thermal motion of species and provides information on the size of the diffusing species and the environment that it is diffusing within–very important information for understanding emulsions.[113,235] NMR diffusion measurements measure motion over a timescale of tens of milliseconds. For a single freely diffusing species, the translational motion is characterized by a diffusion coefficient (D). However, when the impact of restricting geometries on the diffusive motion cannot be accounted for and/or the measurement is not specific to one species, the result is characterized by an apparent diffusion coefficient (ADC).

Unlike traditional NMR, MRI has the advantage that a selected region of interest (ROI) of the sample can be analyzed individually. It should be noted that since the voxel in inhomogeneous samples may contain multiple components, the T_1, T_2, and ADC values are an average over each voxel and are thus sensitive markers for probing the emulsion stability.[113,236]

Several recent studies demonstrated that the distributions of water or fat with varying T_1 and/or T_2 relaxation times as visualized in MRI maps allowed evaluation of creaming and gravitational separation.[236,237] MRI and NMR are also useful for analyzing industrial emulsions such as for measuring droplet size distributions.[238] Fritz et al.[236] investigated ADC values of water in oil-in-water emulsions emulsified with three different molecular surfactants. They suggested that the surfactant limits the water mobility and the degree of limitation depends on the surfactants and their concentrations. Cai et al.[239] and Zhou et al.[240] are, to our knowledge, the only previous investigations of Pickering emulsions using MRI. But, these studies used low-field MRI and only obtained proton density images (in thick 2.5 and 3 mm slices) to measure the oil or water distribution. Zhou et al. [240] also performed bulk sample T_2 relaxation with low-field NMR to look at the overall T_2 distributions. Therefore, the application of high-resolution MRI methods (T_1, T_2, and ADC mapping) is of interest since Pickering emulsions have different stabilization mechanisms than molecular-based emulsions. And thus, high-resolution MRI relaxation and diffusion measurements, and mapping are likely to provide insight into the effects of the stabilizing particles and oil types.

This study employed high-resolution MRI techniques to evaluate the microstructure through relaxation and diffusion studies of probed molecules in oil-in-water Pickering emulsions emulsified with TCNFs isolated from waste HS. MR experiments were performed using two different oils (i.e., dodecane or olive oil) and two different concentrations of TCNFs (i.e., 0.5 and 1.0 wt %). The creaming behavior of the Pickering emulsions was visualized using two-dimensional (2D) and three-dimensional (3D) images over a one-month storage time. The T_1 and T_2 maps were reconstructed from T_1- and T_2-weighted images, respectively. The mean T_1 and T_2 relaxation times of each composition (i.e., free oil, emulsion layer, and serum layer) were determined from the ROIs. MRI diffusion measurements were carried out to obtain ADC maps and the mean ADC values. The relaxation and diffusion data from the emulsions was contrasted with values for neat (i.e., pure) dodecane, olive oil, water in 1.0% TCNF dispersion, and ultrapure water. The data gave deep insight into the time evolution of microstructures and creaming behaviors in Pickering emulsions. The influence of experimental factors on the measurements was considered in detail. To the best of our knowledge, MRI relaxometry and/or diffusion methods have not been utilized to illustrate the instability mechanisms of Pickering emulsions. In addition, the underlying Pickering emulsion dynamics governed by molecular behavior have not yet been quantitatively analyzed.

7.3. Materials and Methods

7.3.1. Sample Preparation

TEMPO-Oxidized Cellulose Nanofibers

TCNFs (1.0%) were isolated from air-dried and mechanically milled HS following the previously reported protocols: the median height of the individualized TCNF was 1.7 ± 0.7 nm from AFM observations.[234] Also, the carboxylate content of the obtained TCNF determined from conductometric titration was 0.59 mmol g^{-1}.[193] The 1.0% dispersion and a 0.5% dispersion prepared by dilution with distilled water were sonicated for 1.5 min just before preparing emulsions using an ultrasonic processor (Qsonica, Q700) in the pulse mode with a maximum amplitude (i.e., tip excursion) of 134 μm.

Preparation of Oil-in-Water Pickering Emulsions

Oil-in-water Pickering emulsions were prepared using two different types of oils: dodecane (99.0+%, density at 20 °C: 0.746–0.752 g mL^{-1}) and olive oil (density at 20 °C: 0.909–0.915 g mL^{-1}). Oil (2 g) was added to 0.5 or 1.0% TCNF dispersions (8 g) for an oil/water ratio of 20:80 by weight. The mixture was maintained at 20 °C and then prestirred gently. TCNF-stabilized oil-in-water dodecane (d-CNF) emulsions and olive oil (o-CNF) emulsions were prepared using an ultrasonic processor for 1 min in the continuous mode at an amplitude of 134 μm. The freshly prepared emulsion was carefully poured into a clear glass vial (28 mm o.d. 61 mm height, sample height ~ 20 mm) with a polypropylene screw cap and stored at ambient temperature for one month while observations and MRI experiments were being made. Note that the emulsification day is defined as day 0 in this paper.

Bulk Sample Preparation

To clarify each component in the emulsions in terms of relaxation and diffusion values, pure dodecane, pure olive oil, TCNF 1.0%, and ultrapure water were dispensed into 10 mm NMR tubes for imaging and measured with identical MR parameters as references. In addition, those bulk samples (500 μL) were dispensed into a 5 mm Wilmad NMR tubes to probe relaxation and diffusion using NMR spectroscopy for comparing with the MRI results.

7.3.2. Magnetic Resonance Measurements

All ^{1}H imaging experiments were performed on a Bruker Avance Neo 500 MHz (11.7 T) wide bore spectrometer equipped with a Micro2.5 gradient set (maximum gradient strength for each axis; ~1.5 T m^{-1}) with an m2m Imaging probe and resonators. A 30 mm ^{1}H single resonator radiofrequency (rf) coil was used for imaging the emulsion vials, and a 25 mm ^{1}H/^{13}C dual resonator was used for imaging the 10 mm NMR tube samples containing the pure components.

All ^{1}H NMR (non-MRI) measurements were performed on a Bruker Avance IIIHD 600 MHz (14.1 T) spectrometer at 298 K. Relaxation measurements were performed with a BBI probe. Diffusion of water in 1.0% TCNF dispersion was measured with a BBI probe equipped with *XYZ* gradients using the z gradient only (maximum gradient strength; 0.627 T m^{-1}). Diffusion of pure olive oil and dodecane were measured with a high gradient DiffBB (BBO) probe with the *z* axis gradient (maximum gradient strength; 15.8 T m^{-1}). Note that olive oil was more slowly diffusing than the other samples and required a much higher gradient.

FLASH and RARE Images

A number of imaging sequences were used: fast low-angle shot (FLASH), rapid acquisition with relaxation enhancement (RARE), RAREVTR (i.e., RARE with variable recycle delay)[124] for acquiring T_1-weighted images, and multi-slice-multi-echo (MSME)[125] for acquiring T_2-weighted images. A series of imaging measurements on each of the four emulsions were carried out at ambient temperature (~297 to 298 K) on the day after emulsification (i.e., day 1), one week later (i.e., day 7), and one month later (i.e., day 30 or 31). The total experiment time to acquire a set of 2D images (i.e., FLASH, RARE, RAREVTR, MSME, and DWI) was 16–18 h, and the single 3D RARE image took 25 h. There was no significant visual change in the emulsions during the experiments.

The internal microstructure of the emulsions was captured using FLASH and RARE sequences with sagittal or axial slices. All 2D FLASH and RARE images were acquired consecutively with the following MR parameters: echo time (T_E) 5 ms, repetition time (T_R) 600 ms, and bandwidth (BW) 300 kHz. The resolution, averages, and imaging time were identical for each sequence: the field of view (FOV) was 50 × 50 mm^2 with in-plane matrix size/resolution 250 × 250, slice thickness 0.2 mm (giving 200 μm isotropic voxels), averages 8, and imaging time 20 min. The flip angle was set at 30° for FLASH images, and the RARE factor was 1 for RARE images. In addition, chemical shift-encoded fat and water (FAW) separation were performed using the RARE sequence. The chemical shift between dodecane or olive oil (i.e., fat) and water was set at 3.5 or 4.0 ppm according to the spectrum of nonlocalized spectroscopy (NSPECT). The FAW parameters were T_E 6 ms, T_R 600 ms, voxel 200 μm, FOV 50 × 50 mm^2, slice thickness 200 µm, averages 8, BW 300 kHz, and RARE factor 1.

The 3D images with RARE were acquired as follows: T_E 6 ms, T_R 600 ms, FOV 50 × 50 × 30 mm^3 with resolution 500 × 500 × 300, giving 100 μm isotropic voxels, average 1, BW 300 kHz, and RARE factor 1. The entire 2D and 3D FLASH and RARE images were collected and processed in ParaVision 360 V3.2 and ImageJ v1.53k. The average thickness of the serum layer was measured with the ImageJ measure tool.

T_1 and T_2 Maps

T_2-weighted images of the emulsions were acquired for sagittal slices with a single T_R of 10 s, twelve T_E of 6–72 ms (6 ms equal increments), and eight averages. T_1-weighted images were acquired for sagittal slices with a single $T_E = 20$ ms; eight $T_R = 90$, 396, 757, 1199, 1766, 2560, 3899, and 9990 ms; and four averages. The other common MR parameters of T_1- and T_2-weighted images were as follows: FOV was 50 × 50 mm^2 with in-plane matrix size/resolution 250 × 250, slice thickness 0.2 mm (giving 200 μm isotropic voxels), and BW 300 kHz. The 2D T_1 and T_2 maps were reconstructed by monoexponential pixel-by-pixel fitting from the signal intensities of the T_1- and T_2-weighted images, respectively,[120] using ParaVision and the T_1 saturation recovery and T_2 relaxation models.

Apparent Diffusion Coefficient Maps

The ADC obtained from DWI provides quantitative information on the translational motion of spins in the direction of the applied diffusion gradient.[121] The ADC maps can be determined by the analysis of the DWI data using the attenuation equation of the pulsed gradient spin-echo (PGSE) signal amplitude given by,[113,114]

$$E(g,\Delta)=\frac{S(g,\Delta)}{S(0,\Delta)} \\ =\exp(-b\times\mathrm{ADC}) \tag{29}$$

where b is the diffusion weighting factor, which incorporates the gyromagnetic ratio γ. the duration (δ) and amplitude (g) of the diffusion measuring magnetic gradient pulses, and the diffusion measuring time, Δ.[121]

DWI was acquired with DtiStandard pulse sequence for sagittal slices with spin-echo (SE) weighting for one direction of the diffusion gradient with $\delta = 2$ ms and $\Delta = 25$ ms. One A_0 image and four different b value (500, 1000, 2000, and 3000 s mm^{-2}) images were acquired with two averages each. The other acquisition parameters for DWI were T_E 31 ms, T_R 8500–10,000 ms, FOV 50 × 50 mm^2 with in-plane matrix size/resolution 200 × 200 or 125 × 125, slice thickness 0.25 mm or 0.4 mm (giving 250 or 400 μm isotropic voxels), and BW 300 kHz.

The ADC maps obtained from DWI were constructed from monoexponential pixel-by-pixel fitting in ParaVision using Eq. (29). Note that ParaVision also includes offset and intercept terms in the fitting function. The Otsu or Li thresholding method was employed to detect the background. The matrices of fitting results from the ADC analysis were transferred to OriginPro 2022, and color-coded 2D and 3D maps were constructed.

Relaxation and Diffusion NMR Measurements on Bulk Samples

The T_1 and T_2 of the bulk samples were measured using the inversion recovery sequence[105] and Carr-Purcell-Meiboom-Gill (CPMG) sequence,[106,241] respectively. Self-diffusion measurements of 1.0% TCNF dispersion with the BBI probe were carried out using the pulsed gradient stimulated echo (PGSTE) sequence[118] with rectangular gradient pulses where the echo signal attenuation is given by Eq. (29) with Eq. (21).

Also, ADC in Eq. (29) becomes D for the bulk samples. Typical acquisition parameters were recycle delay 15 s, $\Delta = 70$ ms, $\delta = 1$ ms, and g from 0.003 T m^{-1} to 0.564 T m^{-1} (0.056 T m^{-1} increments, 11 points for each attenuation curve). Each spectrum was averaged over eight scans with four dummy scans. The water signal was integrated and fitted using Eq. (29) with Eq. (21) (note that the intercept was allowed to float, but the fitted value was typically ~1) with OriginPro 2022 to determine D.

Self-diffusion coefficients of oils (dodecane and olive oil) were measured with the DiffBB probe using the PGSTE sequence with half sine-shaped gradient pulses where the attenuation equation is given by Eq. (29) with D and Eq. (21).[112,116,117] Typical acquisition parameters were: recycle delay 50 s, Δ = 70 ms, δ = 1 ms for dodecane and 2 ms for olive oil, and g from 0.079–1.106 T m^{-1} (0.103 T m^{-1} increments, 11 points for each attenuation curve) for dodecane and 0.079–4.819 T m^{-1} (0.474 T m^{-1} increments, 11 points for each attenuation curve) for olive oil. Each spectrum was averaged over eight scans. The diffusion experiments of oils were done in duplicate. All signals for dodecane (i.e., $CH_2 + CH_3$) were integrated as one peak due to the slight overlap and the main CH_2 peak of olive oil was used for its integrals. D was obtained by fitting Eq. (29) with Eq. (21) to the data using Origin, and the weighted average value of the duplicates is reported. Note that the intercept was allowed to float, but the fitted value was typically ~1.

7.4. Results and Discussion

7.4.1. Visual Observation of Pickering Emulsion Stability

The TCNF-stabilized oil-in-water (o/w = 20:80) d-CNF and o-CNF emulsions were visually observed for one month (**Fig. 47**). The stabilizing effect of TCNFs as an emulsifier differed between 0.5 and 1.0% for either oil, as expected. Our previous study reported that the mean diameter of oil droplets on day 1 was 4.8 μm for 1.0% d-CNF, 7.6 μm for 0.5% d-CNF, 6.9 μm for 1.0% o-CNF, and 7.9 μm for 0.5% o-CNF.[234] Specifically for the d-CNF emulsions, a droplet-depleted serum layer (i.e., water) appeared on day 7 for the 0.5%, whereas on day 31 for 1.0%. The thickness of the transparent serum layer slightly expanded over time in the d-CNF emulsions. The opaque serum layer in 0.5% o-CNF emulsions did not seem to increase after it appeared on day 1. Note that the initial thickness of the serum layer was less than 1 mm, and thus, there was difficulty in measuring the height accurately. Contrary to the 0.5%, there was no visual separation for one month in the 1.0% o-CNF emulsions. MRI was used to characterize the internal microstructures of the emulsions as shown in the next section.

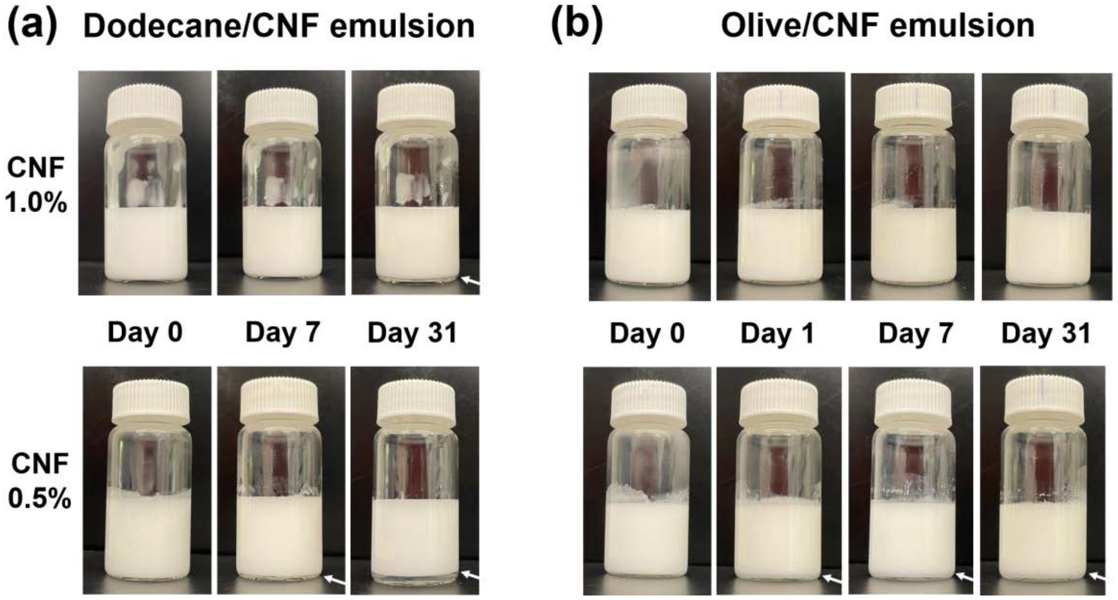

Fig. 47. Photographs of (a) dodecane and (b) olive oil Pickering emulsions stabilized with different concentrations of TCNFs (upper row, 1.0% and bottom row, 0.5%). The oil/water ratio was 20:80 by weight. The white arrows indicate the droplet-depleted serum layer at the bottom of the vials.

7.4.2. 2D and 3D MR Images of Pickering Emulsions

FLASH and RARE images of d-CNF and o-CNF emulsions are shown in **Fig. 48, Fig. S24, Fig. S25, Fig. S26,** and **Fig. S27**. The FLASH and RARE images exhibited different artifacts. Black spots in the emulsion layers most likely indicated susceptibility artifacts due to air bubbles or in some cases, oil droplets or chemical shift artifacts (**Fig. S28**).[121] The bright areas on the top of the day 1 images of the 0.5 and 1.0% d-CNF and 0.5% o-CNF emulsions suggest the presence of free oil, although this was not directly visible in the samples. FAW was consistent with the bright part at the top of the emulsion being oil and the bottom being water (**Fig. S29**). During emulsification, the microtip of the ultrasonic processor was located a few millimeters below the surface of the samples; therefore, a small quantity of oil was likely not emulsified and migrated to the surface due to the lower density.

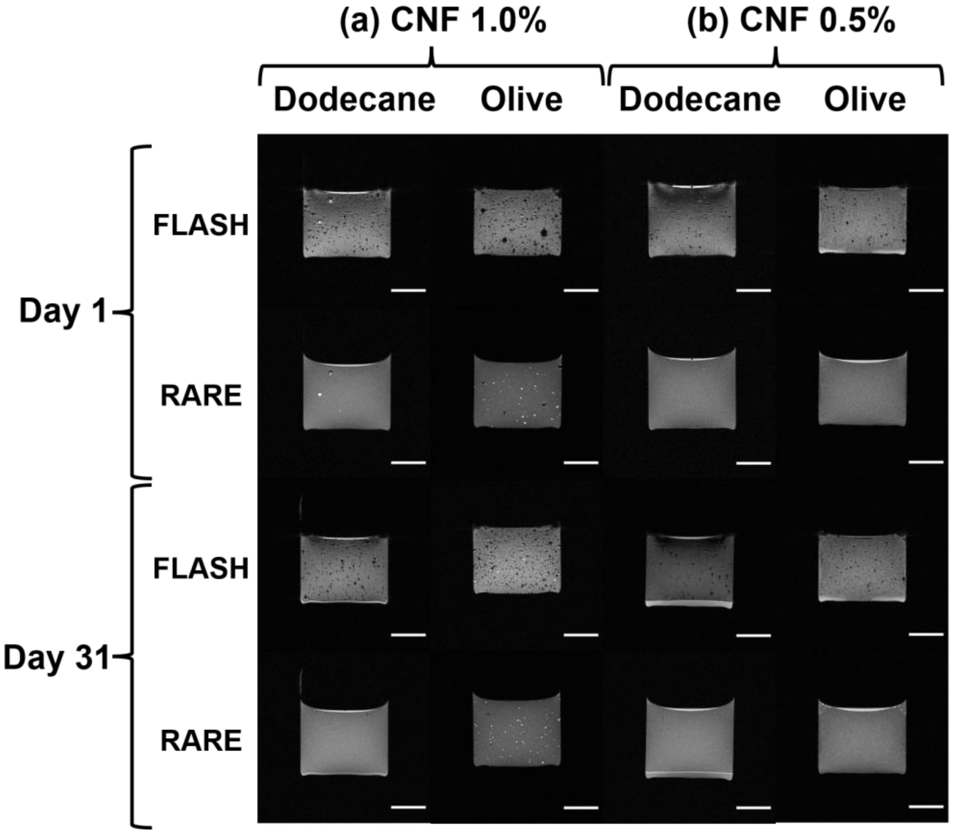

Fig. 48. FLASH and RARE images of dodecane or olive oil Pickering emulsions stabilized by (a) 1.0% TCNF and (b) 0.5% TCNF on days 1 and 31. All images are sagittal slices of the samples. The scale bar represents 10 mm.

Interestingly, the free oil was not observed in 1.0% o-CNF emulsions. Instead, larger droplets (several hundred micrometers), appearing as bright spots in the images, were observed as being dispersed in the emulsion layer. These droplets could be trapped in the emulsion layer because of the high viscosity of the emulsion and/or similar density of olive oil (0.909–0.915 g mL^{-1}) to water. Another possibility is Ostwald ripening. Our previous studies using confocal laser scanning microscopy showed rapid droplet growth in o-CNF emulsions with droplets larger than several tens of micrometers.[234] The serum layer at the bottom was also distinguished in bright contrast in the d-CNF emulsions in both FLASH and RARE. The average thickness of the serum layer was 1.8 mm for 0.5% and 0.6 mm for 1.0% on day 31. As seen in the 0.5% o-CNF emulsion, the contrast for the serum layer was better in the FLASH image, whereas that of the free oil was better in the RARE image. The contrasting reverse of oil and water was also observed in axial slices (**Fig. S27**).

After one month, the maximum intensity of 3D volume rendering revealed the invisible creaming behavior (**Fig. 49**). The entire 1.0% d-CNF and o-CNF emulsion samples were visualized as free oil, oil droplets, emulsion layers, and serum layers. The maximum intensity 3D projection showed that the merged (i.e., coalescence) oil droplets moved upward and condensed near the surface. While the d-CNF emulsion reflected large, individual droplets (**Fig. 49a**), the o-CNF emulsion exhibited droplet flocculation (**Fig. 49b**). Surprisingly, although the area of flocs was greater in o-CNF than in d-CNF, even by day 31 no separation was observed.

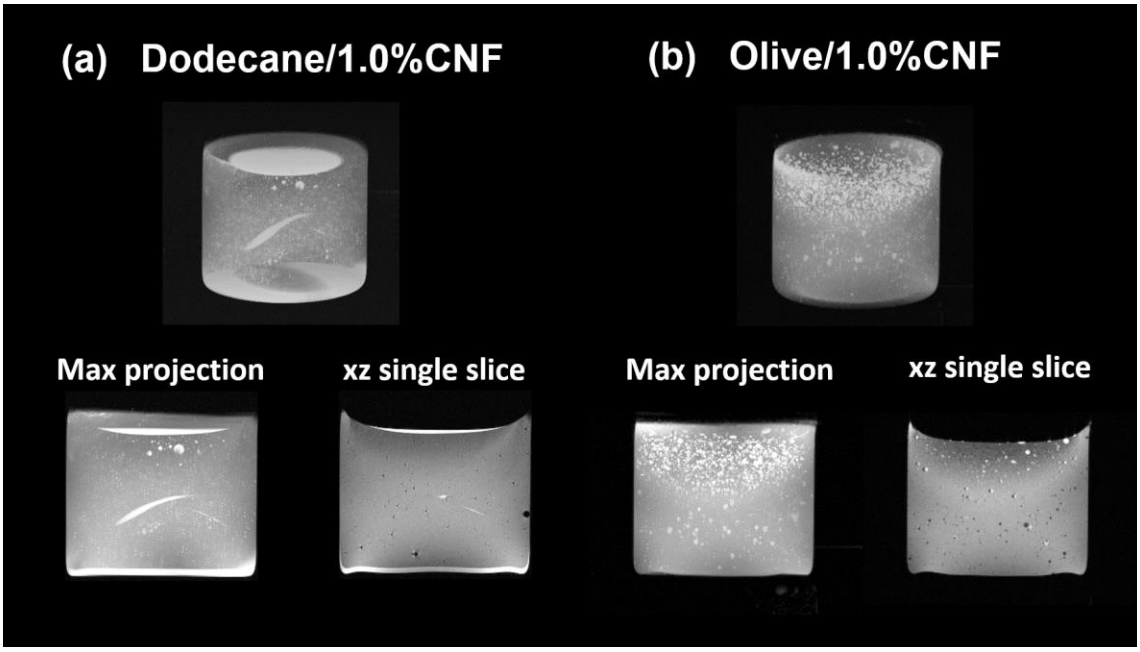

Fig. 49. The 3D volume rendering of (a) d-CNF and (b) o-CNF emulsions stabilized by 1.0% TCNF after one month storage (upper row). The invisible (with the naked eye or MRI single slice) creaming behavior of oil droplet flocculation was revealed. The side view of 3D maximum intensity and single slice image from RARE are also shown (bottom row).

7.4.3. Apparent T_2 Maps

The apparent T_2 maps are shown in **Fig. 50a,d**. Note that the voxels in the emulsion layer included multiple components (e.g., water and oil) and thus gave an average T_2 resulting

(a) Dodecane/CNF

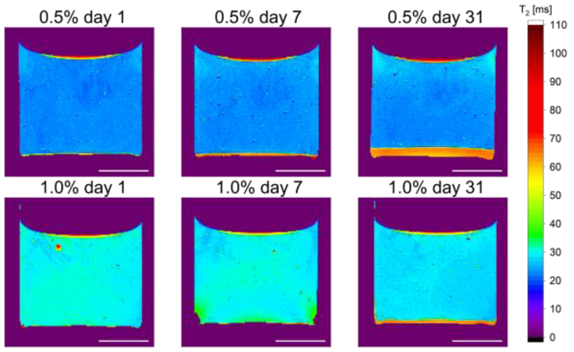

(b) 0.5% d-CNF **(c) 1.0% d-CNF**

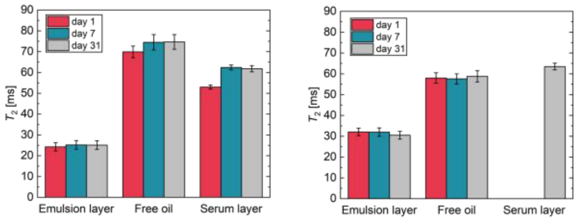

(d) Olive/CNF

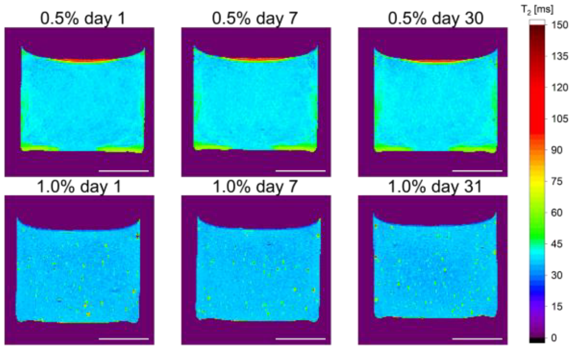

(e) 0.5% o-CNF **(f) 1.0% o-CNF**

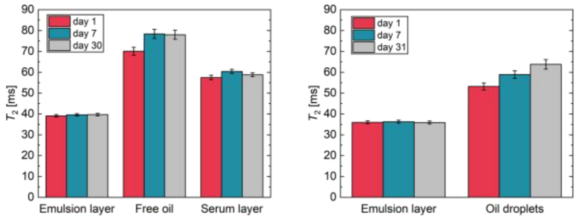

Fig. 50. Apparent T_2 maps of Pickering emulsions (o/w = 20:80) and the mean T_2 values of each layer. (a) d-CNF emulsions and (d) o-CNF emulsions were stabilized by 0.5% (upper row) or 1.0% (lower row) on days 1, 7, and 30 or 31. The emulsion layer is shown in blue for both d-CNF and o-CNF, the free oil at the top in red for both d-CNF and o-CNF, and oil droplets in red to green for o-CNF and the serum layer at the bottom in orange for d-CNF and green for o-CNF. The scale bar represents 10 mm. (b,c,e,f) The mean T_2 values were calculated from the ROIs of each component. The error bars reflect the standard deviation from monoexponential fitting.

in the apparent T_2 map. The mean T_2 values of the emulsion layer, free oil, and serum layer are shown in **Fig. 50b,c,e,f, Fig. S30** and **Fig. S31**. The T_2 of pure samples are compared in **Table 5** and **Fig. S32**. The apparent T_2 maps of d-CNF emulsions in **Fig. 50a** showed that there were significant differences among the three layers. The mean T_2 of the free oil matched well with the T_2 of pure dodecane (80.2 ± 3.0 ms), and the serum layer gave a mean T_2 closer to that of ultrapure water (66.7 ± 1.5 ms), suggesting that these two components were bulk oil and water, respectively.

Generally, a short T_2 indicates a more viscous component or a molecule with slow molecular reorientation [104] The emulsion layers of d-CNF gave significantly shorter mean T_2 values among the three layers and were unchanged over time (**Fig. 50b,c**). Also, the 0.5% d-CNF emulsion layer exhibited a slightly shorter T_2 than the 1.0% emulsion. This result was unexpected from our previous studies, which showed that the viscosity of the 1.0% d-CNF emulsion was significantly higher than the 0.5% d-CNF emulsion at the same shear rate.[234] This unexpected result might be due to measurement using the MSME MRI sequence (described later).

The distinct microstructural differences between the 0.5 and 1.0% o-CNF emulsions were reflected in the apparent T_2 maps (**Fig. 50d**). For the 0.5% o-CNF emulsion, the serum layer was observed not only at the bottom of the vials but also on the walls. In the 1.0% o-CNF emulsions, oil droplets in the emulsion layer were detected in the apparent T_2 map, distinguishable from the emulsion layer. For both TCNF concentrations, the overall apparent T_2 maps remained unchanged for one month.

Artifacts arising from the MRI measurements also appeared in the T_2 maps. At first, chemical shift artifacts were noted near the boundary of each component (e.g., the free oil and emulsion layer). Second, the spatial distortion of the lower part of the image for the 1.0% d-CNF emulsion on day 7 was an artifact arising from the position of the sample with respect to the effective volume of the rf coil.[121]

Table 5. The longitudinal and transverse relaxation of pure oils obtained from MRI and NMR.

Method	MRI	NMR
Sequence	RAREVTR	Inversion recovery
	Mean T_1 ± standard deviation [ms]	T_1 ± standard error [ms]
Dodecane	1360 ± 17	1936 ± 53 ($-C\underline{H}_3$)
		1429 ± 13 ($-C\underline{H}_2-$)
Olive oil	651 ± 10	999 ± 7 ($-C\underline{H}_3$)
		669 ± 6 ($-(C\underline{H}_2)_n-$, $-OCO-CH_2-C\underline{H}_2-$)
		613 ± 7 ($-C\underline{H}_2-CH=CH-$)
		635 ± 13 ($-OCO-C\underline{H}_2$)
		762 ± 77 ($=CH-C\underline{H}_2-CH=$)
		724 ± 13 ($C\underline{H}_2OCOR$)
		938 ± 7 ($>CHOCOR$, $-C\underline{H}=C\underline{H}-$)
Ultrapure water	2284 ± 47	-
Water in TCNF 1.0% dispersion	2170 ± 60	-
Sequence	MSME	CPMG
	Mean T_2 ± standard deviation [ms]	T_2 ± standard error [ms]
Dodecane	80.2 ± 3.0	353 ± 31 ($-C\underline{H}_3$)
		491 ± 19 ($-C\underline{H}_2-$)
Olive oil	79.4 ± 3.3	112 ± 12 ($-C\underline{H}_3$)
		105 ± 8 ($-(C\underline{H}_2)_n-$, $-OCO-CH_2-C\underline{H}_2-$)
		29.7 ± 3.7 ($-C\underline{H}_2-CH=CH-$)
		15.0 ± 7.6 ($-OCO-C\underline{H}_2$)
		95.5 ± 11.7 ($=CH-C\underline{H}_2-CH=$)
		73.6 ± 3.1 ($C\underline{H}_2OCOR$)
		191 ± 21 ($>CHOCOR$, $-C\underline{H}=C\underline{H}-$)
Ultrapure water	66.7 ± 1.5	-
Water in TCNF 1.0% dispersion	57.3 ± 1.1	-

*Assignments of olive oil peaks in ^{1}H NMR spectra were referenced from the report by Jafari et al.[242]

7.4.4. Apparent T_1 Maps

The apparent T_1 maps are shown in Figures 5a and d. Similarly to the T_2, the mean T_1 values of each layer are shown in **Fig. 51b,c,e,f, Fig. S33**, and **Fig. S34** and compared with MRI data of the pure samples in **Table 5** and **Fig. S32**. In the T_1 map, the emulsion layer in the d-CNF emulsions revealed a mixture of similar relaxation properties as water and dodecane since ultrapure water and pure dodecane were 2.3 and 1.4 s, respectively (**Fig. S32** and **Table 5**). Interestingly, the T_1 distribution of the d-CNF emulsion layer in both samples changed over time; most voxels were consistent with the relaxation of water on day 1, and then, more voxels were consistent with relaxation of oil during storage. This implied that water in the continuous phase occupied the major area of a voxel on day 1 and then more voxels were approximated as oil relaxation by being occupied by flocculated or coalesced larger oil droplets after the appearance of droplet-depleted serum (**Fig. 51a**). Each layer in both the 0.5 and 1.0% o-CNF emulsions was distinguished by different colors of the T_1 range (**Fig. 51d**). The free oil in the 0.5% and oil droplets in the 1.0% displayed T_1 values of around 700 ms, which was in good agreement with pure olive oil (651 ± 10 ms in **Table 5**).

The MRI results in this work were obtained using imaging sequences that did not give spectroscopic information for each voxel. NMR spectroscopy can provide the relaxation properties of protons in the same environment since the signal of each molecule typically has a different chemical shift; however, the information is obtained from the entire sample volume. This difference between MRI and NMR can be seen in the variation of the T_1 and T_2 results for the samples obtained from each technique (**Table 5**). Comparing the relaxation properties of methylene protons (i.e., the largest intensities for each oil) in NMR spectroscopy results to the MRI results, dodecane and olive oil exhibited relatively similar T_1 in both methods but gave much shorter T_2 by MRI. The differences in T_2 between NMR and MRI techniques are likely due to the sequence used, e.g., MSME for the MRI results and CPMG for the NMR results. Previous studies[243,244] investigated relaxation in cartilage using MSME MRI as well as a CPMG magnetization-prepared spin-echo imaging sequence and showed how MSME is affected by both T_2 weighting pulses and spatial encoding/mapping pulses, where the T_2 obtained from MSME is shorter and resolution-dependent. Similarly, it could be also seen how MSME

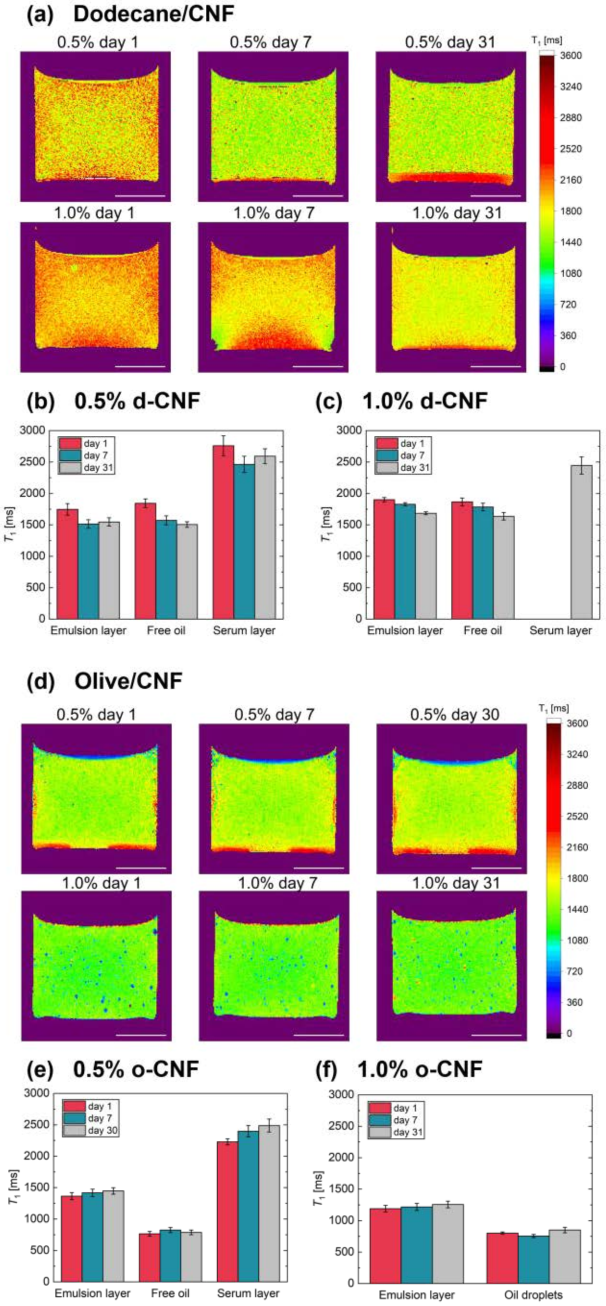

Fig. 51. Apparent T_1 maps of Pickering emulsions (o/w = 20:80) and the mean T_1 values of each layer. (a) d-CNF emulsions and (d) o-CNF emulsions were stabilized by 0.5% (upper row) or 1.0% (lower row) on days 1, 7, and 30 or 31. The emulsion layer is shown in red to green for d-CNF and yellow to green for o-CNF, the free oil at the top in yellow to green for d-CNF and blue for o-CNF, oil droplets in blue for o-CNF, and the serum layer at the bottom in red for both d-CNF and o-CNF. The scale bar represents 10 mm. (b,c,e,f) The mean T_1 values were calculated from the ROIs of each component. The error bars reflect the standard deviation of monoexponential fitting.

results differed even from bulk spectroscopy-based CPMG results.[244] Therefore, the apparent T_2 maps and values in this report are also likely affected by the additional weighting in the MSME MRI sequence; however, all MSME experiments were performed with identical resolution each time and thus provided the qualitative comparison during the course of the experiments.

7.4.5. Apparent Diffusion Coefficient Maps

The ADC maps and values are shown in **Fig. 52a-h** and **Fig. S35**. As for the fast diffusion components in the d-CNF emulsions, the free oil and serum layers had ADC = 0.8×10^{-3} and 2×10^{-3} mm^2 s^{-1}, respectively. The ADC of neat dodecane and ultrapure water obtained from MRI data agreed well with these values (compare **Fig. 52a-d**, **Fig. S36** and **Table S7**). The self-diffusion coefficients of the pure components determined from NMR spectroscopy corresponded well with ADC values, and water in the 1.0% dispersions TCNF was well matched with pure water. Perhaps the TCNF network structure might not affect the translational motion within the diffusion timescale.

For the o-CNF emulsions, while the ADC of the serum layer was identical to the ADC as in the case of d-CNF, the free oil showed the smallest ADC (~ 10^{-5} mm^2 s^{-1}). Neat olive oil could not be measured with the same *b* values used for visualizing the fast diffusion components in the MRI of the o-CNF emulsions (data not shown). The self-diffusion coefficients of pure olive oil obtained from NMR was 1.0×10^{-5} mm^{2}s^{-1} (**Table S7**), which was much slower than dodecane.

For each series of MRI experiments for each measurement day to complete within 24 h, the ADC values obtained from the selected ROIs showed greater noise compared to the apparent T_1 or T_2 maps (data not shown). For this reason, the mean ADC values of the emulsion layer shown in **Fig. 52i** were the averaged values obtained from fitting the results for all individual voxels (i.e., bulk of the results in the histograms) with a Gaussian curve (**Fig. 52i**). The standard errors of the fitted parameters were quite small; therefore, the full width at the half-maximum (FWHM) of the distribution for the emulsion layer was also shown as references for the distribution widths (**Fig. 52j**). Compared to the mean ADC of d-CNF emulsions on days 7 and 30 or 31, 0.5% was almost unchanged at (8.8–9.0) $\times 10^{-5}$ mm^2 s^{-1} whereas 1.0% decreased from 11×10^{-5} to 7.7×10^{-5} mm^2 s^{-1}. For the o-CNF emulsions, there was no significant difference in the mean ADC between days

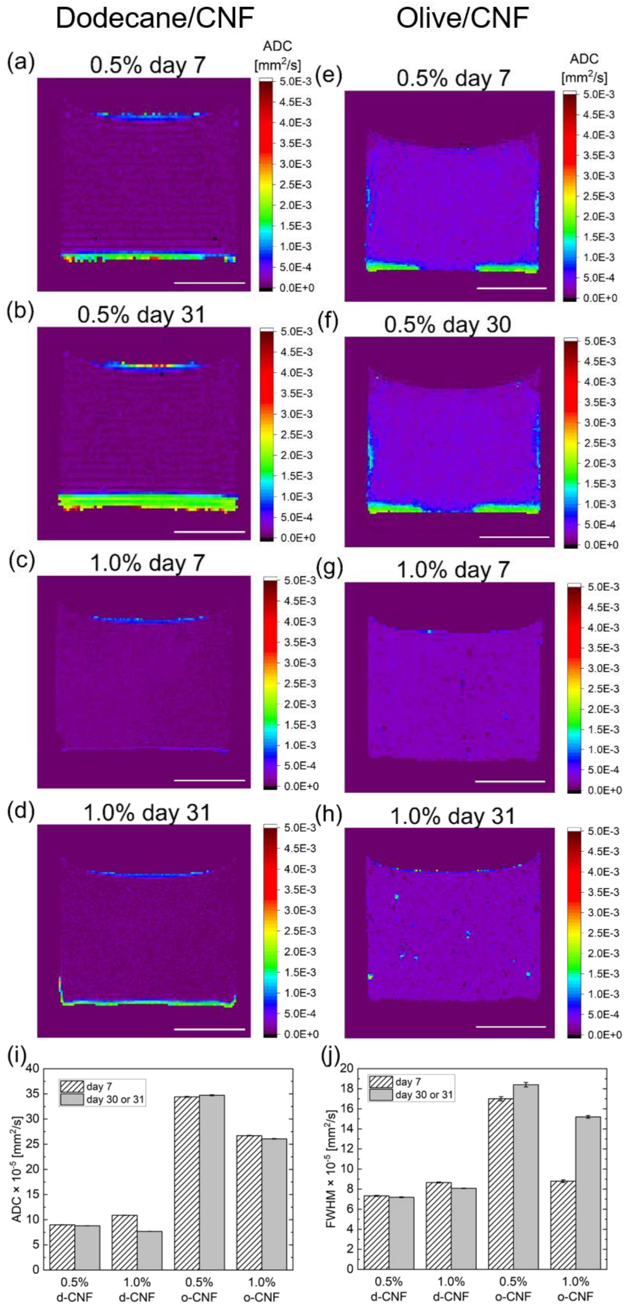

Fig. 52. ADC maps of (a-d) d-CNF and (e-h) o-CNF emulsions stabilized with 0.5 or 1.0% TCNF on days 7 and 30 or 31. ADC maps were reconstructed from 250 or 400 μm isotropic voxels. The scale bar represents 10 mm. The emulsion layer is shown in purple for both d-CNF and o-CNF, free oil in blue for d-CNF, and serum layer in green to blue for both d-CNF and o-CNF. (i) The mean ADC values of the emulsion layer were calculated from Gaussian fittings. (j) The full width at the half-maximum (FWHM) of the distributions for the emulsion layer. The error bars represent the standard errors of the fitted parameters.

7 and 31; however, 1.0% (2.6–2.7) × 10^{-4} mm^2s^{-1} was calculated as smaller than 0.5% (3.4–3.5) × 10^{-4} mm^2 s^{-1}.

The higher ADCs (**Fig. 52i**) for the olive oil emulsion layer compared to the dodecane emulsion layer could reflect the viscosity difference between these emulsions, i.e., the viscosity of the olive oil emulsion showing shear-thinning behavior was lower.[234] While the trend for the ADC for the 1.0 vs 0.5% o-CNF emulsion layer (**Fig. 52i**) could also reflect the emulsion viscosities (higher viscosity for 1.0% o-CNF compared to the 0.5% o-CNF emulsion),[234] the same trend was not observed for the ADC of the emulsion layer of the d-CNF samples. The diffusion of pure olive oil was much slower than pure dodecane, and the diffusion of water in the 1.0% TCNF dispersion alone was similar to pure water (**Table S7**). However, the difference in ADCs in the emulsion layer voxels (i.e., those containing both water and oil, where the contribution of each depends on the emulsion composition and MRI/NMR signal weighting) of the 0.5–1.0% samples was not explicable by the change in viscosity alone. In our previous study, field-emission scanning electron microscopy observations revealed that TCNFs influenced the emulsion dynamics by adsorbing on the oil/water interfaces and forming a solid entangled network structure in the continuous phase.[234] Another rheological study on CNF-stabilized sesame oil Pickering emulsions showed that the locally close packing structure of oil droplets was formed, and this affected the hierarchical structures of droplets.[209] Therefore, the ADC difference likely indicates the effects of restricted diffusion of oil within the droplets and droplet sizes/distributions and obstruction of water diffusion around the oil droplets due to oil droplet size/packing.[235,238] NMR relaxation and diffusion measurements were useful for revealing the internal and rotational mobility of surfactant molecules in the molecular-based emulsions.[245] Therefore, further NMR/MRI studies are needed to examine the restricted effects in CNF-stabilized Pickering emulsion.

7.5. Conclusions

This study demonstrated the power of high-resolution MRI for noninvasively characterizing the destabilizing molecular level mechanisms in Pickering emulsions. High-resolution MRI was used to investigate voxelwise longitudinal relaxation, transverse relaxation, and apparent diffusion coefficients of dodecane or olive oil-in-water Pickering emulsions stabilized by 0.5 or 1.0% TCNF over the period of one month.

All MRI observations highlighted the different microstructure and creaming behavior when using dodecane or olive oil as the dispersed phase. The separation of the oil and water and distribution of coalesced larger oil droplets were visualized in 2D FLASH and RARE images. The 3D RARE images provided excellent visualization showing flocculated/coalesced droplets packed near the surface of the emulsions one month after emulsification.

The apparent T_1, T_2, and ADC maps of the Pickering emulsions present the mean relaxation or diffusion properties of each composition: free oil, coalesced oil droplets, emulsion layer, and serum layer. Importantly, they report on different lengths and timescales and so report on different aspects of the molecular dynamics involved in stabilizing the Pickering emulsions. Unlike the surfactants in molecular-based oil-in-water emulsions, which altered the T_1, T_2, and ADC of water depending on the concentrations,[236] those relaxation and diffusion properties of the serum layer were consistent with each bulk sample regardless of the TCNF concentration and storage time. The T_1 distribution in the d-CNF emulsion layer changed over one month of storage, indicating microstructural changes such as flocculation and coalescence. Therefore, the T_1 map is suggested to be the primary method for investigating the relaxation and microstructure of the Pickering emulsions.

Comparing the T_1 and T_2 of pure dodecane and olive oil obtained from MRI and NMR exhibited similar T_1 but significantly different T_2, therefore, the T_2 maps reconstructed by the T_2-weighted MSME sequence were considered to be only worked as a quantitative comparison of experiments.

The ADC of the free oil and serum layer well matched with pure oil and water, respectively. Also, the diffusion coefficient of olive oil obtained by NMR was much slower than dodecane. Thus, ADC needed more experiment time for capturing both slow (e.g., olive oil) and fast (e.g., water) diffusion components, and detecting the viscous emulsion layer was challenging. The ADC of the d-CNF emulsion layer had no direct correlation between the viscosity of the entire emulsion as the TCNF concentration increased. These unexpected results most likely indicated effects of restricted diffusion of oil from droplet sizes/distributions as well as obstruction of water diffusion around the oil droplets due to oil droplet size/packing.

Chapter 8 – Concluding Remarks

This thesis aimed to elucidate instability mechanisms for Pickering emulsions (PEs) using 2,2,6,6-tetramethylpiperidine-1-oxyl (TEMPO)-oxidized cellulose nanofibers (TCNFs) derived from agricultural/food waste (AFW) as the stabilizer. In the first phase of the thesis, two AFWs of spent coffee grounds (SCGs) in Chapter 4 and hop stems (HSs) in Chapter 5 were explored as the new lignocellulosic biomass. TEMPO-mediate oxidization was selected for the isolation of TCNFs due to their desirable properties as the stabilizer, such as high transparency, viscosity, and uniformity. The second phase was aiming for the development of oil-in-water (o/w) PEs using AFW-derived TCNFs. In Chapter 6, o/w PEs were prepared using the single component oil (dodecane) and multicomponent oil (olive oil), and the long-term stability, the droplet size distribution (DSD), and the microstructure were investigated. In Chapter 7, magnetic resonance imaging (MRI) relaxometry and diffusion techniques were utilized to illustrate the instability mechanisms of PEs governed by molecular behavior.

8.1. Cellulose Nanofibers from Spent Coffee Grounds

In Chapter 4, the SCG-derived TCNFs were isolated and characterized. Due to the low contents of cellulose (about 10 %) in SCGs and higher contents of hemicellulose and lignin (about 50–70% in total), 3–18 times more sodium hypochlorite was required during TEMPO-mediated oxidation than for wood source as discussed in Section 4.5. Section 4.4.2. described the SCGs-derived TCNFs formed the same crystal structure of cellulose I and comparable thermal decomposition temperatures as wood-derived TCNF from the powder X-ray diffraction (XRD) and thermogravimetric analysis (TGA). Also, the SCG-derived TCNFs had an average width of 25 nm from the field-emission scanning electron microscopy images (FE-SEM), and thus pretreatment process will be required to obtain the microfibril widths (4.2 nm). Solid-state nuclear magnetic resonance (NMR) experiments suggested that most hemicellulose and lignin were removed while trace amounts of triacylglycerols (TAGs) as the oil components remained. In Section 4.4.2., the composite film with poly(vinyl alcohol) (PVA) indicated the compatibility; however, further investigations will be needed to confirm applicability for polymers.

8.2. Cellulose Nanofibers from Hop Stems

Agricultural waste of the beer ingredients, HSs were investigated as an unexplored CNF source as described in Chapter 5. Chemical compositional analysis revealed that HS contained 44% cellulose, comparable to wood before pulping process, and similar sugar composition of hardwoods (Section 5.4.1.). Before TEMPO-mediated oxidation, hemicellulose, lignin, and calcium oxalate monohydrate (COM) were removed through Wise method, alkaline treatment, and the trisodium citrate treatment, respectively. The pretreatment process was optimized by comparing the fiber morphology and structural characterization of three HS-derived TCNFs isolated from different isolation methods. Note that the citrate treatment was applied to dissolve COM in Section 6.4.1. in Chapter 6. Atomic force microscopy (AFM) observation revealed that the HS-derived CNFs had similar height distributions of ~ 2 nm regardless of the pretreatment. Solid-state NMR and XRD results indicated that citrate treatment was essential to remove COM crystals otherwise remained in TCNF. Also, the crystallinity of the TCNFs was enhanced by eliminating amorphous (non-crystalline region) components (e.g., hemicelluloses). In conclusion, a new ‘upcycling’ of HS into TCNFs was introduced for the first time. HS-derived TCNFs isolated from dewaxing and citrate pretreatment yielded around 25% from HS and exhibited similar fiber morphology, purity, transparency, and viscosity to wood-derived TCNFs.

8.3. Pickering Emulsion Stability Using Cellulose Nanofibers from Hop Stem

In Chapter 6, TCNF from HSs obtained in Chapter 5 was used as the o/w PE stabilizer, and the stability of PEs was investigated with two different oils, dodecane and olive oil. Required storage time and temperatures for PEs depend on the application, however, one month under ambient temperature was selected as the first assessment condition. The stable PEs were obtained with 1% TCNF concentrations in the continuous phase and less than 20% oil ratios (Section 6.4.2.). The obtained PEs were microemulsions having less than 10 μm average droplet size (Section 6.4.3.). Olive oil including multicomponents of triglycerides and other polar components was less stable than dodecane as the single oil. While the droplet size of dodecane PE became smaller with increasing TCNF concentrations, the droplet size distribution (DSD) was wider in olive PE since more than 100 μm droplets emerged during the storage. As described in Section 6.4.4., Confocal laser microscopy (CLSM) showed that independent oil droplets in dodecane PE gradually aggregated to form flocculated structures and then coalesce during storage. TCNF observed in FE-SEM densely covered oil droplets surfaces as well as entangled each other in the continuous phase thus preventing the coalescence. On the contrary, in olive PE, the oil droplets formed clusters of flocs in several tens of micrometers regardless of the TCNF loadings since on the day after emulsification. This indicated that attractive force due to TCNF concentration gradient and repulsion due to osmotic effect took a role between oil droplets to form the stable flocs in olive PEs. In addition, the rapid growth of droplets was confirmed most likely due to Ostwald ripening. While there are a few different emulsion instability mechanisms (e.g., flocculation, Ostwald ripening, and coalescence), the microscopy and DSD results suggested that dodecane PE and olive PE underwent different deformation contributions.

8.4. Pickering Emulsion Instability Evaluated by MRI and NMR

The microscopy techniques (CLSM and FE-SEM) and droplet size distribution results shown in Chapter 6 had a possibility that they only reflected 'a part of' the microstructures of PEs due to the experimental limitations. For this reason, in Chapter 7, high-resolution magnetic resonance imaging (MRI) evaluation was conducted to elucidate the time evolution of microstructures and creaming behaviors of the 'entire' dodecane and olive PEs.

In Section 7.4.2., 2D MR images captured the initial stage of water/oil separation and the presence of free oil and serum layer, which could not be seen visually or through microscopic observations. In addition, 3D MR images visualized the distinct creaming structure difference between dodecane and olive PEs of aggregated/coalesced oil droplets packed near the PE surface after one month of emulsification. MRI voxelwise relaxation times (T_1 and T_2) as well as apparent diffusion coefficients (ADCs) from the entire PEs were reconstructed in maps to illustrate the different components of the free oil, oil droplet, emulsion layer, and water layer (Section 7.4.3. – 7.4.5.). NMR was also used to determine spectroscopic T_1, T_2, and diffusion coefficient (D) in bulk oils. The T_1 distribution of the emulsion layer correlated with microstructural changes due to aggregation and coalescence, but not for T_2 distributions. A comparison of relaxation properties of bulk oils obtained from MRI and NMR showed that T_1 was comparable, but T_2 differed significantly due to the MRI sequence. Therefore, T_1 map was concluded to be the primary method for studying the relaxations and microstructures of PEs while the T_2 map worked only as a quantitative comparison within the experiment. ADC is generally inversely proportional to viscosity; however, the ADC of the emulsion layer of dodecane PE did not correlate with the viscosity of the emulsion governed by the CNF concentrations. These unexpected results may have reflected the effect of oil diffusion restriction due to oil droplet size/distribution and water diffusion restriction around the oil droplets packings, and further diffusion NMR experiments will be needed (see Section 8.6.).

8.5. Research Significance

At the begging of my PhD research, the primary focus was to answer the important research question: “What is the difference between AFW-derived CNF and wood-derived CNF?” This is because wood, particularly bleached kraft pulp in the laboratory scale, has been extensively used as a source of CNF worldwide. Through the characterizations of SCG-derived TCNF and HS-derived TCNF using solid-state NMR, XRD, TGA, AFM, and FE-SEM, the answer for the question was revealed that those two AFW-derived TCNFs possessed ‘comparable/similar’ fiber morphology, crystal structure, crystallinity, and thermal stability to wood-derived TCNFs although the unique feature of the AFW-derived TCNFs are yet to be undiscovered.

The findings of this research contain several research significances. Firstly, it showcases the isolation of TCNFs from new promising waste sources comparable to wood. Secondly, it provides a systematic elucidation of the stabilization factors when using AFW-derived TCNFs as the PE stabilizer. Lastly, it discovers the application of high-resolution MRI as a novel evaluation technique for understanding instability mechanisms of PEs.

The implications of this research indicate that the conversion of AFW into value-added CNFs, along with their application as environmentally friendly PE stabilizer, can contribute to the development of a circular economy, sustainable waste revalorization or upcycling, and the reduction of local disposal costs.

8.6. Directions for Future Research

For the use of the SCGs-derived TCNFs, the low yield was a critical challenge. Alternatively, the extraction of hemicellulose-contained cellulose nanofibers (holocellulose CNF) through mechanical disintegration may potentially enhance the yield. Further investigation is of interest for the development of the SCG-derived CNFs application.

NMR self-diffusion measurements study the self-diffusion coefficients of the probed molecules over the millisecond to second timescale. However, in o/w emulsions, the oil molecules will reach the oil/water interfaces and thus be subject to restricted diffusion.[112,113] The attenuation of the NMR echo signal described in Eq. (20) can be correlated with the DSD in the emulsion. Precise determination of the DSD can be achieved by simulating the signal attenuations using an theoretical model such as Gaussian phase distribution (GPD) and short gradient pulse (SGP) approximations.[246] Future research should focus on selecting the most appropriate model for accurately determining DSD for PEs. The obtained DSD can be compared with the data from the particle distribution size analyzer in Section 6.4.3.

A recent study by Kaysan et al.[245] on emulsions with molecular-based surfactants revealed the relationship between the internal/rotational mobility of surfactant molecules at the liquid/liquid interface and droplet size using NMR relaxation and diffusion measurements. However, this approach has not been applied to PEs. Investigations on NMR relaxation and diffusion measurements of CNF using solvent suppression (removal of solvent peaks) will provide valuable information on the dynamics of CNF in PE.

In addition, molecular dynamics (MD) simulations of PE can provide insight into the molecular level dynamics of these systems, such as the adsorption behavior of CNF at the water/oil interface. The future focus will be to describe the dynamics of the entire PE system from the results obtained by NMR diffusion measurements and MD simulations.

References

1. French, A. D. Glucose, not cellobiose, is the repeating unit of cellulose and why that is important. *Cellulose* **24**, 4605–4609 (2017).
2. Moon, R. J., Martini, A., Nairn, J., Simonsen, J. & Youngblood, J. Cellulose nanomaterials review: Structure, properties and nanocomposites. *Chem. Soc. Rev.* **40**, 3941–3994 (2011).
3. Isogai, A., Saito, T. & Fukuzumi, H. TEMPO-oxidized cellulose nanofibers. *Nanoscale* **3**, 71–85 (2011).
4. Atalla, R. H. & VanderHart, D. L. Native cellulose: a composite of two distinct crystalline forms. *Science* **223**, 283–285 (1984).
5. Yamamoto, H. & Horii, F. CP/MAS ^{13}C NMR analysis of the crystal transformation induced for *Valonia* cellulose by annealing at high temperatures. *Macromolecules* **26**, 1313–1317 (1993).
6. Nishiyama, Y., Sugiyama, J., Chanzy, H. & Langan, P. Crystal structure and hydrogen bonding system in cellulose I_α from synchrotron X-ray and neutron fiber diffraction. *J. Am. Chem. Soc.* **125**, 14300–14306 (2003).
7. Nishiyama, Y., Chanzy, H. & Langan, P. Crystal structure and hydrogen-bonding system in Cellulose $I\beta$ from synchrotron X-ray and neutron fiber diffraction. *J. Am. Chem. Soc.* **124**, 9074–9082 (2002).
8. Imai, T., Putaux, J. L. & Sugiyama, J. Geometric phase analysis of lattice images from algal cellulose microfibrils. *Polymer* **44**, 1871–1879 (2003).
9. Isogai, A. Development of completely dispersed cellulose nanofiber. *Proc. Jpn. Acad., Ser. B* **94**, 161–179 (2018).
10. Mateo, S., Peinado, S., Morillas-Gutiérrez, F., La Rubia, M. D. & Moya, A. J. Nanocellulose from agricultural wastes: products and applications—a review. *Processes* **9**, 1594 (2021).
11. Isogai, A. Emerging nanocellulose technologies: recent developments. *Adv. Mater.* **33**, 2000630 (2021).
12. Pennells, J., Godwin, I. D. & Martin, D. J. Trends in the production of cellulose nanofibers from non-wood sources. *Cellulose* **27**, 575–593 (2020).
13. *Advanced Technologies of Cellulose Utilization*. (CMC, 2008).
14. セルロースナノファイバー利用促進のための原料評価書. (NEDO, 2020).
15. Vassilev, S. V., Baxter, D., Andersen, L. K., Vassileva, C. G. & Morgan, T. J. An overview of the organic and inorganic phase composition of biomass. *Fuel* **94**, 1–

33 (2012).

16. García, A., Gandini, A., Labidi, J., Belgacem, N. & Bras, J. Industrial and crop wastes: a new source for nanocellulose biorefinery. *Ind. Crops Prod.* **93**, 26–38 (2016).
17. Farah, A. Coffee Constituents. in *Coffee: Emerging Health Effects and Disease Prevention* (ed. Chu, Y.-F.) 21–58 (Blackwell Publishing Ltd., 2012).
18. World coffee consumption. *International Coffee Organization* https://www.ico.org/prices/new-consumption-table.pdf (2021).
19. Mata, T. M., Martins, A. A. & Caetano, N. S. Bio-refinery approach for spent coffee grounds valorization. *Bioresour. Technol.* **247**, 1077–1084 (2018).
20. Murthy, P. S. & Naidu, M. M. Sustainable management of coffee industry by-products and value addition - a review. *Resour. Conserv. Recycl.* **66**, 45–58 (2012).
21. Kovalcik, A., Obruca, S. & Marova, I. Valorization of spent coffee grounds: a review. *Food Bioprod. Process.* **110**, 104–119 (2018).
22. Lavecchia, R., Medici, F., Patterer, M. S. & Zuorro, A. Lead removal from water by adsorption on spent coffee grounds. *Chem. Eng. Trans.* **47**, 295–300 (2016).
23. Wang, C. H., Wen, W. C., Hsu, H. C. & Yao, B. Y. High-capacitance KOH-activated nitrogen-containing porous carbon material from waste coffee grounds in supercapacitor. *Adv. Powder Technol.* **27**, 1387–1395 (2016).
24. Shang, Y. F., Xu, J. L., Lee, W. J. & Um, B. H. Antioxidative polyphenolics obtained from spent coffee grounds by pressurized liquid extraction. *South African J. Bot.* **109**, 75–80 (2017).
25. Ballesteros, L. F., Ramirez, M. J., Orrego, C. E., Teixeira, J. A. & Mussatto, S. I. Optimization of autohydrolysis conditions to extract antioxidant phenolic compounds from spent coffee grounds. *J. Food Eng.* **199**, 1–8 (2017).
26. Acevedo, F. *et al.* Spent coffee grounds as a renewable source of bioactive compounds. *J. Biobased Mater. Bioenergy* **7**, 420–428 (2013).
27. Kanai, N., Yoshihara, N. & Kawamura, I. Solid-state NMR characterization of triacylglycerol and polysaccharides in coffee beans. *Biosci. Biotechnol. Biochem.* **83**, 803–809 (2019).
28. Efthymiopoulos, I. *et al.* Influence of solvent selection and extraction temperature on yield and composition of lipids extracted from spent coffee grounds. *Ind. Crops Prod.* **119**, 49–56 (2018).
29. Atabani, A. E. *et al.* Valorization of spent coffee grounds into biofuels and value-added products: pathway towards integrated bio-refinery. *Fuel* **254**, 115640

(2019).

30. Kasai, N., Konishi, A., Iwai, K. & Maeda, G. Efficient digestion and structural characteristics of cell walls of coffee beans. *J. Agric. Food Chem.* **54**, 6336–6342 (2006).
31. Ballesteros, L. F., Teixeira, J. A. & Mussatto, S. I. Chemical, functional, and structural properties of spent coffee grounds and coffee silverskin. *Food Bioprocess Technol.* **7**, 3493–3503 (2014).
32. Mussatto, S. I., Machado, E. M. S., Martins, S. & Teixeira, J. A. Production, composition, and application of coffee and its industrial residues. *Food Bioprocess Technol.* **4**, 661–672 (2011).
33. Mussatto, S. I., Carneiro, L. M., Silva, J. P. A., Roberto, I. C. & Teixeira, J. A. A study on chemical constituents and sugars extraction from spent coffee grounds. *Carbohydr. Polym.* **83**, 368–374 (2011).
34. Obruca, S., Benesova, P., Kucera, D., Petrik, S. & Marova, I. Biotechnological conversion of spent coffee grounds into polyhydroxyalkanoates and carotenoids. *N. Biotechnol.* **32**, 569–574 (2015).
35. Leonardi, M. *et al.* Characterisation of four popular Polish hop cultivars. *Int. J. Food Sci. Technol.* **48**, 1770–1774 (2013).
36. Haseleu, G. *et al.* Quantitative sensomics profiling of hop-derived bitter compounds throughout a full-scale beer manufacturing process. *J. Agric. Food Chem.* **58**, 7930–7939 (2010).
37. REPORT Hops 2020/2021. *BarthHaas* 1–36 https://www.barthhaas.com/fileadmin/user_upload/kampagnen/barthhaas_bericht/BarthHaas_Report_Hops_2020_21.pdf (2021).
38. Gardea-torresdey, J. *et al.* Use of hop (*Humulus lupulus*) agricultural by-products for the reduction of aqueous lead(II) environmental health hazards. *J. Hazard. Mater.* **91**, 95–112 (2002).
39. Ruggeri, R., Loreti, P. & Rossini, F. Exploring the potential of hop as a dual purpose crop in the Mediterranean environment: shoot and cone yield from nine commercial cultivars. *Eur. J. Agron.* **93**, 11–17 (2018).
40. Zou, Y., Reggy, N. & Yang, Y. Using hop bines as reinforcements for lightweight polypropylene composites. *J. Appl. Polym. Sci.* **116**, 2366–2373 (2010).
41. Reddy, N. & Yang, Y. Properties of natural cellulose fibers from hop stems. *Carbohydr. Polym.* **77**, 898–902 (2009).
42. セルロースナノファイバー 研究と実用化の最前線. (NTS, 2021).

43. Saito, T., Nishiyama, Y., Putaux, J. L., Vignon, M. & Isogai, A. Homogeneous suspensions of individualized microfibrils from TEMPO-catalyzed oxidation of native cellulose. *Biomacromolecules* **7**, 1687–1691 (2006).
44. Isogai, A. & Bergström, L. Preparation of cellulose nanofibers using green and sustainable chemistry. *Curr. Opin. Green Sustain. Chem.* **12**, 15–21 (2018).
45. Isogai, A. TEMPO酸化セルロースナノファイバーの調製と特性解析 (Preparation and Characterization of TEMPO-Oxidized Cellulose Nanofibers）. 東京大学農学部演習林報告 **126**, 1–43 (2011).
46. Shinoda, R., Saito, T., Okita, Y. & Isogai, A. Relationship between length and degree of polymerization of TEMPO-oxidized cellulose nanofibrils. *Biomacromolecules* **13**, 842–849 (2012).
47. McClements, D. J. Critical review of techniques and methodologies for characterization of emulsion stability. *Crit. Rev. Food Sci. Nutr.* **47**, 611–649 (2007).
48. Ramsden, W. Separation of solids in the surface-layers of solutions and ‘suspensions’ (observations on surface-membranes, bubbles, emulsions, and mechanical coagulation).—Preliminary account. *Proc. R. Soc.* **72**, 156–164 (1903).
49. Pickering, S. U. CXCVI.—Emulsions. *J. Chem. Soc. Trans.* **91**, 2001–2021 (1907).
50. Wu, J. & Ma, G. H. Recent studies of Pickering emulsions: particles make the difference. *Small* **12**, 4633–4648 (2016).
51. Binks, B. P. & Lumsdon, S. O. Influence of particle wettability on the type and stability of surfactant-free emulsions. *Langmuir* **16**, 8622–8631 (2000).
52. Cui, F. *et al.* Polysaccharide-based Pickering emulsions: formation, stabilization and applications. *Food Hydrocoll.* **119**, 106812 (2021).
53. Binks, B. P. Particles as surfactants—similarities and differences. *Curr. Opin. Colloid Interface Sci.* **7**, 21–41 (2002).
54. Briggs, T. R. Emulsions with finely divided solids. *Ind. Eng. Chem.* **13**, 1008–1010 (1921).
55. Binks, B. P. & Lumsdon, S. O. Pickering emulsions stabilized by monodisperse latex particles: effects of particle size. *Langmuir* **17**, 4540–4547 (2001).
56. Levine, S., Bowen, B. D. & Partridge, S. J. Stabilization of emulsions by fine particles I . partitioning of particles between continuous phase and oil/water interface. *Colloids and Surfaces* **38**, 325–343 (1989).
57. Melle, S., Lask, M. & Fuller, G. G. Pickering emulsions with controllable

stability. *Langmuir* **21**, 2158–2162 (2005).

58. Chen, T., Colver, P. J. & Bon, S. A. F. Organic–inorganic hybrid hollow spheres prepared from TiO_2-stabilized Pickering emulsion polymerization. *Adv. Mater.* **19**, 2286–2289 (2007).
59. Wang, H. & Hobbie, E. K. Amphiphobic carbon nanotubes as macroemulsion surfactants. *Langmuir* **19**, 3091–3093 (2003).
60. Costa, C. *et al.* Emulsion formation and stabilization by biomolecules: the leading role of cellulose. *Polymers* **11**, 1570 (2019).
61. Tang, C. *et al.* Pickering emulsions stabilized by hydrophobically modified nanocellulose containing various structural characteristics. *Cellulose* **26**, 7753–7767 (2019).
62. Hu, Y. Q. *et al.* Fabrication and characterization of novel Pickering emulsions and Pickering high internal emulsions stabilized by gliadin colloidal particles. *Food Hydrocoll.* **61**, 300–310 (2016).
63. Ding, M. *et al.* Effect of preparation factors and storage temperature on fish oil-loaded crosslinked gelatin nanoparticle pickering emulsions in liquid forms. *Food Hydrocoll.* **95**, 326–335 (2019).
64. Lin, Q., Liang, R., Zhong, F., Ye, A. & Singh, H. Effect of degree of octenyl succinic anhydride (OSA) substitution on the digestion of emulsions and the bioaccessibility of β-carotene in OSA-modified-starch-stabilized-emulsions. *Food Hydrocoll.* **84**, 303–312 (2018).
65. Dai, H. *et al.* Co-stabilization and properties regulation of Pickering emulsions by cellulose nanocrystals and nanofibrils from lemon seeds. *Food Hydrocoll.* **120**, 106884 (2021).
66. Gestranius, M., Stenius, P., Kontturi, E., Sjöblom, J. & Tammelin, T. Phase behaviour and droplet size of oil-in-water Pickering emulsions stabilised with plant-derived nanocellulosic materials. *Colloids Surf. A* **519**, 60–70 (2017).
67. Li, X. *et al.* Stabilization of Pickering emulsions with cellulose nanofibers derived from oil palm fruit bunch. *Cellulose* **27**, 839–851 (2020).
68. Lu, Y., Li, J., Ge, L., Xie, W. & Wu, D. Pickering emulsion stabilized with fibrous nanocelluloses: insight into fiber flexibility-emulsifying capacity relations. *Carbohydr. Polym.* **255**, 117483 (2021).
69. Guo, S. *et al.* Depletion effects and stabilization of Pickering emulsions prepared from a dual nanocellulose system. *ACS Sustain. Chem. Eng.* **10**, 9066–9076 (2022).
70. Kedzior, S. A., Gabriel, V. A., Dubé, M. A. & Cranston, E. D. Nanocellulose in

emulsions and heterogeneous water-based polymer systems: a review. *Adv. Mater.* **33**, 2002404 (2021).

71. Zhu, M. *et al.* Recent development in food emulsion stabilized by plant-based cellulose nanoparticles. *Curr. Opin. Colloid Interface Sci.* **56**, 101512 (2021).
72. Fujisawa, S., Togawa, E. & Kuroda, K. Nanocellulose-stabilized Pickering emulsions and their applications. *Sci. Technol. Adv. Mater.* **18**, 959–971 (2017).
73. Kalashnikova, I., Bizot, H., Cathala, B. & Capron, I. New Pickering emulsions stabilized by bacterial cellulose nanocrystals. *Langmuir* **27**, 7471–7479 (2011).
74. Kalashnikova, I., Bizot, H., Cathala, B. & Capron, I. Modulation of cellulose nanocrystals amphiphilic properties to stabilize oil/water interface. *Biomacromolecules* **13**, 267–275 (2012).
75. Aveyard, R., Binks, B. P. & Clint, J. H. Emulsions stabilised solely by colloidal particles. *Adv. Colloid Interface Sci.* **100–102**, 503–546 (2003).
76. Kalashnikova, I., Bizot, H., Bertoncini, P., Cathala, B. & Capron, I. Cellulosic nanorods of various aspect ratios for oil in water Pickering emulsions. *Soft Matter* **9**, 952–959 (2013).
77. Bai, L., Huan, S., Xiang, W. & Rojas, O. J. Pickering emulsions by combining cellulose nanofibrils and nanocrystals: phase behavior and depletion stabilization. *Green Chem.* **20**, 1571–1582 (2018).
78. Du Le, H., Loveday, S. M., Singh, H. & Sarkar, A. Pickering emulsions stabilised by hydrophobically modified cellulose nanocrystals: responsiveness to pH and ionic strength. *Food Hydrocoll.* **99**, 105344 (2020).
79. Chen, Q. H. *et al.* Surface modification improves fabrication of pickering high internal phase emulsions stabilized by cellulose nanocrystals. *Food Hydrocoll.* **75**, 125–130 (2018).
80. Seo, H. M., Seo, M., Shin, K., Choi, S. & Kim, J. W. Bacterial cellulose nanofibrils-armored Pickering emulsions with limited influx of metal ions. *Carbohydr. Polym.* **258**, 117730 (2021).
81. Teo, S. H. *et al.* Review of functional aspects of nanocellulose-based Pickering emulsifier for non-toxic application and its colloid stabilization mechanism. *Molecules* **27**, 7170 (2022).
82. Saelices, C. J. & Capron, I. Design of Pickering micro- and nanoemulsions based on the structural characteristics of nanocelluloses. *Biomacromolecules* **19**, 460–469 (2018).
83. Silva, C. E. P., Tam, K. C., Bernardes, J. S. & Loh, W. Double stabilization mechanism of O/W Pickering emulsions using cationic nanofibrillated cellulose.

J. Colloid Interface Sci. **574**, 207–216 (2020).

84. Bai, L. *et al.* Adsorption and assembly of cellulosic and lignin colloids at oil/water interfaces. *Langmuir* **35**, 571–588 (2019).
85. Tsabet, È. & Fradette, L. Effect of the properties of oil, particles, and water on the production of Pickering emulsions. *Chem. Eng. Res. Des.* **97**, 9–17 (2015).
86. Goi, Y. *et al.* Dual functions of TEMPO-oxidized cellulose nanofibers in oil-in-water emulsions: a Pickering emulsifier and a unique dispersion stabilizer. *Langmuir* **35**, 10920–10926 (2019).
87. Albert, C. *et al.* Pickering emulsions: preparation processes, key parameters governing their properties and potential for pharmaceutical applications. *J. Control. Release* **309**, 302–332 (2019).
88. Winuprasith, T. & Suphantharika, M. Microfibrillated cellulose from mangosteen (*Garcinia mangostana L.*) rind: preparation, characterization, and evaluation as an emulsion stabilizer. *Food Hydrocoll.* **32**, 383–394 (2013).
89. Winuprasith, T. & Suphantharika, M. Properties and stability of oil-in-water emulsions stabilized by microfibrillated cellulose from mangosteen rind. *Food Hydrocoll.* **43**, 690–699 (2015).
90. Perrin, L., Gillet, G., Gressin, L. & Desobry, S. Interest of Pickering emulsions for sustainable micro/nanocellulose in food and cosmetic applications. *Polymers* **12**, 2385 (2020).
91. Wen, C., Yuan, Q., Liang, H. & Vriesekoop, F. Preparation and stabilization of D-limonene Pickering emulsions by cellulose nanocrystals. *Carbohydr. Polym.* **112**, 695–700 (2014).
92. Angkuratipakorn, T., Sriprai, A., Tantrawong, S., Chaiyasit, W. & Singkhonrat, J. Fabrication and characterization of rice bran oil-in-water Pickering emulsion stabilized by cellulose nanocrystals. *Colloids Surf. A* **522**, 310–319 (2017).
93. Kasiri, N. & Fathi, M. Production of cellulose nanocrystals from pistachio shells and their application for stabilizing Pickering emulsions. *Int. J. Biol. Macromol.* **106**, 1023–1031 (2018).
94. Ni, Y., Li, J. & Fan, L. Production of nanocellulose with different length from ginkgo seed shells and applications for oil in water Pickering emulsions. *Int. J. Biol. Macromol.* **149**, 617–626 (2020).
95. Costa, A. L. R., Gomes, A., Tibolla, H., Menegalli, F. C. & Cunha, R. L. Cellulose nanofibers from banana peels as a Pickering emulsifier: high-energy emulsification processes. *Carbohydr. Polym.* **194**, 122–131 (2018).
96. Li, Q. *et al.* Cellulose nanofibrils from *Miscanthus floridulus* straw as green

particle emulsifier for O/W Pickering emulsion. *Food Hydrocoll.* **97**, 105214 (2019).

97. Franco, S. T. *et al.* Production and technological characteristics of avocado oil emulsions stabilized with cellulose nanofibrils isolated from agroindustrial residues. *Colloids Surf. A* **586**, 124263 (2020).
98. Wen, J. *et al.* Cellulose nanofiber from pomelo spongy tissue as a novel particle stabilizer for Pickering emulsion. *Int. J. Biol. Macromol.* **224**, 1439–1449 (2023).
99. Reif, B., Ashbrook, S. E., Emsley, L. & Hong, M. Solid-state NMR spectroscopy. *Nat Rev Methods Prim.* **1**, 2 (2021).
100. Gupta, A. Development and characterisation of advanced MRI contrast agents. (University of Western Sydney, 2015).
101. Fisher, J. *Modern NMR techniques for synthetic chemistry. Modern NMR Techniques for Synthetic Chemistry* (CRC Press, 2014).
102. Keeler, J. *Understanding NMR Spectroscopy*. (Wiley, 2010).
103. Price, W. S. An NMR study of diffusion, viscosity, and transport of small molecules in human erythrocytes. (University of Sydney, 1990).
104. Gupta, A., Stait-Gardner, T. & Price, W. S. Is it time to forgo the use of the terms ‘spin-lattice’ and ‘spin-spin’ relaxation in NMR and MRI? *J. Phys. Chem. Lett.* **12**, 6305–6312 (2021).
105. Vold, R. L., Waugh, J. S., Klein, M. P. & Phelps, D. E. Measurement of spin relaxation in complex systems. *J. Chem. Phys.* **48**, 3831–3832 (1968).
106. Meiboom, S. & Gill, D. Modified spin-echo method for measuring nuclear relaxation times. *Rev. Sci. Instrum.* **29**, 688–691 (1958).
107. Laws, D. D., Bitter, H.-M. L. & Jerschow, A. Solid-state NMR spectroscopic methods in chemistry. *Angew. Chem. Int. Ed* **41**, 3096–3129 (2002).
108. Andrew, E., Bradbury, A. & Eades, R. Nuclear magnetic resonance spectra from a crystal rotated at high speed. *Nature* **182**, 1659 (1958).
109. J, S. & Stejskal, E. Carbon-13 nuclear magnetic resonance of polymers spinning at the magic angle. *J. Am. Chem. Soc.* **98**, 1031–1032 (1976).
110. Pines, A., Gibby, M. & Waugh, J. Proton-enhanced NMR of dilute spins in solids. *J. Chem. Phys.* **59**, 569 (1973).
111. 齊藤肇, 安藤勲 & 内藤晶. *NMR分光学—基礎と応用—*. (東京化学同人, 2008).
112. Price, W. S. Pulsed-field gradient nuclear magnetic resonance as a tool for studying translational diffusion: part 1. basic theory. *Concepts Magn. Reson.* **9**, 299–336 (1997).

113. Price, W. S. *NMR Studies of Translational Motion: Principles and Applications*. (Cambridge University Press, 2009).

114. Stejskal, E. O. & Tanner, J. E. Spin diffusion measurements: Spin echoes in the presence of a time-dependent field gradient. *J. Chem. Phys.* **42**, 288–292 (1965).

115. Willis, S. A., Stait-Gardner, T., Zheng, G. & Price, W. S. Diffusion: Denition, Description and Measurement. in *Modern NMR Techniques for Synthetic Chemistry* (ed. Fisher, J.) 125–175 (CRC Press, 2014).

116. Price, W. S. & Kuchel, P. W. Effect of nonrectangular field gradient pulses in the Stejskal and Tanner (diffusion) pulse sequence. *J. Magn. Reson.* **94**, 133–139 (1991).

117. Price, W. S. Pulsed-field gradient nuclear magnetic resonance as a tool for studying translational diffusion: part II. experimental aspects. *Concepts Magn. Reson.* **10**, 197–237 (1998).

118. Tanner, J. E. Use of the stimulated echo in NMR diffusion studies. *J. Chem. Phys.* **52**, 2523–2526 (1970).

119. Callaghan, P. T. *Principles of Nuclear Magnetic Resonance Microscopy*. (Oxford University Press, 1991).

120. Price, W. S. NMR imaging. *Annu. Reports NMR Spectrosc.* **35**, 139–216 (1998).

121. Gupta, A., Stait-Gardner, T. & Price, W. S. NMR imaging and diffusion. *Adsorption* **27**, 503–533 (2021).

122. Talagala, S. L. & Lowe, I. J. Introduction to magnetic resonance imaging. *Concepts Magn. Reson.* **3**, 145–159 (1991).

123. Currie, S., Hoggard, N., Craven, I. J., Hadjivassiliou, M. & Wilkinson, I. D. Understanding MRI: basic MR physics for physicians. *Postgrad. Med. J.* **89**, 209–223 (2013).

124. Hennig, J., Nauerth, A. & Friedburg, H. RARE imaging: a fast imaging method for clinical MR. *Magn. Reson. Med.* **3**, 823–833 (1986).

125. Edzes, H. T., Van Dusschoten, D. & Van As, H. Quantitative T_2 imaging of plant tissues by means of multi-echo MRI microscopy. *Magn. Reson. Imaging* **16**, 185–196 (1998).

126. Willis, S. A. *et al.* Expanding NMR Versatility. in *Diffusive Spreading in Nature, Technology and Society* 247–277 (Springer International Publishing, 2023).

127. World coffee consumption. *International Coffee Organization* http://www.ico.org/prices/new-consumption-table.pdf (2020).

128. Cruz, R. *et al.* Espresso coffee residues: a valuable source of unextracted compounds. *J. Agric. Food Chem.* **60**, 7777–7784 (2012).

129. Plaza, M. G., González, A. S., Pevida, C., Pis, J. J. & Rubiera, F. Valorisation of spent coffee grounds as CO_2 adsorbents for postcombustion capture applications. *Appl. Energy* **99**, 272–279 (2012).
130. Campos-Vega, R., Loarca-Piña, G., Vergara-Castañeda, H. A. & Oomah, B. D. Spent coffee grounds: a review on current research and future prospects. *Trends Food Sci. Technol.* **45**, 24–36 (2015).
131. Vítězová, M. *et al.* The possibility of using spent coffee grounds to improve wastewater treatment due to respiration activity of microorganisms. *Appl. Sci.* **9**, 3155 (2019).
132. Dang, C.-H. & Nguyen, T.-D. Physicochemical characterization of *Robusta* spent coffee ground oil for biodiesel manufacturing. *Waste Biomass Valorization* **10**, 2703–2712 (2019).
133. Karmee, S. K. A spent coffee grounds based biorefinery for the production of biofuels, biopolymers, antioxidants and biocomposites. *Waste Manag.* **72**, 240–254 (2018).
134. Kookos, I. K. Technoeconomic and environmental assessment of a process for biodiesel production from spent coffee grounds (SCGs). *Resour. Conserv. Recycl.* **134**, 156–164 (2018).
135. Jenkins, R. W. *et al.* Production of biodiesel from Vietnamese waste coffee beans: biofuel yield, saturation and stability are all elevated compared with conventional coffee biodiesel. *Waste Biomass Valorization* **8**, 1237–1245 (2017).
136. Arya, M. & Rao, L. J. M. An impression of coffee carbohydrates. *Crit. Rev. Food Sci. Nutr.* **47**, 51–67 (2007).
137. Saito, T., Kimura, S., Nishiyama, Y. & Isogai, A. Cellulose nanofibers prepared by TEMPO-mediated oxidation of native cellulose. *Biomacromolecules* **8**, 2485–2491 (2007).
138. Chen, Y. *et al.* Comparative characteristics of TEMPO-oxidized cellulose nanofibers and resulting nanopapers from bamboo, softwood, and hardwood pulps. *Cellulose* **24**, 4831–4844 (2017).
139. Panyasiri, P., Yingkamhaeng, N., Lam, N. T. & Sukyai, P. Extraction of cellulose nanofibrils from amylase-treated cassava bagasse using high-pressure homogenization. *Cellulose* **25**, 1757–1768 (2018).
140. Balakrishnan, P., Sreekala, M. S., Kunaver, M., Huskić, M. & Thomas, S. Morphology, transport characteristics and viscoelastic polymer chain confinement in nanocomposites based on thermoplastic potato starch and cellulose nanofibers from pineapple leaf. *Carbohydr. Polym.* **169**, 176–188

(2017).
141. Pelissari, F. M., Sobral, P. J. D. A. & Menegalli, F. C. Isolation and characterization of cellulose nanofibers from banana peels. *Cellulose* **21**, 417–432 (2014).
142. Rohaizu, R. & Wanrosli, W. D. Sono-assisted TEMPO oxidation of oil palm lignocellulosic biomass for isolation of nanocrystalline cellulose. *Ultrason. Sonochem.* **34**, 631–639 (2017).
143. Ling, Z. *et al.* Effects of ball milling on the structure of cotton cellulose. *Cellulose* **26**, 305–328 (2019).
144. Fu, L. *et al.* Rapid and accurate determination of the lignin content of lignocellulosic biomass by solid-state NMR. *Fuel* **141**, 39–45 (2015).
145. Liitiä, T. *et al.* Cellulose crystallinity and ordering of hemicelluloses in pine and birch pulps as revealed by solid-state NMR spectroscopic methods. *Cellulose* **10**, 307–316 (2003).
146. Saito, T., Shibata, I., Isogai, A., Suguri, N. & Sumikawa, N. Distribution of carboxylate groups introduced into cotton linters by the TEMPO-mediated oxidation. *Carbohydr. Polym.* **61**, 414–419 (2005).
147. Park, S., Baker, J. O., Himmel, M. E., Parilla, P. A. & Johnson, D. K. Cellulose crystallinity index: measurement techniques and their impact on interpreting cellulase performance. *Biotechnol. Biofuels* **3**, 10 (2010).
148. Poletto, M., Pistor, V. & Zattera, A. J. Structural Characteristics and Thermal Properties of Native Cellulose. in *Cellulose - Fundamental Aspects* (eds. Van de Ven, T. & Godbout, L.) 45–68 (IntechOpen, 2013).
149. French, A. D. Idealized powder diffraction patterns for cellulose polymorphs. *Cellulose* **21**, 885–896 (2014).
150. Scherrer, P. Bestimmung der Größe und der inneren Struktur von Kolloidteilchen mittels Röntgenstrahlen. *Nachr Ges Wiss Göttingen* **26**, 98–100 (1918).
151. Lichtenstein, K. & Lavoine, N. Toward a deeper understanding of the thermal degradation mechanism of nanocellulose. *Polym. Degrad. Stab.* **146**, 53–60 (2017).
152. Fukuzumi, H., Saito, T., Okita, Y. & Isogai, A. Thermal stabilization of TEMPO-oxidized cellulose. *Polym. Degrad. Stab.* **95**, 1502–1508 (2010).
153. Cao, X., Ding, B., Yu, J. & Al-Deyab, S. S. Cellulose nanowhiskers extracted from TEMPO-oxidized jute fibers. *Carbohydr. Polym.* **90**, 1075–1080 (2012).
154. Ohno, T. & Nishio, Y. Estimation of miscibility and interaction for cellulose acetate and butyrate blends with *N*-vinylpyrrolidone copolymers. *Macromol.*

Chem. Phys. **208**, 622–634 (2007).

155. Kobayashi, M., Ando, I., Ishii, T. & Amiya, S. Structural and dynamical studies of poly(vinyl alcohol) gels by high-resolution solid-state ^{13}C NMR spectroscopy. *J. Mol. Struct.* **440**, 155–164 (1998).
156. Masuda, K., Kaji, H. & Horii, F. CP/MAS ^{13}C NMR analyses of hydrogen bonding and the chain conformation in the crystalline and noncrystalline regions for poly(vinyl alcohol) films. *J. Polym. Sci. Part B Polym. Phys.* **38**, 1–9 (2000).
157. Comotti, A., Simonutti, R. & Sozzani, P. Morphology of the poly(vinyl alcohol)–poly(vinyl acetate) copolymer in macrodefect-free composites : a ^{13}C magic-angle-spinning nuclear magnetic resonance and ^{1}H spin-diffusion study. *J. Mater. Sci.* **32**, 4237–4245 (1997).
158. Fukuzumi, H., Saito, T., Iwata, T., Kumamoto, Y. & Isogai, A. Transparent and high gas barrier films of cellulose nanofibers prepared by TEMPO-mediated oxidation. *Biomacromolecules* **10**, 162–165 (2009).
159. Lee, S. Y. *et al.* Nanocellulose reinforced PVA composite films: effects of acid treatment and filler loading. *Fibers Polym.* **10**, 77–82 (2009).
160. Börjesson, M. & Westman, G. Crystalline nanocellulose — preparation, modification, and properties. in *Cellulose - Fundamental Aspects and Current Trends* (ed. Poletto, M.) 159–191 (IntechOpen, 2015).
161. Kuramae, R., Saito, T. & Isogai, A. TEMPO-oxidized cellulose nanofibrils prepared from various plant holocelluloses. *React. Funct. Polym.* **85**, 126–133 (2014).
162. Wise, L. E., Murphy, M. & D'Addieco, A. A. Chlorite holocellulose, its fractionation and bearing on summative wood analysis and on studies on the hemicelluloses. *Pap Trade J* **122**, 35–43 (1946).
163. Horii, F., Hirai, A. & Kitamaru, R. Solid-state ^{13}C-NMR study of conformations of oligosaccharides and cellulose - conformation of CH_2OH group about the exo-cyclic C-C bond. *Polym. Bull.* **10**, 357–361 (1983).
164. Miyamoto, H., Yamane, C. & Ueda, K. Structural changes in the molecular sheets along (hk0) planes derived from cellulose I_β by molecular dynamics simulations. *Cellulose* **20**, 1089–1098 (2013).
165. Phyo, P., Wang, T., Yang, Y., O'Neill, H. & Hong, M. Direct determination of hydroxymethyl conformations of plant cell wall cellulose using ^{1}H polarization transfer solid-state NMR. *Biomacromolecules* **19**, 1485–1497 (2018).
166. Yang, H. *et al.* Structural factors affecting ^{13}C NMR chemical shifts of cellulose: a computational study. *Cellulose* **25**, 23–36 (2018).

167. Ioelovich, M. Physicochemical methods for determination of cellulose crystallinity. *ChemXpress* **9**, 245–251 (2016).

168. Park, S., Johnson, D. K., Ishizawa, C. I., Parilla, P. A. & Davis, M. F. Measuring the crystallinity index of cellulose by solid state ^{13}C nuclear magnetic resonance. *Cellulose* **16**, 641–647 (2009).

169. Rongpipi, S., Ye, D., Gomez, E. D. & Gomez, E. W. Progress and opportunities in the characterization of cellulose – an important regulator of cell wall growth and mechanics. *Front. Plant Sci.* **9**, 1894 (2019).

170. Larsson, P. T., Wickholm, K. & Iversen, T. A CP/MAS ^{13}C NMR investigation of molecular ordering in celluloses. *Carbohydr. Res.* **302**, 19–25 (1997).

171. Kirui, A. *et al.* Atomic resolution of cotton cellulose structure enabled by dynamic nuclear polarization solid-state NMR. *Cellulose* **26**, 329–339 (2019).

172. Daicho, K., Saito, T., Fujisawa, S. & Isogai, A. The crystallinity of nanocellulose: dispersion-induced disordering of the grain boundary in biologically structured cellulose. *ACS Appl. Nano Mater.* **1**, 5774–5785 (2018).

173. Okita, Y., Saito, T. & Isogai, A. Entire surface oxidation of various cellulose microfibrils by TEMPO-mediated oxidation. *Biomacromolecules* **11**, 1696–1700 (2010).

174. Puangsin, B., Yang, Q., Saito, T. & Isogai, A. Comparative characterization of TEMPO-oxidized cellulose nanofibril films prepared from non-wood resources. *Int. J. Biol. Macromol.* **59**, 208–213 (2013).

175. *Espresso Coffee: The Science of Quality*. (Elsevier Academic Press, 1995).

176. Yang, E., Qin, X. & Wang, S. Electrospun crosslinked polyvinyl alcohol membrane. *Mater. Lett.* **62**, 3555–3557 (2008).

177. Khalil, H. P. S. A. *et al.* Production and modification of nanofibrillated cellulose using various mechanical processes: a review. *Carbohydr. Polym.* **99**, 649–665 (2014).

178. REPORT Hops 2019/2020. *BarthHaas* 1–36 https://www.hops.com.au/downloads/news-events/BarthHaas-2019-2020-Hop-Report.pdf (2020).

179. Rybáček, V. Biological basis of hop production. in *Hop Production, Developments in Crop Science 16* 25–119 (1991).

180. Donner, M., Gohier, R. & de Vries, H. A new circular business model typology for creating value from agro-waste. *Sci. Total Environ.* **716**, 137065 (2020).

181. Beltrán-ramírez, F. *et al.* Agro-Industrial Waste Revalorization: The Growing Biorefinery. in *Biomass for Bioenergy - Recent Trends and Future Challenges*

(ed. Abomohra, A.) (IntechOpen, 2019).

182. Azelee, N. I. W., Manas, N. H. A., Dailin, D. J., Ramli, A. N. M. & Shaarani, S. M. Biological Treatment of Agro-Industrial Waste. in *Valorisation of Agro-industrial Residues – Volume I: Biological Approaches* (eds. Zakaria, Z. A., Boopathy, R. & Dib, J. R.) 59–79 (Springer Nature Switzerland AG, 2020).
183. Sathishkumar, T. P., Navaneethakrishnan, P., Shankar, S., Rajasekar, R. & Rajini, N. Characterization of natural fiber and composites - a review. *J. Reinf. Plast. Compos.* **32**, 1457–1476 (2013).
184. Chirayil, C. J., Mathew, L. & Thomas, S. Review of recent research in nano cellulose preparation from different lignocellulosic fibers. *Rev. Adv. Mater. Sci.* **37**, 20–28 (2014).
185. Tao, P., Zhang, Y., Wu, Z., Liao, X. & Nie, S. Enzymatic pretreatment for cellulose nanofibrils isolation from bagasse pulp: transition of cellulose crystal structure. *Carbohydr. Polym.* **214**, 1–7 (2019).
186. Nie, S. *et al.* Enzymatic and cold alkaline pretreatments of sugarcane bagasse pulp to produce cellulose nanofibrils using a mechanical method. *Ind. Crops Prod.* **124**, 435–441 (2018).
187. Foster, E. J. *et al.* Current characterization methods for cellulose nanomaterials. *Chem. Soc. Rev.* **47**, 2609–2679 (2018).
188. Shih, Y. F., Chou, M. Y., Chang, W. C., Lian, H. Y. & Chen, C. M. Completely biodegradable composites reinforced by the cellulose nanofibers of pineapple leaves modified by eco-friendly methods. *J. Polym. Res.* **24**, 209 (2017).
189. Meng, F. *et al.* Extraction and characterization of cellulose nanofibers and nanocrystals from liquefied banana pseudo-stem residue. *Compos. Part B Eng.* **160**, 341–347 (2019).
190. Yu, B., Zeng, X., Wang, L. & Regenstein, J. M. Preparation of nanofibrillated cellulose from grapefruit peel and its application as fat substitute in ice cream. *Carbohydr. Polym.* **254**, 117415 (2020).
191. Kanai, N. *et al.* Structural characterization of cellulose nanofibers isolated from spent coffee grounds and their composite films with poly(vinyl alcohol): a new non-wood source. *Cellulose* **27**, 5017–5028 (2020).
192. Abe, K. & Yano, H. Comparison of the characteristics of cellulose microfibril aggregates of wood, rice straw and potato tuber. *Cellulose* **16**, 1017–1023 (2009).
193. Fillat, Ú. *et al.* Assessing cellulose nanofiber production from olive tree pruning residue. *Carbohydr. Polym.* **179**, 252–261 (2018).
194. Miao, Z., Grift, T. E., Hansen, A. C. & Ting, K. C. Energy requirement for

comminution of biomass in relation to particle physical properties. *Ind. Crop. Prod.* **33**, 504–513 (2011).

195. Kvien, I., Tanem, B. S. & Oksman, K. Characterization of cellulose whiskers and their nanocomposites by atomic force and electron microscopy. *Biomacromolecules* **6**, 3160–3165 (2005).
196. Usov, I. *et al.* Understanding nanocellulose chirality and structure-properties relationship at the single fibril level. *Nat. Commun.* **6**, 7564 (2015).
197. Mattos, B. D., Tardy, B. L. & Rojas, O. J. Accounting for substrate interactions in the measurement of the dimensions of cellulose nanofibrils. *Biomacromolecules* **20**, 2657–2665 (2019).
198. Brinkmann, A. *et al.* Correlating cellulose nanocrystal particle size and surface area. *Langmuir* **32**, 6105–6114 (2016).
199. Habets, S., De Wild, P. J., Huijgen, W. J. J. & Van Eck, E. R. H. The influence of thermochemical treatments on the lignocellulosic structure of wheat straw as studied by natural abundance ^{13}C NMR. *Bioresour. Technol.* **146**, 585–590 (2013).
200. Melkior, T., Barthomeuf, C. & Bardet, M. Inputs of solid-state NMR to evaluate and compare thermal reactivity of pine and beech woods under torrefaction conditions and modified atmosphere. *Fuel* **187**, 250–260 (2017).
201. Chen, X. *et al.* Structural characterization and osteogenic bioactivities of a novel *Humulus lupulus* polysaccharide. *Food Funct.* **11**, 1165–1175 (2020).
202. Kang, X. *et al.* Lignin-polysaccharide interactions in plant secondary cell walls revealed by solid-state NMR. *Nat. Commun.* **10**, 347 (2019).
203. Colas, H. *et al.* Whewellite, $CaC_2O_4 \cdot H_2O$: structural study by a combined NMR, crystallography and modelling approach. *CrystEngComm* **15**, 8840–8847 (2013).
204. Perez-Pimienta, J. A. *et al.* Characterization of agave bagasse as a function of ionic liquid pretreatment. *Biomass and Bioenergy* **75**, 180–188 (2015).
205. Tooulakou, G. *et al.* Alarm photosynthesis: calcium oxalate crystals as an internal CO_2 source in plants. *Plant Physiol.* **171**, 2577–2585 (2016).
206. Faradilla, R. H. F. *et al.* Characteristics of a free-standing film from banana pseudostem nanocellulose generated from TEMPO-mediated oxidation. *Carbohydr. Polym.* **174**, 1156–1163 (2017).
207. Wen, Y. *et al.* Preparation and characterization of lignin-containing cellulose nanofibril from poplar high-yield pulp via TEMPO-mediated oxidation and homogenization. *ACS Sustain. Chem. Eng.* **7**, 6131–6139 (2019).
208. Shi, A., Feng, X., Wang, Q. & Adhikari, B. Pickering and high internal phase

Pickering emulsions stabilized by protein-based particles: a review of synthesis, application and prospective. *Food Hydrocoll.* **109**, 106117 (2020).

209. Lu, Y. *et al.* Rheology of the sesame oil-in-water emulsions stabilized by cellulose nanofibers. *Food Hydrocoll.* **94**, 114–127 (2019).

210. Yang, Y. *et al.* An overview of Pickering emulsions: solid-particle materials, classification, morphology, and applications. *Front. Pharmacol.* **8**, 287 (2017).

211. Jiang, H., Sheng, Y. & Ngai, T. Pickering emulsions: versatility of colloidal particles and recent applications. *Curr. Opin. Colloid Interface Sci.* **49**, 1–15 (2020).

212. Ribeiro, E. F., Morell, P., Nicoletti, V. R., Quiles, A. & Hernando, I. Protein- and polysaccharide-based particles used for Pickering emulsion stabilisation. *Food Hydrocoll.* **119**, 106839 (2021).

213. Chen, Y. *et al.* Lignocellulose nanocrystals from pineapple peel: preparation, characterization and application as efficient Pickering emulsion stabilizers. *Food Res. Int.* **150**, 110738 (2021).

214. Otoni, C. G. *et al.* The food-materials nexus: next generation bioplastics and advanced materials from agri-food residues. *Adv. Mater.* **33**, 2102520 (2021).

215. Kanai, N. *et al.* Upcycling of waste hop stems into cellulose nanofibers: isolation and structural characterization. *ACS Agric. Sci. Technol.* **1**, 347–354 (2021).

216. Dell'agli, M. & Bosisio, E. Minor polar compounds of olive oil: composition, factors of variability and bioactivity. *Stud. Nat. Prod. Chem.* **27**, 697–734 (2002).

217. Stefanoudaki, E., Kotsifaki, F. & Koutsaftakis, A. Classification of virgin olive oils of the two major Cretan cultivars based on their fatty acid composition. *J. Am. Oil Chem. Soc.* **76**, 623–626 (1999).

218. Merkus, H. G. *Particle Size Measurements: Fundamentals, Practice, Quality*. (Springer Science+Business Media B.V, 2009).

219. Puangsin, B., Soeta, H., Saito, T. & Isogai, A. Characterization of cellulose nanofibrils prepared by direct TEMPO-mediated oxidation of hemp bast. *Cellulose* **24**, 3767–3775 (2017).

220. Chutipongtanate, S., Chaiyarit, S. & Thongboonkerd, V. Citrate, not phosphate, can dissolve calcium oxalate monohydrate crystals and detach these crystals from renal tubular cells. *Eur. J. Pharmacol.* **689**, 219–225 (2012).

221. Shang, Y., Xu, M., Zhang, G. & Ouyang, J. Concave urinary crystallines: direct evidence of calcium oxalate crystals dissolution by citrate *in vivo*. *Bioinorg. Chem. Appl.* **2013**, 637617 (2013).

222. Liao, J., Pham, K. A. & Breedveld, V. Rheological characterization and modeling

of cellulose nanocrystal and TEMPO-oxidized cellulose nanofibril suspensions. *Cellulose* **27**, 3741–3757 (2020).

223. Zhou, Y., Fujisawa, S., Saito, T. & Isogai, A. Characterization of concentration-dependent gelation behavior of aqueous 2,2,6,6-tetramethylpiperidine-1-oxyl-cellulose nanocrystal dispersions using dynamic light scattering. *Biomacromolecules* **20**, 750–757 (2019).
224. Bai, L. *et al.* Self-assembled networks of short and long chitin nanoparticles for oil/water interfacial superstabilization. *ACS Sustain. Chem. Eng.* **7**, 6497–6511 (2019).
225. Qian, X., Lu, Y., Xie, W. & Wu, D. Viscoelasticity of olive oil/water Pickering emulsions stabilized with starch nanocrystals. *Carbohydr. Polym.* **230**, 115575 (2020).
226. Mazeau, K. & Wyszomirski, M. Modelling of Congo red adsorption on the hydrophobic surface of cellulose using molecular dynamics. *Cellulose* **19**, 1495–1506 (2012).
227. Huang, Y., Liu, H., Liu, S. & Li, S. Cinnamon *cassia* oil emulsions stabilized by chitin nanofibrils: physicochemical properties and antibacterial activities. *J. Agric. Food Chem.* **68**, 14620–14631 (2020).
228. Bai, L. *et al.* Impact of polysaccharide molecular characteristics on viscosity enhancement and depletion flocculation. *J. Food Eng.* **207**, 35–45 (2017).
229. Wooster, T. J., Golding, M. & Sanguansri, P. Impact of oil type on nanoemulsion formation and Ostwald ripening stability. *Langmuir* **24**, 12758–12765 (2008).
230. McClements, D. J., Henson, L., Popplewell, L. M., Decker, E. A. & Choi, S. J. Inhibition of Ostwald ripening in model beverage emulsions by addition of poorly water soluble triglyceride oils. *J. Food Sci.* **77**, C33–C38 (2012).
231. Souza, A. G., Ferreira, R. R., Aguilar, E. S. F., Zanata, L. & Rosa, D. S. Cinnamon essential oil nanocellulose-based Pickering emulsions: processing parameters effect on their formation, stabilization, and antimicrobial activity. *Polysaccharides* **2**, 608–625 (2021).
232. Cano-Sarmiento, C. *et al.* Zeta potential of food matrices. *Food Eng. Rev.* **10**, 113–138 (2018).
233. Courtenay, J. C. *et al.* Salt-responsive Pickering emulsions stabilized by functionalized cellulose nanofibrils. *Langmuir* **37**, 6864–6873 (2021).
234. Kanai, N., Sakai, T., Yamada, K., Kumagai, S. & Kawamura, I. Using cellulose nanofibers isolated from waste hop stems to stabilize dodecane or olive oil-in-water Pickering emulsions. *Colloids Surf. A* **653**, 129956 (2022).

235. Söderman, O., Stilbs, P. & Price, W. S. NMR studies of surfactants. *Concepts Magn. Reson. Part A* **23**, 121–135 (2004).

236. Fritz, V., Martirosian, P., Machann, J., Daniels, R. & Schick, F. A comparison of emulsifiers for the formation of oil-in-water emulsions: stability of the emulsions within 9 h after production and MR signal properties. *Magn. Reson. Mater. Physics, Biol. Med.* **35**, 401–410 (2022).

237. Onuki, Y., Kida, C., Funatani, C., Hayashi, Y. & Takayama, K. MRI as a promising tool for evaluation of the stability of cosmetic emulsions. *Int. J. Cosmet. Sci.* **38**, 272–278 (2016).

238. Johns, M. L. & Hollingsworth, K. G. Characterisation of emulsion systems using NMR and MRI. *Prog. Nucl. Magn. Reson. Spectrosc.* **50**, 51–70 (2007).

239. Cai, X., Wang, Y., Du, X., Xing, X. & Zhu, G. Stability of pH-responsive Pickering emulsion stabilized by carboxymethyl starch/xanthan gum combinations. *Food Hydrocoll.* **109**, 106093 (2020).

240. Zhou, C. *et al.* High internal phase Pickering emulsion by Spanish mackerel proteins-procyanidins: application for stabilizing astaxanthin and surimi. *Food Hydrocoll.* **133**, 107999 (2022).

241. Carr, H. Y. & Purcell, E. M. Effects of diffusion on free precession in nuclear magnetic resonance experiments. *Phys. Rev.* 630–638 (1954).

242. Jafari, M., Kadivar, M. & Keramat, J. Detection of adulteration in Iranian olive oils using instrumental (GC, NMR, DSC) methods. *J. Am. Oil Chem. Soc.* **86**, 103–110 (2009).

243. Wang, N. & Xia, Y. Experimental issues in the measurement of multi-component relaxation times in articular cartilage by microscopic MRI. *J. Magn. Reson.* **235**, 15–25 (2013).

244. Zheng, S. K. & Xia, Y. On the measurement of multi-component T_2 relaxation in cartilage by MR spectroscopy and imaging. *Magn. Reson. Imaging* **28**, 537–545 (2010).

245. Kaysan, G. *et al.* Investigation of the surfactant distribution in oil-in-water emulsions during the crystallization of the dispersed phase via nuclear magnetic resonance relaxometry and diffusometry. *Magn. Reson. Chem.* **60**, 1131–1147 (2022).

246. Tanner, J. E. & Stejskal, E. O. Restricted self-diffusion of protons in colloidal systems by the pulsed-gradient, spin-echo method. *J. Chem. Phys.* **46**, 1768–1777 (1968).

247. Dick-Pérez, M. *et al.* Structure and interactions of plant cell-wall polysaccharides

by two- and three-dimensional magic-angle-spinning solid-state NMR. *Biochemistry* **50**, 989–1000 (2011).

248. Mills, R. Self-diffusion in normal and heavy water in the range 1-45°. *J. Phys. Chem.* **77**, 685–688 (1973).

Acknowledgement

First and foremost, I would like to express my sincere gratitude to my supervisor, Associate Professor Izuru Kawamura. Throughout my undergraduate and PhD, he has been shown excellent guidance, encouragement, and support as my closest mentor in research. Kawamura-sensei taught me to enjoy research with unforgettable moments to discover something new or solve the difficulty. I am truly fortunate to have such a supportive supervisor without whom I would not have completed my doctoral journey. His expertise in solid-state NMR provided me fundamental knowledge/experience and demonstrated the extensive possibilities of magnetic resonance techniques. I am also grateful for the numerous opportunities of domestic/international conferences he provided, which allowed me to experience the most valuable times discussing among researchers around the world.

I am deeply grateful to my supervisor in Australia, Professor William (Bill) S. Price for his wonderful guidance and support during my Master’s and the latter part of my PhD. His exceptional scientific knowledge and experience expanded my understanding of diffusion NMR, relaxation, and MRI. I learned a lot from his incredible writing and editing skills, as well as Australian slang. He has always been kind and offered me valuable advice not only on research but on daily life. When I suffered from the long-term border closure due to the COVID-19 pandemic, Bill kept encouraging me for further stay in his lab. I would not have reached to the research achievement in Australia without his unwavering support.

My research was completed with invaluable cooperation from a number of collaborators in Japan and Australia. I would like to express my sincere gratitude for their willingness to provide guidance and support.

First, I would like to deeply thank Honorary Professor Akira Naito for his insightful feedback. I would also like to acknowledge Honorary Professor Kazuyoshi Ueda for opening up my research focus toward cellulose. I am also grateful to Professor Akira Isogai and Dr Yuko Ono from the University of Tokyo for their valuable advice on the TEMPO-mediated oxidation and structural analysis of cellulose nanofibers. I would like to express my deep appreciation to Professor Toshiyuki Oyama, Mr Takumi Honda,

and Mr Seiryu Umetani for their assistance in thermogravimetric analysis. I would like to deeply thank Mr Takahiro Sakai, Group Leader of the Hasegawa Co., Ltd. for his expertise in particle size distribution measurements, and Mr Naoki Yoshihara from Instrumental Analysis Center for his assistance in scanning electron microscopy and X-ray diffraction measurements. Mr Kosuke Nishimura from Tono Mirai Zukuri College, and Mr Saito Yosuke and Ms Haru Saito from Chuo University are also thanked for suggesting and providing hop stems as a new source of cellulose nanofbers.

In Australia, I would like to acknowledge Dr Scott A. Willis, Dr Abhishek Gupta, and Dr Allan M. Torres from the Nanoscale Organisation and Dynamics Group for their helpful instruction in NMR, relaxation, and analytical techniques. I also sincerely thank Honorary Associate Professor Kenneth R. Harris from the University of New South Wales, Canberra for having me the project on multinuclear diffusion NMR measurements in ionic liquids. As a part of the international collaboration, I express my deep appreciation to Professor Olle Söderman from Lund University, Sweden for his assistance and valuable advice on deuterium diffusion NMR measurements.

I would like to express my sincere gratitude to my thesis committee panels, Professor Chojiro Kojima, Professor Mahito Atobe, Professor Toshiyuki Oyama, and Professor Minoru Takeda for their fair examination and insightful feedback.

I would also like to express my heartfelt appreciation to all my peers from Kawamura and Bill's lab members who have made my seven-year research journey truly enjoyable and valuable.

Lastly, I extend my deepest gratitude to my parents for supporting and encouraging me through all the good and bad times and enjoying the journey with me.

My most heartfelt thanks go to my partner, Scott, for his everyday support and understanding.

At the very end, I would like to express my special appreciation to my dog, Saburo. He was my best mental supporter and wonderful family member for fifteen years but sadly passed in the final year of my PhD. This thesis is dedicated to the memory of him.

May 31, 2023
Noriko Kanai

Appendix

Supplementary Information of Chapter 4

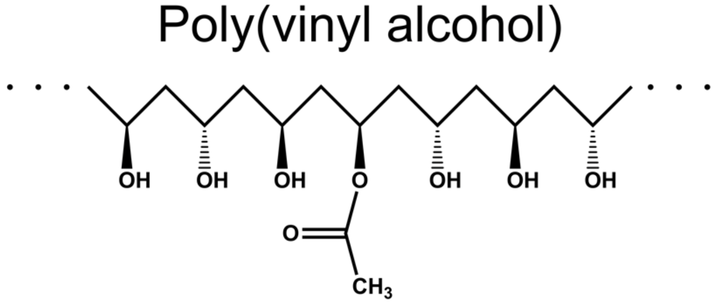

Fig. S1. Chemical structure of poly(vinyl alcohol) with carbon atom numbering corresponding to Fig. 26 in the main text.

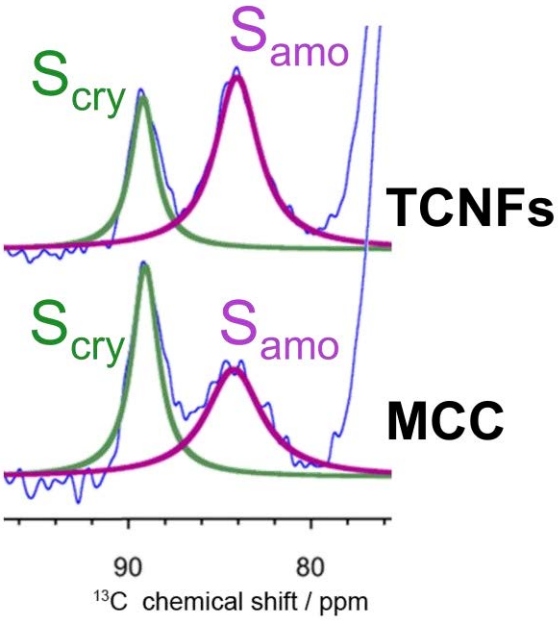

Fig. S2. Peak deconvolutions of ^{13}C CP-MAS NMR spectra of TCNFs compared to MCC. The C4 regions of the experimental spectra (blue line) fitted by Gaussian function. Comparison of the areas of the crystalline (green line) and non-crystalline (purple line) C4 signals.

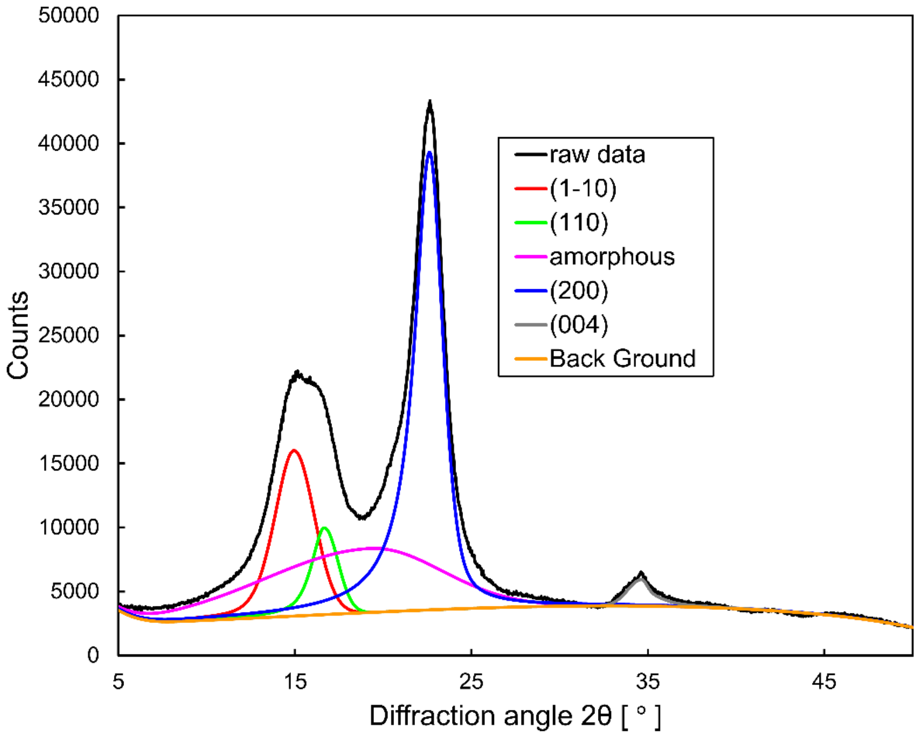

Fig. S3. XRD pattern and of TCNFs derived from SCGs. The black line is experimental result. The Orange line indicates background and the pink line is amorphous region centered at 2 θ = 19.3. Three diffraction peaks at 2 θ = 14.9 (1-10 plane, the red line), 16.7 (110 plane, the green line), 22.6 (200 plane, the blue line) and 34.6 (004 plane, the gray line) are fitted by pseudo-Voigt function.

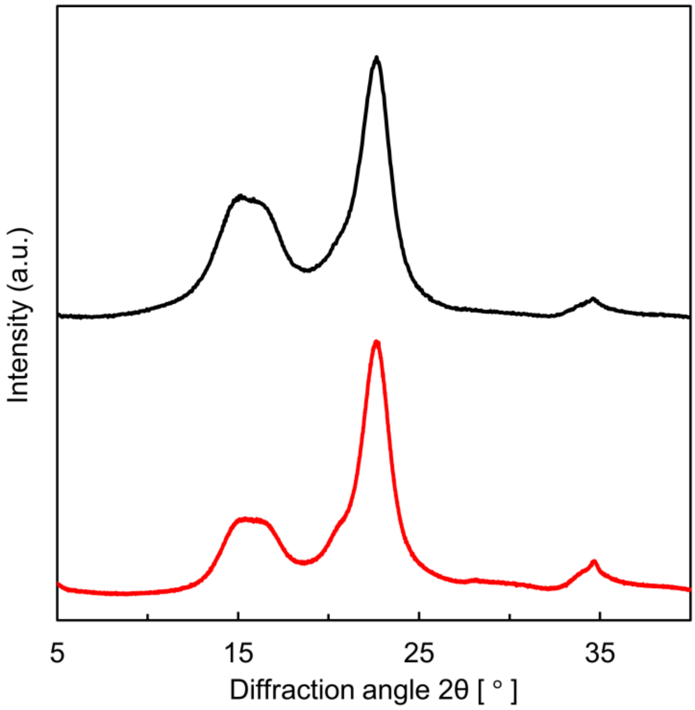

Fig. S4. XRD patterns of SCG-derived TCNFs (the black line) compared to MCC (the red line). The degree of crystallinity (C.I.) was calculated from peak deconvolution method as shown in Fig. S3.

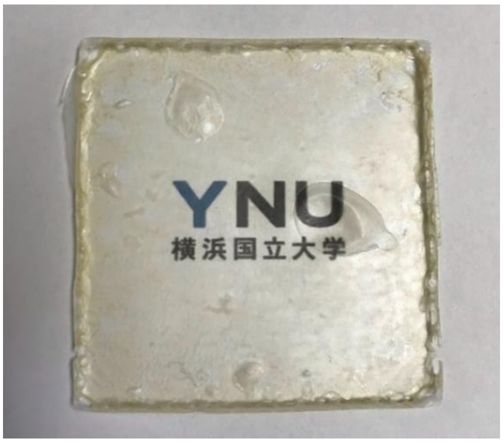

Fig. S5. A 1:1 PVA/TCNF transparent composite film observed by optical photograph.

Supplementary Information of Chapter 5

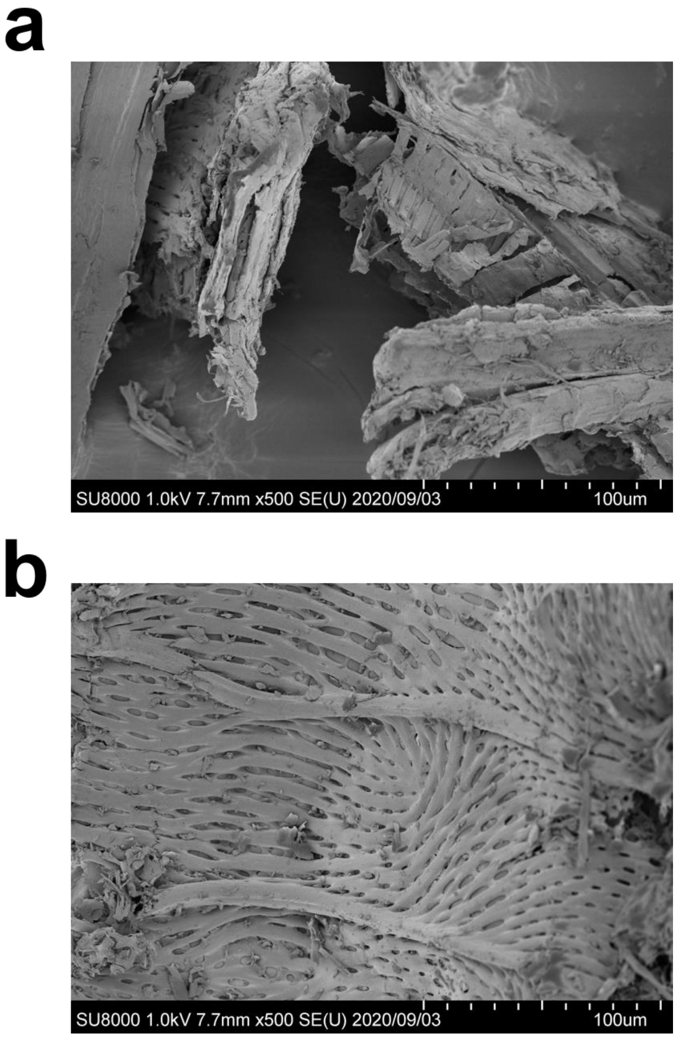

Fig. S6. FE-SEM images of mechanically milled hop stems as shown in Fig. 30d in the main text (a, b). Xylem vessel cells which build up water transport system in stem were clearly found in hop stems (b).

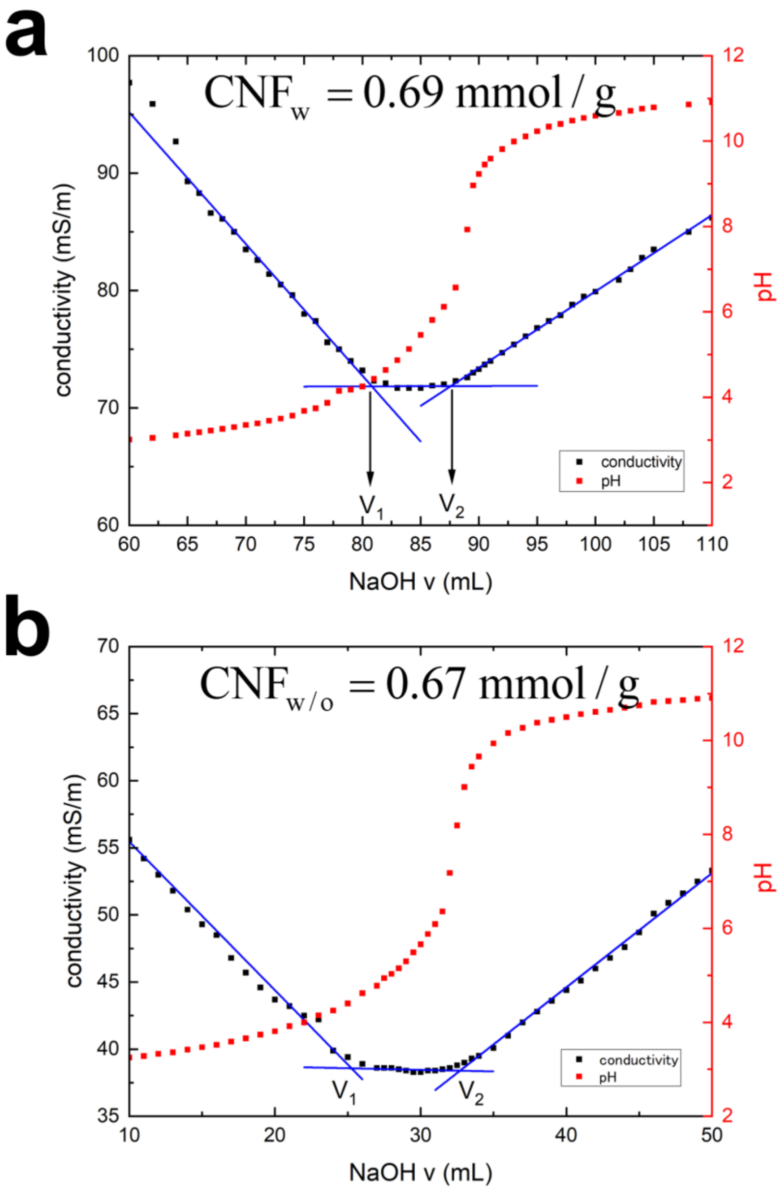

Fig. S7. The conductometric (black) and pH (red) curves of 0.1 g of CNF$_w$ titrated with 10.23 mmol/L NaOH (a) and CNF$_{w/o}$ titrated with 9.11 mmol/L NaOH (b). The two equivalent volumes related to strong and weak acid equivalence points were named V$_1$ and V$_2$, respectively.

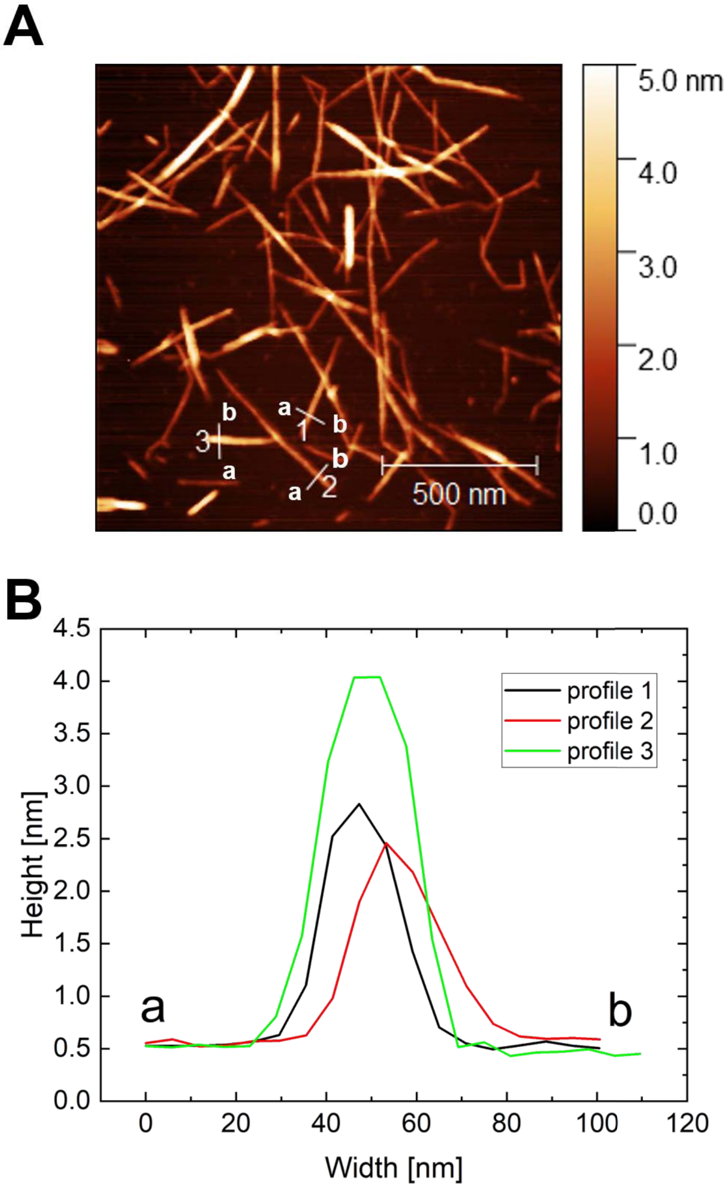

Fig. S8. Typical AFM image (A) and its height profile (B). Lines were drawn from (a) to (b) in the profiles and CNF heights were automatically measured as each peak height.

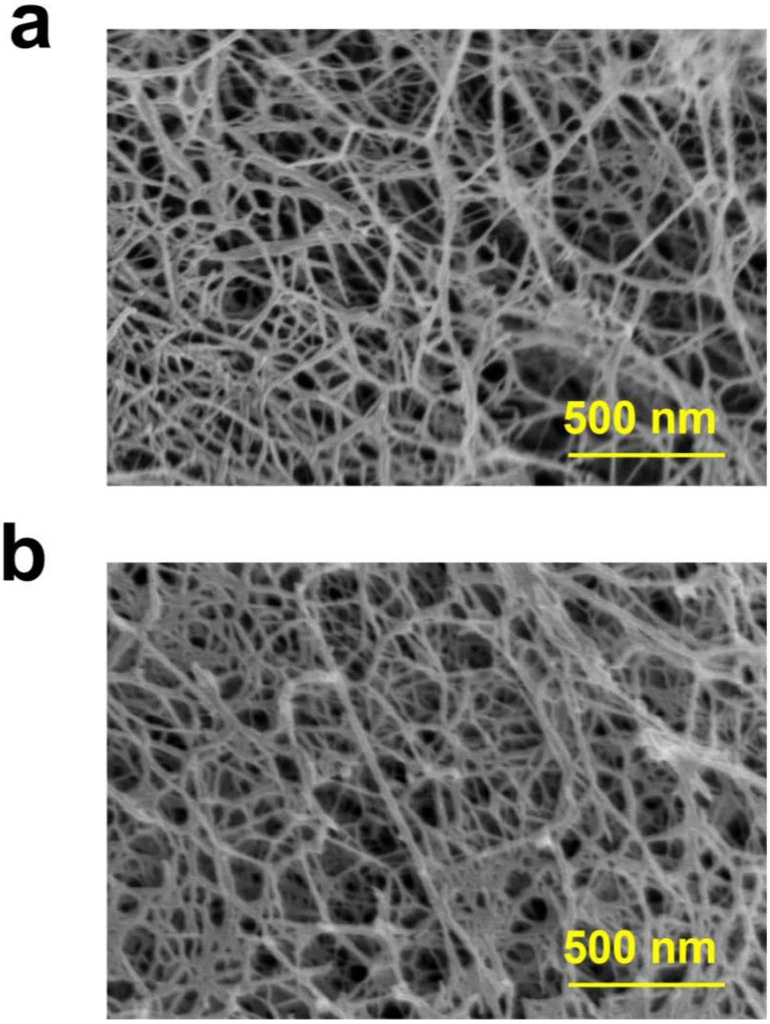

Fig. S9. FE-SEM images of (a) CNF$_{w}$ and (b) CNF$_{w/o}$.

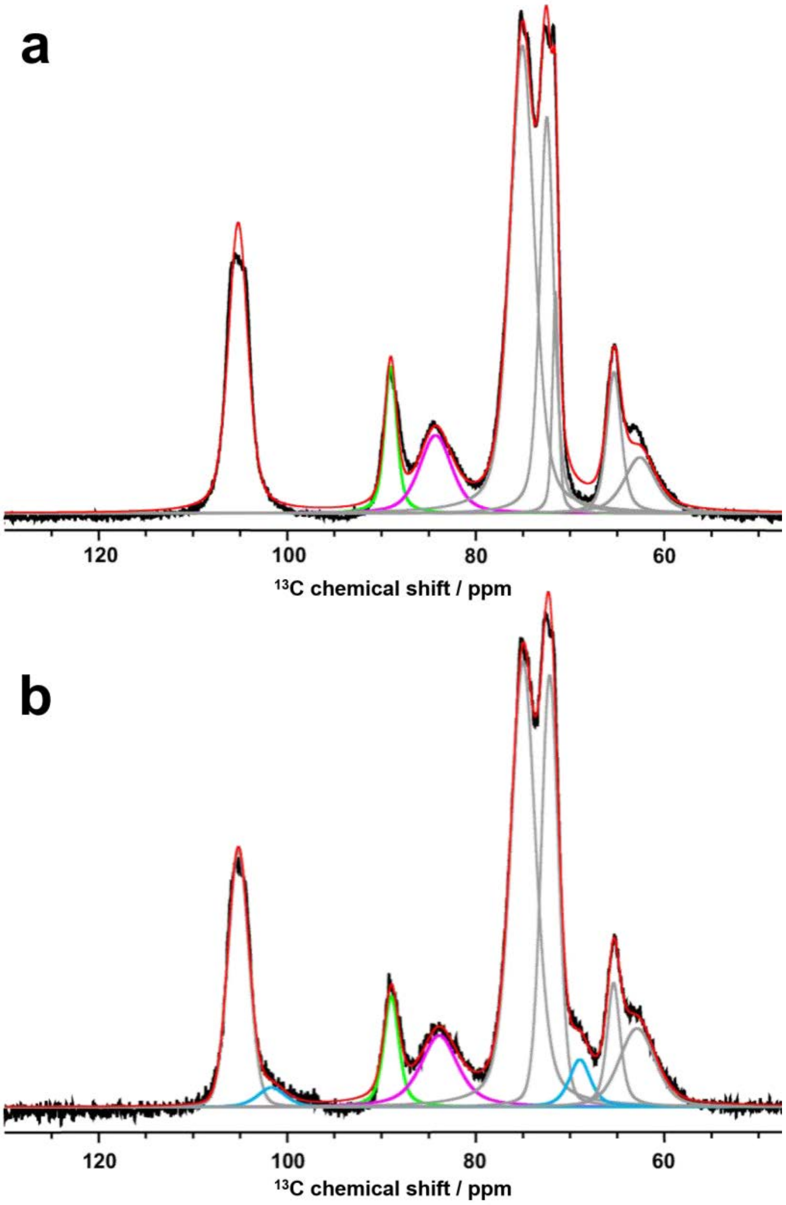

Fig. S10. NMR peak deconvolution of CNF$_{w}$ (a) and CNF$_{w/o}$ (b) to determine the crystallinity (CINMR). Line broadening of both spectra were set as 0 Hz prior to running calculation. The experimental spectra (black) were separated to peaks of C1–6 cellulose (gray, magenta, and green) and hemicellulose (cyan), and then fitting was performed with Gauss/Lorentz curves in the range of 40 to 130 ppm. The best overlapped proportion of each spectrum (red) was 94% for CNF$_{w}$ and 96% for CNF$_{w/o}$. The crystallinity was calculated from the area of the crystalline (magenta) and non-crystalline (green) C4 signals.

Table S1. ^{13}C CP-MAS NMR chemical shifts and assignments.

Signals in **Fig. 33**	Chemical shift / ppm				Assignments[27,200,202,203,247]
	Hop stem	After Wise method	$CNF_{w/o}$	CNF_w	
H_1	21.1	21.2	-	-	$\underline{C}H_3$–COO– (e.g., xylan)
TAG	30–40	30.5	30.1	30.0	$–(\underline{C}H_2)_n–$
L_1	56.2	56.7	-	-	$–O\underline{C}H_3$
C6(amo/cry)	63.5/64.9	63.2/65.2	63.5/65.3	63.4/65.3	
C2,3,5	72.7/74.8	72.6/75.1	72.6/74.9	72.6/75.1	
C4(amo/cry)	83.5/89.0	84.0/89.1	83.9/89.0	84.5/89.1	
H_2	98.7	99.5	97.7	-	C1 in hemicelluloses
C1	105.4	105.4	105.1	105.4	
L_2	116.4	-	-	-	Aromatic carbons
L_3	131.9	-	-	-	Aromatic carbons
L_4	145.0	-	-	-	Aromatic carbons
L_5	154.0	-	-	-	Aromatic carbons
H_3	173.5	172.6	-	-	$CH_3–\underline{C}OO–$ (e.g., xylan)
COM	-	168.6	168.6	168.6	$Ca\underline{C}_2O_4·(H_2O)$
C6 (COO^-)	-	-	175.2	175.1	Oxidized C6 in cellulose

Abbreviations: C1–6, cellulose; amo, amorphous (non-crystalline) region; cry, crystalline region; H_{1-3}, hemicellulose; L_{1-5}, lignin; TAG, triacylglycerol; COM, calcium oxalate monohydrate.

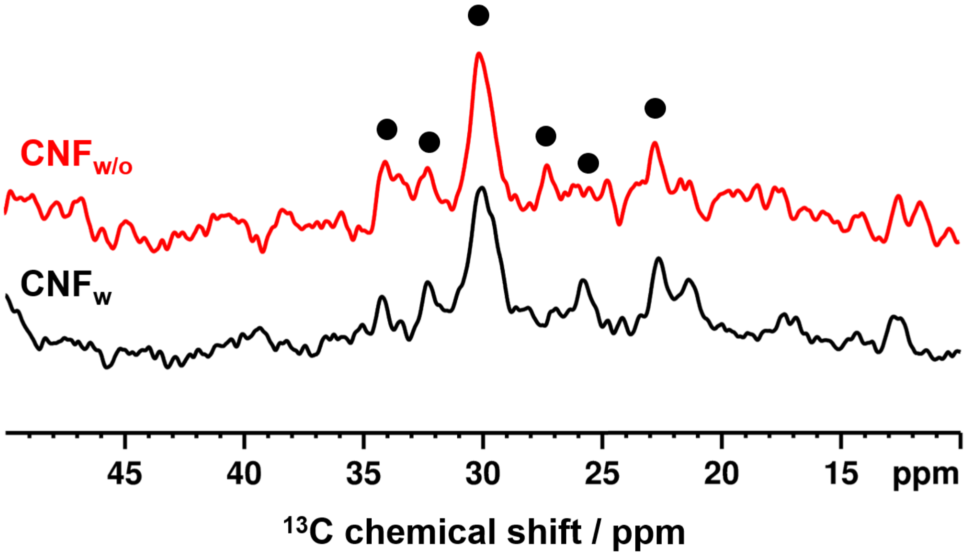

Fig. S11. The methylene carbons in fatty acids of triacylglycerols appeared in CNF$_{w/o}$ (red) and CNF$_w$ (black) spectra shown by black dots (●).

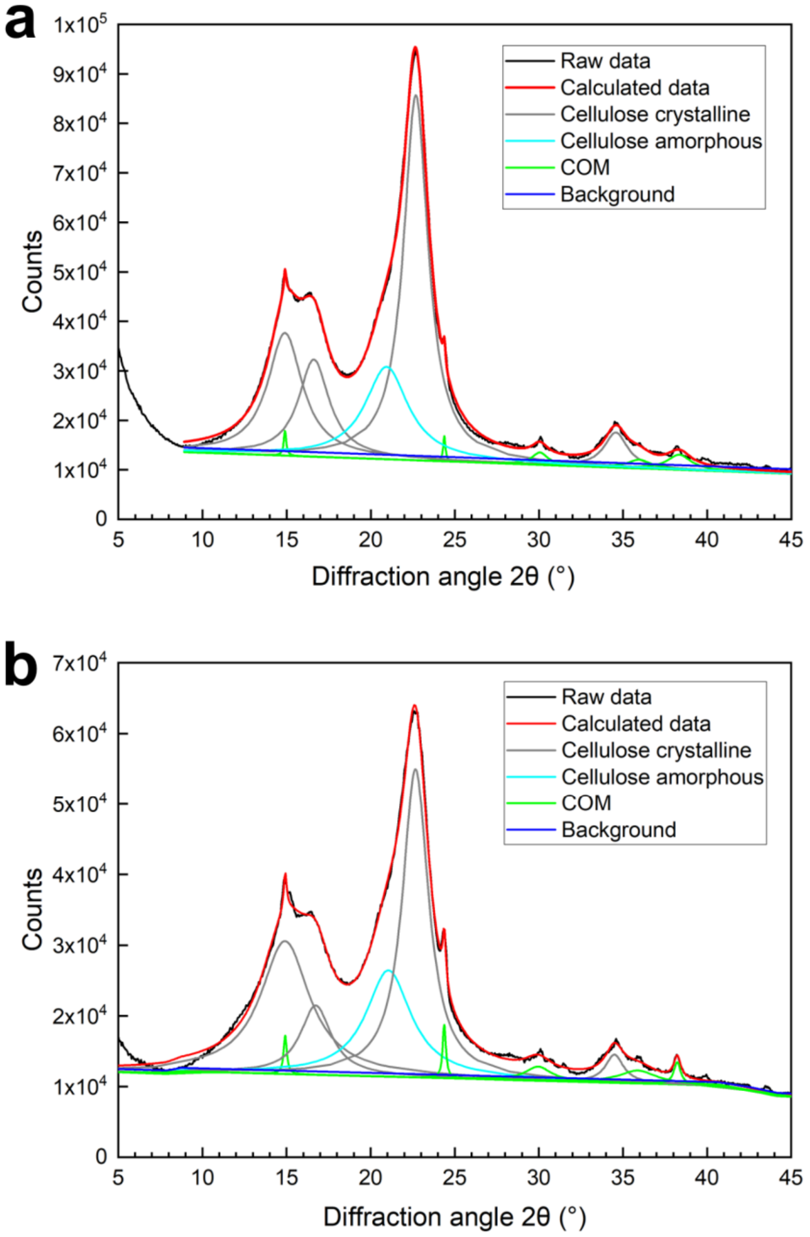

Fig. S12. XRD peak deconvolution of CNFw (a) and CNFw/o (b) to determine crystallinity (CIXRD). The raw data (black) were separated to peaks of cellulose crystalline (gray) at 14.9°, 16.6°, 22.7° and 34.5°, cellulose amorphous (cyan) at 21°, and COM (green) at 14.9°, 24.4°, 30.0° and 38.2°. Fitting was performed with Lorentz curves, and given R-squared values of 0.999 for CNFw, and 0.997 for CNFw/o.

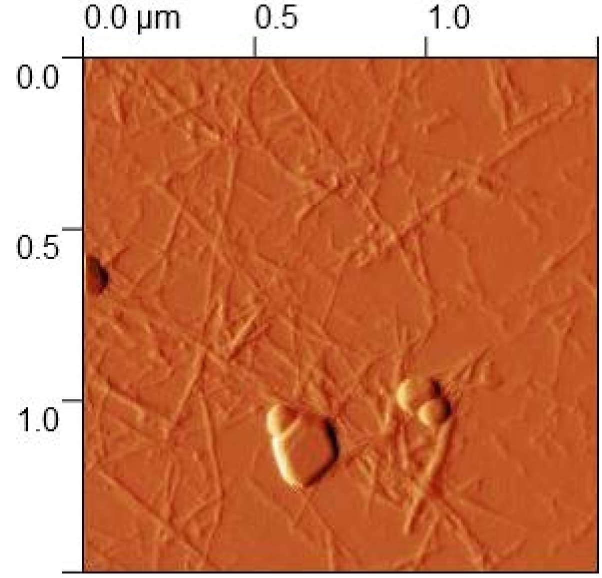

Fig. S13. COM crystals in CNF$_{w/o}$ topography image of AFM

Supplementary Information of Chapter 6

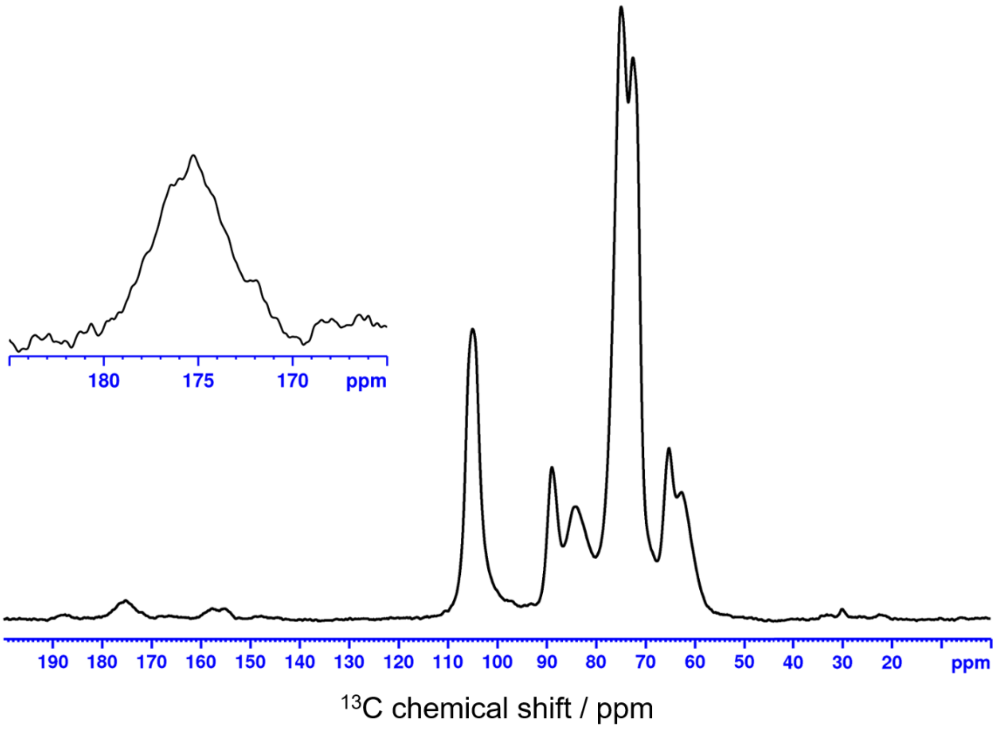

Fig. S14. ^{13}C CP-MAS SSNMR spectrum of TCNF. The inset graph shows carboxyl region.

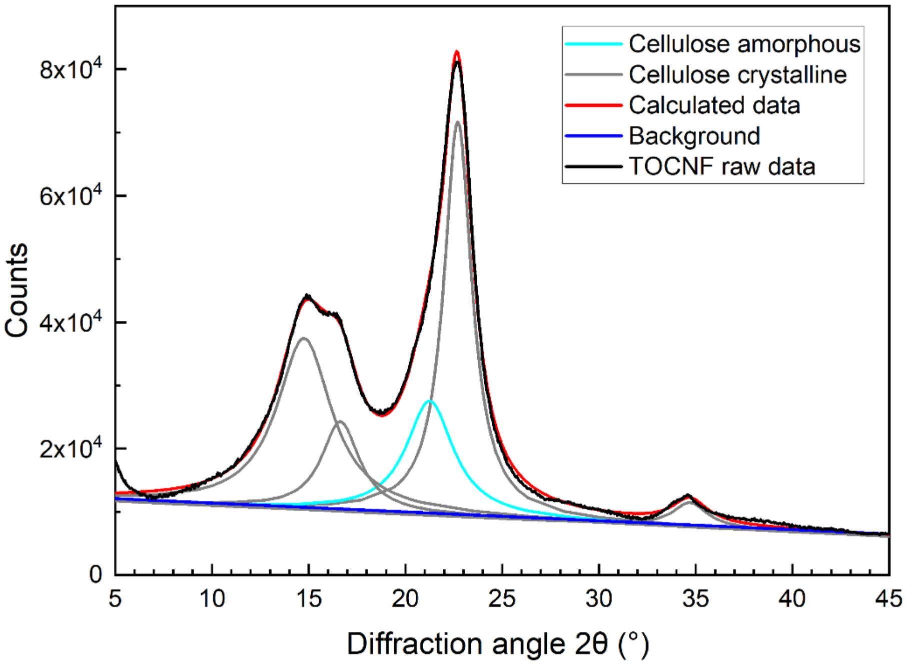

Fig. S15. XRD peak deconvolution of TCNF. The crystallinity was determined from the area of the total crystalline peaks (i.e., 14.8°, 16.6°, 22.7°, 34.7°) over the amorphous peak (i.e., 21.3°). Fitting was performed with Lorentz curves, and given R-squared value of 0.998.

Table S2. pH and turbidity of TCNF suspensions

Suspension used for emulsions	TCNF conc. (wt %)	pH	Turbidity[a)] (mg/L)	Viscosity[b)] (mPa·s)
d-CNF o/w 20:80, o-CNF o/w 20:80, o-CNF o/w 10:90	0.5	7.97	127	35.0
	0.8	7.36	250	95.2
	1.0	7.06	274	282
d-CNF o/w 30:70, o-CNF o/w 30:70	0.5	6.43	92.7	28.8
	0.8	6.53	136	81.1
	1.0	6.23	246	325

a) Turbidity was measured by the transmitted light turbidity method after calibrating with the turbidity standard material according to JIS K0101. Each measurement was triplicated, and the result was averaged.

b) Value at the shear rate of 100 /s.

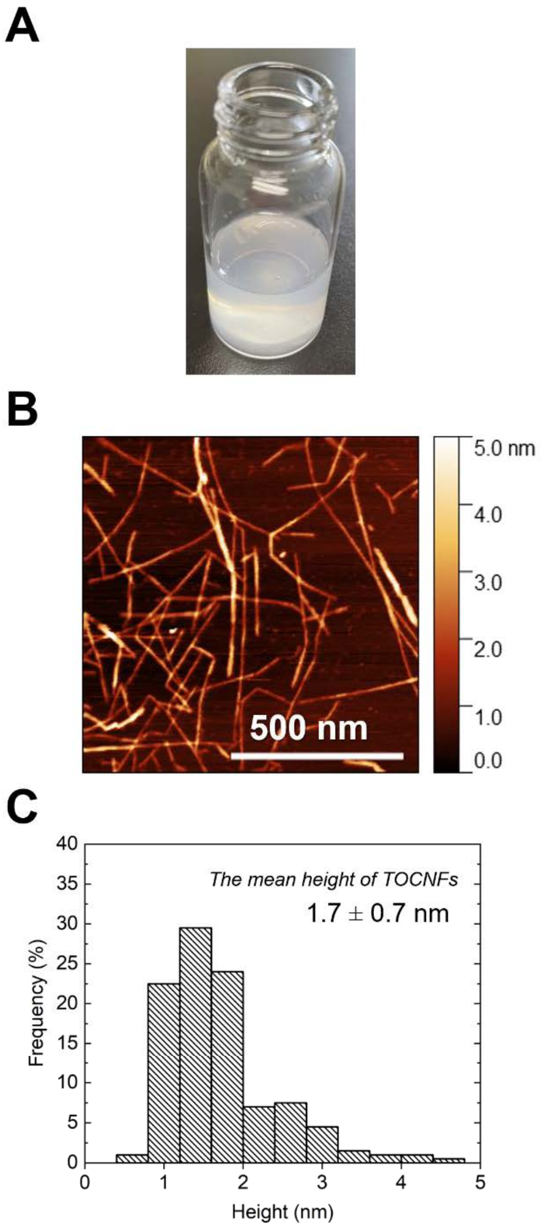

Fig. S16. (A) Photographs of 1.0% TCNF dispersion. (B) TCNF height distribution was investigated by AFM. Two hundred TCNFs were randomly selected from 11 images to measure the peak height in the profile. (C) The mean height of TCNF was calculated to be 1.7 ± 0.7 nm.

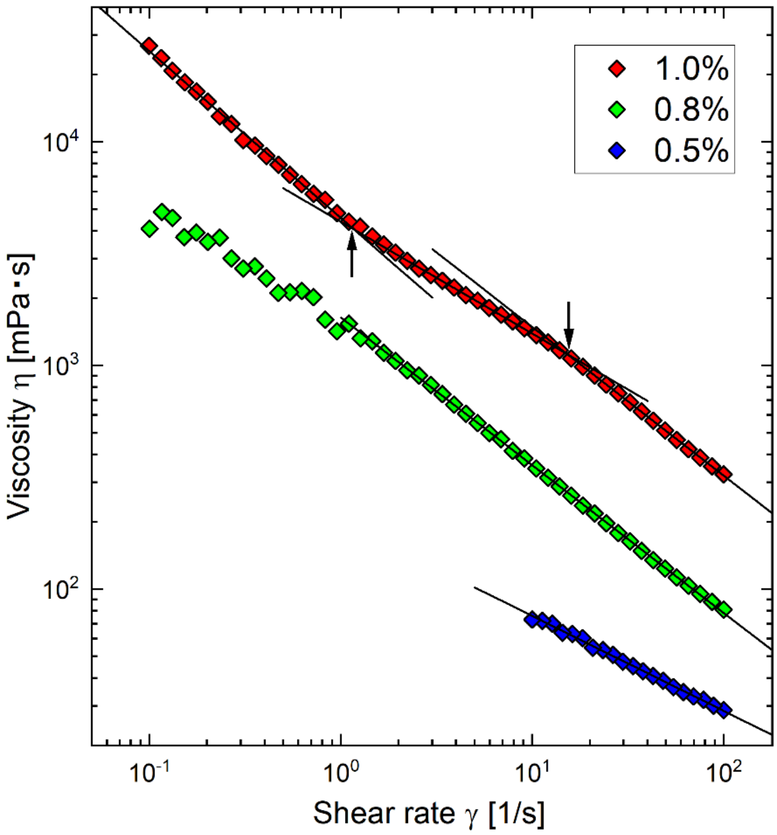

Fig. S17. The viscosity of TCNF dispersions at 20 °C at concentrations of 1.0 wt% (red), 0.8 wt% (green), 0.5 wt% (blue). The slope of viscosity changed twice at the arrow positions for 1.0% dispersion, reflecting the microscopic structural changes during measurements.

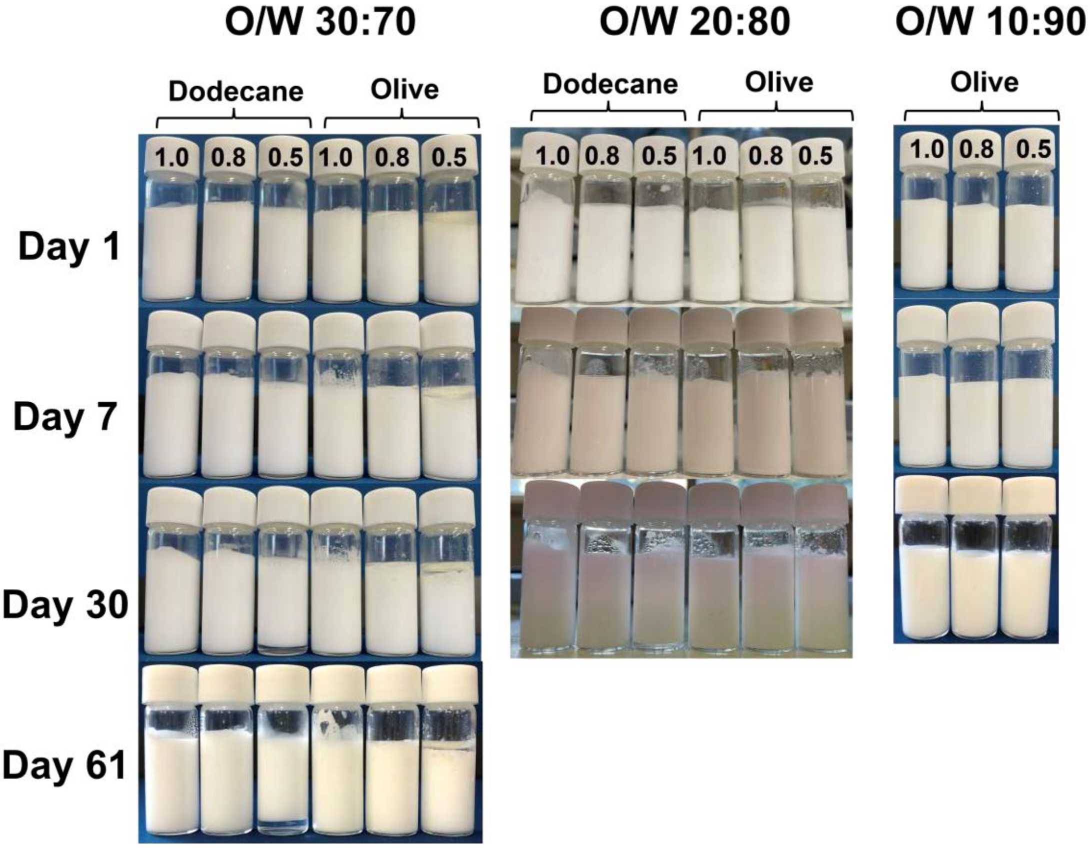

Fig. S18. Photographs of o/w 30:70, 20:80 dodecane/CNF (d-CNF) emulsions, and o/w 30:70, 20:80, 10:90 olive/CNF (o-CNF) emulsions on days 1, 7, 30, and 61.

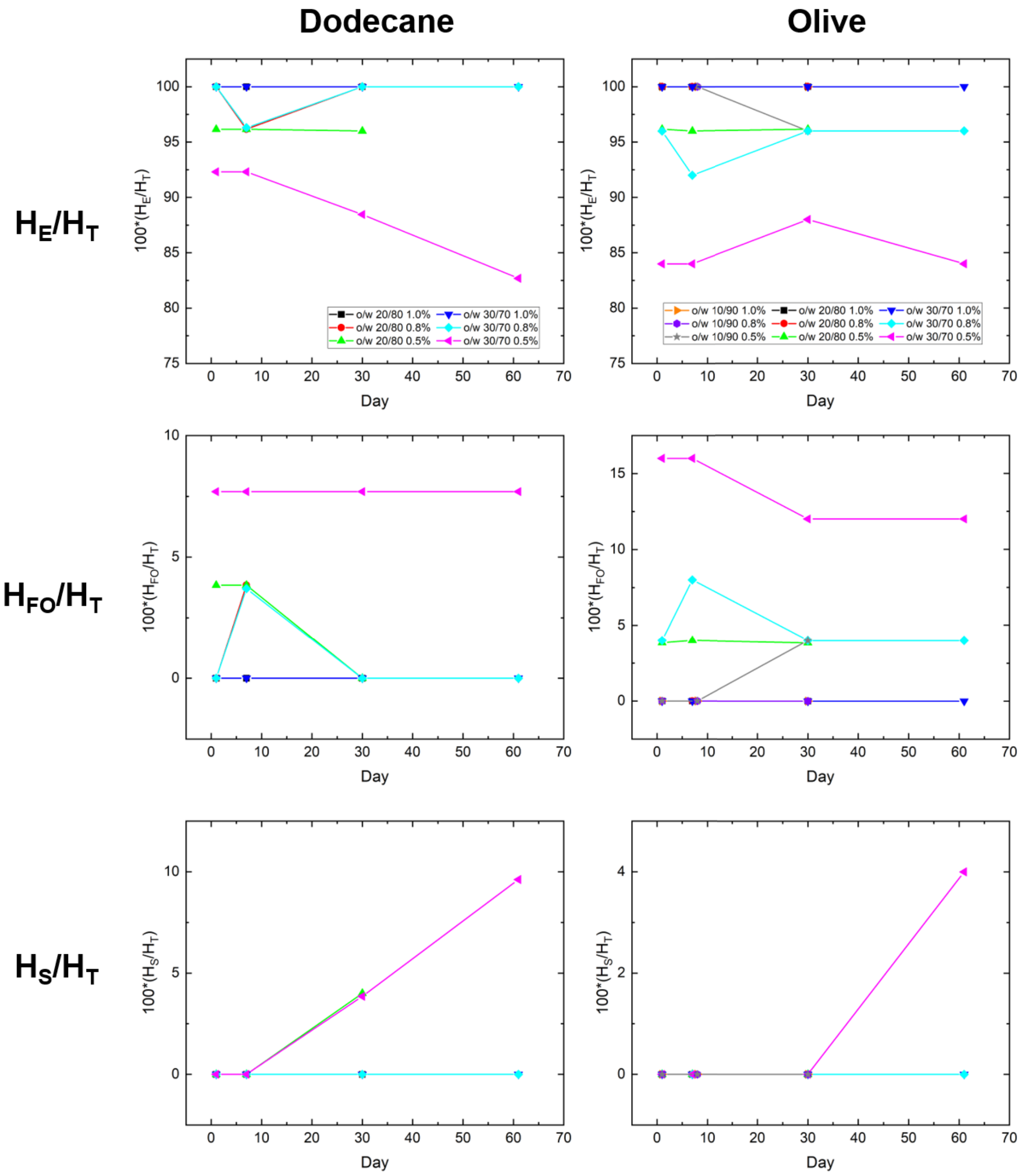

Fig. S19. **The relative height of each layer in d-CNF and o-CNF emulsions as a function of time. Free oil layer on the top (H_{FO}), opaque emulsion/cream layer including cream layer (H_E), and transparent serum layer on the bottom (H_S) was calculated as the ratio of the total height of the samples in the vial (H_T).**

Table S3. D_{10}, D_{50}, D_{90}, and the mean diameter of oil droplets (d_v) of o/w 20:80 d-CNF emulsions on days 1, 7, and 30.

a: The mean diameter of DSD fitted by a log-normal distribution curve.
b: Data from the particle distribution size analyzer (Horiba LA-950V2).

d-CNF	o/w 20:80 Day 1				
TCNF concentration (wt%)	d_v (μm)[a]	D_{50} (μm)[b]	D_{10} (μm)[b]	D_{90} (μm)[b]	D_{90}/D_{10}
0.5	7.6	6.4	4.1	9.8	2.4
0.8	5.0	4.6	4.0	5.4	1.4
1.0	4.8	4.4	3.6	5.3	1.5

d-CNF	o/w 20:80 Day 7				
TCNF concentration (wt%)	d_v (μm)[a]	D_{50} (μm)[b]	D_{10} (μm)[b]	D_{90} (μm)[b]	D_{90}/D_{10}
0.5	5.9	5.5	4.7	6.4	1.4
0.8	6.0	5.5	4.6	6.6	1.4
1.0	5.1	4.1	2.6	6.6	2.5

d-CNF	o/w 20:80 Day 30				
TCNF concentration (wt%)	d_v (μm)[a]	D_{50} (μm)[b]	D_{10} (μm)[b]	D_{90} (μm)[b]	D_{90}/D_{10}
0.5	6.5	6.0	5.0	7.2	1.5
0.8	5.4	4.9	4.0	5.9	1.5
1.0	4.9	4.1	3.6	5.5	1.5

Table S4. D_{10}, D_{50}, D_{90}, and the mean diameter of oil droplets (d_v) of o/w 30:70 d-CNF emulsions on days 1, 7, and 30.

a: The mean diameter of DSD fitted by a log-normal distribution curve.
b: Data from the particle distribution size analyzer (Horiba LA-950V2).

d-CNF	o/w 30:70 Day 1				
TCNF concentration (wt%)	d_v (µm)[a]	D_{50} (µm)[b]	D_{10} (µm)[b]	D_{90} (µm)[b]	D_{90}/D_{10}
0.5	10.5	8.4	5.0	13.5	2.7
0.8	8.9	7.3	4.6	11.4	2.5
1.0	6.9	6.3	5.3	7.5	1.4

d-CNF	o/w 30:70 Day 7				
TCNF concentration (wt%)	d_v (µm)[a]	D_{50} (µm)[b]	D_{10} (µm)[b]	D_{90} (µm)[b]	D_{90}/D_{10}
0.5	11.2	8.9	5.2	14.5	2.8
0.8	10.2	8.4	5.2	13.0	2.5
1.0	5.7	5.2	4.2	6.4	1.5

d-CNF	o/w 30:70 Day 30				
TCNF concentration (wt%)	d_v (µm)[a]	D_{50} (µm)[b]	D_{10} (µm)[b]	D_{90} (µm)[b]	D_{90}/D_{10}
0.5	13.8	11.1	6.5	17.9	2.8
0.8	10.0	8.2	5.2	12.8	2.5
1.0	6.1	5.6	4.6	6.6	1.4

Table S5. D_{10}, D_{50}, D_{90}, and the mean diameter of oil droplets (d_v) of o/w 20:80 o-CNF emulsions on days 1, 7, and 30.

a: The mean diameter of DSD fitted by a log-normal distribution curve.
b: Data from the particle distribution size analyzer (Horiba LA-950V2).

o-CNF	o/w 20:80 Day 1				
TCNF concentration (wt%)	d_v (µm)[a]	D_{50} (µm)[b]	D_{10} (µm)[b]	D_{90} (µm)[b]	D_{90}/D_{10}
0.5	7.9	4.5	1.9	11.2	6.0
0.8	6.3	4.0	1.8	8.3	4.5
1.0	6.9	4.1	1.8	9.7	5.3

o-CNF	o/w 20:80 Day 7				
TCNF concentration (wt%)	d_v (µm)[a]	D_{50} (µm)[b]	D_{10} (µm)[b]	D_{90} (µm)[b]	D_{90}/D_{10}
0.5	5.8	3.8	1.9	8.3	4.4
0.8	6.3	3.9	1.8	10.1	5.5
1.0	6.2	4.1	1.8	32.6	18.2

o-CNF	o/w 20:80 Day 30				
TCNF concentration (wt%)	d_v (µm)[a]	D_{50} (µm)[b]	D_{10} (µm)[b]	D_{90} (µm)[b]	D_{90}/D_{10}
0.5	5.7	3.9	1.9	7.5	4.0
0.8	6.5	4.1	1.9	8.5	4.6
1.0	7.2	4.4	1.8	14.0	7.7

Table S6. D_{10}, D_{50}, D_{90}, and the mean diameter of oil droplets (d_v) of o/w 10:90 d-CNF emulsions on days 1, 7, and 30.

a: The mean diameter of DSD fitted by a log-normal distribution curve.
b: Data from the particle distribution size analyzer (Horiba LA-950V2).

o-CNF	o/w 10:90 Day 2				
TCNF concentration (wt%)	d_v (μm)[a]	D_{50} (μm)[b]	D_{10} (μm)[b]	D_{90} (μm)[b]	D_{90}/D_{10}
0.5	4.1	3.3	1.8	6.6	3.7
0.8	3.5	2.6	1.5	4.9	3.2
1.0	4.7	3.3	1.8	6.6	3.7

o-CNF	o/w 10:90 Day 7				
TCNF concentration (wt%)	d_v (μm)[a]	D_{50} (μm)[b]	D_{10} (μm)[b]	D_{90} (μm)[b]	D_{90}/D_{10}
0.5	3.6	2.8	1.7	4.9	2.9
0.8	4.0	3.0	1.7	5.5	3.2
1.0	4.4	3.3	1.8	6.0	3.3

o-CNF	o/w 10:90 Day 30				
TCNF concentration (wt%)	d_v (μm)[a]	D_{50} (μm)[b]	D_{10} (μm)[b]	D_{90} (μm)[b]	D_{90}/D_{10}
0.5	5.8	3.9	1.9	7.7	4.1
0.8	4.1	3.0	1.7	5.6	3.3
1.0	4.0	3.1	1.8	5.4	2.9

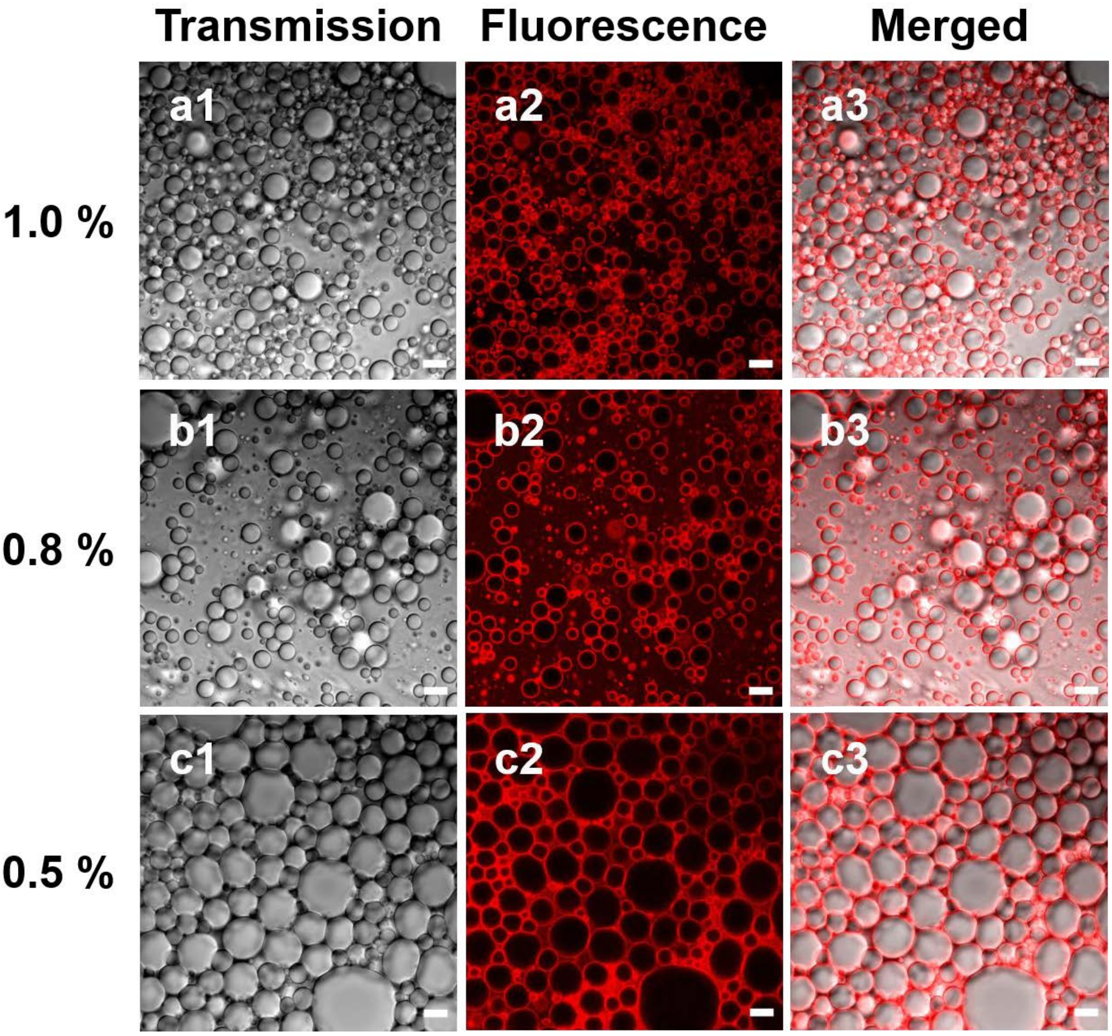

Fig. S20. A series of CLSM images of Congo Red-stained o/w 30:70 d-CNF emulsions on day 1. (a1, b1, c1) light transmission, (a2, b2, c2) fluorescent microscopy and (a3, b3, c3) merged images. Scale bars represent 10 µm.

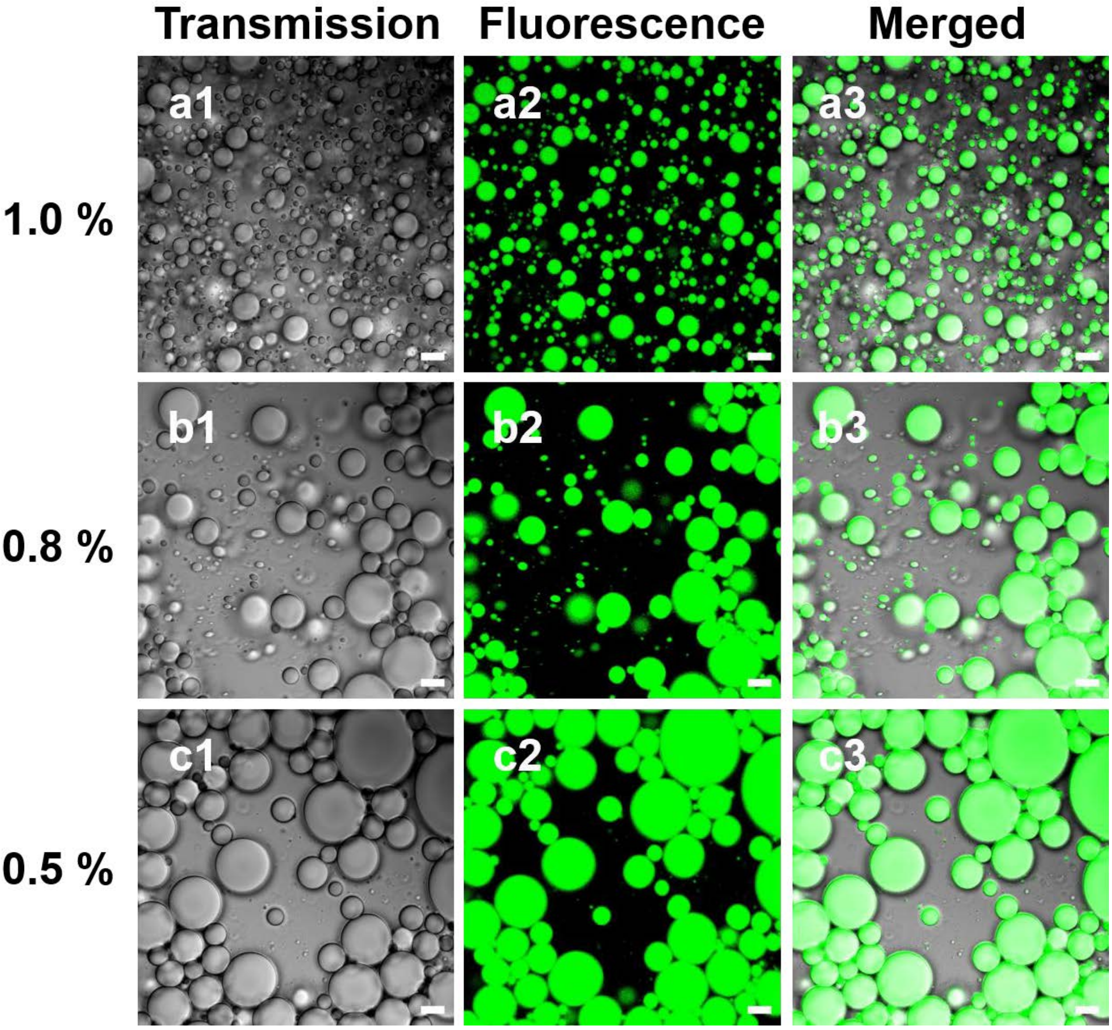

Fig. S21. **A series of CLSM images of Nile Red-stained o/w 30:70 d-CNF emulsions on day 1. (a1, b1, c1) light transmission, (a2, b2, c2) fluorescent microscopy and (a3, b3, c3) merged images. Scale bars represent 10 µm.**

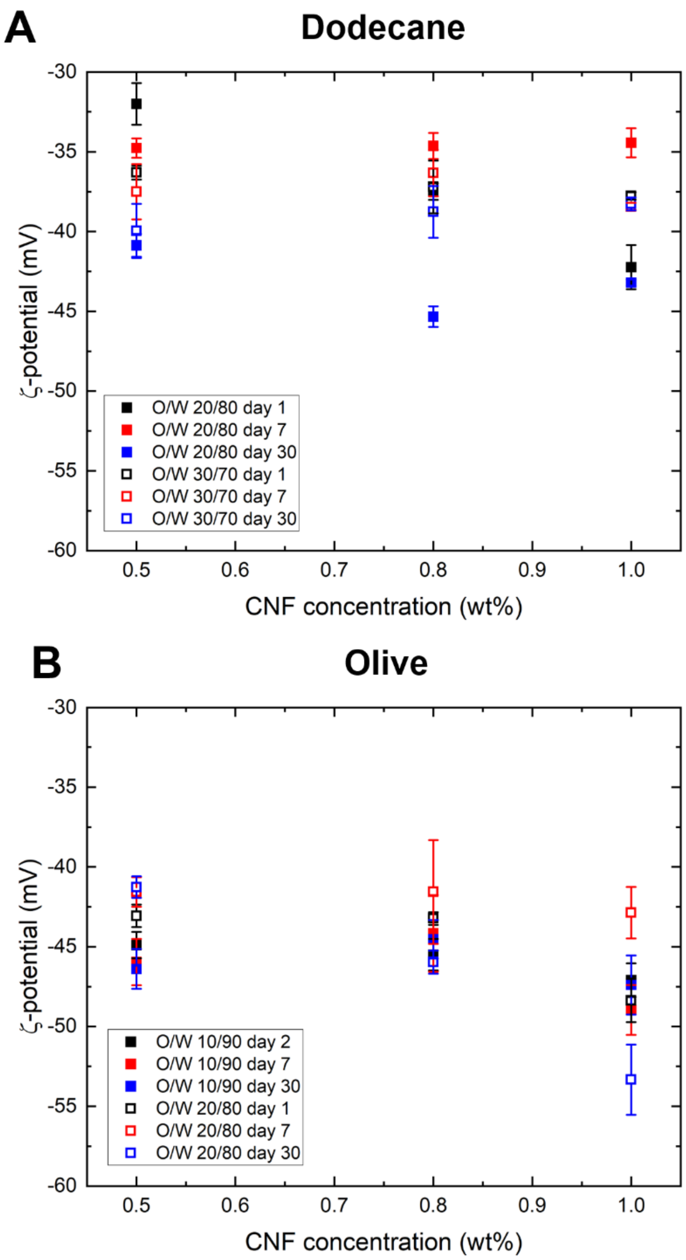

Fig. S22. The ζ-potential values in function of TCNF concentration. (A) d-CNF emulsions at o/w 30:70 and 20:80, and (B) o-CNF emulsions at o/w 20:80 and 10:90. All measurements were conducted on days 1(or 2), 7, and 30. Each value represents the average and standard deviation of the three repetitions.

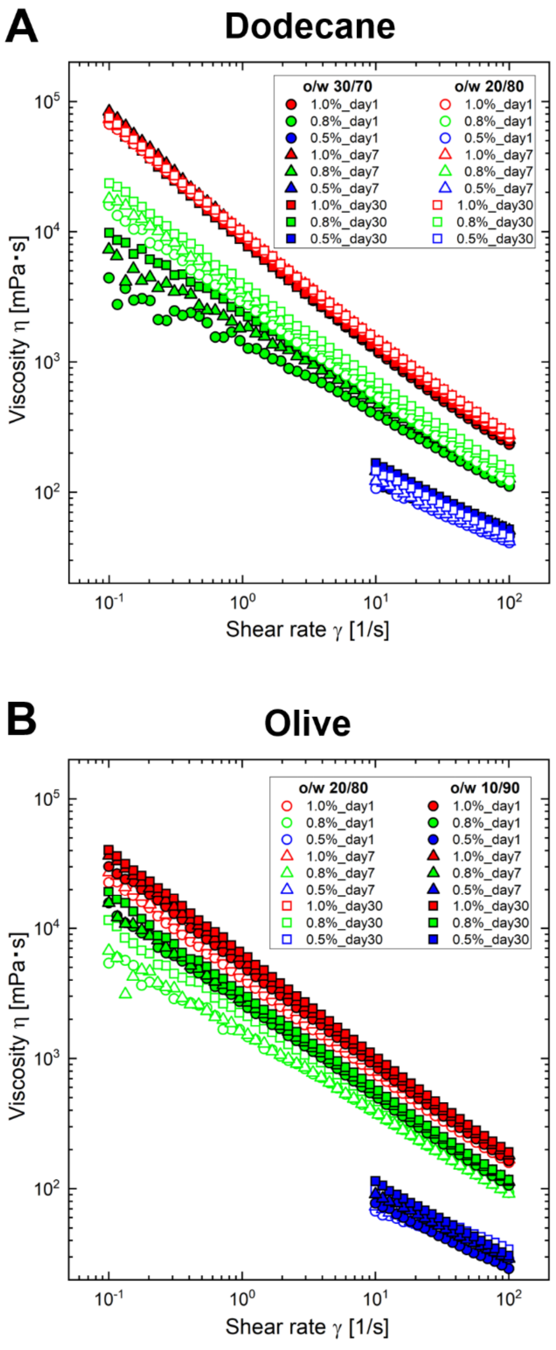

Fig. S23. The viscosity of (A) d-CNF and (B) o-CNF emulsions stabilized by 1.0% (red), 0.8% (green), and 0.5% (blue) TCNF dispersions on days 1 (circle), day 7 (triangle), and day 30 (square).

Supplementary Information of Chapter 7

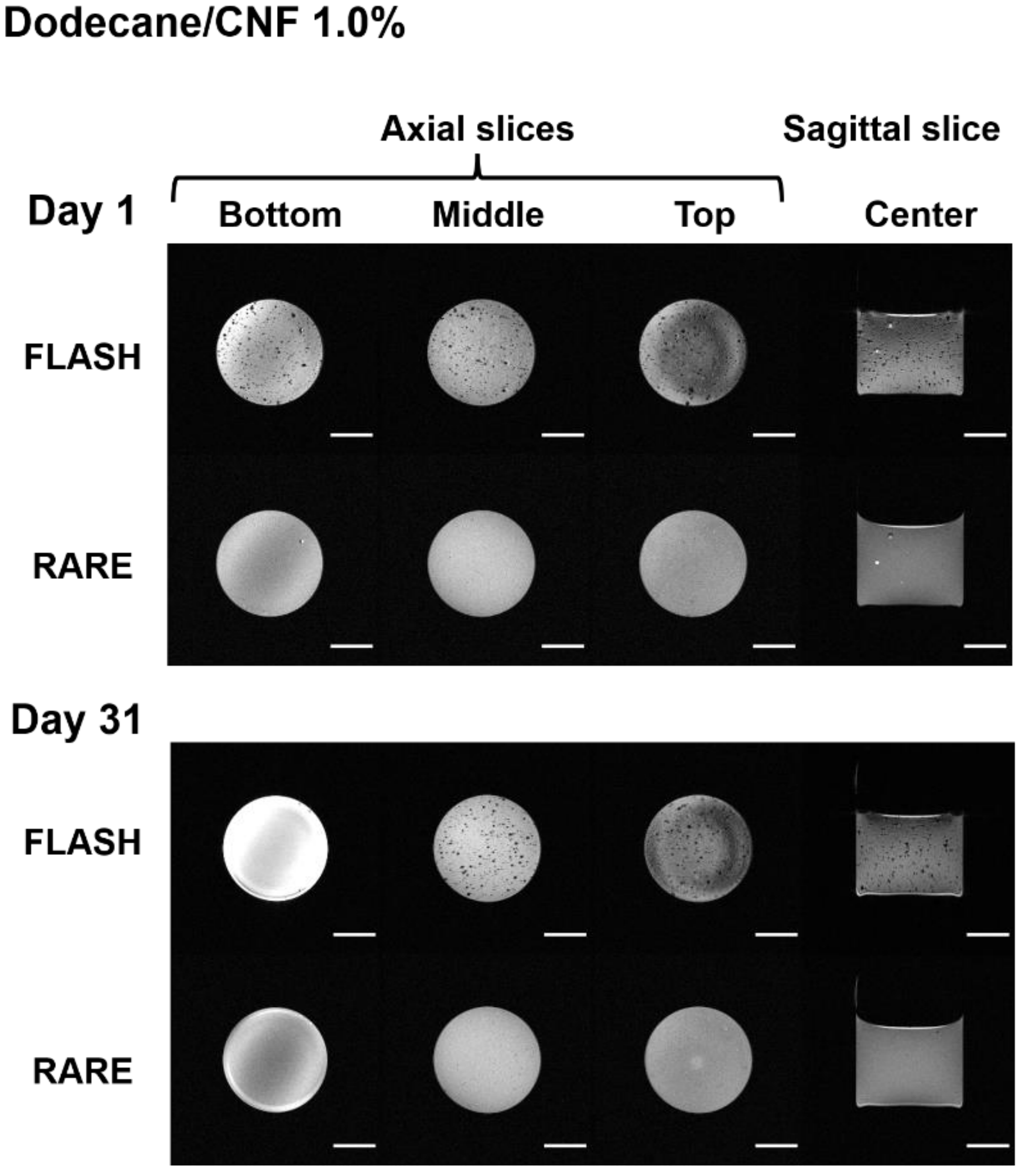

Fig. S24. FLASH and RARE images of d-CNF 1.0% emulsion on days 1 and 31

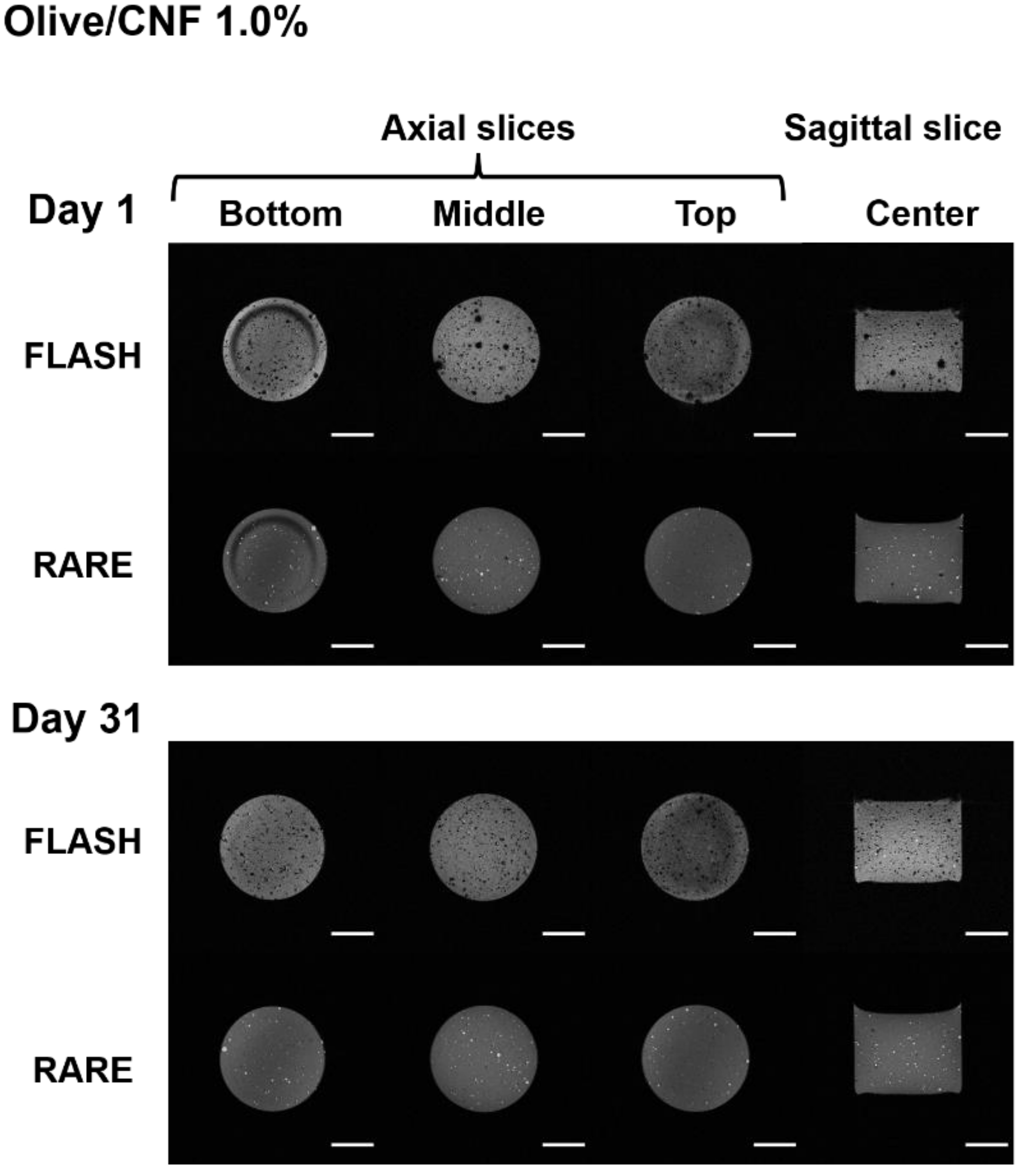

Fig. S25. FLASH and RARE images of o-CNF 1.0% emulsion on days 1 and 31

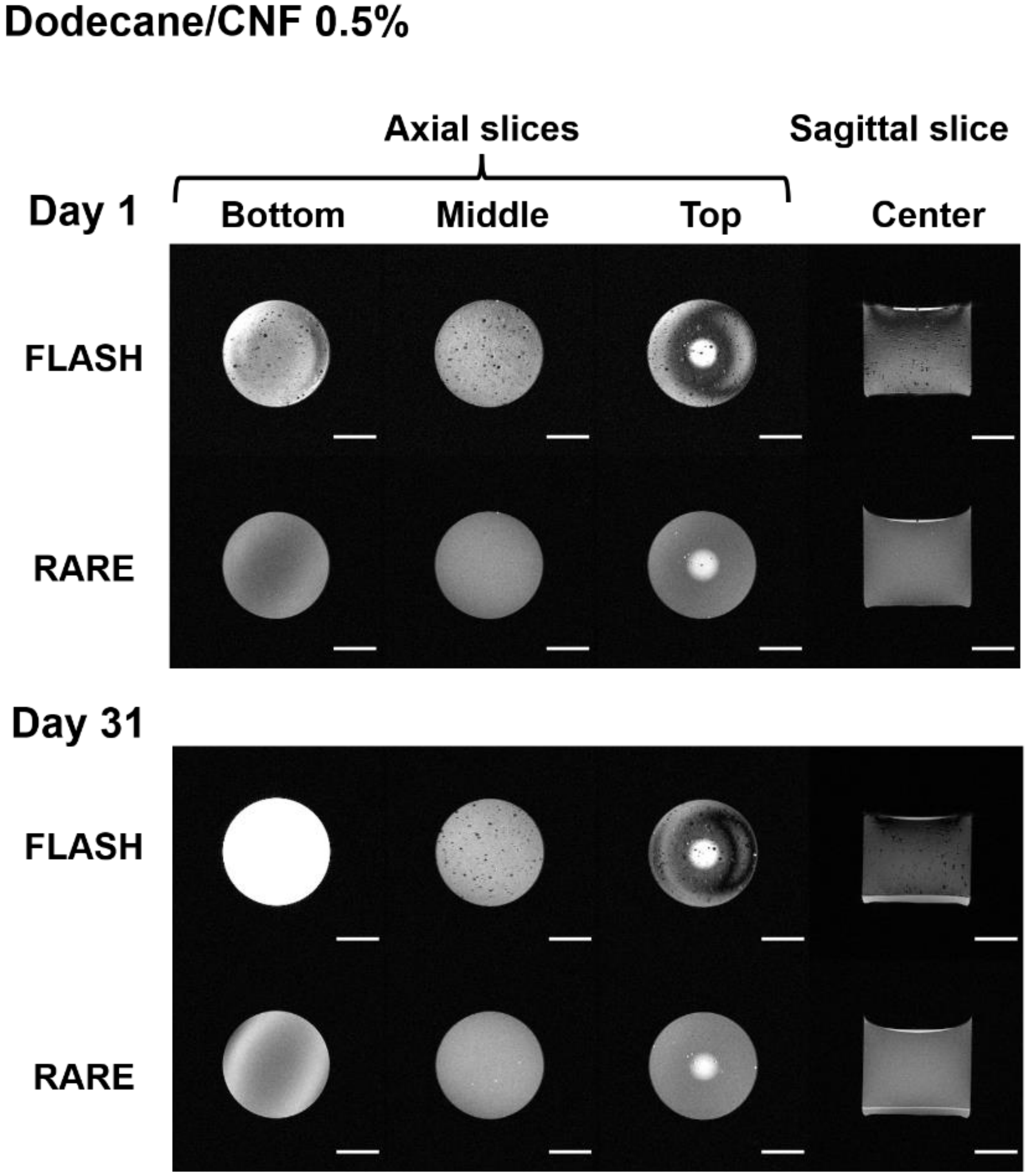

Fig. S26. FLASH and RARE images of d-CNF 0.5% emulsion on days 1 and 31

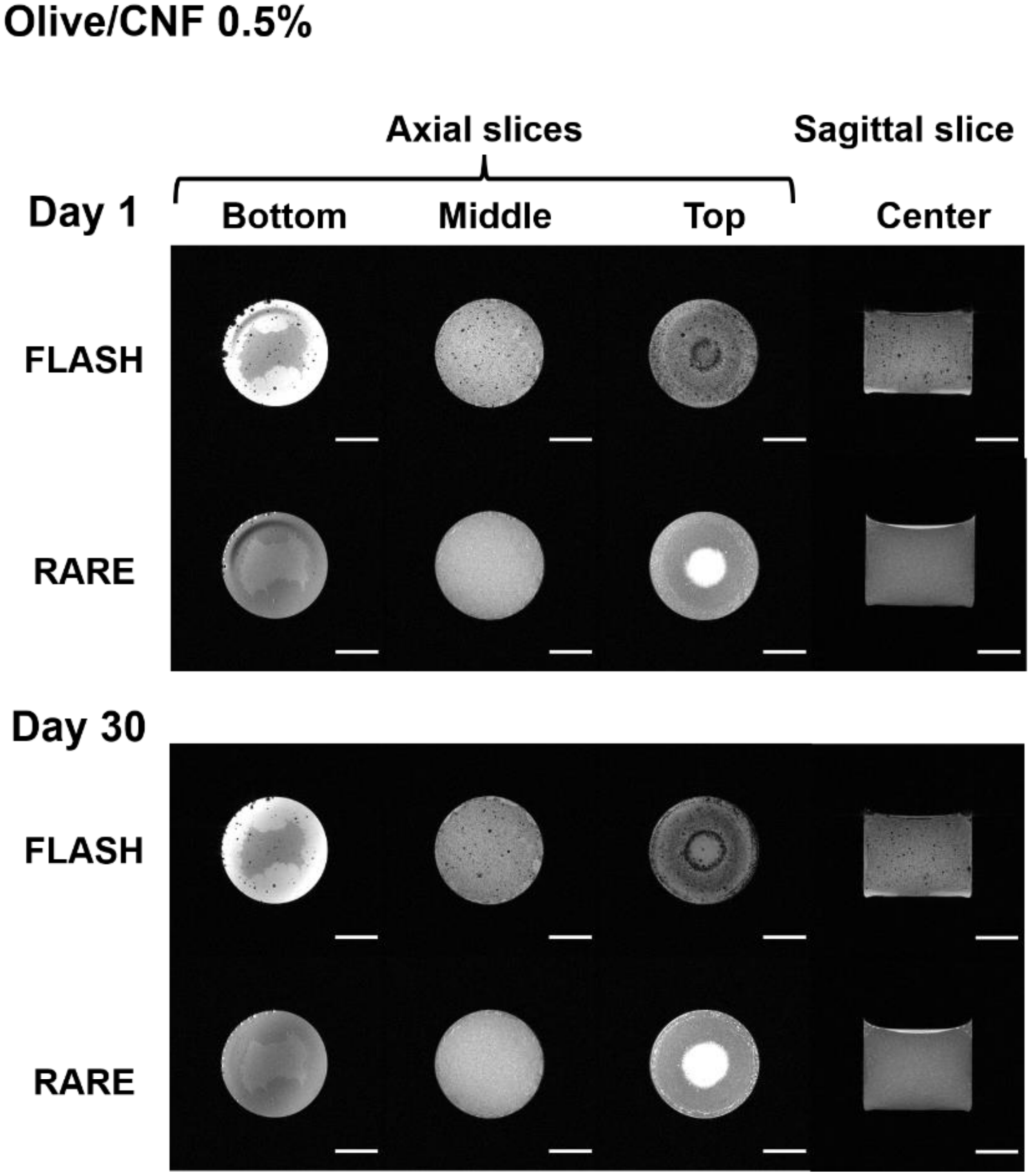

Fig. S27. FLASH and RARE images of o-CNF 0.5% emulsion on days 1 and 30

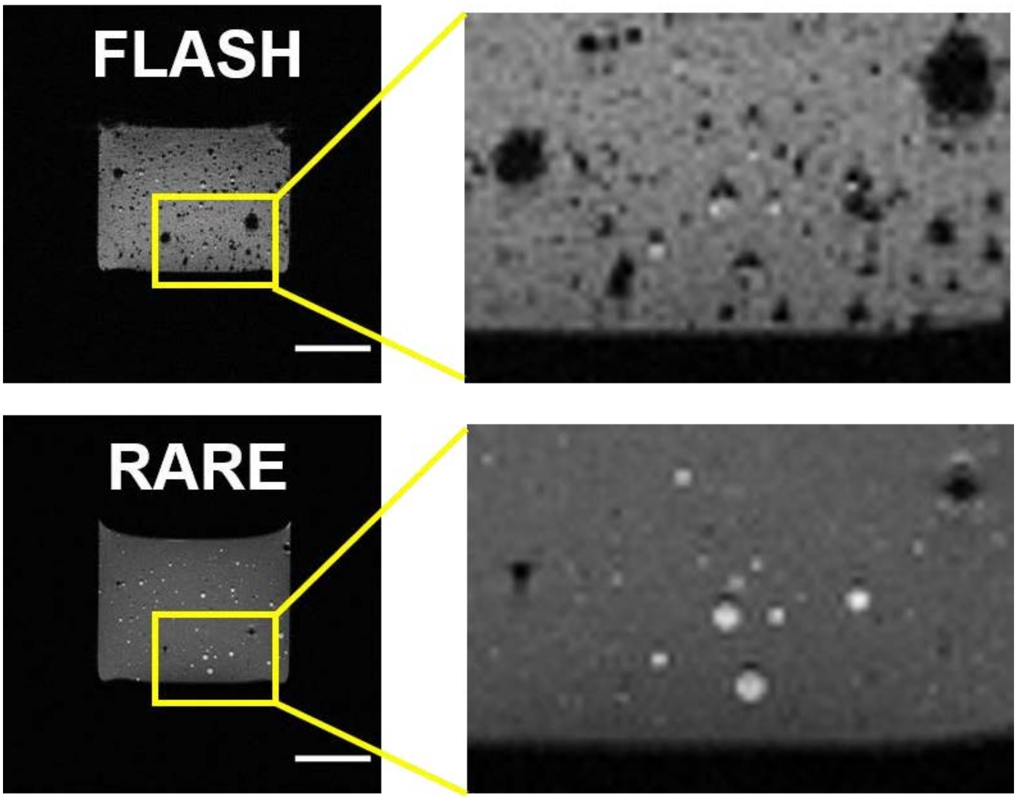

Fig. S28. The enlarged FLASH and RARE images of 1.0% o-CNF emulsions on day 1

Scale bar represents 10 mm. Black spots in the emulsion layers most likely indicated susceptibility artefacts due to air bubbles or in some cases oil droplets or chemical shift artefacts. Note the oil droplets in RARE appear brighter than FLASH due to different relaxation weighting.

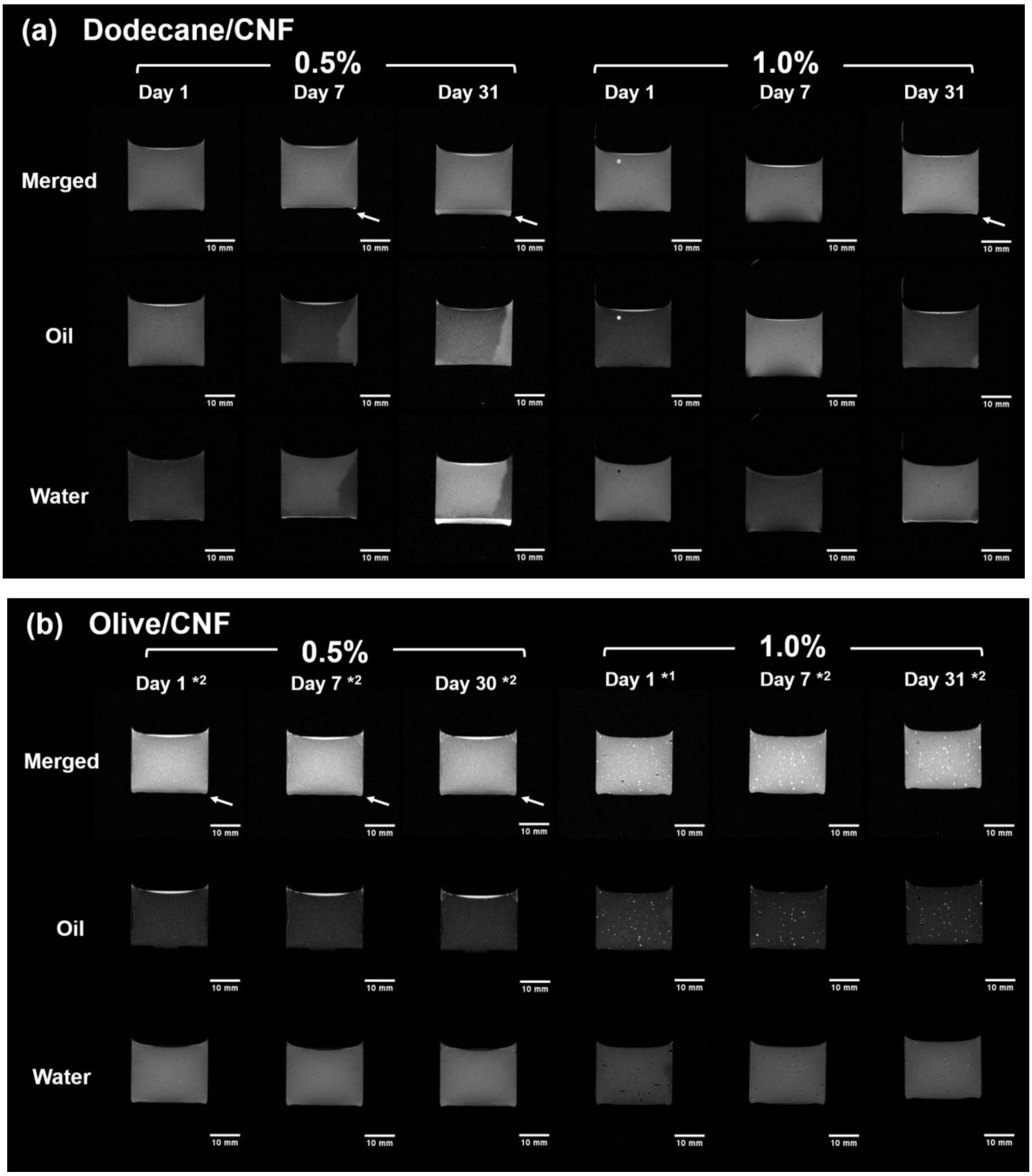

Fig. S29. Fat and water separation combined with RARE

The chemical shift was set at (a) 4.0 ppm for dodecane/CNF emulsions, (b) 3.5 ppm (*1) or 4.0 ppm (*2) for olive/CNF emulsions. In the emulsion layer, some pixels had incorrect identification between fat and water, derived from reconstruction artefacts. White arrows in the merged images represent the serum layer at the bottom.

Dodecane/CNF

0.5% day 1

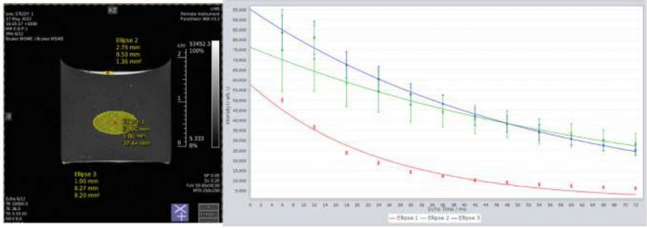

1.0% day 1

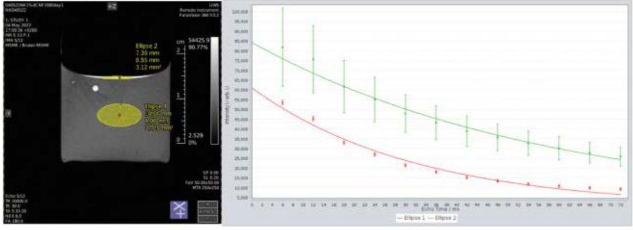

0.5% day 7

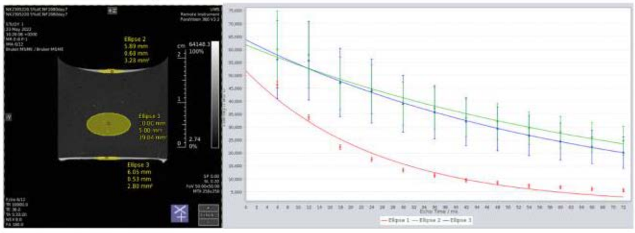

1.0% day 7

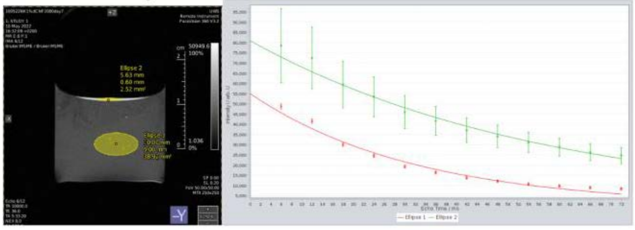

0.5% day 31

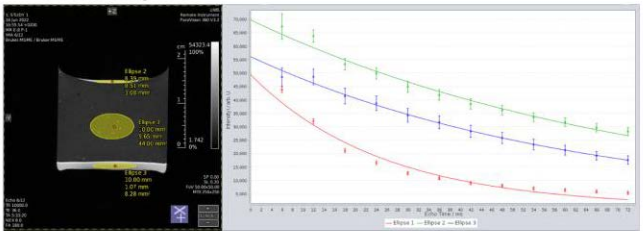

1.0% day 31

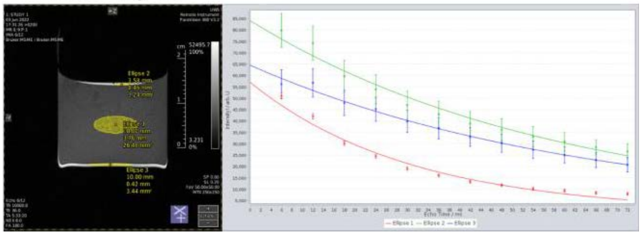

Fig. S30. The ROIs and their mono-exponential fitting to obtain the mean T_2 values of each layer in the d-CNF emulsions

The attenuation data corresponds to the emulsion layer (Ellipse 1, red), free oil (Ellipse 2, green), and serum layer (Ellipse 3, blue). The error bars are given by the standard deviation.

Olive/CNF

0.5% day 1 1.0% day 1

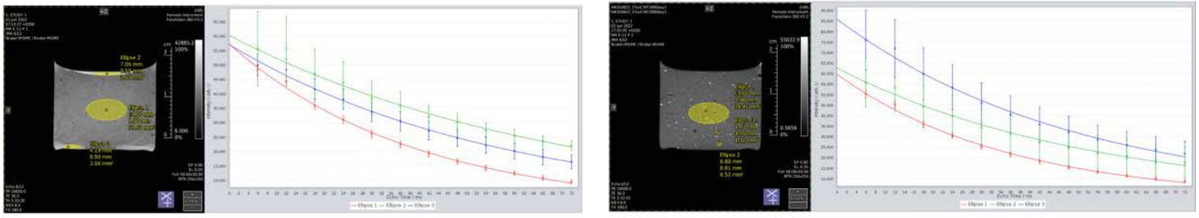

0.5% day 7 1.0% day 7

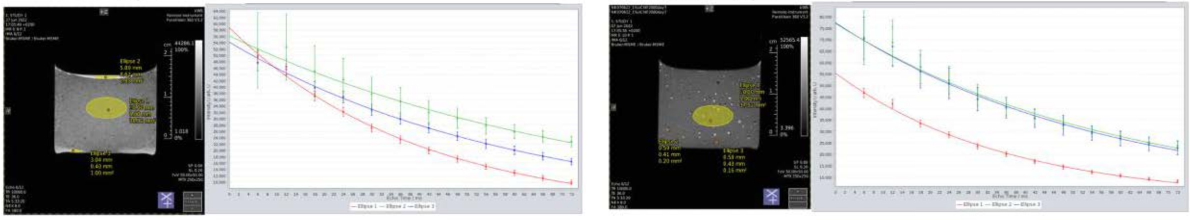

0.5% day 30 1.0% day 31

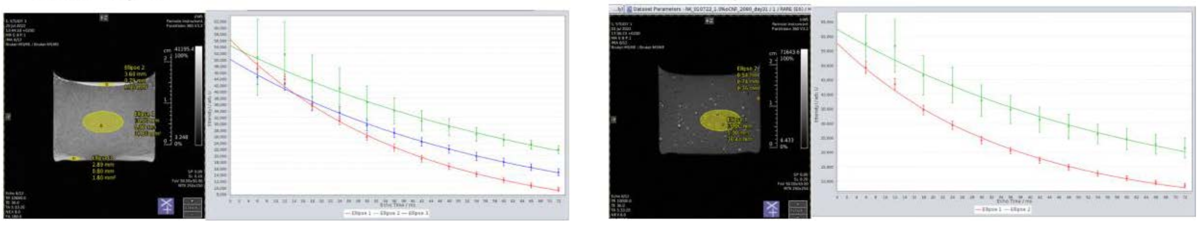

Fig. S31. The ROIs and their mono-exponential fitting to obtain the mean T_2 values of each layer in the o-CNF emulsions

The attenuation data of 0.5% CNF corresponds to the emulsion layer (Ellipse 1, red), free oil (Ellipse 2, green), and serum layer (Ellipse 3, blue). The attenuation data of 1.0% CNF corresponds to the emulsion layer (Ellipse 1, red), and oil droplets (Ellipse 2 and 3, green and blue). The error bars are given by the standard deviation.

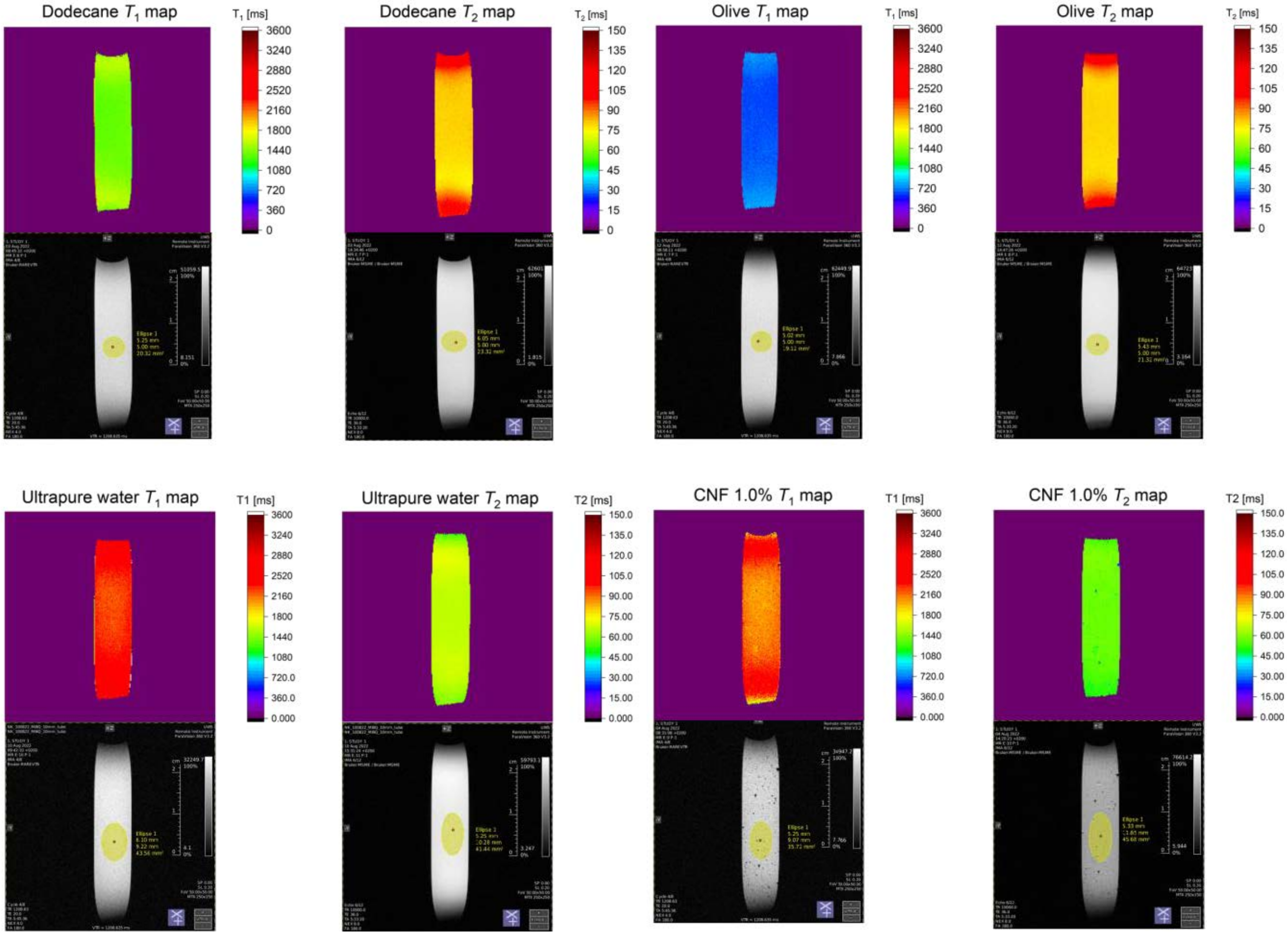
Dodecane T_1 map

Dodecane T_2 map

Olive T_1 map

Olive T_2 map

Ultrapure water T_1 map

Ultrapure water T_2 map

CNF 1.0% T_1 map

CNF 1.0% T_2 map

Fig. S32. T_1 and T_2 maps of neat dodecane, olive oil, ultrapure water, and CNF 1.0%

Each image was reconstructed by 200 μm isotropic voxels. The mean T_1 and T_2 were extracted from the center part (yellow circle) of each sample shown in the graph below each map, i.e., the best position within the RF coil (to avoid the artefacts at the edge of the samples or image window).

Dodecane/CNF

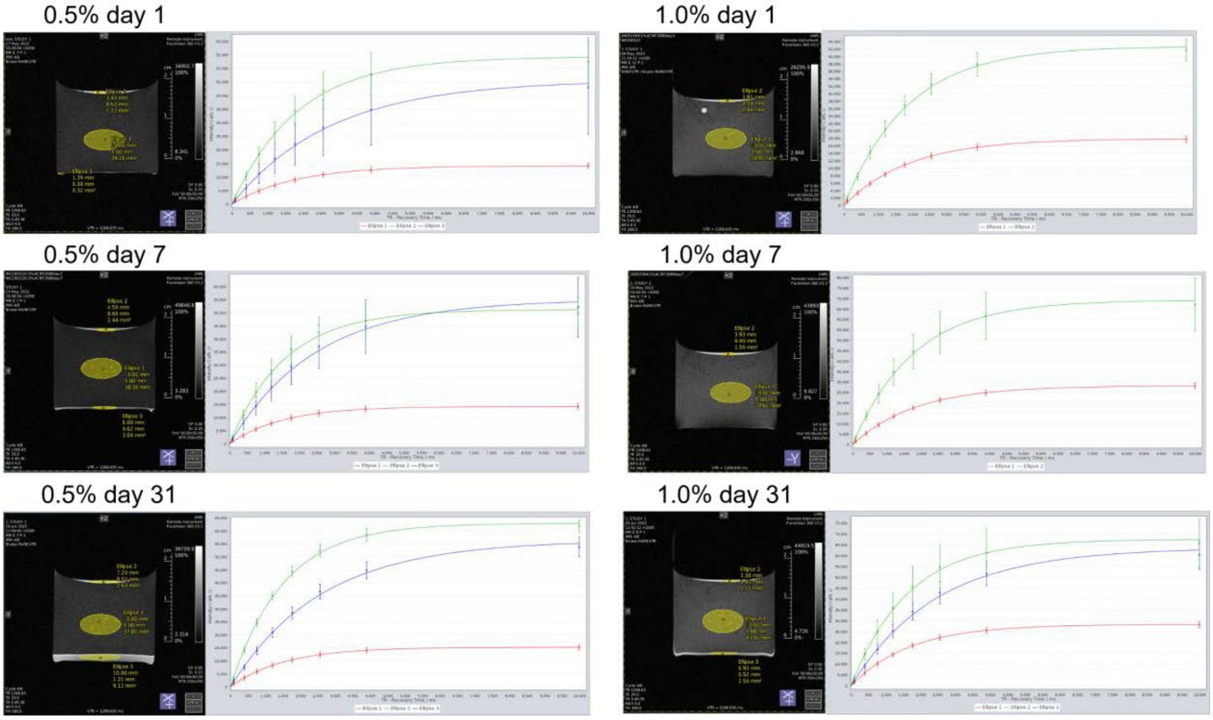

Fig. S33. The ROIs and their mono-exponential fitting to obtain the mean T_1 values of each layer in the d-CNF emulsions

The attenuation data corresponds to the emulsion layer (Ellipse 1, red), free oil (Ellipse 2, green), and serum layer (Ellipse 3, blue). The error bars are given by the standard deviation.

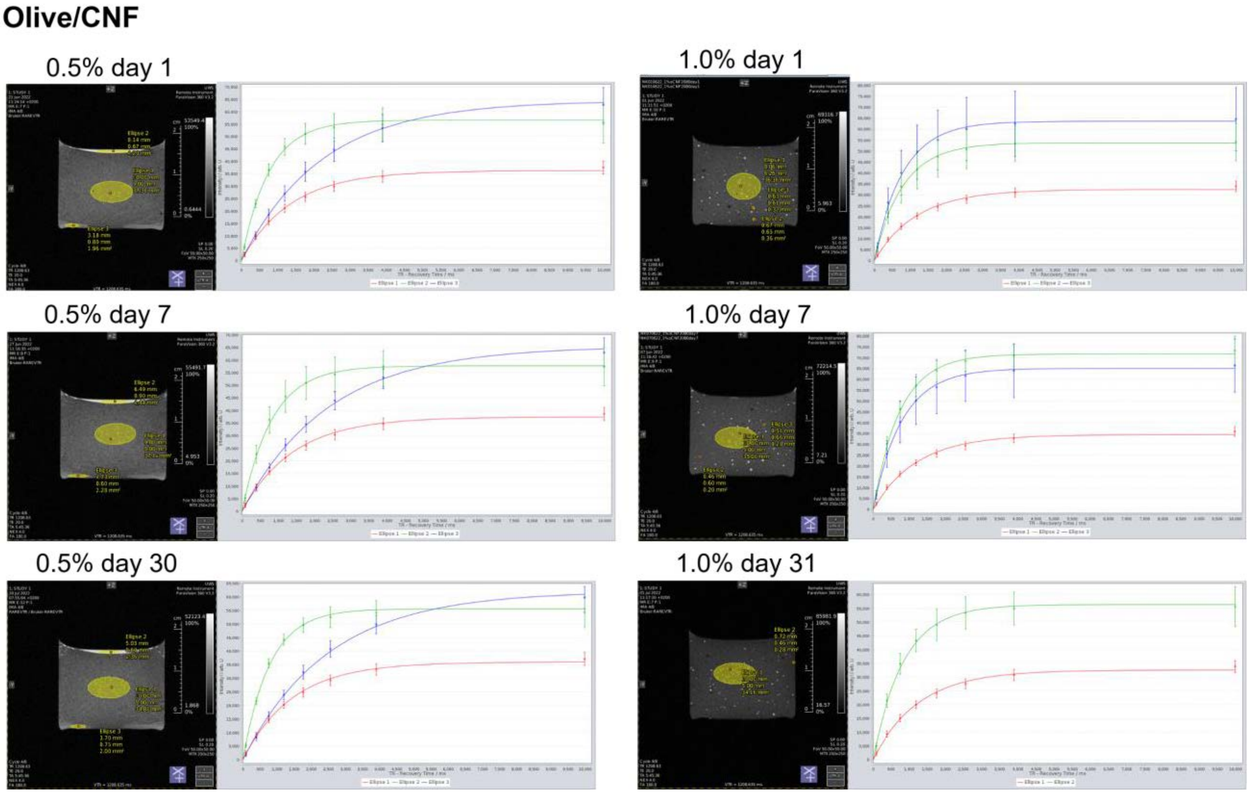

Fig. S34. The ROIs and their mono-exponential fitting to obtain the mean T_1 values of each layer in the o-CNF emulsions

The attenuation data of 0.5% CNF corresponds to the emulsion layer (Ellipse 1, red), free oil (Ellipse 2, green), and serum layer (Ellipse 3, blue). The attenuation data of 1.0% CNF corresponds to the emulsion layer (Ellipse 1, red), and oil droplets (Ellipse 2 and 3, green and blue). The error bars are given by the standard deviation.

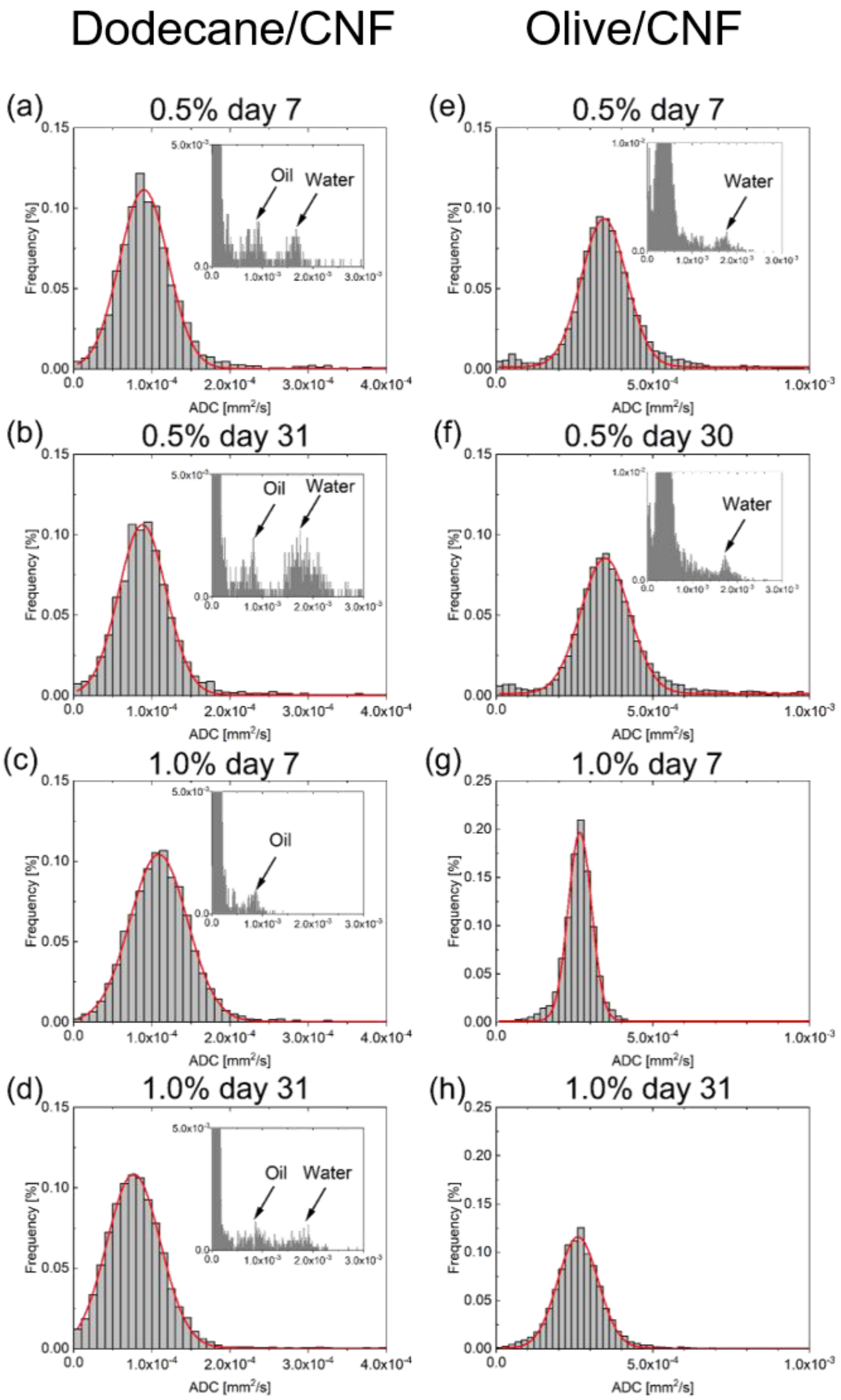

Fig. S35. The histograms of ADC values of the d-CNF and o-CNF emulsions

(a)-(d) represent d-CNF, and (e)-(h) represent o-CNF. The solid red lines are gaussian fitting curves and given R-squared values > 0.99. The inset graphs are expanded regions of fast diffusion components; free oil and/or water.

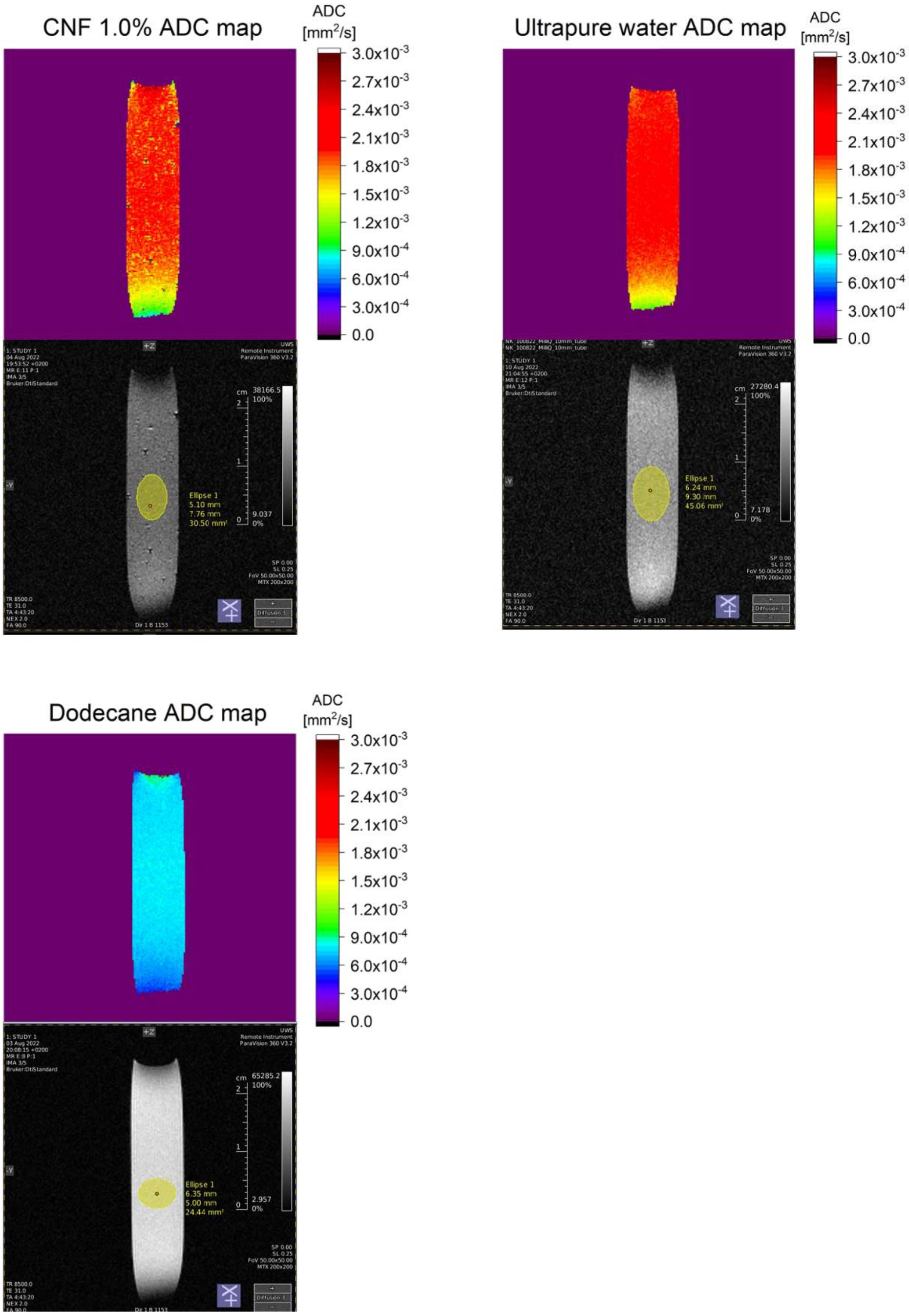

Fig. S36. ADC maps of CNF 1.0%, ultrapure water, and neat dodecane

The mean ADC values were extracted from the center part (yellow circle) of each sample shown in the graph below each map, i.e., the best position within the rf coil (to avoid the artefacts at the edge of the samples or image window).

Table S7. A comparison of the mean ADC calculated from the selected ROIs and the diffusion coefficients determined from spectroscopy NMR at 298 K

	Mean ADC ± standard deviation × 10^{-3} [$mm^2\ s^{-1}$]	D ± standard error × 10^{-3} [$mm^2\ s^{-1}$]
Dodecane	0.787 ± 0.002	0.961 ± 0.002*
Olive	n.d.	(1.007 ± 0.004) × 10^{-2}*
Ultrapure water	2.06 ± 0.07	2.299 from Ref. [248]
H_2O in CNF 1.0% dispersion	1.95 ± 0.12	2.20 ± 0.03

*The experiments were performed in duplicate and the results are given as weighted averages.